

ON-OFF α-hemolysin photopore

Xingzao Wang

Linacre College
University of Oxford
Department of Chemistry

A thesis submitted for the degree of
Doctor of Philosophy

Trinity Term 2024

Abstract

Alpha-hemolysin (αHL) is a robust transmembrane protein pore that can be engineered to accommodate a wide range of biological functions. However, an αHL nanopore capable of regulating ionic flow across a lipid bilayer in a photoreversible manner has never been prepared. Such spatiotemporal control of ionic flow would aid in developing synthetic bio-iontronic circuits and provide a means of transmembrane communication. Previous studies in our group have demonstrated that the β barrel of the αHL pore can be modified with irreversible photocage or reversible azobenzene photoswitch. Here, we improve the photoswitchable nanopore by introducing seven arylazopyrazole at the constriction of αHL. This thesis demonstrates a nanopore $(E111C\text{-}pzMe)_7$ combining the properties of quantitative reversible photoswitching and diode-like rectification in the low-conductance state. By conjugation of azo photoswitches to a specific site on the αHL polypeptide, we create a heptameric αHL nanopore with 95% current gating (ON/OFF switching) at the single molecule level and 85% current gating at the ensemble level. A rectification ratio of >5 is achieved with photopores in the diode state by either direct or alternating voltage input. The second study explores and pursues the mechanistic understanding of photoswitching in the nanopore–through single-molecule nanopore spectroscopy. This novel technique extracts the photoisomerization kinetics of the photoswitch from an electrical recording of a heteroheptameric photopore. The line shape of the single-molecule excitation spectrum is in agreement with ensemble spectroscopy data. In summary, the photopores offer solutions for optical control of transmembrane ionic communication and stochastic spectroscopic methodology for single-molecule chemistry. These are potentially valuable for synthetic biology, neuroscience, photopharmacology, and bioelectronics.

Dedication

This thesis is dedicated to my family.

Declaration

I, Xingzao Wang, declare that this thesis is entirely my work, except where otherwise stated.

The following experiments were conducted in collaboration with other researchers:

- Synthesis of photoswitches Br-pzMe, Br-pzH and Br-fAzo was performed by Aidan Kerckhoffs under the supervision of Matthew Langton.
- Single-channel recording chambers were designed by Xingzao and fabricated by Howard Lambourne.
- Ultraviolet–visible absorption spectra in chapter 2 were collected by Aidan Kerckhoffs.
- Morse code in chapter 2 was inspired by Matthew Cornell.
- Nuclear magnetic resonance spectra in chapter 2 were measured by Aidan Kerckhoffs, and the spectra in chapter 3 were measured by Lemuel Szeto and Jie-Ren Deng.
- Droplet networks in the final chapter were printed by Jorin Riexinger.

Acknowledgements

I want to thank everyone who helped me during my DPhil study. In the past four years, I have harvested plenty of worthwhile experiences that will be valuable for the future. However, the most memorable lesson is to find and identify people who genuinely support me and never leave me alone:

1. I want to thank Hagan and Yujia for giving me the opportunity to work on the project freely. The freedom and 'off-track' work fueled the stochastic exploration events throughout my entire DPhil, including the electric-catfish droplet battery, purification of heteroheptameric αHL isomers and droplet toothpaste, etc.

2. Without Aidan's and Matt's (Langton) fantastic azobenzene, the αHL alone would just be a filthy toxin. I still miss Aidan's stamppot and hope he can cook it again someday.

3. I sincerely thank Jorin, Matt (Cornall) and Leonie for their adoption in Crete and daily support as close friends.

4. I will never forget the help from the rest of the group, in particular from Hanxiao, Chih-Wei, Lemuel and Kenny.

5. Without the help of the PTCL mechanical workshop, there will be no research about photopore. All thanks to Howard's great work on the recording chamber, it provides a solid foundation for my research.

6. I want to thank my parents for their financial and emotional support over the past four years.

I would also like to thank the European Research Council Advanced Grant (SYNTISU) and a University of Oxford John Fell Fund (0013248) for supporting my research.

Publications

Chapter 2:

Wang, X., Kerckhoffs, A., Riexinger, J. et al. ON–OFF nanopores for optical control of transmembrane ionic communication. Nat. Nanotechnol. (2025). https://doi.org/10.1038/s41565-024-01823-x

Chapter 3:

Wang, X. et al. Nanopore-based single-molecule excitation spectroscopy. In preparation.

Contents

Abstract 2
Dedication 3
Declaration 4
Acknowledgements 5
Publications 6
Contents 7
Abbreviations 9
Chapter 1 11
1.1 Light-controlled ionic flow in synthetic biology 20
1.2 Azo photoswitch: pzMe 24
1.3 Nanopore: αHL 27
1.4 Overview of the thesis 31
Chapter 2 32
Abstract 33
2.1 Introduction 34
2.2 Construction of photoreversible nanopores 35
2.3 Reversible ON-OFF photopores 44
2.3 Switchable iontronic diode properties 60
2.4 Light-to-ionic signal conversion 63
2.5 Conclusions 66
2.6 Methods 67
2.6.1 General information 67
2.6.2 Custom recording chamber 67
2.6.3 Site-directed mutagenesis of αHL cysteine mutants 68
2.6.4 Expression and purification of αHL cysteine mutants 68
2.6.5 Conjugation of photoswitches 69
2.6.6 Formation and purification of photopore homoheptamers 70
2.6.7 Single-channel and ensemble experiments 70
2.6.8 Ion selectivity and electro-osmotic flow 71
2.6.9 Transmembrane signal transmission by light-to-current conversion 72
2.7 Appendix 75
Chapter 3 79
Abstract 80

3.1 Introduction 81
3.2 Preparation of heteroheptamer nanopore 85
3.3 Photoisomerization in the nanopore 87
3.4 Irradiance-dependent photoisomerization rates 90
3.5 Single-molecule excitation spectra 93
3.6 pzMe Spectrum in the polarizable environment 100
3.7 Acid-accelerated isomerization 105
3.8 A minimum spectrophotometer 112
3.9 Conclusions 115
3.10 Methods 117
3.10.1 General information 117
3.10.2 Expression and purification of αHL cysteine monomers 117
3.10.3 Conjugation of photoswitches 118
3.10.4 Oligomerization and purification of photopore heteroheptamers 118
3.10.5 Ensemble electrical recording 119
3.10.6 UV/Vis absorption spectrum and ^{1}H-NMR of Br-photoswitches 119
3.10.7 Acid-accelerate thermal relaxation kinetics 120
3.11 Equations 120
3.12 Appendix 122
Chapter 4 129
4.1 Case study 1 : Photopore in the droplet network 137
4.2 Case study 2 : Illumination setup for the photopore droplet network 139
4.3 Case study 3 : A ‘nanodrop’ based on single-molecule photosensor 140
References 143

Abbreviations

αHL	Alpha-hemolysin
ANOVA	Analysis of variance
AR20	Silicone oil AR20
ATP	Adenosine triphosphate
ChR2	Channelrhodopsin 2
CI	Conical intersection
Cl-azo	Chloroacetyl-azobenzene
CMC	Critical micellar concentration
DIB	Droplet interface bilayer
DMSO	Dimethyl sulfoxide
DPhPC	2-Diphytanoyl-sn-glycero-3-phosphocholine
DTT	Dithiothreitol
EtOH	Ethanol
EDTA	Ethylenediaminetetraacetic acid
(Br)-fAzo	(Bromoacetyl) *ortho*-fluoroazobenzene
IEX	Ion exchange chromatography
iGluR	Ionotropic glutamate receptor
IPTG	Isopropyl β-D-1-thiogalactopyranoside
IVTT	*In-vitro* transcription translation
LA-DNA	Light-activated DNA
LB	Lysogeny broth
LC-MS	Liquid chromatography–mass spectrometry
LED	Light-emitting diode
MQ	Milli-Q water
MS	Mass spectrometry

MscL	Mechanosensitive channel of large conductance
NA	Numerical aperture
Ni-NTA	Nickel-nitrilotriacetic acid
NMR	Nuclear magnetic resonance
OD	Optical density
PEG	Poly(ethylene glycol)
PLB	Planar lipid bilayer
PMMA	Poly(methyl methacrylate)
POPC	Palmitoyl-2-oleoyl-sn-glycero-3-phosphocholine
PR	Proteorhodopsin
PSII	Photosystem II
PSS	Photostationary state
(Br)-pzH	(Bromoacetyl) arylazopyrazole
(Br)-pzMe	(Bromoacetyl) methylarylazopyrazole
SDS-PAGE	Sodium dodecyl-sulfate polyacrylamide gel
SMS	Single-molecule excitation spectroscopy
Tris	Tris(hydroxymethyl)aminomethane
TCEP	Tris(2-carboxyethyl)phosphine
UV	Ultraviolet
v/v	Volume per volume
WT	Wild-type
w/v	Weight per volume

Chapter 1

Introduction

The chemical composition of our body resembles a complicated big soup, rich in nutrients, proteins, DNA, and other biomolecules[1]. However, what truly distinguishes us from the big soup[2] on the dining table is probably not as simple as a mixture of substances, but how they are compartmentalized as minimum units of life—cells[3]. While soup is often contained in isolated tins, the cells of our bodies compartmentalize a unique collection of functional biomolecules in the biological membranes and exercise the missions of proliferation, motility, and communication.

Although synthetic biology renders it possible to create artificial cells by encapsulating cell membrane components[4–6], enzymes and their substrates[7,8], or liposomes[9] as droplets, these 'Frankenstein' cells could only preserve the essential molecular-level functions such as enzymatic reactions[8], chemical sensing[10], and cell-free expression of protein[11]. These functions are achievable within a single artificial cell, but the loss of signal transmission amongst the cells impedes the development of advanced biological functions. For example, the signal transduction in neuron cells is mainly associated with the flow of ions across the cell membrane of axons[12]. During neuron activation, an action potential is generated due to the depolarization of sodium ions flowing into the axon; then, the repolarization occurs when potassium flows out of the axon. This process is the cornerstone of the neuronal activities that enable us to perceive and think about the world around us.

In order to control the transmembrane communication, especially the transmembrane ionic flow, the most successful examples in the past 30 years were achieved through optogenetics which employed the ion pumps or ion channels in the opsin family (**Fig. 1a**). For instance, the bacteriorhodopsin discovered in purple bacteria which colored a lake in Namibia into purple, initiated the bottom-up synthetic biology applications to control transmembrane ion concentrations (**Fig. 1b,c**).

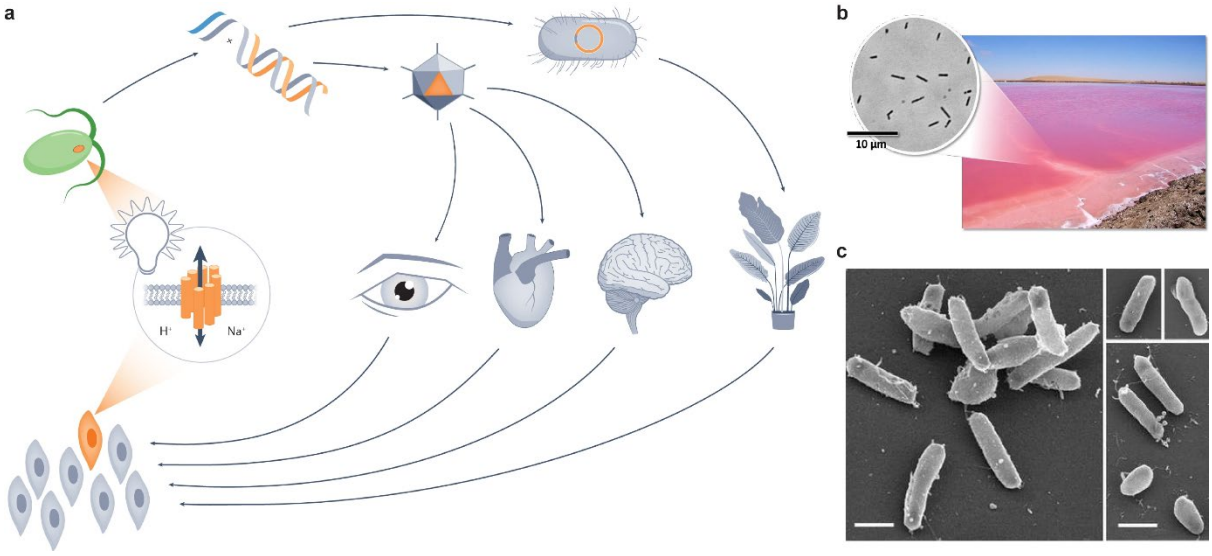


Fig. 1 | Optogenetics as a tool to control transmembrane ionic communication. a, Transfection of microorganism ion channels into host cells to control the cellular communication in animals or plants. The rhodopsin (orange) in optogenetics relies on DNA engineering and viral vector transfection to deliver the foreign DNA encoding the ion channel. Reproduced from Emiliani *et al.*[13]. **b,** A photo of a hypersaline lake in Namibia. The *Halobacterium salinarum* stains its habitat purple due to their purple membrane. Reproduced from Bollschweiler[14]. **c,** Scanning electron microscopy of *Halobacterium salinarum*. Scale bar: 1 µm. Reproduced from Gruber *et al.*[15].

Bacteriorhodopsin is a light-driven proton pump in which a retinal molecule is covalently bound to a lysine side chain via an imine moiety. Upon irradiation with light in the 500–650 nm range, the retinal chromophore absorbs a photon and undergoes isomerization from the *all-trans* to the *13-cis* configuration. This conformational change triggers a response in the surrounding protein residues, leading to changes in ion flow. Using bacteriorhodopsin proton pump, light-driven transmembrane proton gradient can be harvested to generate adenosine triphosphate (ATP) synthesis in the artificial cells[16] (**Fig. 2a**). Likewise, a synthetic nerve made from droplets containing archaerhodopsin-3 transduces light stimulus into ionic signal and spread through the hydrogel neurons[17] (**Fig. 2b**). However, protein engineering and expression of rhodopsins in the eukaryote cells (*Leishmania tarentolae*[18]) usually takes more than six weeks for the proper incorporation of the retinal chromophore in the protein. Similarly, archaea (*Halorubrum sodomense*[19]) purification requires 110,000 × *g* centrifugation for 15 h at 15 °C. These time-consuming approaches, compared to protein expression in *Escherichia coli*, are not ideal for synthetic biological applications. Another prime example is channelrhodopsin-2 (ChR2), a cation-selective photoresponsive ion

channel. In a study of optogenetic cortical spreading depolarizations by Chung *et al.*, a non-invasive optogenetics approach is established to trigger the spreading depolarization in mice brain expressing channelrhodopsin-2 in neurons[20] (**Fig. 2c**). However, a heat-generating 10 mW transcranial illumination is required and might cause pain and fear of the animal. This invasive surgical treatment is not uncommon for animals in the optogenetics labs. Another concern of opsin ion channels is the fast off-kinetics. Although ChR2 mutant C128 lengthens the activated state up to 31 min[21], the off-kinetics of microbial opsins generally falls in the range of 0.01-0.1 s[13] (**Fig. 2d**). To tackle these challenges, we aim to lay the foundation for an alternative optical approach for transmembrane communication—combining animal-free synthetic tissue and easy-to-prepare nanopore-based photoswitchable ion channel with slow off-kinetics. Thus, ON-OFF α-hemolysin is the theme of this work.

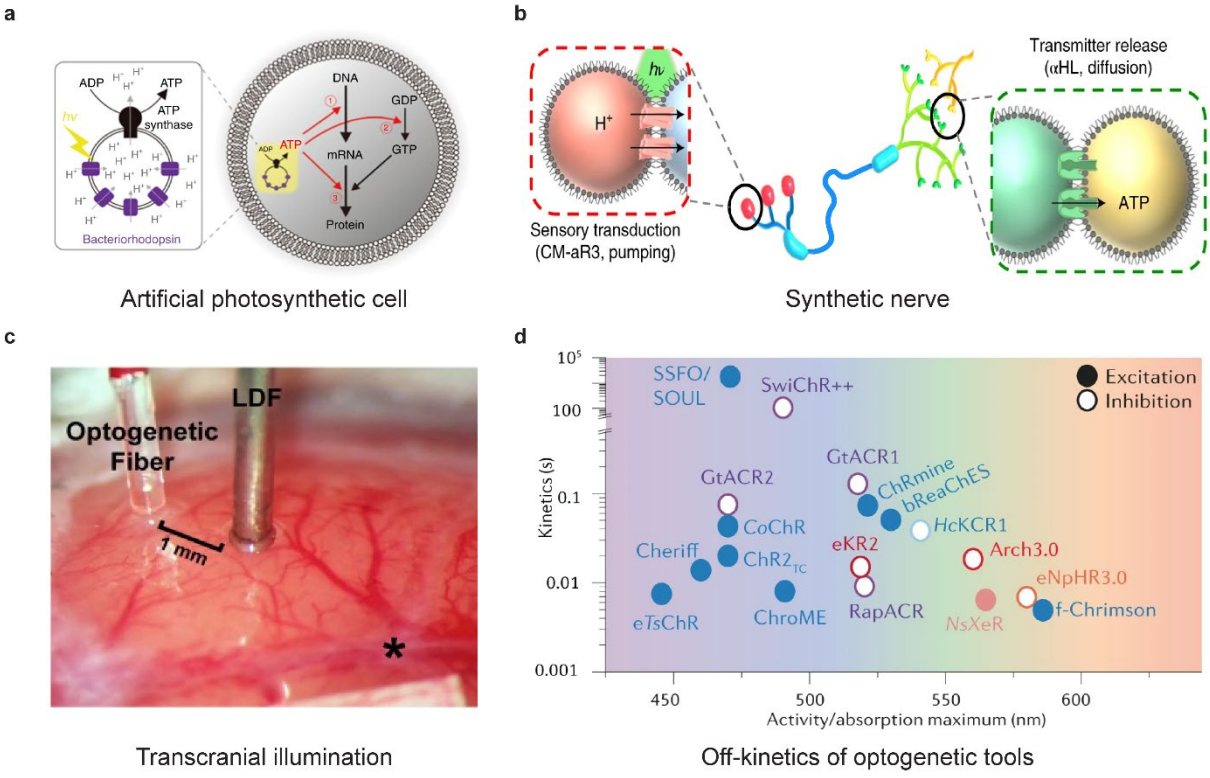


Fig. 2 | Achievements and drawbacks of opsin tools. a, Light-controlled ATP synthesis driven by bacteriorhodopsin. The bacteriorhodopsin pumps the proton inside the liposome lipid bilayer, and F_oF_1-ATP synthase synthesizes ATP by pumping the proton outward. Reproduced from Berhanu *et al.*[16]. **b,** Propagation of light stimulus through the synthetic nerve. The terminal droplet interface bilayer contains archaerhodopsin-3 pumping the protons to the synthetic nerve. Reproduced and adapted from Hoskin *et al.*[17]. **c,** An optical fiber and a laser Doppler probe placed on the brain of a mouse through the skull. Reproduced from Chung *et al.*[20] **d,** Commonly used optogenetic tools. The

channelrhodopsin-2 is labelled as $ChR2_{TC}$. The vertical axis is the temporal off-kinetics for the lifetime of activated state in the dark after irradiation. Reproduced from Emiliani *et al*.[13].

In this thesis, we combine two key components to build the photoswitchable nanopore: the methylarylazopyrazole (pzMe) photoswitch and the alpha-hemolysin (αHL) nanopore. The pzMe photoswitch lies in the family of azobenzene derivatives, which have been known by humanity for over 150 years[22]. Originally, azobenzene and its derivatives were used as dyes[23] and antibiotics[24] (**Fig. 3a,b**). When the first time the *cis* form of azobenzene was separated from the 'ordinary' azobenzene by chloroform extraction, Hartley discovered that the photometric absorption analysis of this *cis*-azobenzene sample showed an apparent 2.17-fold increased absorption of blue light than the ordinary *trans*-azobenzene[25]. Due to the ratios of *cis*- (*Z*-) to *trans*- (*E*-) forms, under the sunlight, the absorption spectrum of the azobenzene solution changes. The underlying chemistry was also elucidated in 1953 in the work of Campbell *et al*.[26]. By absorption spectrum, melting point and dipole moment calculations, the photochromic effect of azobenzene was attributed to interconversion between more stable *E* and less stable *Z* isomers rather than disproportionation to a mixture of hydrazobenzene and azoxybenzene.

The azobenzene *E/Z* photoisomerization starts with excitation from ground state S_0 to excited states S_1 or S_2 by ultraviolet and visible irradiation as shown in **Fig. 3c**. The S_2 state (~320 nm, ~22000 L mol^{-1} cm^{-1}) is a symmetry allowed π-π* transition, while the S_1 state (~440 nm, ~4000 L mol^{-1} cm^{-1}) is a symmetry-forbidden n-π* transition[27]. At both excited states, the molecules explore the energy landscape as the dihedral angle of CNNC bond changes. Eventually, the azobenzene funnels at the conical intersection and promotes isomerization to the S_0 of the *E* or *Z* isomer. Because the S_0-S_1 and S_0-S_2 excitation have different quantum yields, the azobenzene violates Kasha's rule[28], which is a key assumption in chapter 3. From a geometry viewpoint, photoisomerization happens in three approaches: inversion, rotation and twisting (**Fig. 3d**). If the azobenzene or its derivative has limited rotation, the in-plane inversion results in similar quantum yields and satisfies Kasha's rule.

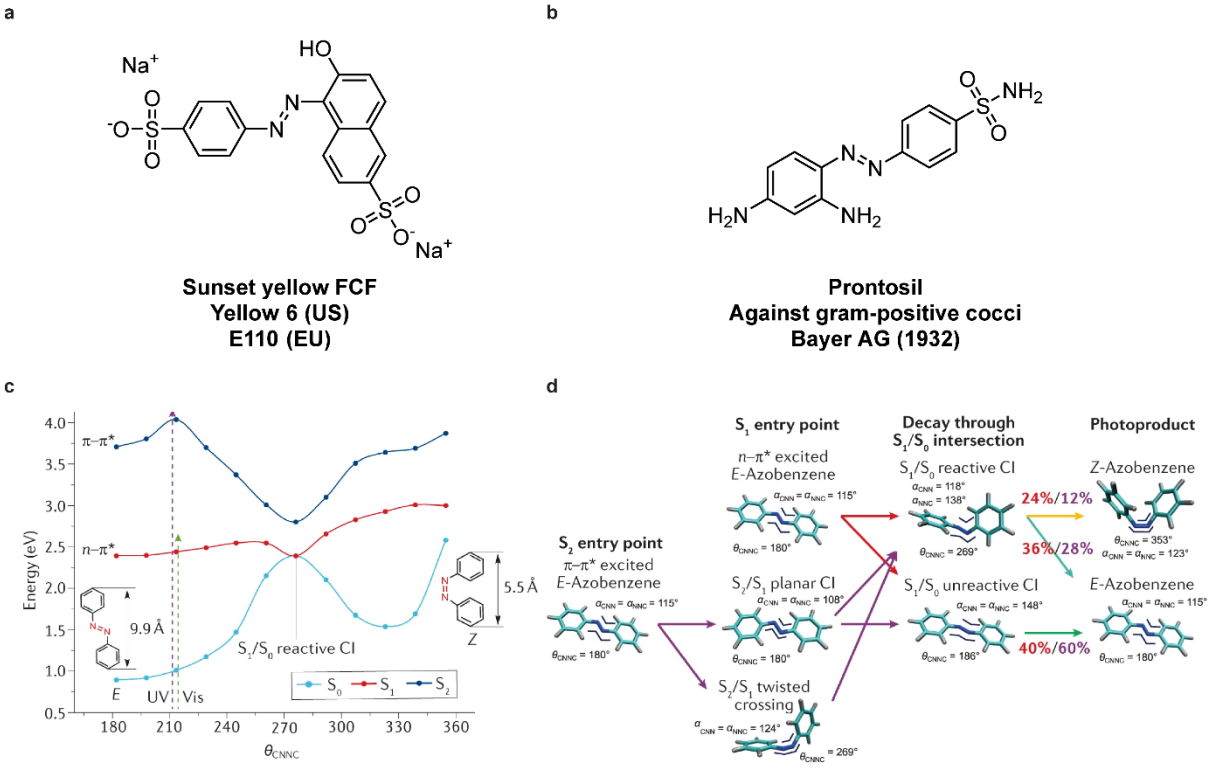


Fig. 3 | Azo compounds and azobenzene photoisomerization. a-b, Structures of sunset yellow and protonsil. **c,** Potential energy surface of ground-state and excited-state azobenzene at different CNNC torsion angles. The ground state S_0 is in cyan; The excited states through π-π* transition (S_2) and n-π* transition (S_1) are in blue and red, respectively. The CNNC torsion angles refer to the dihedral angle of the two nitrogen atoms and two adjacent arene carbons. At around θ_{CNNC} 270°, the excited states gain access at the conical intersection (CI) and relax to the ground state of *E* or *Z* isomer. **d,** The geometry of azobenzene through rotational, inversional and twisting relaxation paths. The S_2 and S_1 entry points correspond to the ultraviolet (purple dashed line) and visible light (green dashed line) excitation in a. The yellow, blue and green arrows correspond to the reactive *Z*-, reactive *E*- and unreactive *E*- isomers, respectively. Reproduced from Jerca *et al*.[29].

The photochromic properties of azobenzene give us an impressive visual impact, but the percentages of either orange (*Z*) or yellow (*E*) states are never close to 100%. After long enough irradiation until the isomer percentage reaches a photostationary state (PSS), the maximum percentage of *E* and *Z* isomers are 90% ($PSS_{436\ nm}$) and 80% ($PSS_{313\ nm}$), respectively[30]. This 10% or 20% remaining isomeric 'impurities' caused high background or limited activation in the downstream applications, in particular in enzymatic reactions. For instance, Reis *et al*. synthesized a small-molecule inhibitor containing azobenzene scaffold for light-controlled modulation of gene expression[31]. Due to the limited azobenzene PSS percentages, >5% isomers cannot be switched off, and they caused significant

background noise. Thus, the original azobenzene cannot achieve quantitative switching.

To improve either percentage of *E/Z* isomers at PSS to 100%, Weston *et al*. created a heteroaryl photoswitch (pzMe) that has a $PSS_{355\ nm}$ of >98% *Z* and $PSS_{532\ nm}$ of >98% *E* in acetonitrile[32]. Alternatively, Bléger *et al.* reported *ortho*-fluoroazobenzene (fAzo) that had a $PSS_{500\ nm}$ of >86% *Z* and $PSS_{410\ nm}$ of >91% *E*[33]. Both pzMe and fAzo showed thermal half-life for over 10 days at room temperature, and appeared to solve the challenge of quantitative switching and slow off-kinetics.

With the pzMe and fAzo in hands, the second component for a photoswitchable nanopore is the αHL nanopore. From a historical perspective, the initial attention to αHL was drawn on the pathogenesis of *Staphylococcus aureus*. In 1928, 21 children contracted the pathogen secreting αHL after injecting a contaminated diphtheria toxin-antitoxin prepration[34]. Tragically, 12 students lost their lives within 48 hours. The toxin αHL was isolated from the preparation that was improperly stored without refrigeration and infested by the *Staphylococcus aureus*. As a water-soluble protein consisting of seven 33.2 kDa-monomers, αHL was studied as a hemolytic toxin for a long time, until Song *et al.* resolved the crystal structure of αHL heptamer at 1.9 Å resolution (PDB: 7AHL)[35]. The 100-Å transmembrane β barrel extends through biological membrane, and the narrowest and widest diameters are 14 and 46 Å, respectively. In the meantime, based on the pioneering work of Hladky and Haydon, net ion movements across biological or synthetic lipid membranes was measured to estimate the number of nanopores[36]. With a pair of Ag/AgCl electrodes (**Fig. 4a**), Teflon film and external clamping potential, Bayley and Cremer adapted Hladky's work and fostered the concept of stochastic sensors inspired by biology[37] (**Fig. 4b**). The stochastic sensing offered a label-free identification of small molecules such as metal ions[38], arsenic compounds[39], and saccharides[40]. Also, the sequence information of DNA[41] and peptide[42], as well as post-translational modification[43] of protein, could be analyzed.

In chapter 3 of this thesis, the photoswitchable nanopore can be regarded as a stochastic sensor for photons, considering the light intensity as 'concentration'. The αHL is chosen as the platform for photopore for the following reasons. First, αHL

monomers tolerate extensive mutagenesis and still retain the oligomerization activity. Maglia *et al.* reported a monomer with 7 arginine mutations, and the heptamer formed stable heptamer with a total of 49 arginine[44]. Similarly, truncation of up to 10 amino acids for each monomer also allowed pore formation[45]. Covalent modification of the pore at the selected residues was expected not to inhibit pore formation. Second, crystal structures of αHL monomer and heptamer were available for the structure-based rational design of the photopore. We estimated that seven azobenzene would block the β barrel lumen completely. Third, Loudwig and Bayley reported photoisomerization of a covalently tethered single sulfo-azobenzene in αHL, which showed a constant 3% current change under irradiation[46]. This precedent work provisionally offered the starting point of photopore. Consequently, the photoswitch was conjugated to the αHL cysteine mutant Glu111Cys (E111C). Under irradiation, the ionic flow through the nanopore constriction should be regulated by the photoisomerization of azo photoswitch. Ideally, the photopore should switch between ON-OFF states, where the OFF state should have no leakage of ionic flow. In chapter 2, we will discuss the photopore design in more detail.

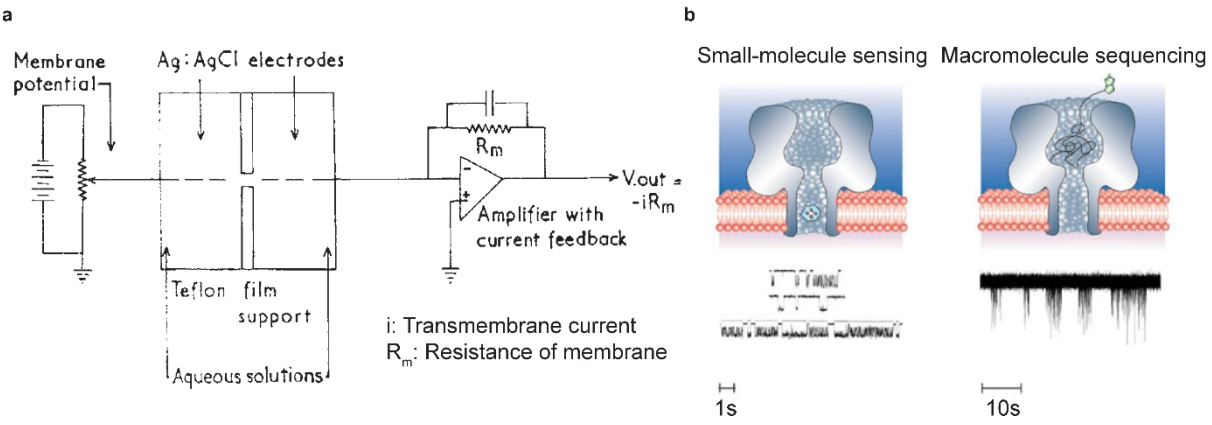


Fig. 4 | Stochastic sensing by transmembrane ionic current. a, Diagram of the electrical recording setup. Membrane potential is applied to a lipid bilayer on the Teflon film support. Ag/AgCl electrodes are placed in the aqueous solution containing 2 M KCl on each side. The current is measured as output voltage by an amplifier with current feedback. Reproduced from Hladky.[36]. **b,** Detection of small molecules or macromolecules by stochastic sensing. Small-molecules cause stochastic events visualized as blocks of current changes. The extent of the current blockage contains the sequence information of the macromolecule. Reproduced and adapted from Bayley[37].

On the path to building the ON-OFF photopore for transmembrane communication, the photochemistry of a single pzMe in the nanopore is equally attractive. For instance, to maximize the ion conductance difference between ON-OFF states, the PSS difference at the switch-ON and switch-OFF wavelengths should be ideally 100%. However, it is not straightforward to characterize the PSS of photopores through nuclear magnetic resonance (NMR), as for the small molecules. We propose a single-molecule nanopore-based approach to measure photopore's PSS and excitation spectra of the pzMe photoswitching. This leads to chapter 3, where the excitation spectrum of a single pzMe is studied at room temperature in the nanopore.

In the following sections of this chapter, we will continue to discuss more technical background of the photopore, which answers four questions. First, why do we need the photopore? Second, why is pzMe the best among the azo photoswitches? Third, why is pzMe studied in an αHL nanopore? Fourth, how is the single-molecule chemistry of azo photoswitch studied with a nanopore?

1.1 Light-controlled ionic flow in synthetic biology

The bottom-up assembly of an artificial cell is the ultimate goal in the field of synthetic biology. By engineering, synthesizing, and assembling the biomolecules present in the cell *in vitro*, the function of a cell is recreated to some extent, or a new function is grafted to the existing ones[47]. Compared to the top-down synthetic biology that manipulates existing natural systems, the bottom-up methods reduce or eliminate molecule crosstalk, cell metabolism and off-target interactions because the composition of the system is predetermined.[48] A synthetic cell constructed in this way should at least achieve supply of energy, protein production, transmembrane transport or communication.[47] However, controlling cells is not simple; it is highly valuable to determine precisely where, when, and to what extent a programmed cellular chemical or physical process started or ended. In other words, synthetic biology experiments require spatiotemporal control of stimulation, and light is an ideal non-invasive option[49].

Considering the transmembrane communication of ionic flow, the pioneering approaches included the use of ion pumps, ion-selective channels or covalent inhibitors for ion channels. Similar to the case of bacteriorhodopsin and archaerhodopsin (**Fig. 2**), Lee *et al.* reported a photoswitchable light-harvesting organelle containing ATP synthase, plant-derived photosystem II and proteorhodopsin[50] (**Fig. 5a**). Resolved by the absorption spectrum of PSII (absorption at 440 and 670 nm) and PR (absorption at 520 nm), the red light facilitated while green light inhibited ATP synthesis due to competitive depletion of proton gradient. A minimum 15-min white light irradiation was required to reach the effective pH in the synthetic organelle. Although this design demonstrated energy supply with light-powered pumps, the output lagged on the minute-to-hour scale. A possible solution to this temporal challenge was to use a light-responsive ion channel, like the photopore, to ‘deplete’ or eject the protons through the concentration gradient.

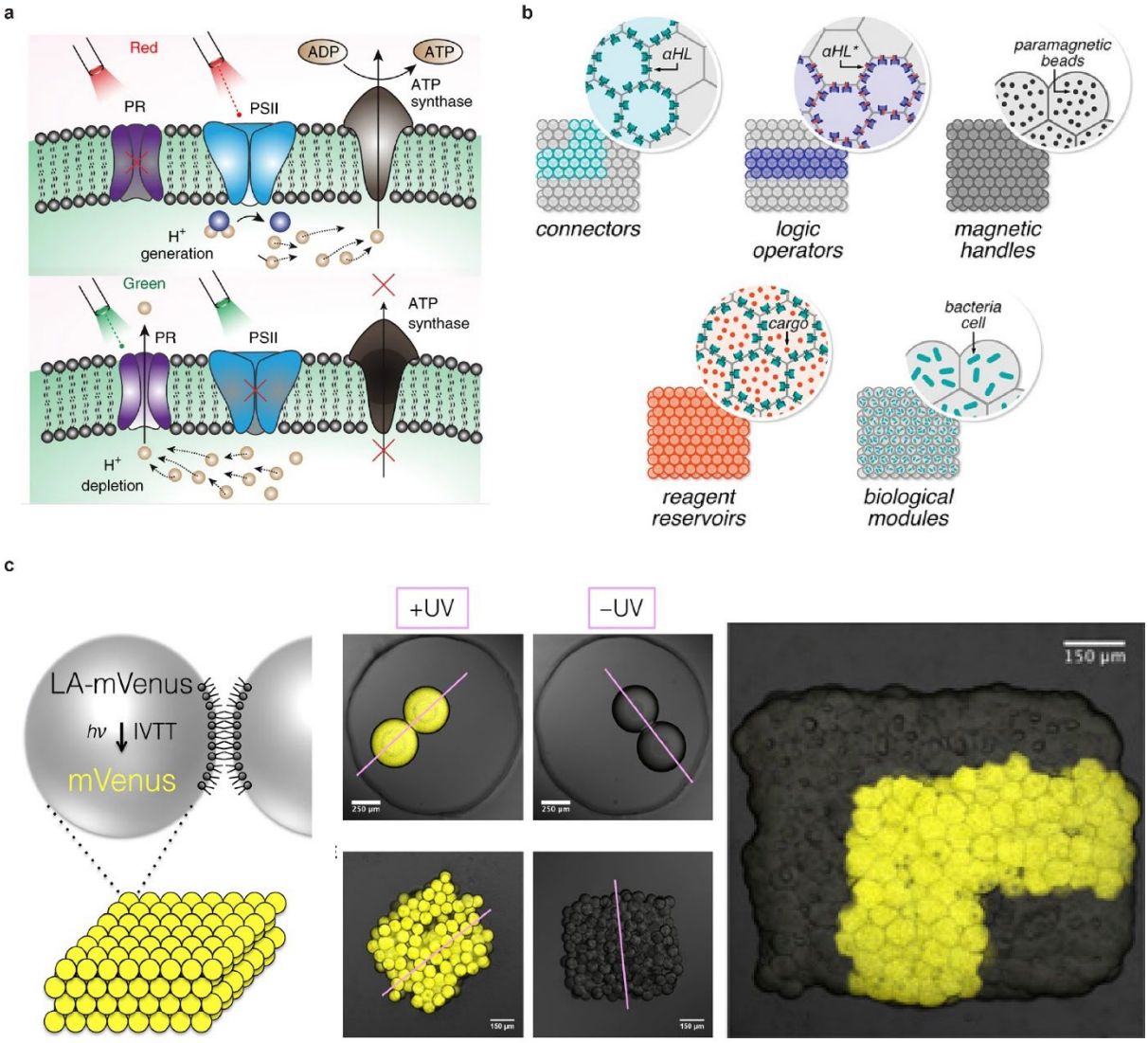


Fig. 5 | Control of transmembrane communication with light. a, A photosynthetic artificial organelle based on light-activated transmembrane proton concentration gradient. The red light activates photosystem II (PSII), inhibits proteorhodopsin (PR) and results in ATP generation. The green light inhibits PSII, activates PR, and results in the depletion of the proton gradient. Reproduced and adapted from Lee[50]. **b,** Modular 3D-printed droplet network. Each droplet interface has lipid bilayer, where αHL inserts to achieve patterned transmembrane-communication paths for ions and small molecules. Reproduced and adapted from Alcinesio[51]. **c,** Light activation of patterned expression of mVenus or αHL from light-activated DNA (LA-DNA) by UV irradiation. The irreversible activated DNA triggers in vitro transcription translation and produces fluorescent mVenus or αHL. Only the droplets containing αHL allow ionic communication. Reproduced and adapted from Booth[11].

The temporal control was even more important when multiple synthetic compartments were assembled into a synthetic tissue. Alcinesio *et al.* developed modular synthetic tissues using 3D bioprinting[51] (**Fig. 5b**). The 3D-printed networks of picolitre-sized droplets were used to release reagents in patterns, perform logic operations *in situ*, and respond to external magnetic fields. In the network for reagent release, each aqueous droplet formed lipid bilayer with the neighbors. Encapsulated αHL nanopores were inserted into these bilayers, and dye or ion reagents only translocated through the droplets containing αHL. However, this technique generated the paths or patterns by 3D printing, and the source of the reagent was only applied externally after printing. If the reagent was contained in the tissue, it would be impossible to know and control when the diffusion started. In contrast, a possible solution to this spatial-resolution challenge was to use an irreversible photoresponsive system as in **Fig. 5c**. A synthetic tissue consisting of light-activated DNA (LA-DNA) allowed pattered activation of the caged DNA, and triggered the in vitro transcription translation of fluorescent mVenus[52] or αHL nanopore. Compared to the solute-based system like LA-DNA, manipulating the transmembrane communication with photoresponsive nanopore offered an orthogonal reversible membrane-based approach. The diffusion pattern or path of solute could be reversibly activated by patterned irradiation after 3D printing.

In 2005, three impactful papers aiming to control ion channels with light were published in high-level journals, including Science[53], Nature Neuroscience[54] and Nature Chemical biology[55]. Although the target biological ion channels were mechanosensitive channel of large conductance (MscL), Shaker K^+ channel and ionotropic glutamate receptor (iGluR), all of these works used reactive photoswitch to modify the ion channels covalently. These photoswitches were structurally inspired by the original inhibitors for these ion channels used as pharmaceutics. The ion channels were mutated to accommodate a reactive cysteine with thiol. Treatment of the channel-containing membrane system with hundreds of micromolar reactive photoswitch allowed modification of channels *in situ*. To react with the thiol, iodoacetyl group or maleimide was used. However, the iodoacetyl group was photosensitive and promiscuous to amines and other nucleophilic groups[56]. The maleimide reaction formed racemic mixtures of the adduct, and complicated the stereochemistry of the adducts[57]. In the protocol of modification,

the reactive photoswitches for ion chancel must be present from the beginning of the experiment and activation with UV lead to channel opening. Thus, starting and ending points of transmembrane communication could be determined (**Fig. 6**). However, the inhibitors could diffuse away from the membrane of interest[49], effectively lose control of the communication, and crosstalk with other thiols in the system. Overall, for synthetic biology, the ideal photopore should have minimal leakage of ions at the OFF state, long ON-state lifetime and quantitative switching.

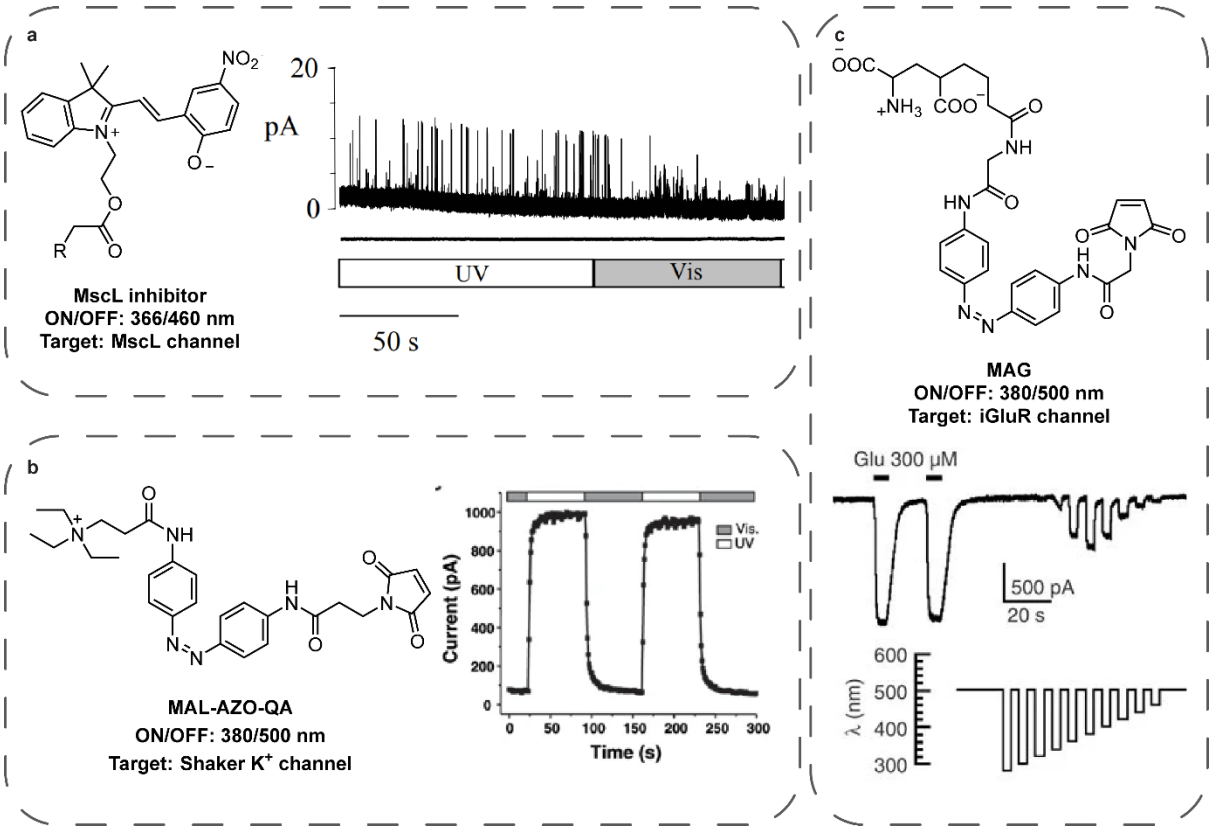


Fig. 6 | Reactive photoswitchable inhibitors for thiol-containing ion channels. Each panel contains the structure of the inhibitor and the electrophysiological trace under irradiation. In **a**, the modified MscL with a spiropyran photoswitch through iodoacetyl group (-R = -I) generates opening spikes under UV, while fewer spikes under visible light. Both **b** and **c** use maleimide handle, but *R/S* isomers might form when thiol attacks the maleimide double bond. Reproduced and adapted from Kocer[53], Banghart[54] and Volgraf[55].

1.2 Azo photoswitch: pzMe

To date, the original azobenzene is still the predominant choice of photoswitch[29] since its photochemistry is well-characterized and easy to synthesize. However, azobenzene and most of its derivatives suffer from the *E/Z* ratios that are often lower than 100%[30,58]. Consequently, No matter whether the *E* or *Z* isomer corresponds to the ON or OFF state, the quantitative *E/Z* switching, lifetime of thermal relaxation and the wavelengths of absorption should be optimized. Here, we listed the azobenzene completely or partially fulfill these requirements in **Fig. 7**. The most important characteristic is the PSS because the remaining undesired isomer of the photoswitch might generate an overwhelming background signal in the OFF state. Based on the results in chapters 2 and 3, the author believes that PSS > 95% is a boundary for an ON-OFF photopore. The compounds **pzMe**[32], **pzH**[59] and **3**[60] appear to fulfill the PSS requirement.

Second, the thermal lifetime of azobenzene derivatives ranges from nanoseconds to days at room temperature[61,62]. The photopore can be made with fast OFF-kinetics that resemble the bacteriorhodopsin ion pumps, while the photopore with slow OFF-kinetics has a similar application as the step-function opsins[21]. To improve sensitivity and reduce the light intensity required for switching, the long thermal lifetime longer than a day is favored. The compounds have days of lifetime include **1**, **pzMe**, **pzH**, **2**[59], **3** and **fAzo**[33,63]. Interestingly, the lifetime of **2** and **fAzo** is longer than two years.

Third, A redshifted absorption maxima could be advantageous for tissue penetration[64]. The visible and near-IR wavelengths are preferred, which matches the absorption of compounds **3**, fAzo, **4**[65] and **5**[66]. Notably, the absorption band of each isomer is directly associated with the PSS, as the PSS is determined by the ratio between *E/Z* isomer at given wavelengths. Thus, fining tuning of PSS and absorption maxima concurrently is a challenging dilemma.

Fourth, the solubility of the photoswitch in water is crucial as the αHL monomer has to retain its ability of oligomerization to a heptamer[56] if the conjugation requires denaturing organic solvents or surfactants. The conjugation reaction between the photoswitch and the αHL is preferably in the aqueous solution, with <30% DMSO.

The DMSO content is a practical concern because over 30% (v/v) DMSO suppresses the LC-MS signal, and might impede the oligomerization capability of the monomer. Experiments in chapters 2 and 3 showed that the compounds **pzMe**, **pzH**, **fAzo** were all water soluble, and complete conjugation only requires 50 equivalence of photoswitch to the protein. However, for the water-insoluble dyes or photoswitch, the reaction for over three days with more than 1000 equivalence of photoswitch could only reach 30% conversion.

Fifth, the azobenzene derivative undergoes acid-accelerated thermal relaxation, which may reduce its lifetime considerably[67]. Meantime, at low pH down to pH −0.8, the diazo nitrogen atoms might be protonated to azonium, which is reported for redshifted absorption bands, leading to a change in PSS. Therefore, the photoswitch preferably should avoid internal acid groups such as carboxylic acids or sulfonic acids if long thermal lifetime is the goal. Despite this limitation, the acid-accelerated thermal relaxation enables the development of pH-sensitive nanopores. Fast off-kinetics also allow tight control of the pore opening, as the pore closes rapidly after irradiation. In chapter 3 we showed that the acid-accelerated thermal relaxation[68] of pzMe shortened the lifetime of 10 days to 4 minutes at pH 3.4.

Sixth, the absorption spectrum is also dependent on the solvation environment. It is difficult to predict how the photoswitch behaves in the nanopore confinement[69], nor compare it to any solvents[70]. Thus, the photoswitch insensitive to the solvation environment is preferred. The aryl azocyclopropenium **6**[71] might be a good option for its small size.

Finally, for future biological applications, the photoswitch should be redox-resistant. Previous studies showes that azobenzene and BF_2-coodinated azo compound **5** is susceptible to reductants such as DTT and NADH[29], which cleaves the diazo double bond, leading to two aryl amino groups. The potential solution to reduction is ortho-thiol substituted azobenzene **7**[72], despite poor PSS and half-life.

Overall, these are the seven criteria for choosing photoswitches, where the scope is narrowed down to three candidates: the methylarylazopyrazole (pzMe), arylazopyrazole (pzH) and ortho-fluoroazobenzene (fAzo). However, we conjugated pzMe, pzH and fAzo to the nanopore, and discovered that only pzMe offers > 30%

ion flow change in ON-OFF switching cycles and more details are available in chapter 2. In addition to the ON-OFF switching, the azobis-triazole **8**[73] shows absorption ranging from 200-800 nm, which is excellent for the wavelength detection or single-molecule spectrophotometer proposed in chapter 3.

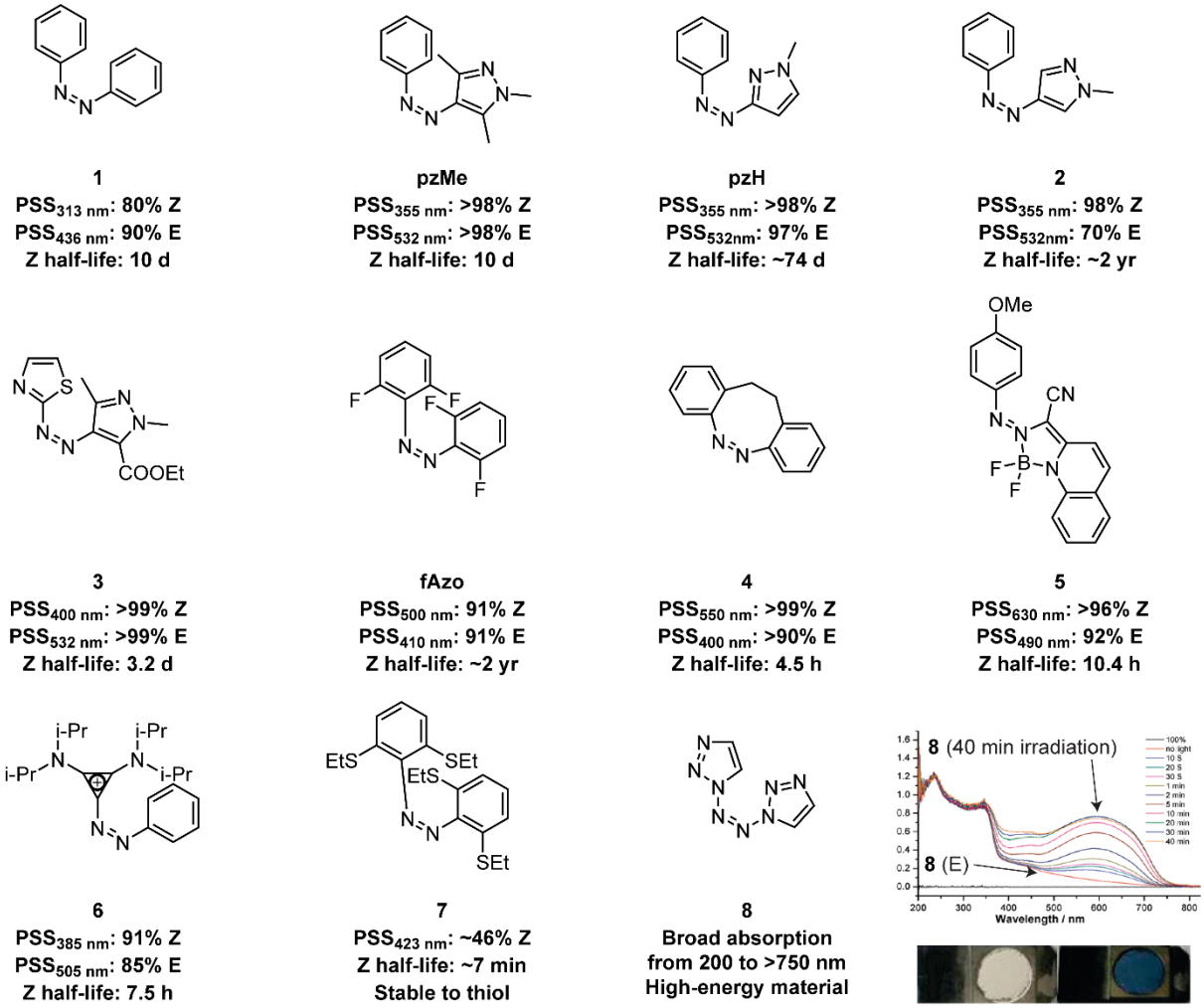


Fig. 7 | Structures, PSSs and thermal half-life of azo compounds. The right-bottom UV-Vis spectrum shows the absorption of compound 8 from 200 to 800 nm. The *E* isomer (white) turns to *Z* isomer (blue). Reproduced and adapted from multiple sources[32,33,59,60,65,66,71–73].

1.3 Nanopore: αHL

Nanopore is a type of transmembrane protein that extends a hollow channel through the biological membrane. They have a wide range of applications in molecule sensing for small molecules[42] or sequencing of biopolymers[74]. αHL is a 33.2 kDa pore-forming toxin initially separated from *Staphylococcus aureus*[75]. This nanopore consists of seven identical monomer subunits and has a preference on phosphocholine containing lipid bilayers (**Fig. 8a**). By binding to the receptors or lipid bilayer, αHL monomer forms pre-pore, opens its N-terminal latch (Ala1-Val20) and penetrates the membrane as a homoheptamer (**Fig. 8b**). With the established characterizations such as crystal structure[35], protein engineering[76] and hemolysis activity[56], αHL became a popular choice for sensing or single-molecule chemistry studies.

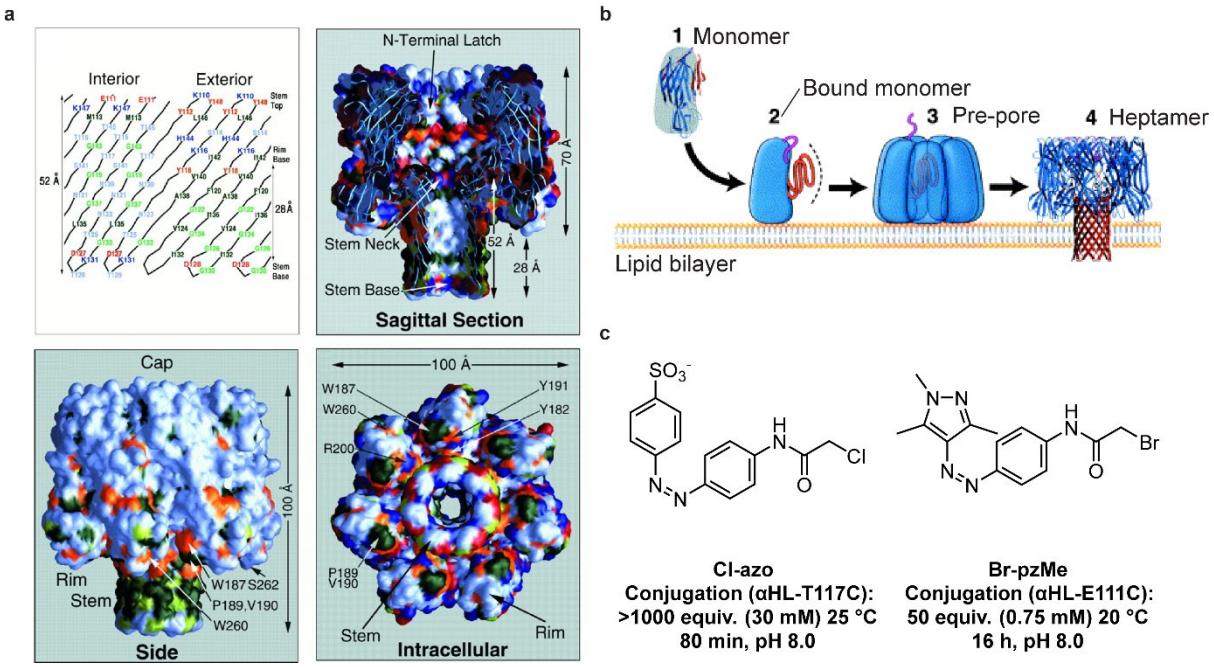


Fig. 8 | Models of αHL and haloacetyl photoswitch for αHL cysteine mutants. a, Schematic representation of αHL dimensions. The first insets show the residues in the β barrel from E111 to K147. **b**, Mechanism of αHL assembly. The monomer N-terminal latch is shown in pink, and the folded transmembrane domain is shown in orange. Reproduced and adapted from Song[35] and Montoya[77]. **c**, Schematic representation of haloacetyl photoswitches.

The αHL is adequately robust to accommodate various mutations or engineering in the transmembrane domain. Even by truncating the whole transmembrane domain

(ΔT115-T125)[45] or introducing seven arginine residues[44] by site-directed mutagenesis, the monomers still express in *E. coli* and form heptamers. For the mutants designed for sensing electrophiles such as arsenic[39] compounds, a residue in β barrel is often mutated to cysteine to perform nucleophilic attack on the analyte. The single-channel recording experiment (**Fig. 4**) reveals the conductance change of the pore by the reversible reaction, and allows determination of the analyte identity, concentration and reaction mechanisms. On the other hand, by conjugating thiol-selective maleimide or halo-acetyl moieties to the cysteine residue, the covalently modified αHL are also used to detect metals ions[78] through N-propyliminodiacetic acid and saccharides[40] through boronic acid.

Furthermore, αHL is chosen as a nanoreactor to study the photoisomerization of azobenzene (Cl-azo)[46] (**Fig. 8c**). Compared to the previous work using the chloroacetyl group; this work of Br-pzMe reduces the amount of chemical for conjugation from >1000 to 50 equivalence. While the Cl-azo study shows a single azobenzene photoswitching by electrical recording, the nanopore conjugation is not verified by LC-MS as for the Br-pzMe in chapters 2 and 3. Empirically, we observe over-modification and off-target modification in the E111C monomer when more than 50 equivalence of Br-pzMe was used, and 3~5 Br-pzMe could be conjugated to the E111C mutant when the reaction was not quenched after 18 h

On the way to explore the photoswitchable nanopore, a precedent work published in 1995 reported an irreversible photocaged αHL monomer, which has a Norrish type II α-carboxy-2-nitrobenzyl photocage preventing the monomer from oligomerization[79]. Under 365 nm irradiation, this nanopore became uncaged and triggered oligomerization, resulting in hemolysis activity in rabbit red blood cells. Likewise, another attempt to build photoresponsive nanopore was the synthesis of a photoswitchable gramicidin A channel, which was an oligopeptide of 15 amino acids[80]. Borisenko *et al.* elegantly synthesized a gramicidin with an N-terminal phenylazo-phenylalanine, and observed single-channel current amplitude difference between the *E* and *Z* states. In 1 M NaCl solution, the conductance reduced from 8 pS to 6 pS, which meant 25% current gating. For comparison, the Cl-azo (**Fig. 8c**) study reported 3% gating, while the Br-pzMe in chapter 2 increased it to 95%. Similar to the photocaged αHL, Mutter *et al.* created a fragaceatoxin C

(FraC) photoresponsive nanopore, where the azobenzene *E* isomer restricted the pore assembly, and the pore formation occurred only under 365 nm irradiation[81]. However, once the pore was assembled, the pore could not be photoswitched back to a non-conductive state. Apart from the peptide- or nanopore-based design, Offenbartl-Stiegert *et al.* focused on the photoresponsive DNA nanopore[82], where a photoswitch controlled a DNA lid blocking the transmembrane barrel. This work also demonstrated controlled release of biomolecules across the lipid bilayer of liposomes, which paved the way for nanopore-assisted controlled drug release in liposomes.

The concept of photoresponsive nanopore was also expanded to solid-state nanopores. For instance, Hagan *et al.* fabricated a photoregulated thin-film nanopore on silicon nitride film[83]. The nanopore of 10 nm diameter was covalently modified by azobenzene. In the off state, the 10-nm diameter could be switched to ~6 nm and lead to ~30% current change. However, the solid-state nanopore was often >10 nm thick compared to the ~3 nm lipid bilayer, and hundreds of photoswitches were congesting the channel. Another interesting solid-state photopore by Li *et al.* was synthesized by assembling azobenzene-modified DNA strands on polyethylene terephthalate film[84]. The nanopore reduced the conductance from 24.6 nS to 3.4 nS (~86% current change) after irradiation, and showed a similar rectification property to pzMe. However, the photopore in chapter 2 was a well-defined system of seven azobenzene in a channel of 1.4 nm; whereas the solid-state nanopore had a diameter of 22 nm and the number of azobenzene was not mentioned. Finally, spiropyran-modified photo-controllable ion-gated MIL-53 reported by Liu *et al.* achieved a current change of 94% after UV irradiation[85]. However, the pore size in the MIL-53 is ~4 Å and each repeating unit had a spiropyran. It was difficult to compare protein-based nanopores to the solid-state ones based on the membrane system, diameter of pore, number of photoswitch and applications.

From a mechanistic perspective, the control of ion flow through a photopore could be achieved in four ways. First, the transmembrane channel could be geometrically blocked by the photoswitch[80,82]. Because of the 1.4 nm width of the αHL channel, any molecules of a bigger diameter could block the pore. Second, the internal

surface charge of the nanopore could be altered for a ‘depletion zone’ like in an electronic diode[84,85]. A prime example was the rectification of outer membrane protein F with mutated diode-like RREE residues. In the work of Miedema *et al.* the non-rectifying porin was changed into an ionic diode with two- or three-fold rectification[86]. In the double arginine (RR) mutant or double aspartic acid mutant (EE), the rectification ratio was weakly rectifying 0.89 and 0.81, respectively. In contrast, the RREE mutant showed a rectification ratio of 0.22 and favored negative potential significantly. Interestingly, a triple arginine (RRR) mutant rectified the current at a ratio of 3.14. Since the pzMe photopore in chapter 2 was also rectifying in the OFF state, the Coulombic effect or diode-like depletion of charge might be crucial for the current gating. Third, the photoswitching could induce a huge conformational change in the channel, or collapse the channel. For instance, Maglia *et al.* reported a diode αHL with 49 arginine residues in the β barrel[44]. When it was in the diode mode, it took ~200 milliseconds for the pore to collapse. If the β barrel of αHL was connected through a linker of photoswitch, we might control the spatial conformation of the whole transmembrane region. Fourth, the photoswitching of monomeric αHL might control the pore assembly. However, the challenge of this approach was that controlling the potential of assembly did not necessarily promise the control of the ion flow through the assembled pore. For instance, the monomer in the FraC study could be switched ON to assemble, or switched OFF to prevent assemble[81]. However, the assembled FraC could not be disassembled by switching, and the wavelength of switching monomer OFF did not switch OFF the oligomer conductance.

1.4 Overview of the thesis

In this thesis, we report the development of photoresponsive nanopore (E111C-pzMe)$_7$ and (E111C-pzMe)$_1$WT$_6$ in chapters 2 and 3, respectively. The primary goal is to leverage the photoreversible control of transmembrane ionic current by the isomerization of arylazopyrazole at the nanopore constriction. In chapter 2, a current change of 95% is reported at the single-molecule level, and 85% at the ensemble level. Based on the results of (E111C-pzMe)$_7$ photopore, the single-molecule kinetics of photoisomerization was explored in chapter 3. A single photoswitch was tethered at the same E111C position, and the *E*→*Z* / *Z*→*E* isomerization kinetics were determined by stochastic events in the electrical recording. Since the kinetics is correlated with the extinction coefficient, this is the first example of recording the single-molecule excitation spectrum of a non-fluorescent photoswitch in aqueous solution at room temperature. In the end, the conclusion chapter summarizes the findings regarding these two classes of photophores and discusses the future of this project in the aspects of synthetic biology, single-molecule chemistry, and nanopore-based single-molecule spectroscopy.

Chapter 2

ON-OFF nanopores for optical control of transmembrane ionic communication

Abstract

Nanoscale photoswitchable proteins could facilitate precise spatiotemporal control of transmembrane communication and support studies in synthetic biology, neuroscience, and bioelectronics. Through covalent modification of the α-hemolysin protein pore with arylazopyrazole photoswitches, we have produced "photopores" that transition between iontronic resistor and diode modes in response to irradiation at orthogonal wavelengths. In the diode mode, a low-leak OFF-state nanopore exhibits a reversible increase in unitary conductance of more than 20-fold upon irradiation at 365 nm. A rectification ratio of >5 was achieved with photopores in the diode state by either direct or alternating voltage input. Unlike conventional electronic phototransistors with intensity-dependent photoelectric responses, the photopores regulated current output solely based on the wavelength(s) of monochromatic or dual-wavelength irradiation. Dual-wavelength irradiation at various relative intensities allowed graded adjustment of photopore conductance. By using these properties, photonic signals encoding text or graphic messages were converted into ionic signals, highlighting the potential applications of photopores as components of smart devices in synthetic biology.

2.1 Introduction

Remote control of transmembrane ionic communication can be facilitated by various molecular tools that respond to external stimuli (e.g. light[13,53,54,87,88], temperature[89], magnetic[90] or electrical fields[12]). Among them, optically activated devices fitted with photo-responsive functional groups have garnered attention, which leverage light inputs to achieve spatiotemporal modulation of ionic signaling across membranes[3,91,92].

In top-down synthetic biology, ion fluxes across cell membranes can be modulated by nanodevices containing photoswitchable chromophores. For example, natural light-driven ion transporters, such as microbial rhodopsins[93,94], generate or dissipate electrochemical gradients through chromophore isomerization. This enables regulation of the electrical activities of rhodopsin-expressing cells, thereby manipulating basic biological activities, such as calcium signalling[95,96] and neuronal firing[97,98]. These optogenetic tools also function as integral parts of miniaturized bioelectronic systems[99,100]. Optical control can also be introduced into natural ion channels through the use of synthetic photoisomerizable allosteric ligands that regulate the opening (ON) and closing (OFF) of ligand-gated receptors, such as ionotropic glutamate receptors[55], transient receptor potential channels[101], and voltage-gated K^+ or Ca^{2+} channels[54,102].

In bottom-up synthetic biology, to modulate transmembrane ionic signaling, there is a strong demand for photoresponsive devices featuring modular design, ease of assembly, immediate and reversible ON-OFF responses, sustained ON and complete OFF states, and the potential to respond to additional input stimuli. Fully synthetic systems offer broad design and application scopes, but face challenges in affording efficient, real-time and light-actuated ion movements across membranes. For example, DNA nanopores equipped with a photoisomerizable lid strand were optically activated before inserting into lipid bilayers[82]. Synthetic ion transporters with built-in photoswitches moved ions down a transmembrane gradient one at a time[103,104]. Semi-synthetic approaches are also pursued to leverage the natural ON-OFF machinery of protein channels. Chemical engineering of proteins with photoswitches enabled transient light-activated opening of

mechanosensitive channels[53] or timed irreversible formation of protein nanopores[79,81]. New designs are required to achieve prolonged activation and reversible ionic responses to light.

Here, we describe reversible ON-OFF photopores, which exhibit a long open lifetime in the ON state and a low background current in the OFF state. The ON-OFF machinery was engineered into a protein construct not originally evolved to open and collapse, and can be activated in real time when embedded in membranes. This was achieved by covalent modification of α-hemolysin (αHL) monomers with arylazopyrazoles that exhibit almost quantitative photoswitching between *E* and *Z* isomers and exhibit high thermal stability in both states. The photopores were characterized at both the single-molecule and ensemble levels to showcase their ability to permit or restrict transmembrane ionic current in response to light. The pores exhibit behaviors analogous to both electronic diodes (i.e. one-way current flow) and light-tunable resistors (i.e. current modulation) depending on the irradiation wavelength. The properties of the photopores were exploited to generate light-to-ionic signal conversion.

2.2 Construction of photoreversible nanopores

To construct photopores, we functionalized α-hemolysin (αHL), a heptameric protein nanopore, with photoisomerizable chemical groups on the interior of the channel (**Fig. 1**). The αHL monomers containing a single cysteine residue at position 111, 115, 125 or 129 were separately modified with one of the three types of photoswitches—*o*-fluoroazobenzene (fAzo)[33], arylazopyrazole (pzH)[59], or methyl arylazopyrazole (pzMe)[32]—by using thiol-specific chemistry (**Fig. 1a,b and Figs. 2-3**). These representative cysteine mutation sites were selected from the pore constriction, the middle of the barrel, and the flexible end of the beta sheets, as shown in **Fig. 3a**. Upon assembly into heptamers, the side chains of these residues project into the lumen of the transmembrane β barrel[56]. The modification of αHL monomers (**Fig. 4**) with one molecule of either fAzo, pzH, or pzMe was confirmed by liquid chromatography-mass spectrometry (LC-MS) (**Fig. 1c and Figs. 5-6**). Modified monomers self-assembled to form homoheptameric pores when

introduced into a synthetic lipid bilayer consisting of 1,2-diphytanoyl-sn-glycero-3-phosphocholine (DPhPC) or in the presence of sodium deoxycholate (**Fig. 1a**).

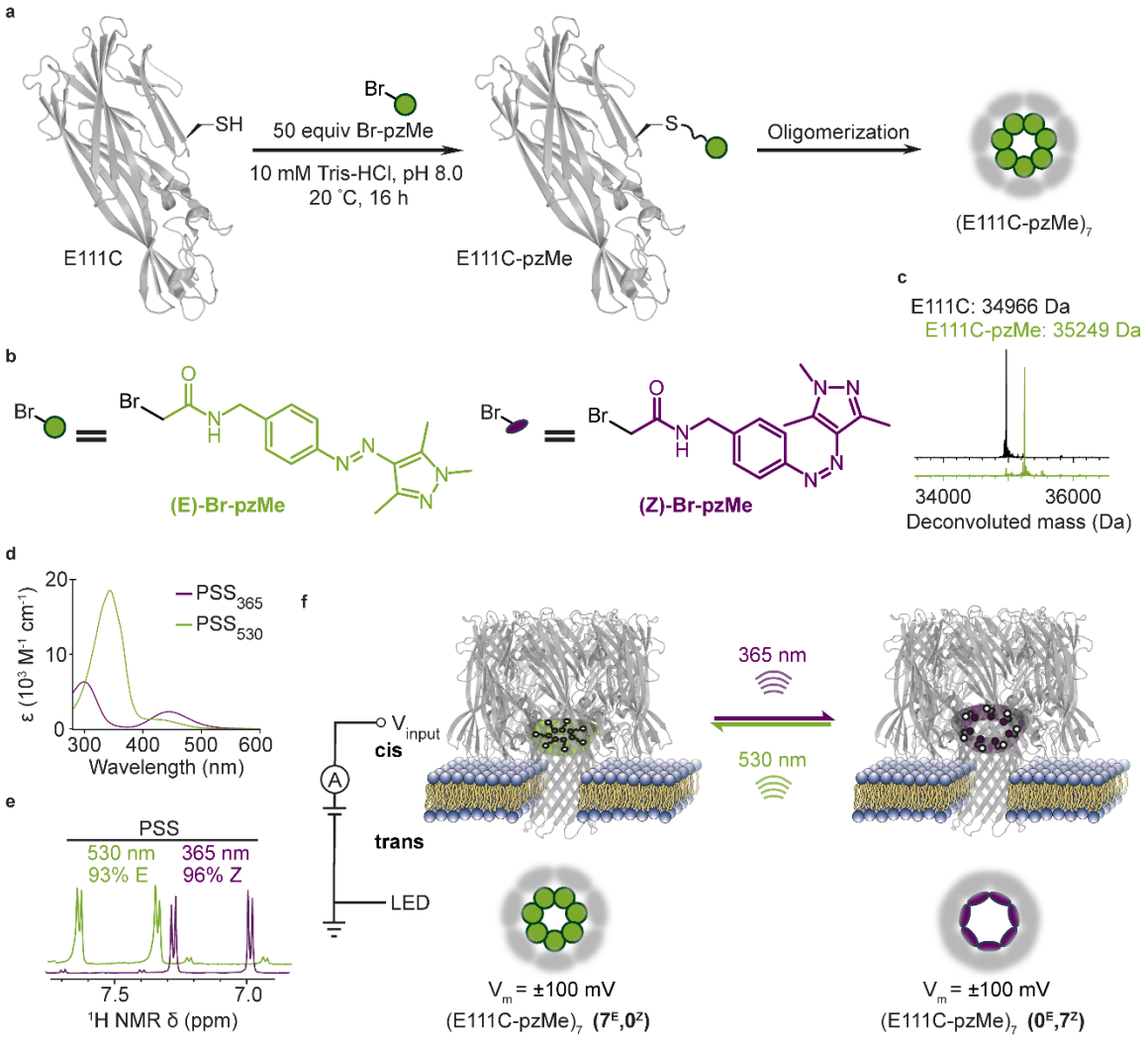


Fig. 1 | Construction and characterization of the (E111C-pzMe)$_7$ photopore. a, The α-hemolysin (αHL) monomer containing a cysteine at position 111 was modified with (*E*)-bromoacetyl arylazopyrazole (Br-pzMe) before oligomerization to form the (E111C-pzMe)$_7$ photopore. **b,** The Br-pzMe exists either as the *E* isomer (green) or the *Z* isomer (purple). **c,** Deconvoluted mass of E111C and E111C-pzMe monomer confirming quantitative modification of the αHL monomer with pzMe. **d,** UV/Vis spectra of *E* (green) or *Z* isomers (purple) of Br-pzMe in DMSO at room temperature. **e,** The photostationary states (PSS) of Br-pzMe examined by the ^{1}H NMR chemical shifts of the aromatic protons in DMSO-d_6. **f,** The modulation of ionic current passing through single or multiple photopores was evaluated by using voltage–clamp electrical recording, in which a transmembrane potential (V_m) was defined as one in which positive charge moved through the bilayer from the trans side of the pore to the cis. LED light was collimated and projected onto the bilayer from the trans side. Irradiation at 530 nm or 365 nm isomerized arylazopyrazole groups within individual pores, thereby populating photopores in either *E* or *Z* states. When all seven

arylazopyrazoles adopted the *E* or *Z* configuration, such configurations were named as (7^E,0^Z) or (0^E,7^Z).

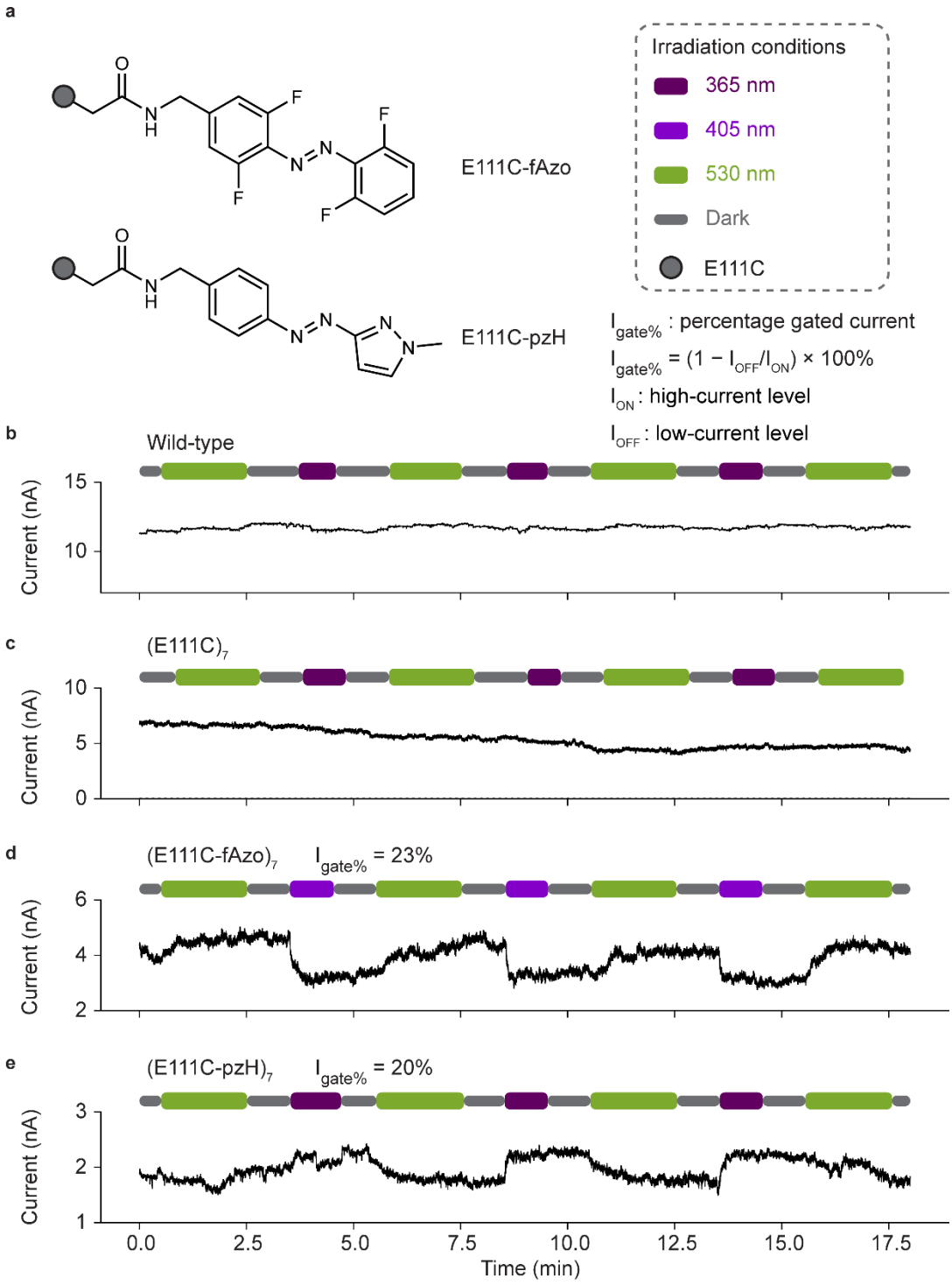


Fig. 2 | (E111C-fAzo)$_7$ and (E111C-pzH)$_7$ photopores. a, The fAzo or pzH photoswitches were covalently attached to the cysteine residues at position 111 (E111C) through thioether bond formation. The photoswitches are shown as *E* isomers. The electrical traces with ensembles of wild-type (WT) α-hemolysin (αHL) (**b**), unmodified (E111C)$_7$ (**c**), (E111C-fAzo)$_7$ (**d**), and (E111C-pzH)$_7$ (**e**) were recorded under alternating light cycles. Wavelengths

of irradiation are color-coded: 365 nm, burgundy; 405 nm, purple; 530 nm, green; dark, grey. The WT αHL and $(E111C)_7$ were not photoresponsive. The ensembles of $(E111C\text{-}fAzo)_7$ and $(E111C\text{-}pzH)_7$ responded to irradiation by *E/Z* isomerization. The percentage gated current $I_{gate\%}$ was around ~20%. For $(E111C\text{-}fAzo)_7$, irradiation at 405 nm closed the pore, and 530 nm opened the pore. In contrast, for $(E111C\text{-}pzH)_7$, irradiation at 530 nm closed the pore, and irradiation at 365 nm opened the pore. The current traces were recorded at +100 mV using a 5 kHz in-line Bessel filter at 25 kHz sampling frequency, and a 20 Hz digital Bessel filter was used for data analysis. Recording conditions: 2 M KCl, 10 mM Tris-HCl, 0.1 mM EDTA, pH 8.5, 24 ± 1 °C.

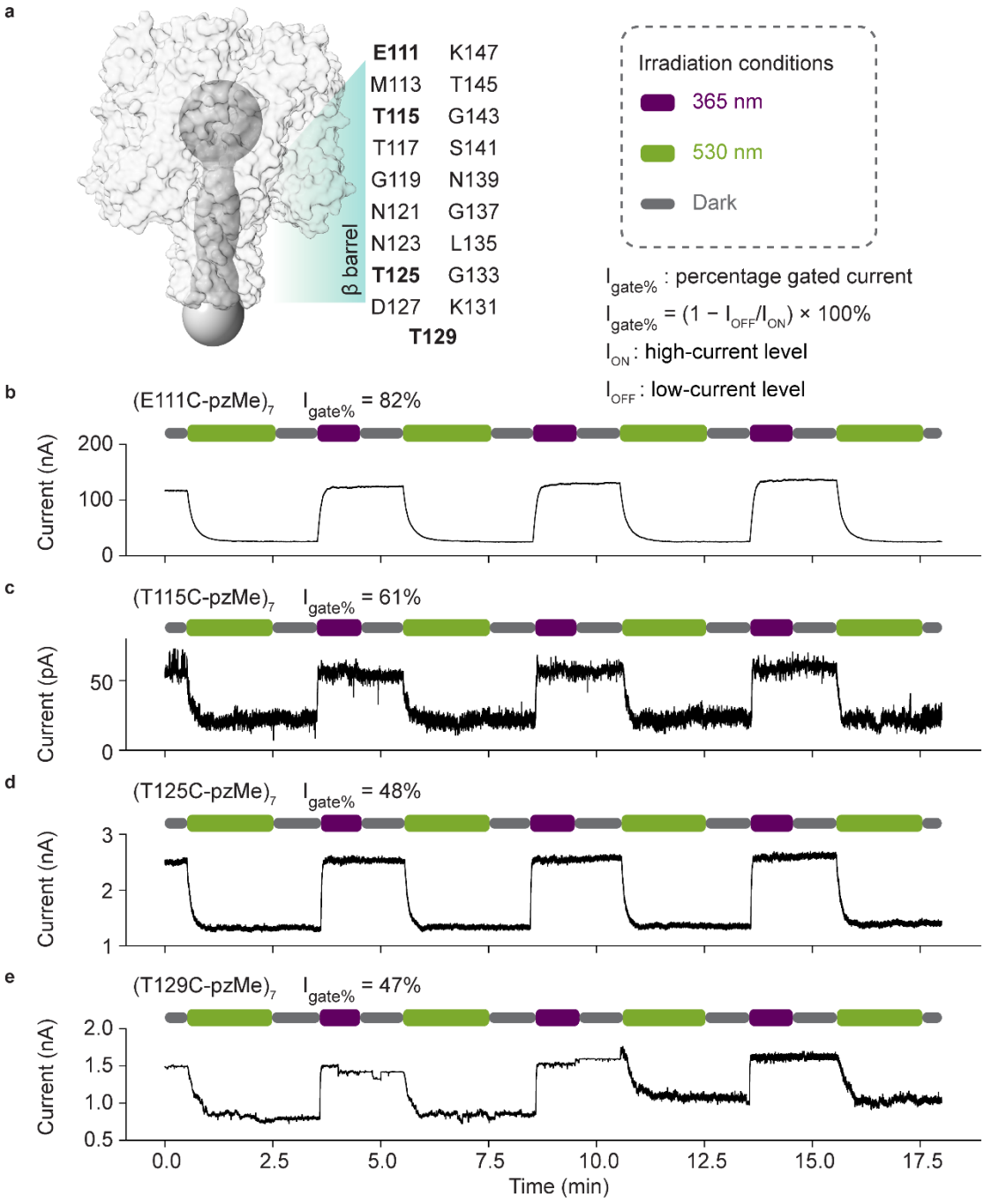


Fig. 3 | Photopores with pzMe modification in the αHL β barrel. a, Representation of the αHL pore and residues in the β barrel. The grey semi-transparent structure of the αHL heptamer was generated from PDB: 7AHL with PyMOL The grey solid dumbbell model showing the protein channel volume was retrieved from ChannelsDB[105]. Electrical traces from ensembles of $(E111C\text{-}pzMe)_7$ (**b**), $(T115C\text{-}pzMe)_7$ (**c**), $(T125C\text{-}pzMe)_7$ (**d**) and $(T129C\text{-}pzMe)_7$ (**e**) were recorded under alternating light cycles. Wavelengths of irradiation are color-coded: 365 nm, burgundy; 530 nm, green; dark, grey. The $(E111C\text{-}pzMe)_7$ showed the largest percentage gated current ($I_{gate\%}$) at 82% in the illustrated trace. All pzMe photopores showed the following correlation—*Z*, ON; *E*, OFF. The current traces were recorded at +100 mV using a 5 kHz in-line Bessel filter at 25 kHz sampling frequency, and a 20 Hz digital Bessel filter was used for data analysis. Recording conditions: 2 M KCl, 10 mM Tris-HCl, 0.1 mM EDTA, pH 8.5, 24 ± 1 °C.

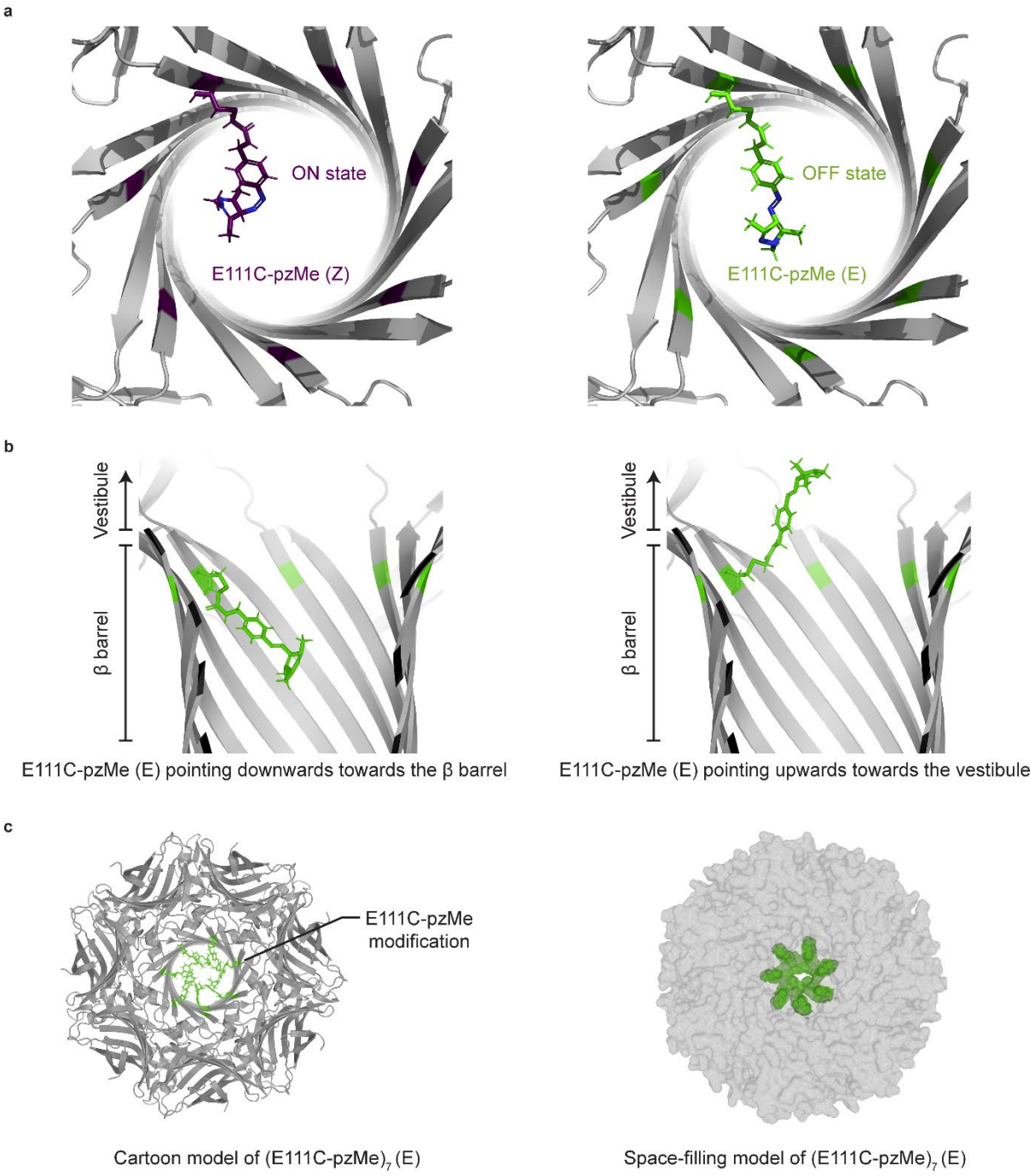


Fig. 4 | Structural models for pzMe-modified αHL at position 111. a, Top views of a single pzMe group, in either the *Z* or *E* state, covalently attached to the E111C position and extended into the central lumen of an αHL pore. **b,** Side views of a single pzMe group in the *E* state pointing towards either the cis vestibule or the trans opening of the β barrel. c. Top views of seven pzMe groups inside an αHL pore, oriented towards the trans opening of the β barrel. Models were created and modified manually from PDB: 7AHL.

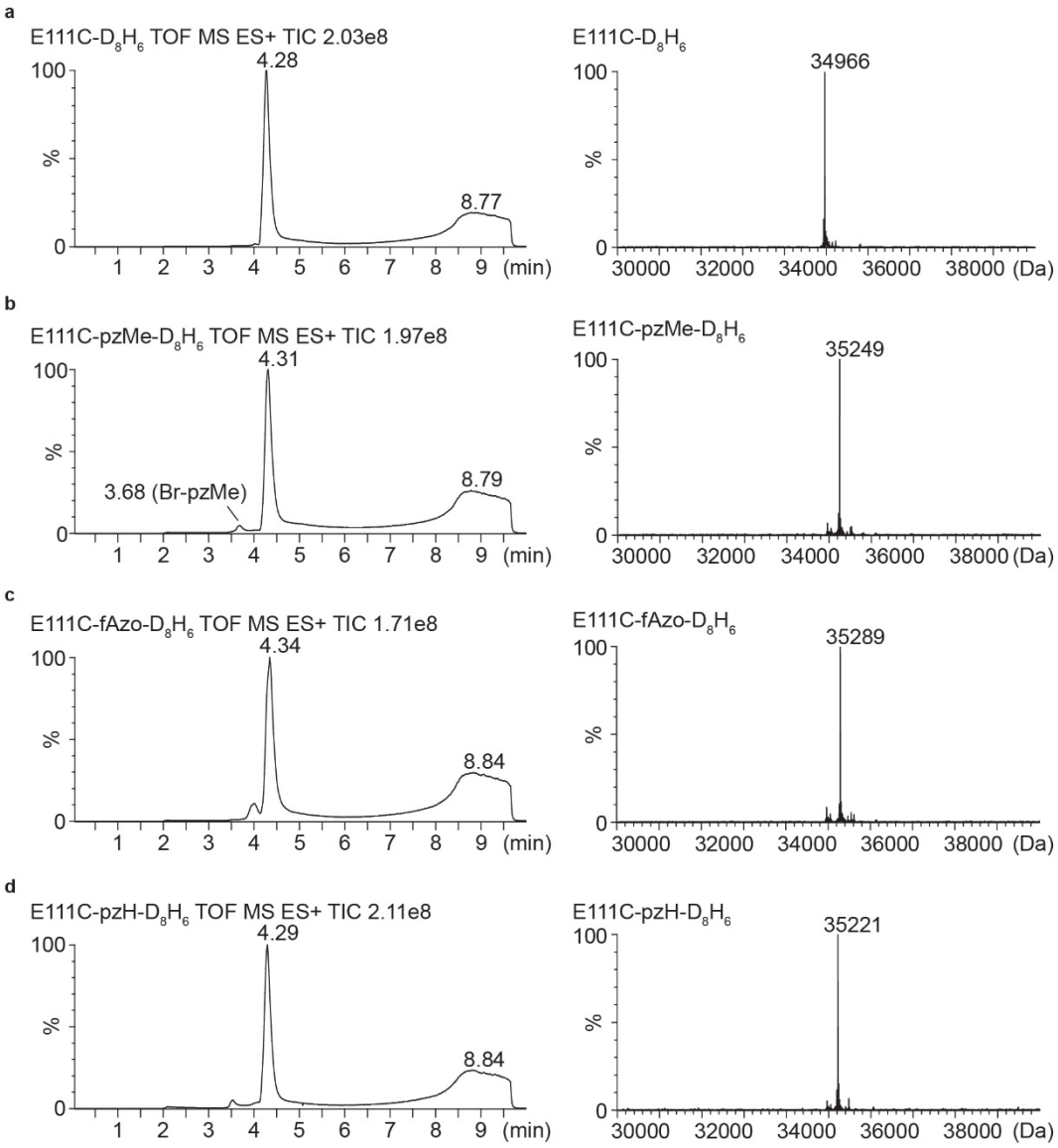


Fig. 5 | LC–MS characterization of E111C monomers before and after chemical modification. The left panels are total ion current chromatograms. The right panels are deconvoluted ESI–MS spectra in the range of 30-40 kDa. **a,** E111C-D_8H_6 monomer: mass = 34966 (calculated) and 34966 (observed). **b,** E111C-pzMe-D_8H_6 monomer: mass = 35249 (calculated) and 35249 (observed). **c,** E111C-fAzo-D_8H_6 monomer: mass = 35289 (calculated) and 35289 (observed). **d,** E111C-pzH-D_8H_6 monomer: mass = 35221 (calculated) and 35221 (observed).

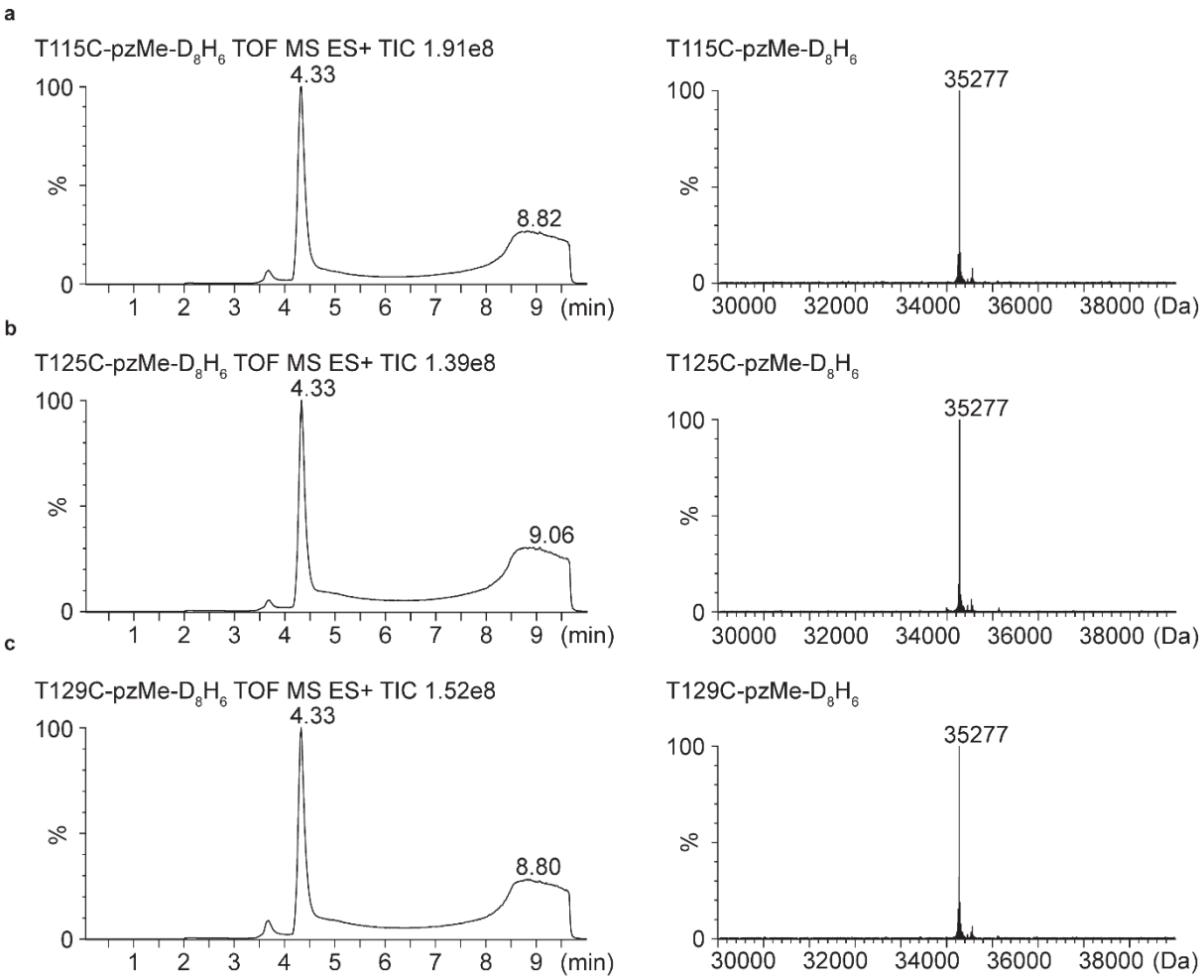


Fig. 6 | LC–MS characterization of photopores obtained by modification with Br-pzMe. The left panels are total ion current chromatograms. The right panels are deconvoluted ESI–MS spectra in the range of 30-40 kDa. **a,** T115C-pzMe-D_8H_6 monomer: mass = 35277 (calculated) and 35277 (observed). **b,** T125C-pzMe-D_8H_6 monomer: mass = 35277 (calculated) and 35277 (observed). **c,** T129C-pzMe-D_8H_6 monomer: mass = 35277 (calculated) and 35277 (observed).

The fAzo, pzH, and pzMe photoswitches were reported to exhibit high *E/Z* or *Z/E* isomer ratios at photostationary states (PSSs) and thermal stability in the *Z* state.[33,59] Determined by ultraviolet/visible (UV/Vis) and proton nuclear magnetic resonance (^{1}H NMR) spectroscopy, the bromoacetamide derivative of pzMe (Br-pzMe) demonstrated the highest isomer ratios at PSSs generated by 'orthogonal' wavelengths (**Fig. 1d,e**). Upon LED irradiation at 365 nm, Br-pzMe was converted primarily to the *Z* isomer (PSS_{365} = 96% *Z*), while when irradiated at 530 nm, Br-pzMe was present predominantly as the *E* isomer (PSS_{530} = 93% *E*) (**Fig. 1e and Fig. 7**). By contrast, Br-fAzo was 85% in the *E* form at PSS_{405} and 91% in the *Z* form at PSS_{530}, while Br-pzH was 65% *E* at PSS_{530} and 85% *Z* at PSS_{365} (**Fig. 7**). High

isomer ratios were expected to produce tight control of ionic communication through modified nanopores.

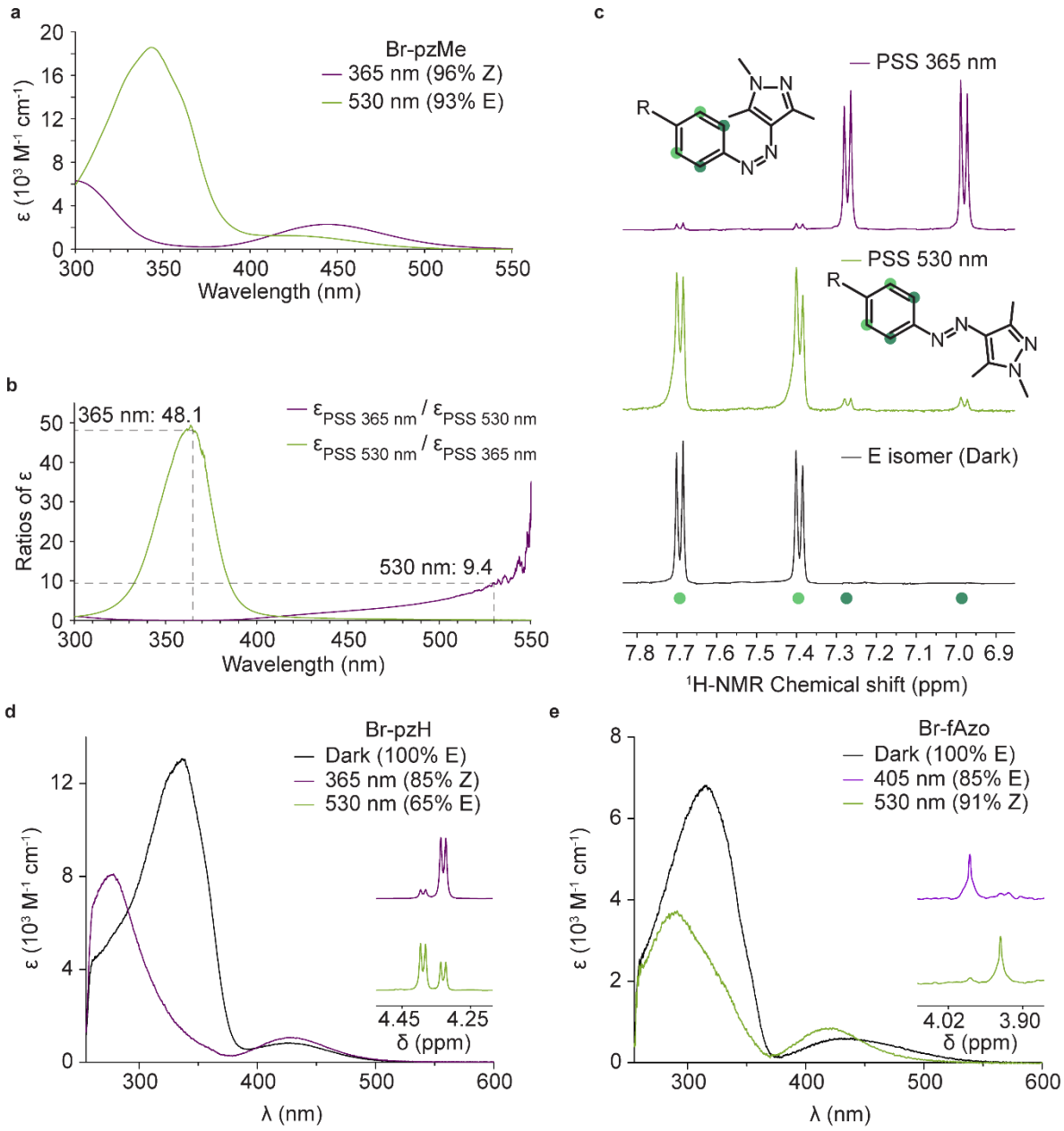
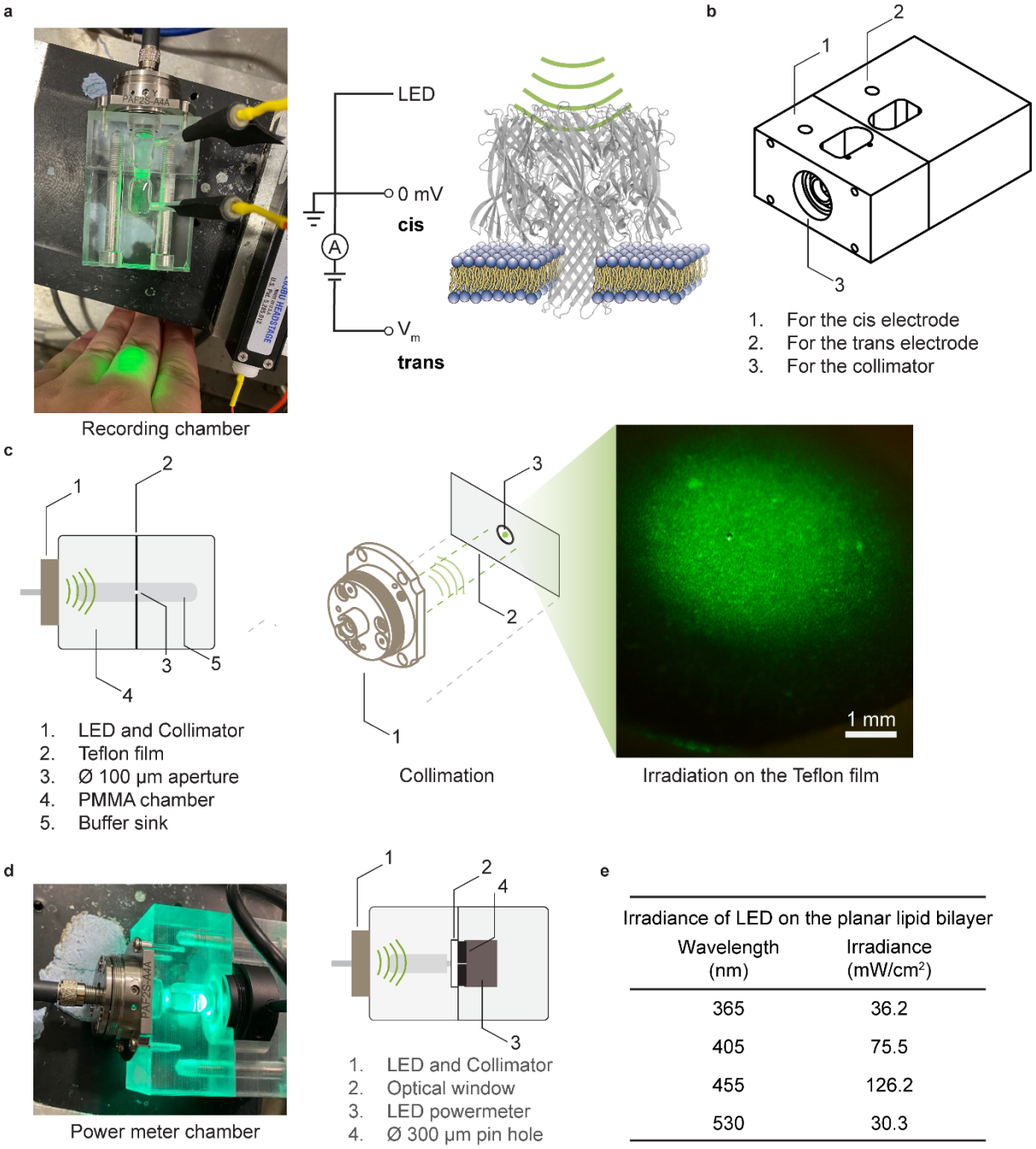


Fig. 7 | Quantitative photoswitching of Br-pzMe. a, UV/Vis absorption spectra of Br-pzMe in photostationary states (PSS) in DMSO. **b,** The ratio of Br-pzMe extinction coefficients (ε) between 365 and 530 nm calculated from the data in **a**. The high ε of the *E* isomer and the low ε of the *Z* isomer of Br-pzMe at 365 nm biased the photoequilibrium towards the *Z* isomer at PSS 365 nm. Similarly, the *Z* isomer of pzMe exhibited higher ε at 530 nm, which favored isomerization to the *E* isomer at PSS 530 nm. **c,** ^{1}H NMR signal of the aryl protons (green) of Br-pzMe in DMSO-d_6. **d,** UV/Vis absorption spectra of Br-pzH in the dark after heating and at PSS 365 nm. The right panel shows parts of the ^{1}H NMR spectra of Br-pzH at PSS 365 and 530 nm. **e,** UV/Vis absorption spectra of Br-fAzo in the dark after heating and at PSS 530 nm. The right panel shows the parts of the ^{1}H NMR

spectra of Br-fAzo at PSS 405 and 530 nm. The UV/Vis spectra and ^{1}H NMR were recorded in DMSO-d_6 at 298 K.

2.3 Reversible ON-OFF photopores

The photoreversible modulation of ionic current passing through αHL nanopores containing fAzo, pzH, or pzMe photoswitches was first characterized by ensemble electrical recordings in planar lipid bilayers, i.e. in bilayers containing hundreds or thousands of pores. A bespoke poly(methyl methacrylate) chamber was made, equipped with a collimated fiber-coupled LED, for electrical recording under illumination over a range of intensities from the grounded side (trans) of the bilayer (**Fig. 1f and Fig. 8**). To align with the convention of reporting current through αHL pores, we defined a positive current as one in which positive ions moved through the bilayer from the trans side of the pore to the cis (i.e. from the bottom of the barrel towards the vestibule). The transmembrane potential (V_m) was given as the potential on the trans side relative to the cis side.



Irradiance of LED on the planar lipid bilayer

Wavelength (nm)	Irradiance (mW/cm²)
365	36.2
405	75.5
455	126.2
530	30.3

Fig. 8 | Custom recording chamber for planar lipid bilayer (PLB) experiments under irradiation. a, A recording chamber for photopore characterization. An electrical potential was applied across the PLB with Ag/AgCl electrodes (yellow wires). The cis electrode was grounded, and the compartment with the trans electrode was connected to an optical fiber (Ø 1000 µm, NA = 0.39). **b,** Technical schematic of the chamber. The front hole was attached to a collimator and an optical window (not shown). Electrodes were inserted into buffer-containing compartments contained 1 mL buffer each. **c,** Components of the chamber. The fiber-coupled LED projected light to a Teflon film between the compartments. When adjusted, a collimated beam was projected onto the aperture (Ø ~100 µm). **d,** Measurement of light intensity. The irradiance of the light was measured with a power meter by replacing the trans part of the chamber. The collimated light was masked by a Ø 300 µm

pinhole. The beam profile through the pinhole was approximately the same as that through the aperture in the Teflon. **e,** Irradiance values of LEDs measured at 365 nm, 405 nm, 455 nm and 530 nm. The irradiance was calculated from the intensity through the pinhole. Irradiance (Q) = Intensity / Pinhole area.

Interconversion between a high-current level (I_{ON}) and a low-current level (I_{OFF}) was recorded at +100 mV with pores equipped with fAzo, pzH, or pzMe under alternating wavelengths (365 nm/530 nm for pzH and pzMe, or 405 nm/530 nm for fAzo) (**Fig. 9a and Figs. 2-3**). We refer to the lower-current state as the OFF state, in which the ionic flow is partially or almost completely restricted, by comparison with the highest obtainable current level, which is the ON state. In general, the photoreversible nanopores switched to the ON state after irradiation at the shorter wavelength (photoswitches in the *Z* state), and to the OFF state following irradiation at the longer wavelength (photoswitches in the *E* state).

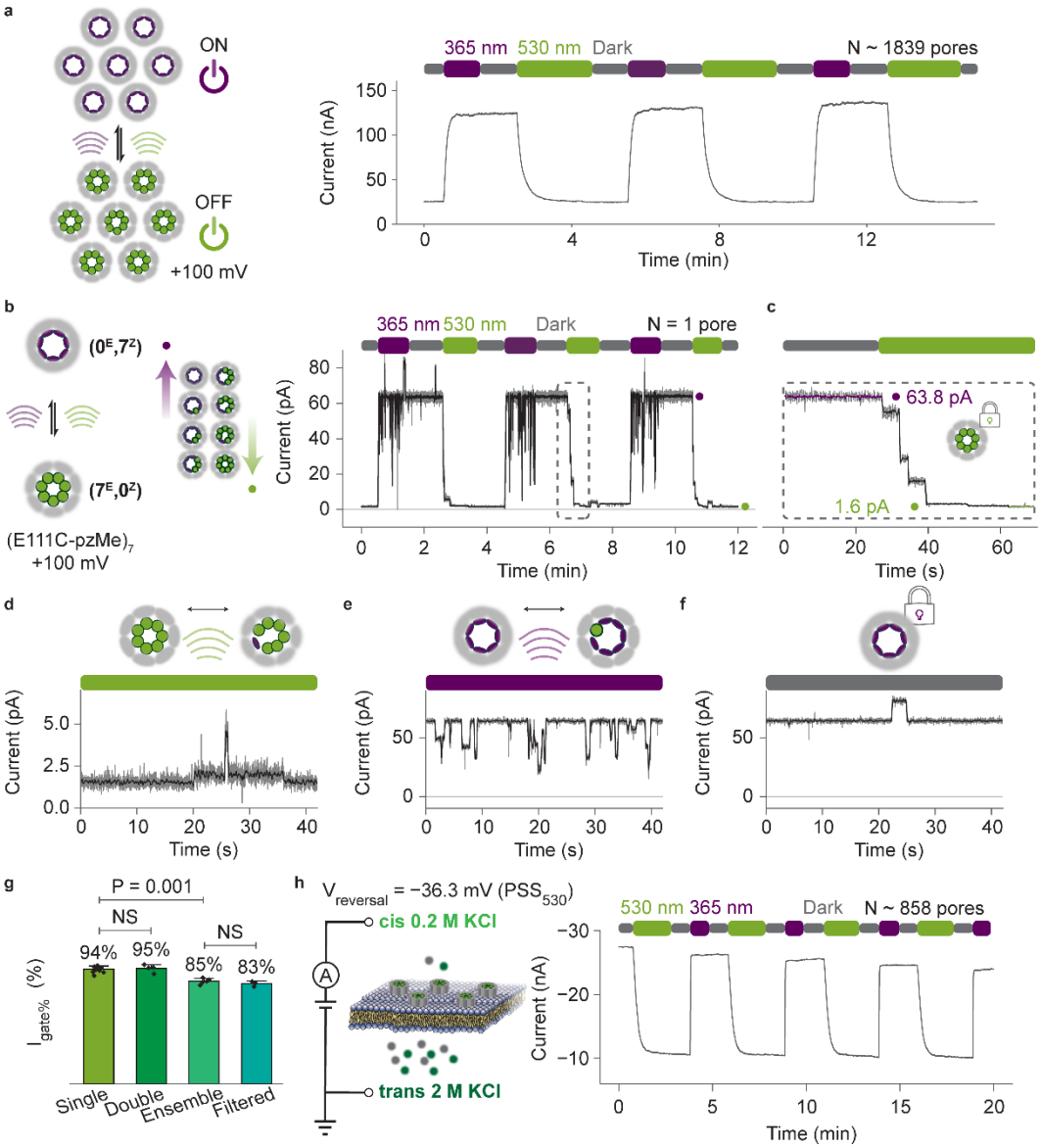


Fig. 9 | Reversible ON-OFF switching of (E111C-pzMe)$_7$ photopore. a, Optical control of ionic flow through an ensemble of ~1839 photopores. Irradiation at 365 nm (purple) converted photopores to an ON state, while irradiation at 530 nm (green) produced an OFF state. The current trace demonstrates ON-OFF switching of the photopore ensemble effected by cycles of UV (365 nm) → dark → green (530 nm) → dark. **b,** Optical control through a single photopore switching between (0^E,7^Z) and (7^E,0^Z) states. The same light cycle as in **a** was applied. The moving average of the ionic current (grey) is shown in black, which was smoothed with a Savitzky–Golay filter (400 ms window length). During 365 nm irradiation, the photopore switched constantly, causing the black downwards events. By contrast, in the dark, these events stopped. **c,** Zoom-in of the dashed-line box in **b**. Each stepwise decrease in the current was attributed to the isomerization of one or more pzMe photoswitches. **d-e,** Ionic current under continuous irradiation. The current fluctuated due to switching between the (7^E,0^Z) and neighboring (6^E,1^Z) states at 530 nm in panel **d** or between the (0^E,7^Z) and neighboring (1^E,6^Z) states at 365 nm in panel **e**. **f,** Ionic current in the dark. The current remained stable with occasional upward bursts of seconds in duration. Such a dark event was irrelevant to the photoisomerization. **g,** Mean percent gated current

($I_{gate\%}$) in bilayers containing one (N = 11 separate pores), two (N = 4 experiments), or an ensemble of pores (N = 4 experiments). Two tailed t-tests were performed among the $I_{gate\%}$ values. In-line filters (355-nm filter for 365 nm LED; 532-nm filter for 530 nm LED) were applied to an ensemble of pores with little effect on $I_{gate\%}$. **h,** ON-OFF switching of an ensemble of photopores under the electrochemical driving force generated by an asymmetrical KCl concentration across the membrane in the absence of an externally applied transmembrane potential. The current traces were recorded at +100 mV at 25 kHz sampling frequency and filtered using a 5 kHz in-line Bessel filter and a 20 Hz digital Bessel filter. Recording conditions: 2 M KCl (**a-f**), 0.2 M KCl (cis)/2 M KCl (trans) (**h**), 10 mM Tris-HCl, 0.1 mM EDTA, pH 8.5, 24 ± 1 °C. The number of pores in ensemble experiments was estimated, assuming each (0^E,7^Z) pore contributed +64 pA at +100 mV.

Of the homoheptamers modified at position 111 with fAzo, pzH, or pzMe, (E111C-pzMe)$_7$ produced the largest percent gated current [$I_{gate\%} = (1 - I_{OFF}/I_{ON}) \times 100\%$] of 85% at the ensemble level, whereas the other two photoswitches produced low $I_{gate\%}$ values of ~20% (**Fig. 3**). When the pzMe modification was moved to positions 115, 125, or 129, a decreased $I_{gate\%}$ was recorded. Without further investigating the mechanism underlying the position- and photoswitch-dependent efficiency of current gating, we proceeded to characterize the (E111C-pzMe)$_7$ photopore and explore its applications.

We investigated the photochemistry underlying the ON-OFF behavior of (E111C-pzMe)$_7$ photopores at the single-channel level (**Fig. 9b-f**). Sequential insertions of pre-formed heptamers, pre-irradiated at 365 nm, revealed that the ON-state conductance of individual photopores ranged from 0.12 to 1.27 nS. The average conductance of a pore (0.62 ± 0.30, N = 42 pores) was three times smaller than wild-type αHL (1.81 ± 0.17 nS, N = 17 pores) (**Figs. 10-11**).

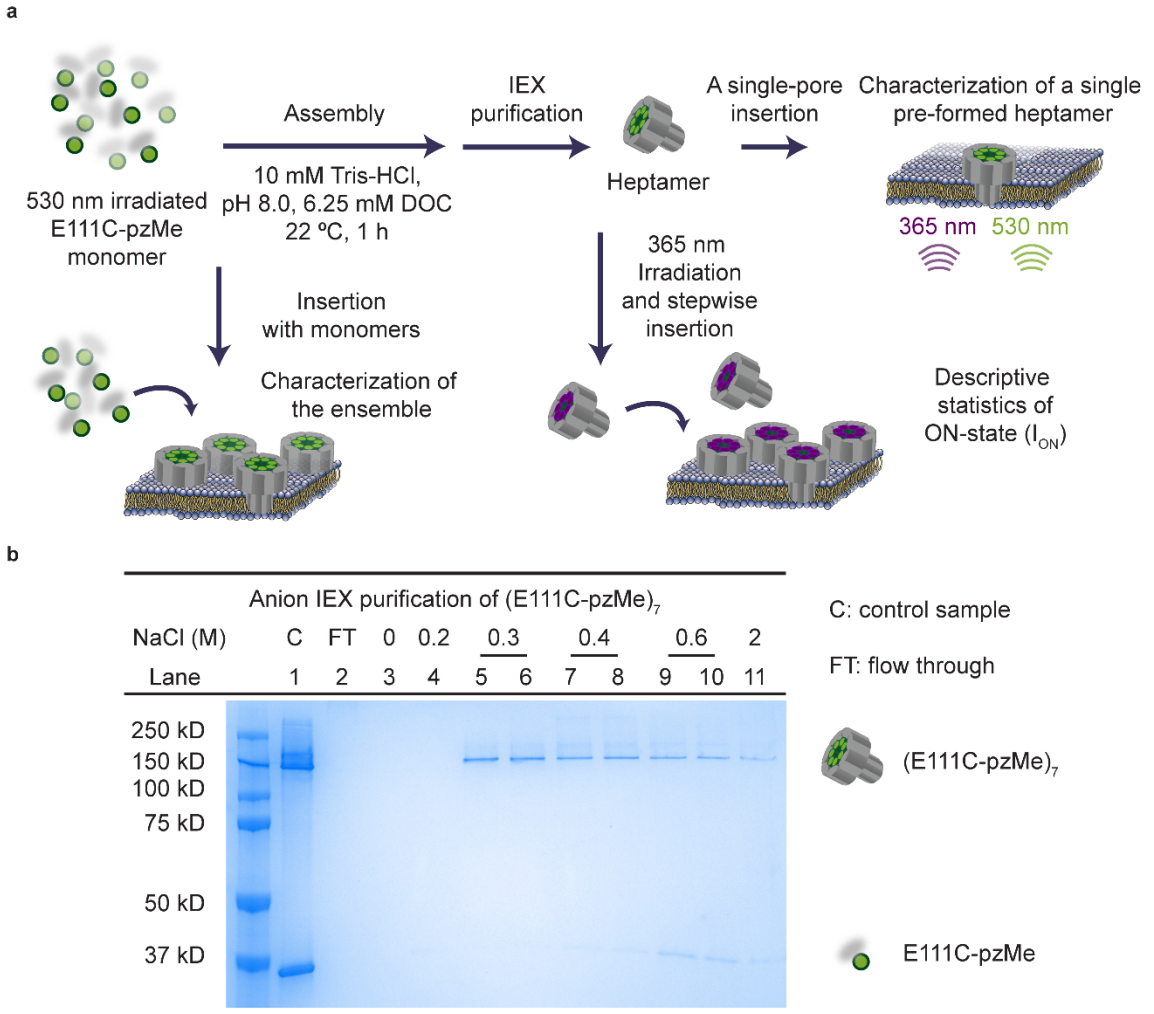


Fig. 10 | Photopore preparation and characterization. $(E111C\text{-}pzMe)_7$ is described as an example, but the procedures apply to other photopores. **a,** To obtain homoheptamers, monomers were incubated with sodium deoxycholate (DOC) buffer after 530 nm irradiation. Remaining monomer was removed by anion exchange chromatography (IEX). The purified homoheptamer was examined by electrical recording at the single-molecule level. A population of ON-state currents (I_{ON}) was examined by observing the stepwise insertion of homoheptamers generated with DOC and irradiated at 365 nm. The OFF-state current was not pursued as each pore only contributed few pA, which was indistinguishable from noise. For ensemble characterization, monomers irradiated at 530 nm were added directly to the recording chamber. **b,** Monitoring the IEX purification by gel electrophoresis. Each monomer had a D_8H_6 tag, which caused distinct electrophoretic shifts of the monomer and homoheptamer on the gel due to the negative charges of the octa-aspartic acid tail. The homoheptamer in lanes 5 and 6 was used for recording. Anion IEX conditions: 20 mM Tris-HCl, pH 7.5, NaCl gradient 0.2→0.6 M. Gel: 10% SDS-PAGE with Tris-Glycine SDS buffer.

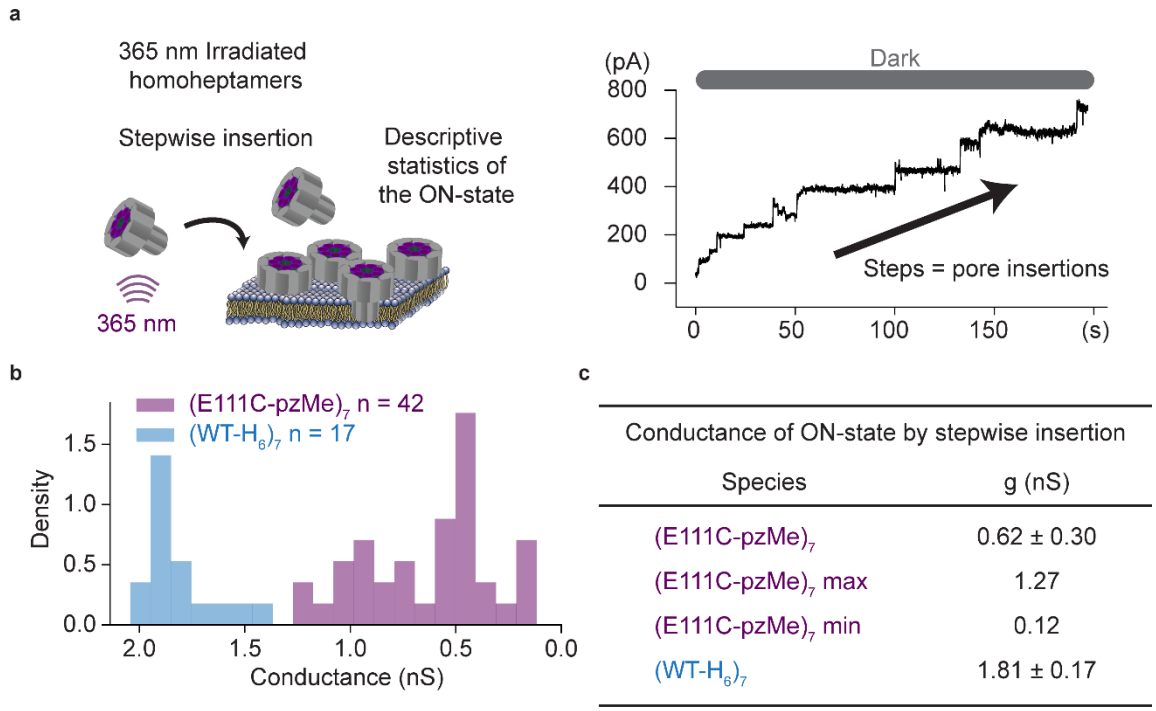
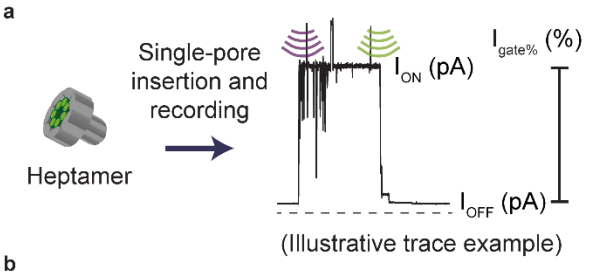
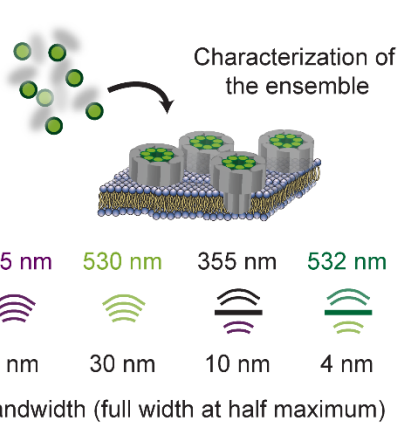


Fig. 11 | Stepwise insertion of (E111C-pzMe)$_7$ irradiated at 365-nm. a, Insertion of (E111C-pzMe)$_7$ in the (0^E,7^Z) state in the dark. (E111C-pzMe)$_7$ was irradiated at 365 nm for 30 minutes and then introduced into the cis compartment. **b,** Histogram of the current steps produced by pore insertions in **a**. The current units in pA were converted to conductance units in nS consistent with the recording conditions. (WT-H$_6$)$_7$ exhibited a mono-disperse distribution of conductance values. In contrast, the distribution of (E111C-pzMe)$_7$ conductance values was broader. **c,** Pore conductance values. The mean unitary conductance of (WT-H$_6$)$_7$ was three times that of (E111C-pzMe)$_7$ after 365 nm irradiation. The current trace was recorded at +100 mV using a 5 kHz in-line Bessel filter at 25 kHz sampling frequency, and a 20 Hz digital Bessel filter was used for data analysis. Recording conditions: 2 M KCl, 10 mM Tris-HCl, 0.1 mM EDTA, pH 8.5, 24 ± 1 °C.

An I_{gate}% of 95 ± 2.5% (N = 21) was consistently recorded at the single-channel level across all the (E111C-pzMe)$_7$ photopores (**Figs. 12-13**). Reversible photogating was observed by voltage–clamping individual single photopores and exposing them to ten repeats of UV (365 nm) → dark → green (530 nm) → dark (**Fig. 9b and Fig. 14**). Upon UV irradiation, a photopore switched from ON to OFF with a mean response time of 1.8 ± 0.8 s (N = 9 transitions), and the OFF-to-ON transition occurred on average within 31.4 ± 7.7 s (N = 9 transitions) under the green light. The LED irradiance values (365 nm: 36.2 mW/cm^2; 530 nm: 30.3 mW/cm^2) were derived from measurements of light intensities through a 300 µm-diameter pinhole in place of the bilayer (**Fig. 8**).





b

ON-OFF switching of $(E111C\text{-}pzMe)_7$ Single pre-heptamerised pore insertion			
Repeat	I_{ON} (pA)	I_{OFF} (pA)	$I_{gate\%}$ (%)
1	98.7	1.5	98.5
2	98.5	4.1	95.8
3	95.6	8.7	90.9
4	93.4	2.5	97.4
5	92.8	3.4	96.3
6	85.7	2.7	96.8
● 7	64.0	1.7	97.4
8	55.5	1.3	97.7
9	50.1	4.3	91.4
10	49.7	3.2	93.6
11	49.3	3.9	92.1
12	48.8	5.1	89.5
13	40.8	3.0	92.5
14	26.0	0.9	96.4
15	24.5	1.4	94.3
16	21.9	0.5	97.7
17	20.6	1.6	92.3
18	15.9	0.5	96.9
19	14.0	0.6	95.7
20	13.3	0.5	96.2
21	9.9	0.4	96.0
$I_{gate\%}$ (%) = 95.0 ± 2.5			

d

ON-OFF switching of $(E111C\text{-}pzMe)_7$ ensemble			
Number of pores	I_{ON} (pA)	I_{OFF} (pA)	$I_{gate\%}$ (%)
120	7692	1167	84.8
106	6808	961	85.9
113	7256	892	87.8
46	2977	550	81.5
161	10297	1649	84.0
$I_{gate\%}$ (%) = 84.8 ± 2.1			

e

ON-OFF switching of $(E111C\text{-}pzMe)_7$ ensemble with in-line filter			
Number of pores	I_{ON} (pA)	I_{OFF} (pA)	$I_{gate\%}$ (%)
535	34259	5421	84.2
337	21585	3639	83.1
706	45225	6986	84.6
173	11057	2178	80.3
$I_{gate\%}$ (%) = 83.0 ± 1.7			

Fig. 12 | ON-OFF switching of $(E111C\text{-}pzMe)_7$. a, Illustrative scheme for the single-channel recording of pre-heptamerized $(E111C\text{-}pzMe)_7$ pore. ON-state current (I_{ON}), OFF-state current (I_{OFF}) and percentage gated current ($I_{gate\%}$) were determined by the current traces recorded with pre-formed homoheptamer. **b,** ON-OFF switching performance of individual pre-formed homoheptamers. Each repeat refers to a new pore, and the data are sorted with descending I_{ON}. Despite the diverse values of I_{ON} (0.51 ± 0.31 nS, n = 21 repeats), which are consistent with the stepwise insertion results, the mean value of $I_{gate\%}$ is more tightly defined. The seventh repeat was with the pore used to collect the 40-minute recording of ON-OFF switching (**Fig. 2b**). **c,** Illustrative scheme for an $(E111C\text{-}pzMe)_7$

ensemble generated by the insertion of monomers. The ensemble was characterized with a pair of in-line filters to shift the LED irradiation wavelengths from 365/530 nm to 355/532 nm. The filter also narrowed the spectral bandwidth from 9/30 nm to 10/4 nm while reducing the output intensity. **d-e,** ON-OFF switching of the ensemble without and with the filters. The current and $I_{gate\%}$ values were calculated from traces recorded at +100 mV using a 5 kHz in-line Bessel filter at 25 kHz sampling frequency. Recording conditions: 2 M KCl, 10 mM Tris-HCl, 0.1 mM EDTA, pH 8.5, 24 ± 1 °C.

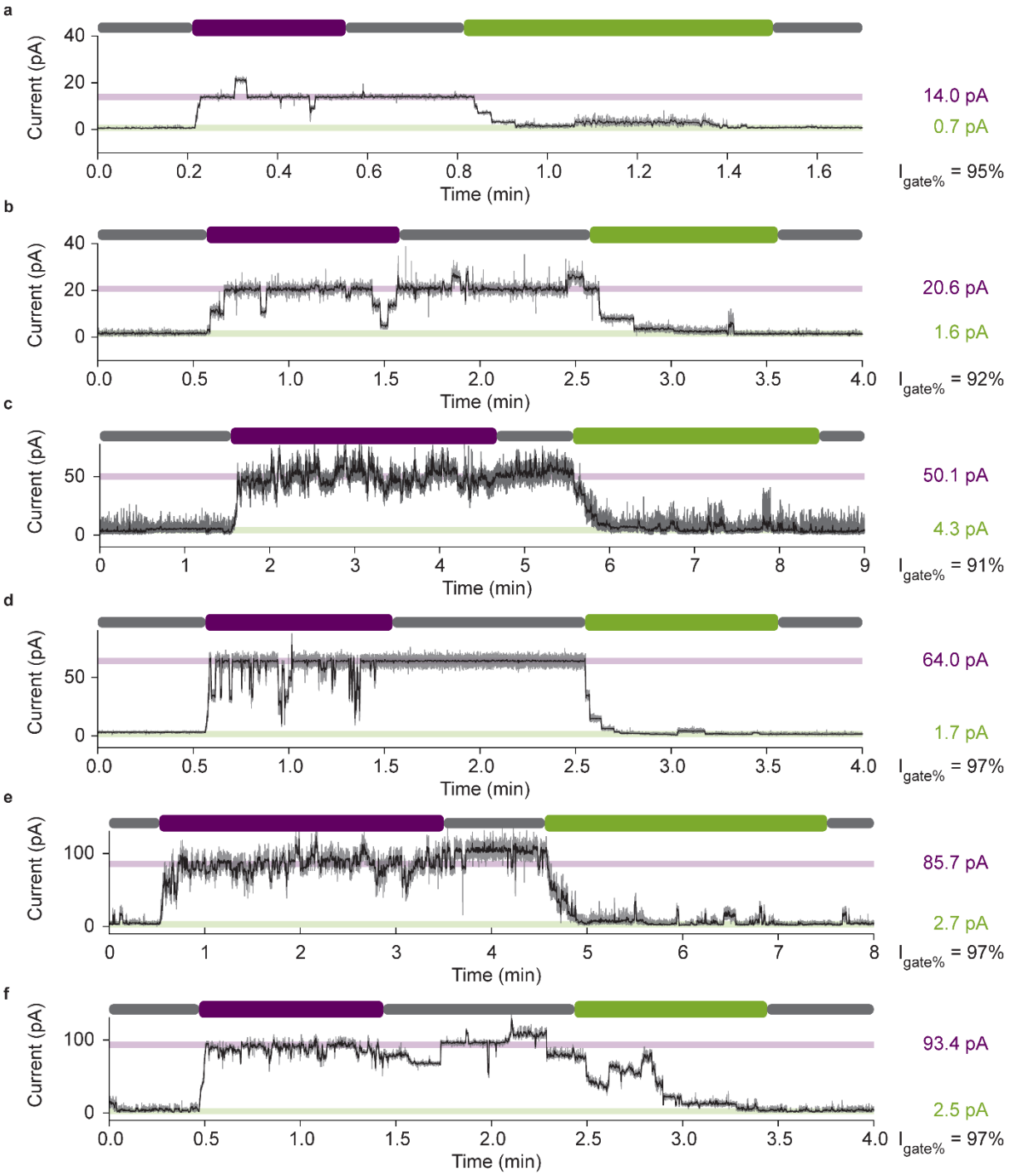


Fig. 13 | Representative determinations of $I_{gate\%}$ values for single $(E111C\text{-}pzMe)_7$ pores. The moving averages of the ionic currents (grey traces) were generated with a

Savitzky–Golay filter and shown in black. The top bar shows the irradiation cycle of dark→365 nm→dark→530 nm→dark. The $I_{gate\%}$ of all traces is >90%, suggesting that $I_{gate\%}$ appears to be consistent regardless of the absolute current (I_{ON} and I_{OFF}). The current traces were recorded at +100 mV using a 5 kHz in-line Bessel filter at 25 kHz sampling frequency, and a 20 Hz digital Bessel filter was used for data analysis. Recording conditions: 2 M KCl, 10 mM Tris-HCl, 0.1 mM EDTA, pH 8.5, 24 ± 1 °C.

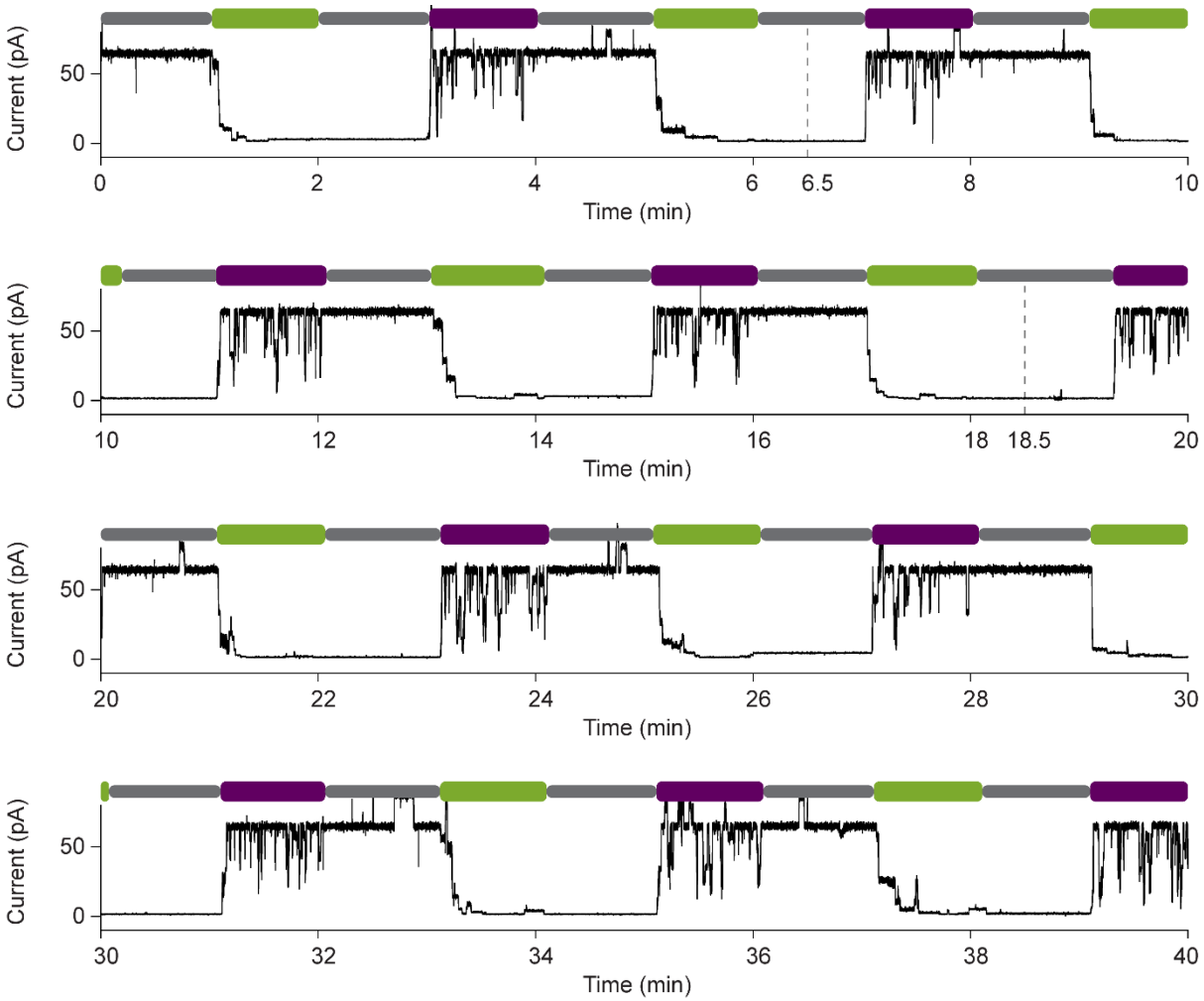


Fig. 14 | Prolonged trace of ON-OFF cycles recorded with a single (E111C-pzMe)$_7$ pore. Ten cycles were recorded over 40 minutes. **Fig. 2d** was taken from the region between the two grey dashed lines at 6.5 and 18.5 min. The current trace was recorded at +100 mV using a 5 kHz in-line Bessel filter at 25 kHz sampling frequency, and a 20 Hz digital Bessel filter was used for data analysis. Recording conditions: 2 M KCl, 10 mM Tris-HCl, 0.1 mM EDTA, pH 8.5, 24 ± 1 °C.

The intermediate current levels between I_{ON} and I_{OFF} were likely produced by the stepwise isomerization of individual pzMe molecules (**Fig. 9c**). Based on the number of pzMe switches in the *E* or *Z* state within a photopore, we designated the configuration of an ON-state photopore as (0^E, 7^Z), the photopore at the maximum OFF state as (7^E, 0^Z), and a partially OFF pore as one ranging from (1^E, 6^Z) to (6^E,

1^Z) (**Fig. 9b**). Notably, the intermediate current levels recorded with a single photopore during its ON-to-OFF or OFF-to-ON transitions differed from one transition to another. For example, during the stepwise reduction of the current recorded through an $(E111C\text{-}pzMe)_7$ photopore under 530-nm irradiation, over 10 distinct current levels were recorded across multiple transitions (**Fig. 15a**). In other words, each configuration, except for (0^E, 7^Z) and (7^E, 0^Z), corresponds to multiple current levels. The complexity was attributed to both the 20 combinatorial possibilities of the *E/Z* configurations of seven photoswitches[106], and the conformations of the photoswitches. As shown in **Fig. 4**, the seven *E*-pzMe molecules fully occluded and congested the photopore channel, suggesting that the current levels are influenced by pzMe stacking interactions and the orientation of pzMe towards the vestibule or the β barrel. For example, in the (5^E, 2^Z) state, there are three possible arrangements of the two *Z*-state pzMe photoswitches around the central axis of the pore (**Fig. 15**).

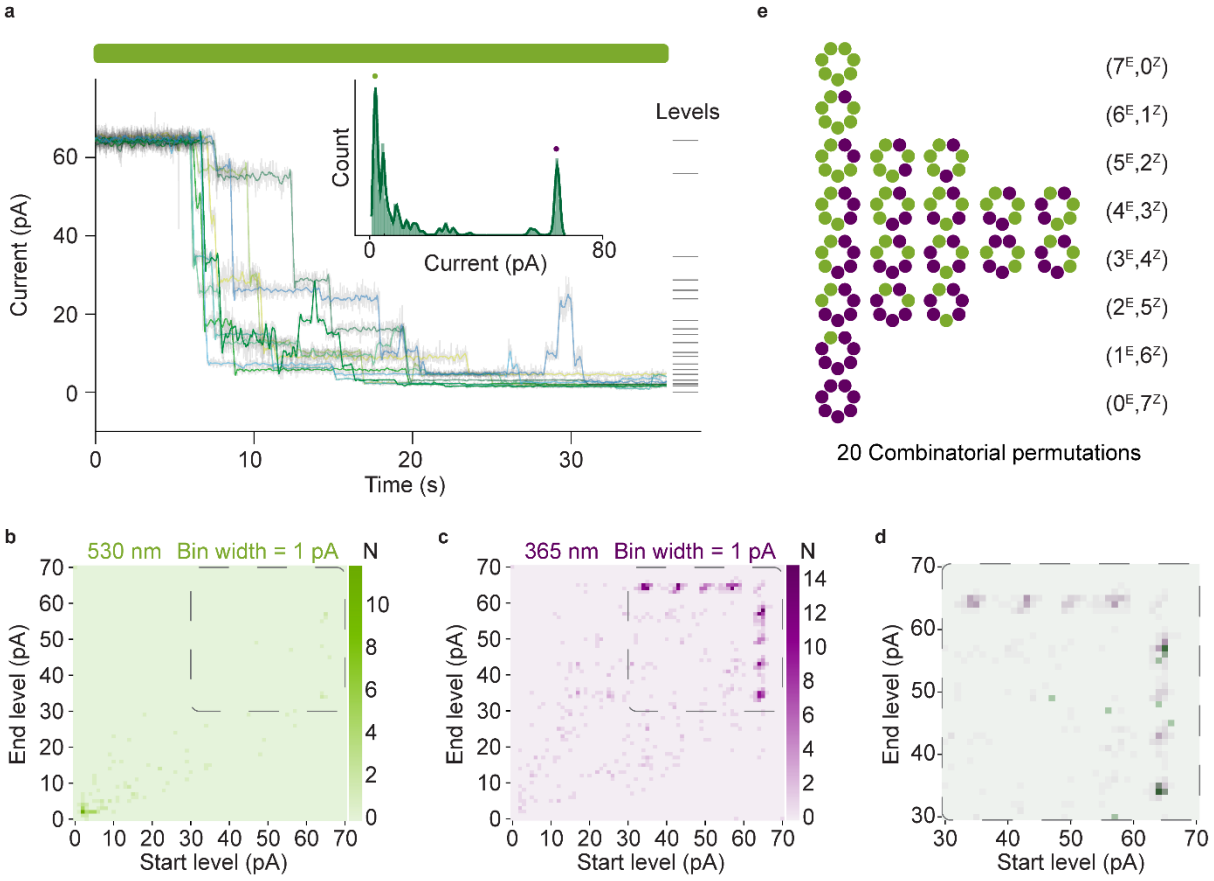


Fig. 15 | Multiple current levels arise from the single (1^E,6^Z) combination of the $(E111C\text{-}pzMe)_7$ pore. a, Overlay of ten *Z*-to-*E* transitions recorded with a single $(E111C\text{-}pzMe)_7$ pore. The transitions consistently started from the 64 pA level (ON) and ended at

1.6 pA (OFF). The inset histogram summarizes the all the current levels observed during the ten transitions from ON to OFF. The green and purple dots are the OFF and ON states. **b-c,** Heatmaps of all transitions observed with a single $(E111C\text{-}pzMe)_7$ pore under continuous 530-nm (**b**) or 365-nm (**c**) irradiation. The color bar on the right indicates the number of events (N). **d**, Overlay of transitions between current levels above 30 pA. Four dominant transitions are present between $(0^E,7^Z)$ and $(1^E,6^Z)$. According to the permutational isomer model (**e**), we expect only one $(1^E,6^Z)$ state. Therefore, a convincing model based simply on *E/Z* isomerization cannot be built.

Once a single photopore reached a terminal ON or OFF state, the current level exhibited fluctuations under continuous irradiation, while remaining relatively stable in the dark (**Fig. 9d-f**). This was expected as continuous irradiation would drive the reversible isomerization of photoswitches within a photopore: for example, switching between $(0^E, 7^Z)$ and $(1^E, 6^Z)$ states under 365 nm or $(7^E, 0^Z)$ and $(6^E, 1^Z)$ states under 530 nm. In the dark, $(E111C\text{-}pzMe)_7$ was locked in a single configuration; no *Z*-to-*E* thermal relaxation was observed for over 1 hour after irradiation ceased (**Fig. 16**).

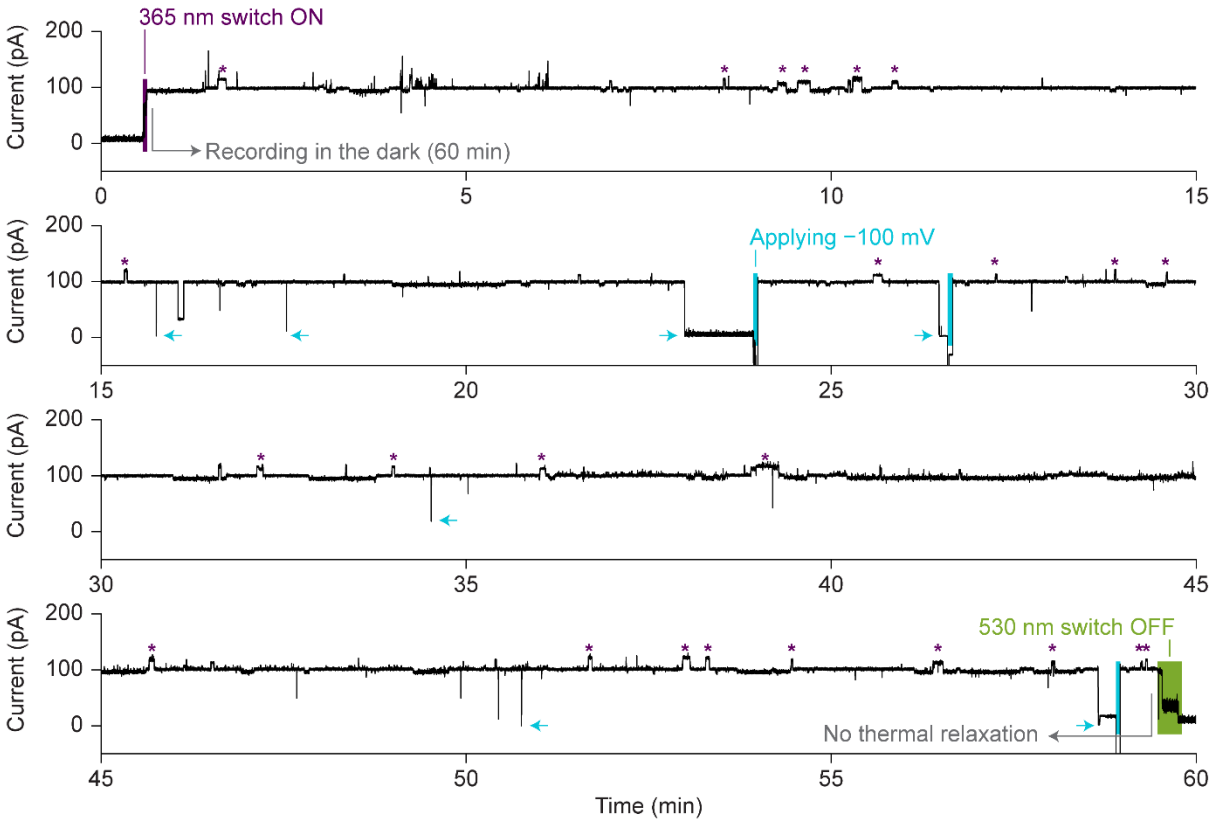
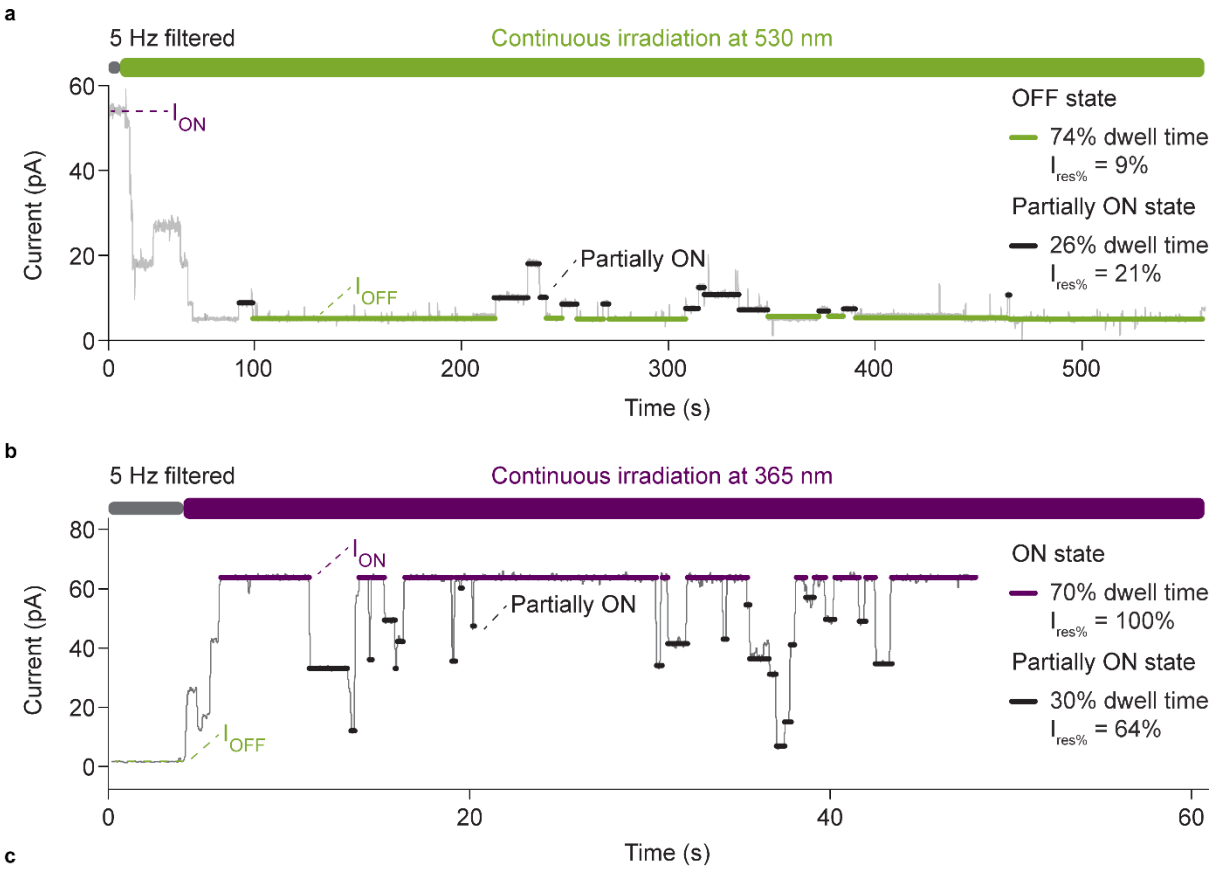


Fig. 16 | Prolonged recording with a single ON-state $(E111C\text{-}pzMe)_7$ pore in the dark. A single $(E111C\text{-}pzMe)_7$ photopore was switched on by 365-nm irradiation at 1 min. The ON-state current level was 98 pA at +100 mV. Subsequently, the light was turned off and the electrical recording of the ON-state $(E111C\text{-}pzMe)_7$ photopore, with photoswitches in

the *Z* state, was conducted for 1 hour. The current level remained stable in the dark, with occasional reversible events up to ~110 pA (purple asterisks) and infrequent gating events to almost 0 pA (blue arrows). The gating was reversed automatically or by briefly applying -100 mV. No pore closure caused by *Z*-to-*E* thermal relaxation was observed. The photopore was switched off by 530-nm irradiation at 59 min. The current trace was recorded at +100 mV at 25 kHz sampling frequency using a 5 kHz in-line Bessel filter and a 20 Hz digital Bessel filter. Recording conditions: 2.0 M KCl, 10 mM Tris-HCl, 0.1 mM EDTA, pH 8.5, 24 ± 1 °C.

The behavior of the $(E111C\text{-}pzMe)_7$ photopores at the ensemble level was compared to that at the single-channel level (**Fig. 9g**). The $I_{gate\%}$ value was ~10% lower with multiple pores compared to that of a single pore. This was likely caused by the presence of photopores in partially ON configurations as predicted by the single-channel photoswitching kinetics under continuous irradiation (**Fig. 17**).



c

Wavelength	Fractional time in complete OFF state ($I_{res\%}$ = 9%)	Fractional time in partially ON state ($I_{res\%}$ = 21%)	Macroscopic OFF-state current
530 nm	74%	26%	74% × 9% + 26% × 21% = 12%
365 nm	Fractional time in complete ON state ($I_{res\%}$ = 100%)	Fractional time in partially ON state ($I_{res\%}$ = 64%)	Macroscopic ON-state current
	70%	30%	70% × 100% + 30% × 64% = 89%

Fig. 17 | Estimation of the $I_{gate\%}$ values for an ensemble of (E111C-pzMe)$_7$ based on single-channel recording. a, Under 530-nm continuous irradiation, the photopore remained in the complete OFF state (green line) for 74% of the time (N = 84 transitions between OFF and partially ON states). For 26% of the time, the photopore was partially ON (black line) with an average percent residual current ($I_{res\%}$ = I/I_{ON}) of 21%. **b,** Under 365-nm continuous irradiation, the photopore remained in the complete ON state (purple line) for 70% of the time (N = 349 transitions between ON and partially ON states). For 30% of the time, the photopore was partially ON (black line) with an average $I_{res\%}$ of 64%. **c**, The incomplete closure under 530 nm and the incomplete opening under 365 nm reduced the macroscopic gating efficiency. Based on single-channel observations, the ensemble $I_{gate\%}$ was estimated to be 100% − 12%/89% = 86%, which aligns with the experimental value of a mean $I_{gate\%}$ of 85% (**Fig. 9g**). Recording conditions: 2.0 M KCl, 10 mM Tris-HCl, 0.1 mM EDTA, pH 8.5, 24 ± 1 °C.

The incorporation of in-line bandpass filters to reduce the LED bandwidths to 10 nm did not improve the $I_{gate\%}$ value. Although ON-OFF switching was successfully demonstrated in a planar lipid bilayer experiment with an externally applied electrical potential, we envisage the future application of photophores in biological cell membranes. For example, animal cells, such as neurons and muscle cells, exhibit resting and action potentials that vary under electrical or chemical stimulation. These potentials arise from the asymmetric distribution of sodium, potassium, and calcium ions. To mimic the physiologically relevant membrane potential observed during an action potential, we employed an asymmetric KCl concentration across a membrane (**Fig. 18**). Under these conditions, the photoswitching behavior was reproduced without the need for an externally applied transmembrane potential (**Fig. 9h**).

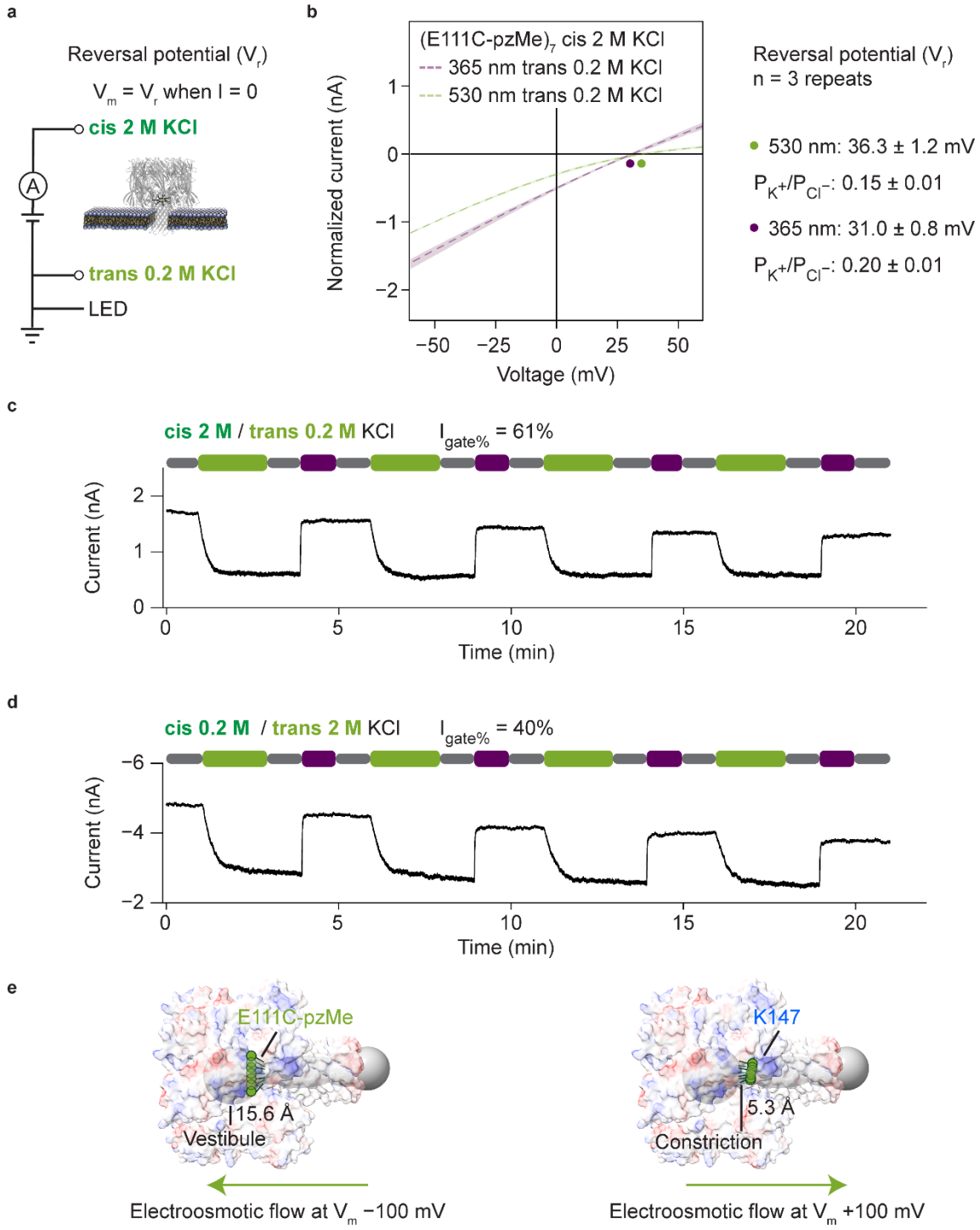


Fig. 18 | Charge selectivity of (E111C-pzMe)$_7$. a, Transmembrane potential generated by an asymmetric KCl concentration across the lipid bilayer. The reversal potential (V_r) is defined as the potential required to bring the current flow to zero. **b**, I–V characterization of an ensemble of (E111C-pzMe)$_7$. The reversal potential was measured after 530- and 365-nm irradiation. The shading around the mean current represents the 95% confidence interval for three repeats. The measured V_r suggests anion selectivity. **c-d,** Currents driven by a KCl concentration gradient. The values of $I_{gate\%}$ in **c** and **d** was consistent with the voltage-dependence of $I_{gate\%}$ reported in **Fig. 19c**. **e,** Model for the electroosmotic flow generated by the charge selectivity. Under negative potential, the pzMe was pushed

towards the vestibule. Conversely, the pzMe pointed towards the β barrel adjacent to positively charged K147 residue under positive potential. The experiment was recorded at 25 kHz sampling frequency and filtered using a 5 kHz in-line Bessel filter. Recording conditions: (**b**, **c**) 2 M / 0.2 M KCl, (**d**) 0.2 M / 2 M KCl, 10 mM Tris-HCl, 0.1 mM EDTA, pH 8.5, 24 ± 1 °C.

2.3 Switchable iontronic diode properties

The ON-OFF behavior of the (E111C-pzMe)$_7$ photopore was further demonstrated in a broader range of applied potential by ramping the voltage from −200 mV to +200 mV in 10-mV steps. We characterized the current-voltage (I–V) behavior of a single (E111C-pzMe)$_7$ in the dark after reaching the ON state at 365 nm or the OFF state at 530 nm (**Fig. 19a**). After irradiation at 530 nm, the photopore exhibited a diode-like non-linear I–V response; almost no current passed through the pore at positive potentials (0 to +200 mV, V_m applied to trans, **Fig. 1f**), whereas the current demonstrated resistor-like behavior at negative potentials (G = I/V = 0.32 ± 0.11 nS at −100 mV, N = 3 pores) (**Fig. 19a**). After irradiation at 365 nm, a less obvious rectification was observed (G = I/V = 0.46 ± 0.06 nS at +100 mV and 0.58 ± 0.12 nS at −100 mV, N = 3 pores) (**Fig. 19a**). In other words, the photopore functioned as a photoresistor after irradiation at 365 nm and as an iontronic diode after irradiation at 530 nm. We speculate that the voltage-dependent behavior of (E111C-pzMe)$_7$ photopores arises from the biased orientation of photoswitches confined within an asymmetric nanopore. The orientation of these charge-neutral photoswitches could be influenced by electroosmotic flow, which is directionally dependent on the applied voltage (**Fig. 18e**). Depending on their orientations, the seven photoswitches could adopt various configurations, promoted by the surrounding protein environment, thereby altering the ionic flow.

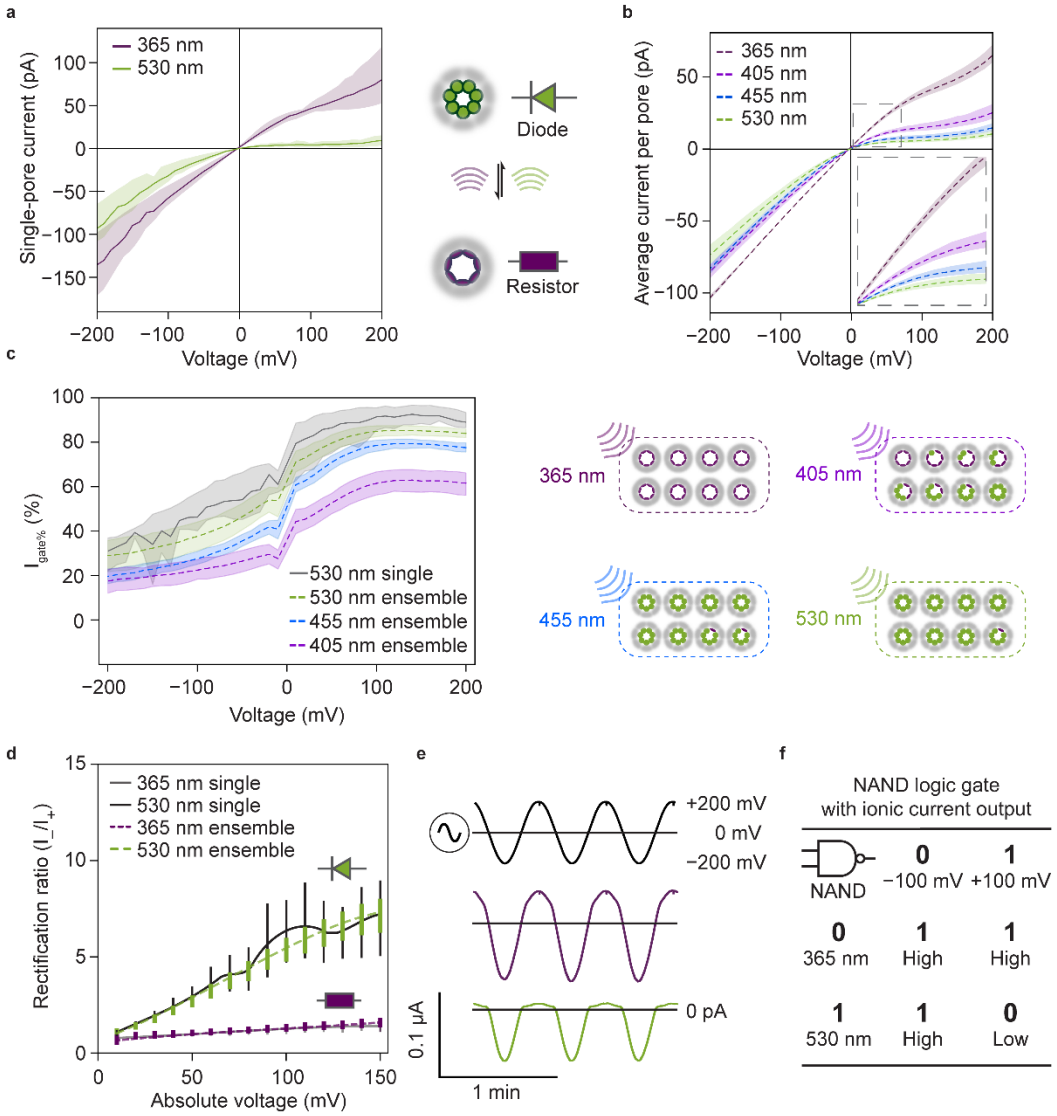


Fig. 19 | Diode properties of (E111C-pzMe)$_7$ photopore. a, The current–voltage (I–V) curves of a single (E111C-pzMe)$_7$ after 365-nm or 530-nm irradiation reveals photoswitchable resistor and diode behaviors. Mean current levels are shown with 95% confidence interval (N = 3 separate pores). **b,** The I-V responses of ensembles of (E111C-pzMe)$_7$ recorded after irradiation at four wavelengths (365 nm, 405 nm, 455 nm, and 530 nm) and normalized according to the number of pores. Each pore was assumed to contribute +64 pA at +100 mV after 365-nm irradiation. The number of pores in each experiment ranged from 60 to 904 (N = 7 experiments). Mean current levels are shown with 95% confidence interval. **c,** Voltage- and wavelength-dependences of the percent gated current [$I_{gate\%} = (1 - I_{OFF}/I_{ON}) \times 100\%$], where I_{ON} is the current after 365-nm irradiation and I_{OFF} is the current at the wavelength of interest. The error bands are 95% confidence intervals. The right schematic shows an estimated distribution of intermediate states at PSS of four wavelengths. **d,** Voltage-dependence rectification ratio (I_-/I_+) of a single or multiple (E111C-pzMe)$_7$ photopores (N = 3 experiments, data are mean I_-/I_+ with standard deviations shown as error bars). **e,** Current passing through an ensemble of (E111C-pzMe)$_7$ photopores in response to an alternating potential. The curves from the top to bottom are the applied voltage, and the current responses at 365 nm and at 530 nm. **f,** A truth table for the NAND logic achieved using photopores. High and low current levels are achieved by

combinations of the input wavelength (λ) and the applied potential. The current I–V curves were recorded with a 5 kHz in-line Bessel filter at 25 kHz sampling frequency, and a 20 Hz digital Bessel filter was used for data analysis. Recording conditions: 2 M KCl, 10 mM Tris-HCl, 0.1 mM EDTA, pH 8.5, 24 ± 1 °C.

The dual-mode feature (i.e., diode and photoresistor) demonstrated with single pores was reproduced with hundreds of pores in ensemble experiments (N = 8 experiments, 100 to 600 pores per experiment) under 365-nm and 530-nm irradiation (**Fig. 19b**). Irradiation at 405 nm and 455 nm was also tested; these wavelengths generated current levels between those produced by 365 nm and 530 nm at all applied potentials (**Fig. 19b**). To give an overview of the voltage-dependent behavior in the ensemble, $I_{gate\%}$ was calculated following $I_{gate\%} = (1 - I_{OFF}/I_{ON}) \times 100\%$, where the current level after 365-nm irradiation was I_{ON} and that after 405 nm, 455 nm, or 530 nm was I_{OFF} (i.e. $I_{gate\%(405\ nm)} = (1 - I_{405}/I_{365}) \times 100\%$) (**Fig. 19c**). Between −150 mV to +100 mV, $I_{gate\%}$ increased with decreasing negative potential and increasing positive potential for all three wavelengths. The difference in PSS ratios associated with irradiation wavelengths was the primary reason for the wavelength dependence of $I_{gate\%}$. The rectification ratio of $(E111C\text{-}pzMe)_7$ (RR = I_-/I_+, the ratio of currents recorded under opposite polarities at the same potential) scaled almost linearly with the amplitude of the applied potential up to ±150 mV (**Fig. 19d**), and was 5.5 ± 0.7 at ±100 mV in the diode mode after 530-nm irradiation (**Fig. 19d**).

Nanopore diodes can be used in soft devices as half-wave rectifiers[44] to convert alternating current to direct current. We tested our photopore as a switchable iontronic diode to effect a unidirectional current across a synthetic bilayer under an alternating voltage at 0.03 Hz (**Fig. 19e**). After 530-nm irradiation, ~900 $(E111C\text{-}pzMe)_7$ photopores collectively conducted currents only under a negative potential. After 365-nm irradiation, the current flow replicated the sinusoidal shape of the alternating voltage input, albeit weakly rectified. At higher input frequencies, the capacitive current caused by the bilayer would override the resistive current through the pore, diminishing the rectification. The ionic current output through $(E111C\text{-}pzMe)_7$ photopores was therefore determined by both the wavelength and the applied potential, resembling the NAND Boolean function. This NAND logic gate leveraged the irradiation wavelength as input 1 (0 = 365 nm, 1 = 530 nm) and the

applied potential as input 2 (0 = −100, 1 = +100 mV). A low current output only occurs at +100 mV after irradiation at 530 nm (**Fig. 19f**).

2.4 Light-to-ionic signal conversion

The rate of photoisomerization of a photoswitch is typically proportional to the light intensity[46,54,107]. Accordingly, 365-nm irradiation of more than 600 $(E111C\text{-}pzMe)_7$ pores at 36.2, 28.2 and 13.4 mW/cm^2 (**Fig. 8**) increased the duration of OFF-ON transition from 5.8 ± 0.5 s to 7.1 ± 0.6 s, and then to 11.4 ± 2.6 s (N = 4 ensembles, **Fig. 20a**). After the photoequilibrium current level was reached under a given wavelength of irradiation, reducing the light intensity led to no current change (**Fig. 20b**). In contrast, common electronic components and optogenetic tools often exhibit transient current responses that vary with light intensity.

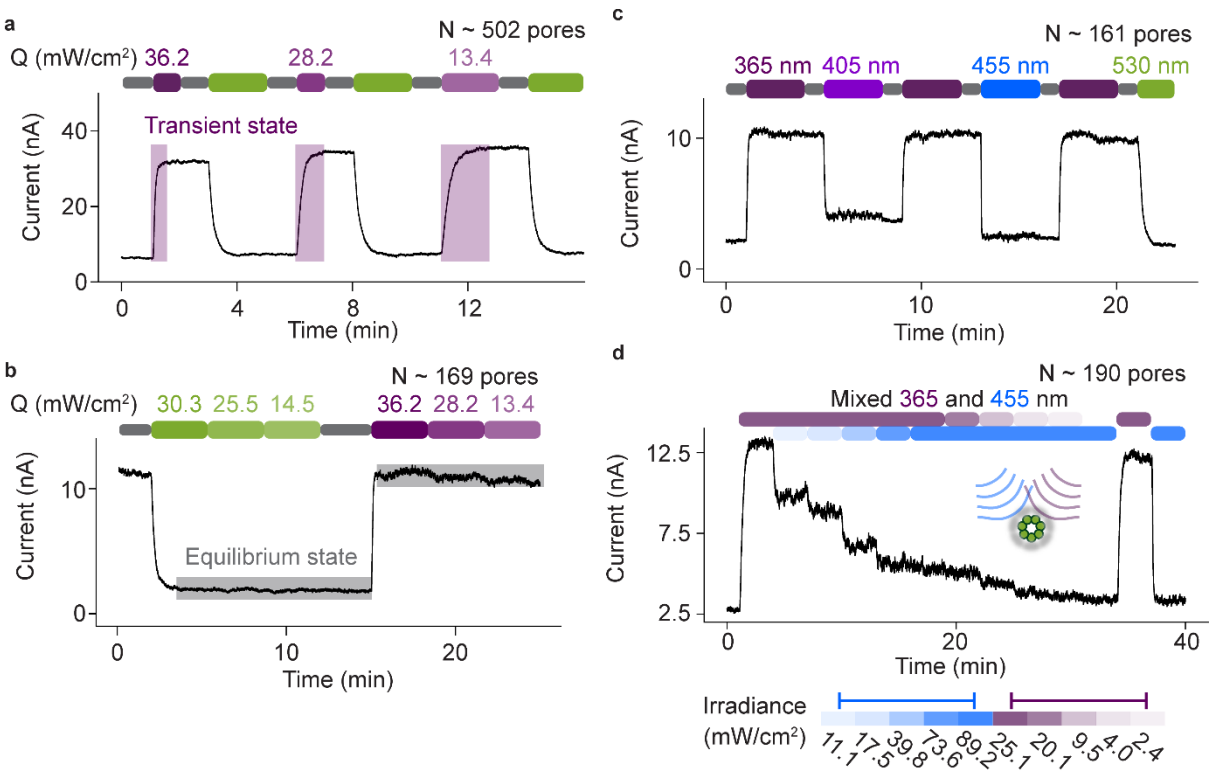


Fig. 20 | Effects of light intensity and wavelength on the conductance of $(E111C\text{-}pzMe)_7$ ensembles. a, Reduced rate of transition from the low-conductance state (I_{OFF}) to the high-conductance state (I_{ON}) due to reductions in the intensity of 365 nm irradiation (purple). The light irradiance (Q) is shown above the light sequence. The baseline drift is caused by the degradation of Ag/AgCl electrodes when recording for minutes at the nA level. **b,** Insensitivity of output current to light intensity after an photoequilibrium state is reached. When photopores reached photoequilibrium states of I_{ON} = 11.4 nA (530 nm, green) or I_{OFF} = 1.8 nA (365 nm, purple) (purple), reductions in the light intensity from high

to low Q did not cause further changes in the current. **c,** At photoequilibrium, wavelengths of continuous irradiation result in: an ON state at 365 nm (purple), partially OFF states at 405 nm (violet) and 455 nm (blue) and a fully OFF state at 530 nm (green). **d,** Intermediate current levels can be accessed by polychromic light. Mixed-wavelength irradiation over 3-min intervals with various ratios of 365-nm and 455-nm light allowed fine-control of the PSS ratios with >200 photopores. The current traces were recorded at +100 mV using a 5 kHz in-line Bessel filter at 25 kHz sampling frequency, and a 20 Hz digital Bessel filter was used for data analysis. Recording conditions: 2 M KCl, 10 mM Tris-HCl, 0.1 mM EDTA, pH 8.5, 24 ± 1 °C.

An ionic signal conducted by multiple $(E111C\text{-}pzMe)_7$ photopores at an intermediate current level between I_{ON} and I_{OFF} could be accessed by switching off the irradiation immediately after reaching the desired current level during an ON-OFF transition at a given wavelength. However, it was challenging to reproducibly capture a transient current level of interest during rapid ON-OFF transitions. An alternative strategy was devised using polychromic light to produce equilibrium current levels as determined by the PSS of photoswitches (**Fig. 20c,d**), which would be unattainable by continuous irradiation at either one of the wavelengths. Light from 365-nm and 455-nm LEDs was combined through a fiber-coupler. The graded modulation of ionic signal was demonstrated by varying the relative intensity of the 365-nm and 455-nm irradiation projected onto the multiple $(E111C\text{-}pzMe)_7$ pores in 3-minute steps. Ionic signal levels between those recorded at PSS_{365} and PSS_{455} were obtained (**Fig. 20d**). This approach allowed for finer control over the graded modulation of ionic current through $(E111C\text{-}pzMe)_7$ photopores.

Inspired by the slow thermal relaxation of arylazopyrazole and the graded modulation of the ionic signal, we proposed light-to-ionic signal conversion by an ensemble of iontronic photopores. We first encrypted information-bearing binary data within light sequences that alternated between 365-nm and 455-nm radiation (**Fig. 21a**). Functioning as a light-to-current converter, the $(E111C\text{-}pzMe)_7$ photopores translated the light sequences into two-level current patterns (**Fig. 21a**), as illustrated by a representative segment of a trace with an input rate of 20 s/bit (**Fig. 21b**). Higher input rates were achieved with increased light intensities, reaching 1.5 s/bit at 365 nm and 1.9 s/bit at 455 nm using the maximum LED outputs. Over a 90-minute experiment, no photobleaching was observed. By associating the ON-state with a black pixel and the OFF state with a white pixel, a pixel art spelling “OXFORD” was reconstructed from a binary light message.

Furthermore, adding mixed irradiation at both 365 nm (36.2 mW/cm^2) and 455 nm (56.3 mW/cm^2) expanded the alphabet to a three-state system, which was applied to demodulate a pixel art representation of a protein nanopore and a text message written in Morse code (**Fig. 21c**,**d**). In principle, by using mixed-wavelength irradiation, the (E111C-pzMe)$_7$ photopores could output a series of current levels, between the levels at PSS$_{365}$ and PSS$_{530}$, as the basis of complex encoding systems. With our equipment, the current levels fluctuate ± 0.3% in the dark after a 20 Hz digital filter, and the $I_{gate\%}$ was 0~85%. Thus, an upper-level estimate for the number of assignable levels would be ~300.

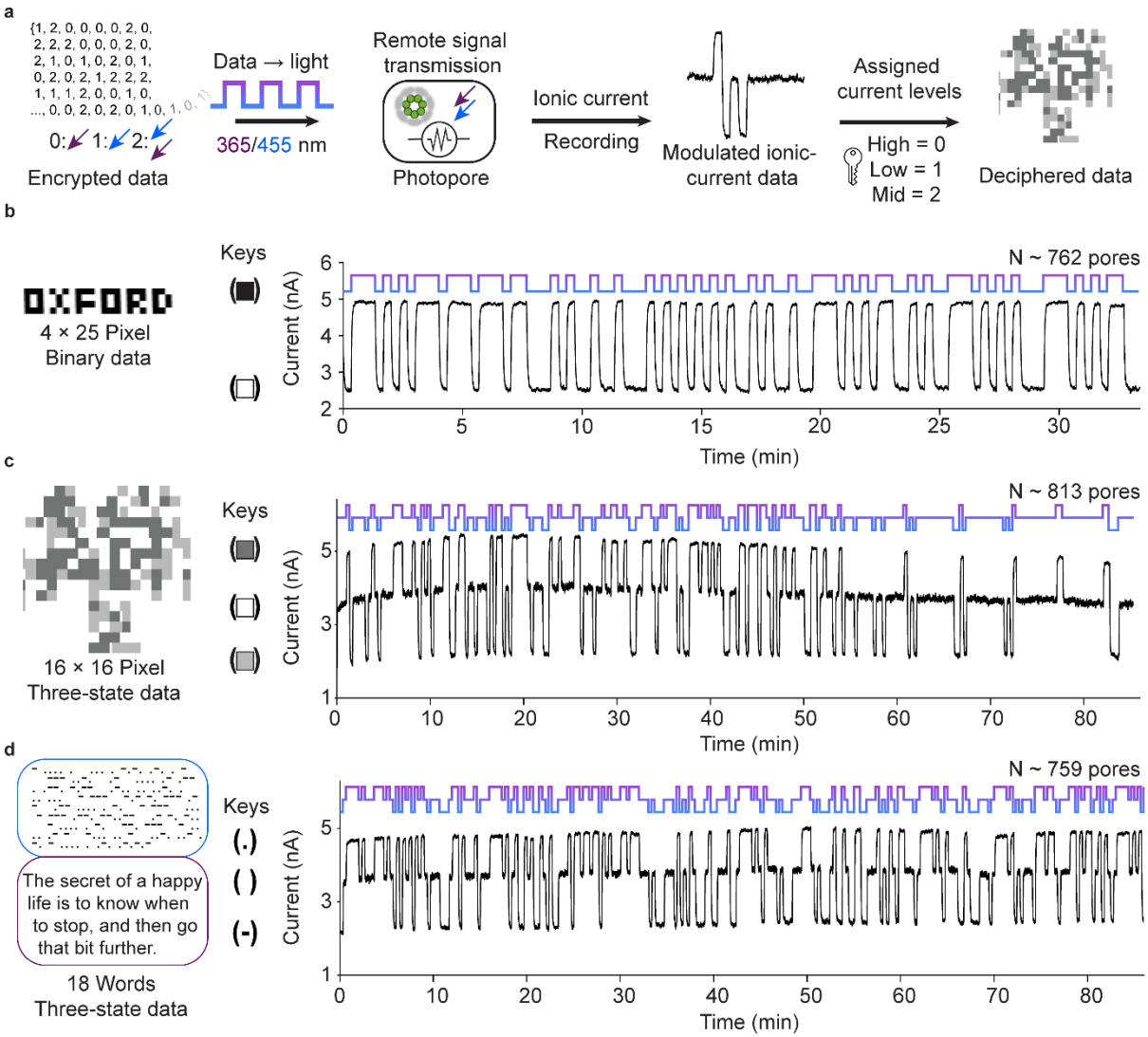


Fig. 21 | Light-to-current signal conversion. a, Overview. Image or text data were encoded as light sequences that produced ionic current responses from (E111C-pzMe)$_7$. By using predetermined keys to assign the current levels, the ionic currents were deciphered to reconstruct the original data. **b,** Transmission of a binary pixel pattern with

monochromic 365- and 455-nm irradiation. **c,** Transmission of a three-state pixel art in a light sequence. The image of the αHL pore was generated from PDB: 7AHL and converted to three-color pixel art. Each pixel was assigned to 0, 1 or 2 based on the color. The matrix of pixels was flattened to 1D to produce the light sequence. **d,** Transmission of three-state Morse code. The blue box is the Morse code from the deciphered current trace, and the purple box is the translated text. The light sequence was the input at wavelengths of 365 nm, 455 nm or mixed 365/455 nm at a rate of 20 s per bit to generate a current pattern consisting of three levels. The current traces were recorded at +100 mV using a 5 kHz in-line Bessel filter at 25 kHz sampling frequency, and a 20 Hz digital Bessel filter was used for data analysis. Currents from $(E111C\text{-}pzMe)_7$ ensembles were recorded in 150 mM KCl, 20 mM Tris-HCl, 0.1 mM EDTA, pH 8.5, 24 ± 1 °C.

2.5 Conclusions

In this work, we constructed protein nanopores with unitary conductance values that changed under remote light control. Among the tested photopores, we achieved quantitative, prolonged, and reversible modulation of ionic currents within $(E111C\text{-}pzMe)_7$ pores following irradiation at 365 nm (ON, high conductance) and 530 nm (OFF, low conductance). Notably, when an ON-state $(E111C\text{-}pzMe)_7$ was switched OFF at +100 mV, the unitary conductance reduced by >95%. Similarly, a current reduction of >85% occurred when multiple $(E111C\text{-}pzMe)_7$ pores were used in ensemble experiments. This sustained ON state and the almost complete OFF state are highly advantageous for real-time control over transmembrane ionic communication in nanotechnology or synthetic biology applications.

The photopores described here differ from previously described photoregulated nanopores in two aspects. First, the photoswitches controlled the conductance of a fully assembled nanopore reversibly, rather than the process of irreversible nanopore assembly[79]. Second, the current-voltage characteristics of $(E111C\text{-}pzMe)_7$ exhibited two switchable states: a resistor-like ON-state, after 365-nm irradiation, and a diode-like OFF-state, after 530-nm irradiation. In the diode mode, there is no delay in the rectification of $(E111C\text{-}pzMe)_7$ after the reversal of the polarity of the applied potential, in contrast to the previous (non-photoswitchable) arginine-rich αHL diode[44].

One impact of photopores in the field of nanoscale iontronics might be in light-to-ionic current signaling. In the case of the $(E111C\text{-}pzMe)_7$ pore, we have used the ability to produce multiple output current levels, such as the three-state system (blue,

mixed, and UV), to demonstrate the ability to reconstruct images or text encoded in light pulses. It follows that by hosting light-modulated nanopores in a 2D array of lipid bilayers, an artificial retina might be created to detect colored images. Our previous work on droplet-hydrogel-bilayer bio-pixels reported a related approach for monochromic 530 nm light[108].

The photopores might also be incorporated into 3D-printed droplet-based synthetic tissues where the spatiotemporal control of communication between compartments is key to the control of tissue-like behavior[52,109]. There, they could be used, amongst other things, to trigger the release of ions or small molecules[52], mediate shape changes[109] or produce motion[110]. We further envisage the development of additional photopores by the conjugation protocol reported here to gain control over additional properties such as selectivity in the transport of small molecules and the ability to mediate the translocation of biopolymers.

2.6 Methods

2.6.1 General information

All chemicals were purchased from Merck and used as received unless otherwise stated. Br-pzMe, Br-fAzo and Br-pzH were prepared (see Synthesis and characterization of photoswitches) and used as 3 mM DMSO stock solutions for bioconjugation experiments. Details of synthesis are available in the synthesis section. The fiber-coupled LEDs were purchased from Thorlabs (M405FP1, M455F3 and M530F2). An optical fiber (Ø1000 µm, 0.39 NA) was supplied by Mightex. LC-MS of αHL monomers were recorded on a benchtop QTOF mass spectrometer (Waters Xevo G2-XS) with a ProSwift RP-2H column (ThermoFisher, linear-gradient acetonitrile/water, 0.1% (v/v) TFA, 10 min), and the results were deconvoluted using MassLynx software (Waters). An Arduino UNO microcontroller was programmed to trigger and log the time points of irradiation. Molecular modelling was carried out by using open-source PyMol on GitHub (Schrodinger).

2.6.2 Custom recording chamber

Planar lipid bilayer recording experiments were performed in a custom poly(methyl methacrylate) (PMMA) recording chamber. The chamber accommodated an LED

light source through an adjustable FiberPort collimator (Thorlabs), allowing accurate alignment and direct irradiation of the aperture in the Teflon film (Ø100 µm). Before recording, the collimator was adjusted to achieve consistent projection of the maximum light intensity onto the aperture through a 3-mm-thick sapphire window (Thorlabs). Fiber-coupled LEDs of various wavelengths (365, 405, 455, 530 nm, Thorlabs) were connected to the collimator through a UV-compatible multimode fiber (0.39 NA, Ø1000 µm, Mightex). In the experiments with mixed wavelengths, a bifurcated fiber bundle (0.39 NA, Ø1000 µm, Thorlabs) was connected to two LEDs. Band-pass filters (Thorlabs) were used for the data presented in **Fig. 9g** to achieve a narrow bandwidth of 10 nm for 355 nm and 4 nm for 532 nm (**Fig. 12c**). These filters were loaded onto an integrated in-line reflective fiber optic filter (Thorlabs).

2.6.3 Site-directed mutagenesis of αHL cysteine mutants

Genes encoding αHL mutants with a single cysteine residue at position E111, T115, T125 or T129 were prepared from the pT7-αHL-D_8H_6 plasmid by site-directed mutagenesis (QuikChange II XL, Agilent) with the primers listed in Table 1. The template plasmid have been previously reported[111], where the octaaspartate and hexahistidine tag (-D_8H_6) was designed for anion exchange (IEX) and Ni-NTA purification. The polymerase chain reaction was initiated by mixing 5 µL 10 × reaction buffer, 10 ng DNA template, 125 ng forward and reverse primers, 1 µL dNTP mix, 3 µL QuikSolution, 2.5 U PfuUltra HF DNA polymerase and nuclease-free water to make a final volume of 50 µL. After thermal cycling (1 × 95˚C:1 min → 18 × 95˚C: 50 s, 60˚C: 50 s, 68˚C: 5 min → 1 × 68˚C: 7 min), 1 µL DpnI (10 U) was added and the mixture was incubated for 1 h at 37˚C to digest the template DNA. Transformation of *E. coli* was performed by incubating 2 µL of the digested PCR product with 45 µL XL-10 Gold competent cells (Agilent) on ice, followed by 30 s heat shock at 42˚C. Subsequently, a Luria-Bertani (LB)-agar plate containing carbenicillin (50 µg mL^{-1}, Merck) was inoculated with the transformed cells. All mutants were verified by DNA sequencing.

2.6.4 Expression and purification of αHL cysteine mutants

BL21(DE3)pLysS *E. coli* cells (Agilent) were transformed with the mutated plasmid and inoculated onto LB-agar plates containing antibiotics (carbenicillin, 50 µg mL^{-1}; chloramphenicol, 34 µg mL^{-1}). A single colony from the plate was picked to inoculate

10 mL LB for the preculture. A 400 mL LB culture containing the same antibiotics was inoculated with 4 mL overnight pre-culture. This expression culture was shaken at 37˚C at 250 rpm for approximately 3 h until the OD reached 0.6, when it was cooled 18˚C before the addition of 2 mL 0.1 M IPTG (Fluorochem) to induce protein expression. The culture was further shaken at 18˚C at 200 rpm overnight. The cells were then harvested by centrifugation in a Beckman J25 centrifuge at 4000 × g for 20 min at 4˚C and resuspended in 10 mL lysis buffer (50 mM Tris-HCl, pH 8.0, 150 mM NaCl, 10 mM imidazole, 0.1% Triton X-100, 5% glycerol, 2 mM TCEP with an EDTA-free protease-inhibitor tablet (ThermoFisher)). Lysis was then performed by the addition of 250 µL 40 mg/mL lysozyme (ThermoFisher), 2 µL 250 U/µL universal nuclease (ThermoFisher) and 25 µL 2 M $MgCl_2$, and incubation on ice for 1 h. The lysate was sonicated at 40% amplitude for 3 min in a 30 s-ON-30 s-OFF pulse train on ice (VCX 500, Sonics). The supernatant was cleared by centrifugation at 29000 x g for 45 min at 4˚C and transferred to a gravity column containing 1 mL (bed volume) Ni-NTA resin (ThermoFisher). The lysate supernatant and resin mixture was mixed at 4˚C on a platform rotator for 1 h. The column was washed with 2 x 15 mL washing buffer (50 mM Tris-HCl, pH 8.0, 500 mM NaCl, 20 mM imidazole, 2 mM TCEP, 0.1% Triton X-100 and 5% glycerol) and eluted with elution buffer (50 mM Tris-HCl, pH 8.0, 500 mM NaCl, 250 mM imidazole, 2 mM TCEP, 0.1% Triton X-100 and 5% glycerol). The fractions (~10 mL) containing αHL were combined and loaded onto a HiLoad 26/600 Superdex 200pg (Cytiva) SEC column equilibrated with SEC buffer (10 mM Tris-HCl, pH 8.0, 150 mM NaCl, 2 mM TCEP and 5% glycerol) at 4˚C. Fractions containing monomers of αHL cysteine mutants were concentrated to 1 mg/mL and stored at −80˚C as aliquots. The mass of the monomer was verified by LC-MS. On average, 9 mg pure αHL-D_8H_6 monomer after SEC purification was obtained from 400 mL culture.

2.6.5 Conjugation of photoswitches

Br-pzMe, Br-pzH or Br-fAzo (the photoswitches) were dissolved at 3 mM in dimethyl sulfoxide (DMSO). Purified monomers of the αHL cysteine mutants were buffer-exchanged and diluted to 0.5 mg/mL in low TE buffer (10 mM Tris-HCl, pH 8.0, 0.1 mM EDTA). A photoswitch was added to a monomer solution stepwise over 18 h to a final concentration of 750 µM. The mixture was incubated at 20˚C and cooled to 4˚C before the removal of the excessive photoswitch. The extent of reaction was

assessed by LC-MS. The conjugated protein solution was passed through a desalting spin column (ThermoFisher) equilibrated in the low TE buffer to remove excess photoswitch and the eluent was stored at −80˚C.

2.6.6 Formation and purification of photopore homoheptamers

The photopore monomer was concentrated with a PES protein concentrator (ThermoFisher) to ~8 mg/mL, and exchanged into low TE buffer (10 mM Tris-HCl, pH 8.0, 0.1 mM EDTA) with a desalting spin column. Heptamerization was performed by adding 10% (w/v) sodium deoxycholate solution to the concentrated protein solution, reaching a final concentration of 6.25 mM. The mixture was incubated at 22˚C for 1 h. To separate oligomerized photopores from the remaining monomers, the mixture was loaded onto a membrane-based strong cation exchange spin column (ThermoFisher), which was equilibrated with 20 mM MOPS, pH 7.5. The sample was eluted with the same buffer containing NaCl (0.2, 0.3, 0.4, 0.6, 2 M) (**Fig. 10b**). The homoheptamer eluted at ~0.3 M NaCl, and fractions were combined and frozen at −80˚C. Before electrical recording, the MOPS buffer was exchanged for low TE buffer (10 mM Tris-HCl, pH 8.0, 0.1 mM EDTA).

2.6.7 Single-channel and ensemble experiments

The Teflon aperture of the recording chamber was pre-treated with hexadecane (~5 µL 1% in pentane). After 10 min, recording buffer (1 mL, 10 mM Tris-HCl pH 8.5, 2 M KCl, 0.1 mM EDTA) was added to both the cis and trans compartments. A lipid bilayer was formed on the aperture by adding 1,2-diphytanoyl-3-sn-phosphatidylcholine (DPhPC, Avanti Polar Lipids) to each compartment. A pair of Ag/AgCl electrodes was placed in each compartment through a salt bridge (3 M KCl in 2% (w/v) agarose). The electrodes were covered with black tape to avoid exposure to light from the LED.

To insert a single pore into the bilayer (**Fig. 12a**), homoheptamer (0.1 µL, 0.2 mg/mL) was added to the cis compartment. Once a pore had inserted and showed photoresponse, the buffer was perfused five times to prevent further insertions. To achieve the stepwise insertion of multiple pores, more homoheptamer (10 µL, 0.2 mg/mL) was used (**Fig. 11a**).

The characterization of the photopore ensemble was recorded using photopore monomers pre-irradiated at 530 nm for 30 min prior to use to ensure the reproducibility of pore insertion (**Fig. 12c**). The monomers (~5 µL 0.2~0.5 mg/mL) were added to the cis compartment while 530 nm LED was switched on. Pore insertion occurred under an alternating applied potential of ±20 mV, and the insertion rate slowed down over 15 min. Excess monomers were removed by perfusion of the cis compartment.

Ionic currents were recorded through Ag/AgCl electrodes connected to a patch clamp amplifier (Axopatch 200B, Axon Instruments). The signal was filtered with an in-line 4-pole low-pass Bessel filter (80dB/decade, 5 kHz). A Digidata 1322A digitizer (Molecular Devices) was used to convert the analogue signal to digital form. The data were analyzed with the pCLAMP 10.3 software suite (Molecular Devices). Electrical traces were plotted with Python (3.8.8), Pyabf (2.3.5), Matplotlib (3.3.4) and Seaborn (0.11.1).

2.6.8 Ion selectivity and electro-osmotic flow

The current–voltage response of $(E111C\text{-}pzMe)_7$ was measured over an applied potential ranging from −200 mV to + 200 mV in 10 mV increments with an asymmetric KCl gradient: 2 M KCl (cis) / 0.2 M KCl (trans) (**Fig. 18**). The permeability ratio (P_{K^+}/P_{Cl^-}) was determined from the potential at the zero current intercept (the reversal potential, V_r) by using the Goldman-Hodgkin-Katz (GHK) equation[112]:

$$\frac{P_{K^+}}{P_{Cl^-}} = \frac{[Cl^-]_{trans} - [Cl^-]_{cis} e^{\frac{V_r F}{RT}}}{[K^+]_{trans} e^{\frac{V_r F}{RT}} - [K^+]_{cis}} \quad (1)$$

where F is the Faraday constant; R is the ideal gas constant; T is 298K.

The magnitude of the electro-osmotic flow (J_{EOF}) under symmetrical KCl conditions could then be determined from[113]:

$$J_{EOF} \propto V_m \frac{\frac{P_{K^+}}{P_{Cl^-}} - 1}{\frac{P_{K^+}}{P_{Cl^-}} + 1} \quad (2)$$

where P_{K^+}/P_{Cl^-} was 0.15 ± 0.01 (530 nm, N = 4 repeats) and 0.20 ± 0.01 (365 nm, N = 4 repeats).

2.6.9 Transmembrane signal transmission by light-to-current conversion

To achieve light-to-current signal conversion, three steps are required. First, the encrypted digital data, as pixel art or text, were converted into a monochromatic or polychromatic 1D light sequence. In the 4 × 25 pixel pattern of the 'OXFORD', the pixel art plotted with Matplotlib was unraveled to a 100 × 1 string of two states (black/white), which were further assigned to '365 nm'/'455 nm' to obtain a light sequence. For example, a list of colors ['black', 'black', 'white', …, 'black'] was converted to a light sequence ['365 nm', '365 nm', '455 nm', …, '365 nm'].

In the αHL pixel art, a snapshot of the PDB:7AHL nanopore model was first converted to a three-color 16 × 16 pixelated image by Adobe Illustrator. The value of each pixel was extracted with Python Imaging Library to generate a 16 × 16 × 3 array, where the 3 was for the RGB color code. This array was unraveled to a 256 × 3 array, and the RGB color code was further replaced by the wavelength. For instance, the RGB color code of white (0,0,0) was assigned to 'mixed (365 + 455) nm'. The assignment of grey and dark grey colors to '455 nm' and '365 nm' lead to a 256 × 1 light sequence. Likewise, the 18-word Morse code sequence (dot/ space/ dash) was converted to the same three wavelengths to generate a light sequence.

In the second step, the 1D light sequence was sent to an Arduino UNO microcontroller to trigger the 365 nm and 455 nm LEDs accordingly. Due to the switching rate of the photopore, each unit of irradiation (a bit) was optimized to last for 20 s to observe the rectangular signals. A higher rate of data transmission might be obtained at increased light intensities. During the lifetime of a bit, the LEDs were coupled through the bifurcated fiber bundle and switched on or off according to the light sequence to produce a high (365 nm), middle (mixed), or low (455 nm) ionic current response through the photophore.

The final step was to process the electrical recording to visualize and analyze the output signal. The electrical recording trace was processed in reverse from the 1 × N current signal to the pixel image or text. A continuous recording trace sampled at 25 kHz was segmented into bits of 20 s (one 20-second bit = 500000 data points of

0.04 ms), and each bit was denoted as ‘high’, ‘middle’ or ‘low’ state based on the mean value compared to manually chosen thresholds. The state values were further replaced by (‘black’/’white’ for the ‘OXFORD’ pattern), (‘dark grey’/’white’/’grey’ for the αHL pixel art) or (‘dot’/’space’/’dash’ for the Morse code). Finally, the new array was transformed into the proper dimension and displayed with Matplotlib to visualize the image or text.

Table 1. Primers used for site-directed mutagenesis.

Primers	Forward and reverse primer sequences (5′→3′)	Length (nt)	GC %
E111C	GAAATTCGATTGATACAAAATGCTATATGAGTACTTTAACTTATGG CCATAAGTTAAAGTACTCATATAGCATTTTGTATCAATCGAATTTC	44	28
T115C	GATACAAAAGAGTATATGAGTTGCTTAACTTATGGATTCAACGG CCGTTGAATCCATAAGTTAAGCAACTCATATACTCTTTTGTATC	44	34
T125C	GGATTCAACGGTAATGTTTGTGGTGATGATACAGGAAAAATTGGCGGCC GGCCGCCAATTTTTCCTGTATCATCACCACAAACATTACCGTTGAATCC	49	45
T129C	GTTACTGGTGATGATTGTGGAAAAATTGGCGGCC GGCCGCCAATTTTTCCACAATCATCACCAGTAAC	34	50

2.7 Appendix

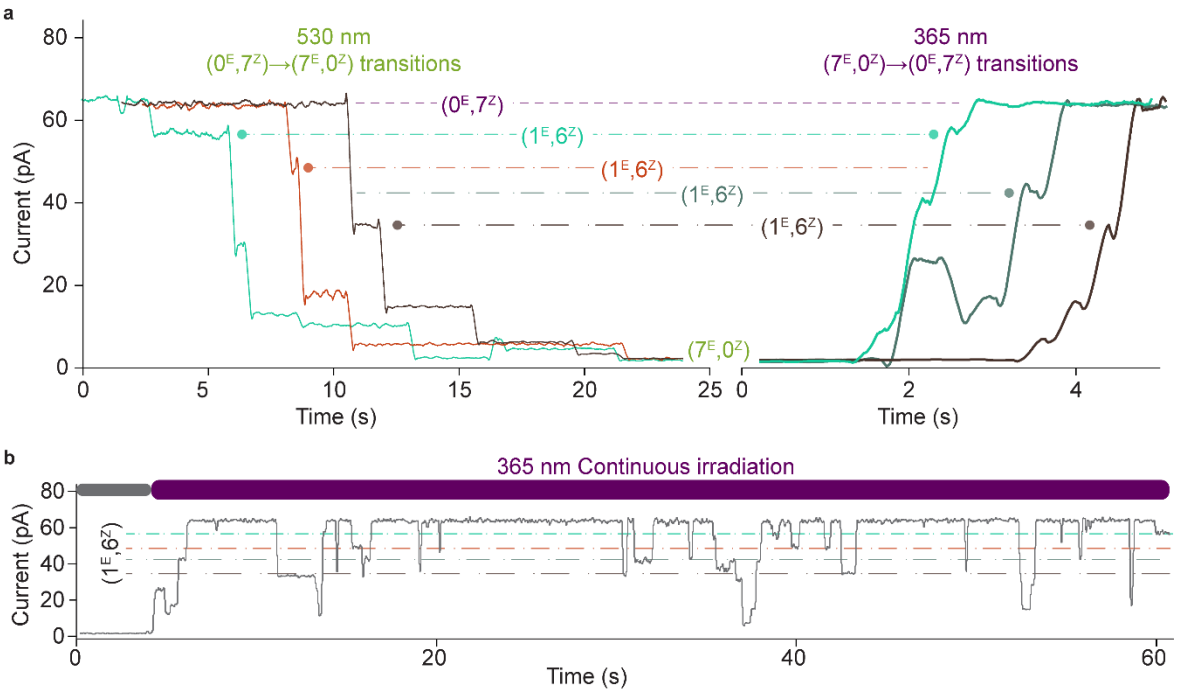


Fig. 22 | Multiple current levels arise from the (1^E,6^Z) configuration of the (E111C-pzMe)$_7$ pore. a, Photoisomerization transitions selected from **Fig. 14** to illustrate four non-overlapping (1^E,6^Z) intermediate current levels. Traces were smoothed with a 5 Hz Bessel filter and a Savitzky–Golay filter (400 ms window length). The various levels connected to (0^E,7^Z) were ascribed to the (1^E,6^Z) configurations. **b,** Absence of interconversion among the (1^E,6^Z) levels. The trace of a single (E111C-pzMe)$_7$ pore was recorded under 365-nm continuous irradiation. The (1^E,6^Z) returned to (0^E,7^Z) before switching to a (1^E,6^Z) displaying a different current amplitude. Multiple (1^E,6^Z) states indicated that the model with 20 combinations and permutations, proposed in **Fig. 15e,** was an oversimplification.

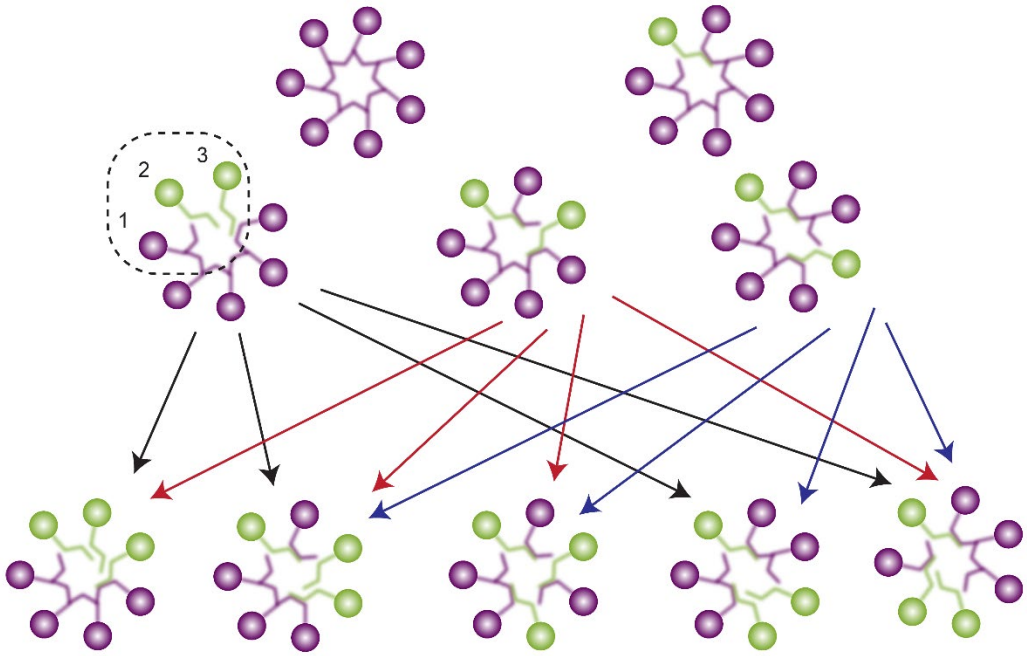


Fig. 23 | Directional reaction network of (E111C-pzMe)$_7$ pore from (0^E,7^Z) to (3^E,4^Z) state**.** The pore is symbolized as green (*E*) or purple (*Z*) subunits. Considering the permutational isomers only, the transition between (2^E,5^Z) and (3^E,4^Z) is only possible following the colored edges. For instance, if the encircled (1,2,3) subunits are (*Z*,*E*,*E*) configuration, the accessible following states are the ones connected to the black edges. This is an interesting perspective to understand the **Fig.15**.

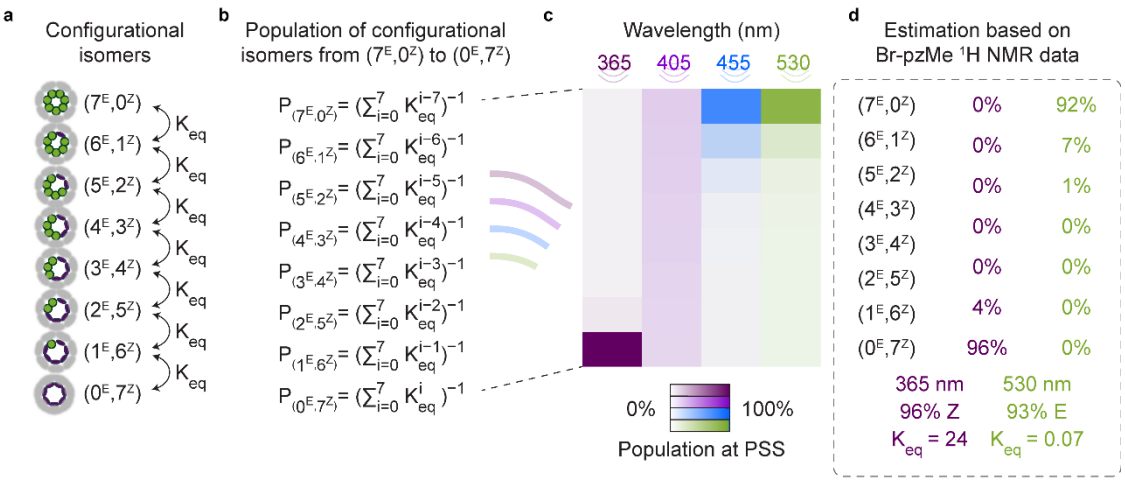


Fig. 24 | Population distribution of (E111C-pzMe)$_7$ pore configurational isomers. Assuming that the pzMe photoswitching was independent of the neighboring pzMe, we calculated the distribution of photopore configurational isomers at the photostationary state. **a,** Population of configurational isomers as a function of the equilibrium constant. **b,** The percent population of each isomer. **c,** A color map of the population at four wavelengths. **d,** Listed percent population estimated from the equilibrium constant determined by ^{1}H-NMR.

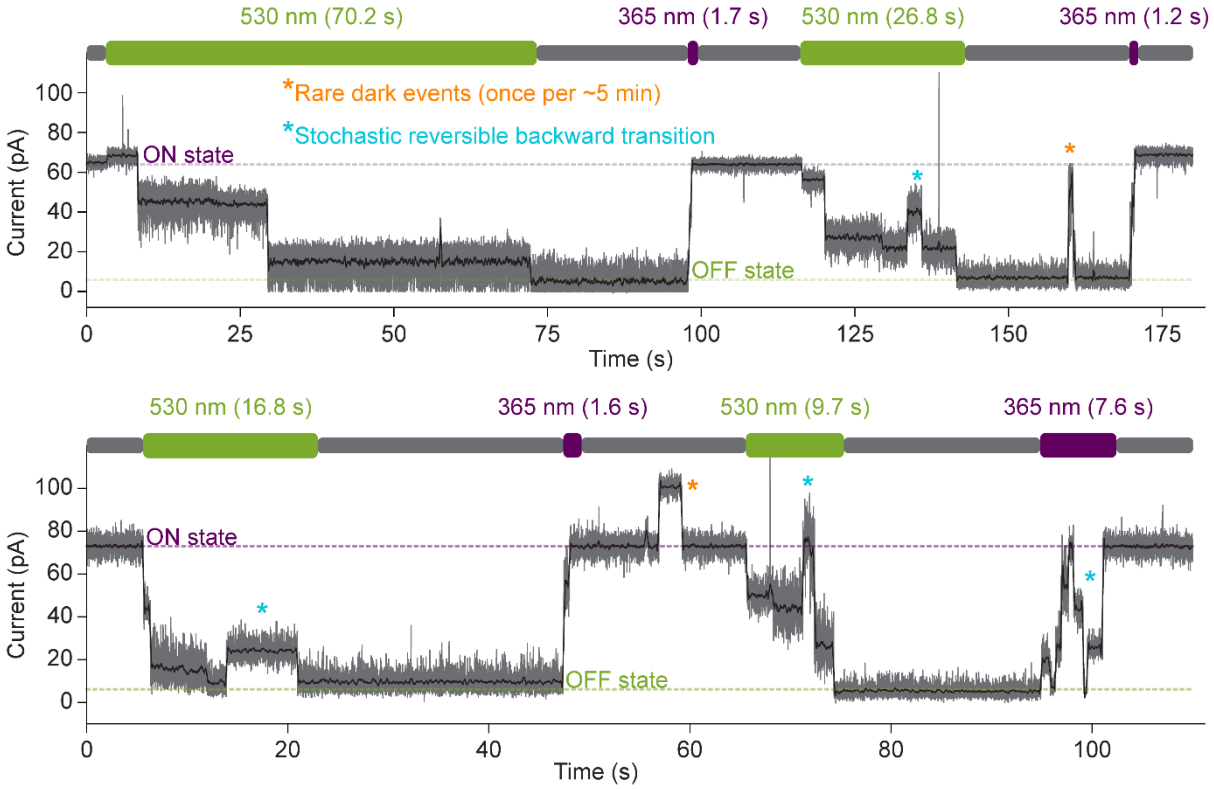


Fig. 25 | Minimal irradiation for ON-OFF switching of a single (E111C-pzMe)$_7$ pore. The moving averages of the ionic currents (black traces) were generated with a Savitzky–Golay filter. Rare reversible dark events (orange asterisks) occurred less than once in 5 minutes. Occasional backward steps are labeled with blue asterisks. These reversals did not impede the overall direction of switching. The current trace was recorded at +100 mV using a 5 kHz in-line Bessel filter at 25 kHz sampling frequency, and a 20 Hz digital Bessel filter was used for data analysis. Recording conditions: 2.0 M KCl, 10 mM Tris-HCl, 0.1 mM EDTA, pH 8.5, 24 ± 1 °C. LED irradiance: (365 nm: 36.2 mW/cm^2; 530 nm: 30.3 mW/cm^2).

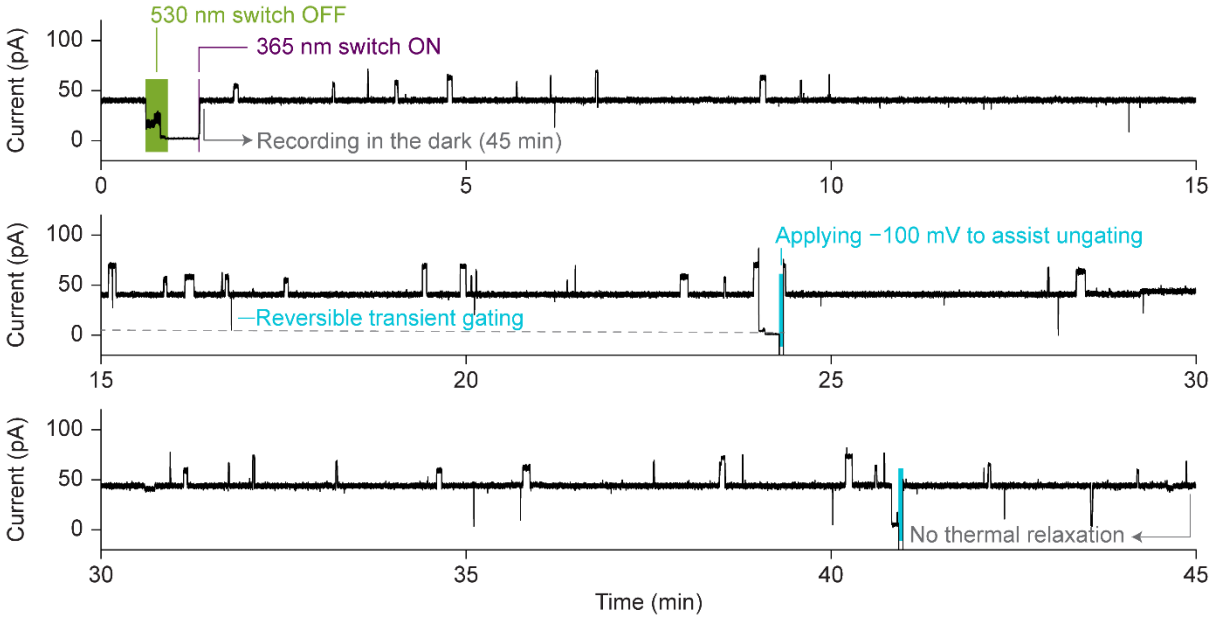


Fig. 26 | Prolonged recording with a single *Z*-state (E111C-pzMe)$_7$ pore in the dark. The open-pore current was 41 pA at 100 mV. ON-OFF photoswitching was demonstrated briefly at 1 min. The recording of the *Z*-state (E111C-pzMe)$_7$ was continued in the dark for 45 min. No pore closure caused by *Z*→*E* thermal relaxation was observed. The current trace was recorded at +100 mV using a 5 kHz in-line Bessel filter at 25 kHz sampling frequency, and a 20 Hz digital Bessel filter was used for data analysis. Recording conditions: 2 M KCl, 10 mM Tris-HCl, 0.1 mM EDTA, pH 8.5, 24 ± 1 °C.

Chapter 3

Nanopore-based single-molecule excitation spectroscopy for photoswitches

Abstract

Since the first single-molecule excitation spectrum of pentacene was measured in a cryogenic solid matrix in 1989, optical studies of single molecules have been hindered by the sensitivity of photodetector—to detect the absorption of a single photon. Although direct and indirect detection methods were developed to serve this purpose, the tested molecules are limited to highly fluorescent dyes immobilized on polymer matrices. Here, we report an indirect measurement of an alternative excitation spectrum of a single arylazopyrazole photoswitch under room temperature in the aqueous solution. Instead of detecting light transmission or emission, the photoisomerization events of an arylazopyrazole tethered in a nanopore were measured through the photoresponsive nanopore conductance. The lifetime of these events was determined by the product of molar extinction coefficient and photoisomerization quantum yield of the arylazopyrazole. This single-molecule approach allowed us to measure spectra from 100% *Z*-arylazopyrazole without extensive purification of the isomers.. The single-molecule excitation spectrum varied depending on the protein environment surrounding the photoswitch and the pH value of the solution. Taking the change of arylazopyrazole excitation spectrum as a readout, we incorporated the nanopore as a photodetector into a minimum functional spectrophotometer repurposed from the nanopore-recording device.

3.1 Introduction

Excitation spectrum of a chromophore is often the first selection criteria for a photoresponsive chemical, such as microscope dye[114,115], photovoltaics dye[116] and photoswitches[30,61,62,64]. Conventional excitation spectroscopy characterizes the chromophore in a cuvette at micromolar concentration (~10^{18} molecules per liter) and yields a smoothed statistical average of spectral lines from individual molecules. The neglect of single-molecule chemistry conceals possible heterogeneity of chemical structures, conformations, protonation states and interactions with the neighboring environment[69,117]. Single-molecule excitation spectroscopy (SMS) is a powerful quantitative analytical tool to study a chromophore molecule at a time where the individual excitation spectral characteristics, such as maximum excitation wavelength and molar extinction coefficient, do not vanish as in the macroscopic sample.

The simplest direct way of measuring SMS is by Beer–Lambert law with a highly sensitive photodetector with suppressed laser noise. At the single-molecule level, the photodetector must differentiate the absorption of a single photon, but this approach was limited by the development of photodetectors in the 2000s[118] and achieved only recently at room temperature[119]. Alternatively, the indirect techniques were based on line narrowing at cryogenic temperature[120], homodyne interferometry[121,122], photothermal effect[123] and stimulation emission[124]. Despite the latest Beer–Lambert law and interferometric measurements achieved ultra-fast single-molecule sensitivity at room temperature, these precedent SMS techniques are limited to measurements of fluorescent molecules embedded in a solid matrix[122,125,126] (**Table 1**).

Table 1. Comparison with previous single-molecule excitation or absorption spectroscopy techniques.

Year	Group	Dye	Phase*	Temp	Ex**	Em	Technique
1989	Moerner[120]	Pentacene	p-Terphenyl	1.4 K	592 nm		Frequency modulation
1993	Betzig[127]	Carbocyanine	PMMA	1.5 K		543 nm	Near-field scanning
2004	Svishchev	MEH-PPV	PMMA	RT	500 nm		Dark-field Rayleigh scattering
2007	Basché[129]	MEH-PPV	PMMA	1.2 K	488 nm	543 nm	Beer–Lambert law
2010	Orrit[130]	BHQ1	Glycerol		514 nm		Photothermal contrast
2010	Xie[131]	Atto647N	PMMA	RT	642 nm		Ground-state depletion
2010	Sandoghdar[119]	Atto647N	PMMA	RT	633 nm		Beer–Lambert law

2011	Sandoghdar[121]	TDI***	PMMA	RT	633 + 671 nm		Beer–Lambert law
2014	Subramaniam[132]	Perylene***	Polystyrene	RT	460-580 nm		White-light laser source
2016	Van Hulst[125]	QDI***	PMMA	RT	655-770 nm	650 - 900 nm	Fourier-related interferogram
2018	Van Hulst[126]	DBT***	Anthracene	RT	800-1000 nm		Time-resolved
2019	Hauer[122]	TDI***	Polystyrene	RT	450-550 nm	520 - 620 nm	
This work		pzMe and pzH photoswitch	Tris-HCl buffer pH 8.5	RT	365 + 405 + 455 + 470 + 530 nm		Single channel recording

* Except for Orrit (2010), all experiments were based on solid matrices.
** Excitation light irradiance of the conventional methods was ~10-100 W/cm^{-2} whereas this work used LED light source of ~30-120 mW /cm^{-2}.
*** Rylene dyes were the most popular model molecules. Apart from the BHQ1 quencher, all molecules were fluorescent.

Alternative to fluorophores, SMS of photoswitches has never been studied to authors' knowledge. Arylazopyrazole is a noteworthy photoswitch widely used in photoreversible molecules for quantitative switching, long thermal lifetime and red-shifted irradiation[30,133]. Despite successful applications as azologization drugs[101,134,135], energy storage materials[136] and light-responsive electronic devices[137–139], the photoswitching properties of arylazopyrazole at single molecule level were underexplored. The behavior of photoswitch might also vary in confined biological environment[69,117] and cause a mismatch between absorptivity and photochemical reactivity[140]. However, it is challenging to study the spectra of noncovalent photoswitch-protein complexes in large quantities. In addition, the UV/Vis spectrum of a non-fluorescent single photoswitch (quantum yield ~ 10^{-6} for azobenzene)[141] in aqueous biological environment at room temperature was not measured with any existing SMS technique. Besides, irradiation alone cannot achieve quantitative photoswitching (100% *Z* isomer) for most azobenzene derivatives[62,87] in macroscopic aqueous solution, although pure Z isomer could be separated by chromatography. At single-molecule level, the photoswitch must be either *E*- or *Z*-state; measurement of *Z*-state spectrum is advantageous by SMS without interference from the *E*-state impurity.

Here, we present a nanopore-based SMS characterizing arylazopyrazole excitation spectra at the single-molecule level. Assuming Vavilov rule was valid[32] for arylazopyrazole, the excitation of photoswitch was indirectly detected by photoswitching events rather than transmission or emission of photons. These events were measured as blockade of ion flow through the nanopore when transmembrane electrical potential was applied. Nanopore-based SMS enabled spectral characterization of '100%' *Z*-arylazopyrazole that does not involve separation of *E/Z* isomers. We studied the influence of the nanopore confinement on the maximum excitation peak, and related it to polarizability of the local environment. The acid-accelerated thermal relaxation of a single arylazopyrazole was also investigated at low pH. We determined the pK_a of arylazopyrazole and confirmed it was consistent in ensemble and nanopore. Finally, the determined spectra of single arylazopyrazole allowed us to explore its application as a miniaturized biological photodetector. Integrating of this single-molecule

photodetector into a model spectrophotometer, we determined the absorption of blood heme and the optical density of silica beads suspension.

3.2 Preparation of heteroheptamer nanopore

In a nanopore-based SMS experiment, a pre-assembled heteroheptameric α-hemolysin (αHL) nanopore with a single covalently bound photoswitch at the αHL constriction was inserted into a planar lipid bilayer of 1,2-Diphytanoyl-3-sn-phosphatidylcholine (DPhPC) (**Fig. 1a**).

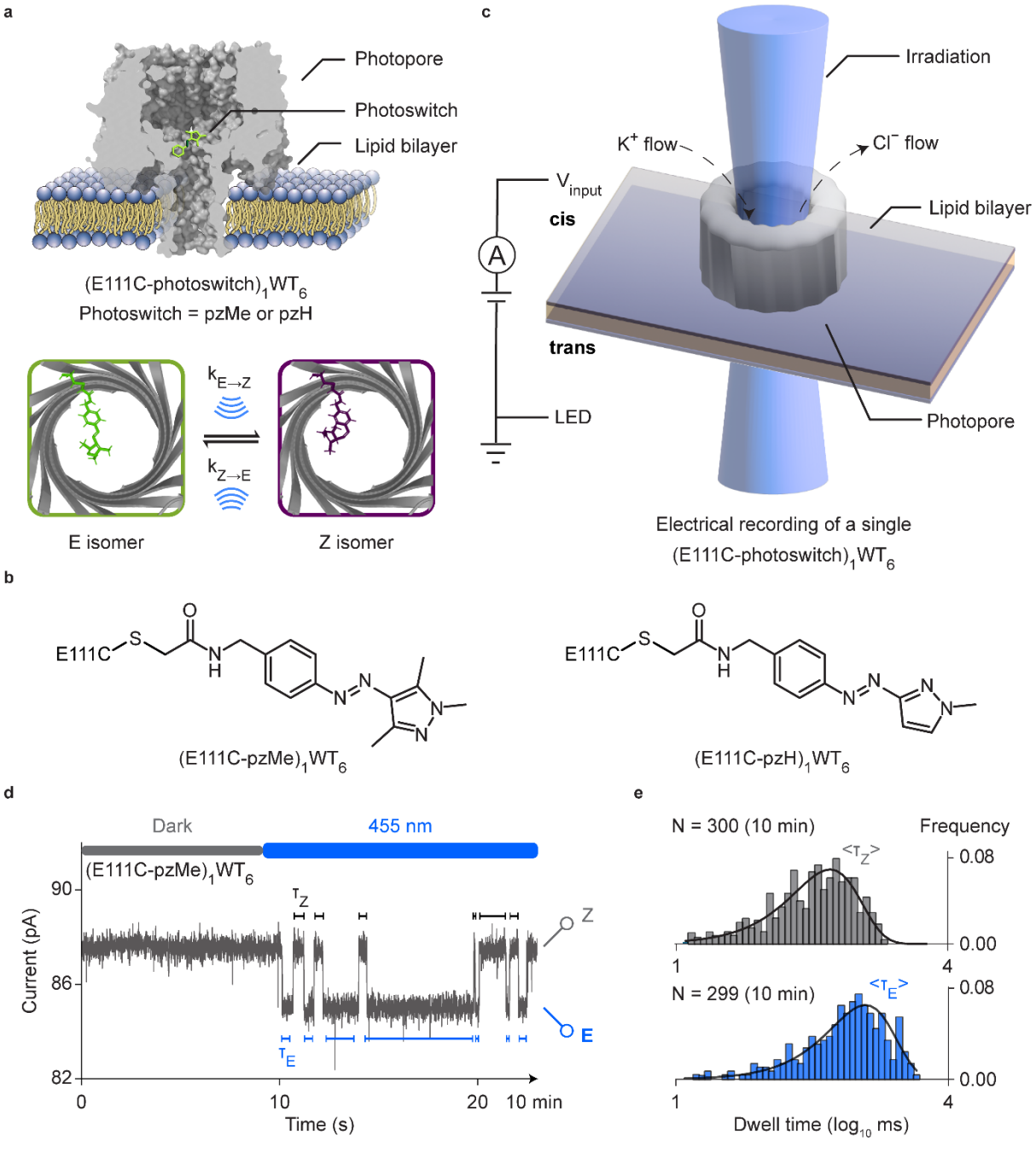


Fig. 1 | Photoisomerization in the (E111C-photoswitch)$_1$WT$_6$ nanopore. a, (E111C-photoswitch)$_1$WT$_6$ nanopore switches between *E*- and *Z*-isomers under continuous irradiation. Isomerization rates ($k_{E\rightarrow Z}$ and $k_{Z\rightarrow E}$) depend on the light wavelength and intensity. **b,** Arylazopyrazole photoswitch tethered to the E111C cysteine. **c,** Electrical recording of the nanopore under transmembrane potential (V_{input}). The nanopore isomerizes under the irradiation (blue cone), and alters the unitary conductance. Photoisomerization events are recorded as KCl ionic current. The positive current is defined as the flow of K^+ ions from the cis to the trans side of the lipid bilayer. **d,** Photoisomerization events embodied in the ionic current signal. Each *E* or *Z* isomer state lasted for a stochastic dwell time (τ_E or τ_Z). **e,** Exponential distribution of the dwell times in a 10-minute recording. The current trace was recorded at +50 mV using a 5 kHz in-line Bessel filter at 25 kHz sampling frequency. Recording conditions: 2 M KCl, 10 mM Tris-HCl, 0.1 mM EDTA, pH 8.5, 24 ± 1 °C.

To construct (E111C-photoswitch)$_1$WT$_6$, we functionalized monomeric αHL cysteine mutant E111C-D$_8$H$_6$ with bromoacetyl-arylazopyrazole (Br-pzH) and bromoacetyl-methylarylazopyrazole (Br-pzMe) following established protocol (**Fig. 1b**). The completion of conjugation reaction was confirmed by liquid chromatography-mass spectrometry (**Fig. 2**).

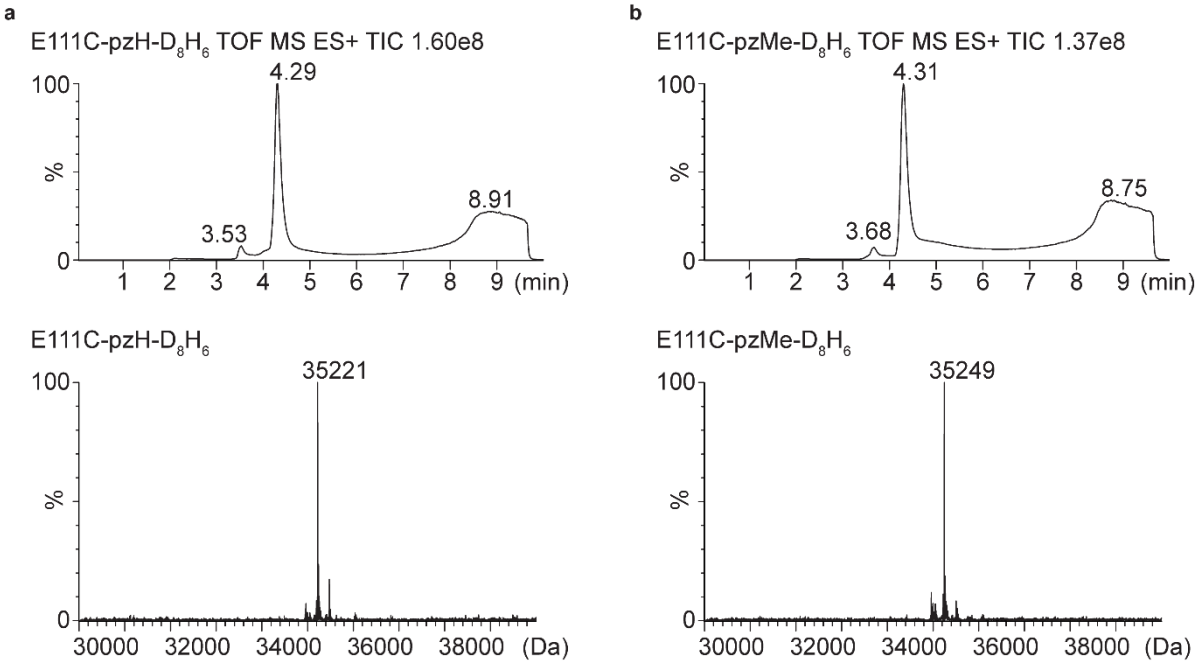


Fig. 2 | LC–MS characterization of E111C-photoswitch. The top panels are total ion current chromatograms. The bottom panels are deconvoluted ESI–MS spectra in the range of 30-40 kDa. **a,** E111C-pzH-D$_8$H$_6$ monomer: mass = 35221 (calculated) and 35221 (observed). **b,** E111C-pzMe-D$_8$H$_6$ monomer: mass = 35249 (calculated) and 35249 (observed).

The E111C-pzMe-D$_8$H$_6$ or E111C-pzH-D$_8$H$_6$ monomers were mixed with ^{35}S-labeled wild-type monomers (WT-H$_6$) at 1:8 (v:v) ratio, and oligomerized into

heteroheptamers in rabbit erythrocyte membrane[38]. Purification of (E111C-photoswitch)$_1$WT$_6$ with negatively-charged octaaspartic acid (-D$_8$H$_6$) and a positively-charged hexahistidine (-H$_6$) tags was performed by SDS-PAGE visualized by autoradiography, as reported previously[38] (**Fig. 3**). Each (E111C-photoswitch)$_1$WT$_6$ nanopore contains one photoswitch strictly.

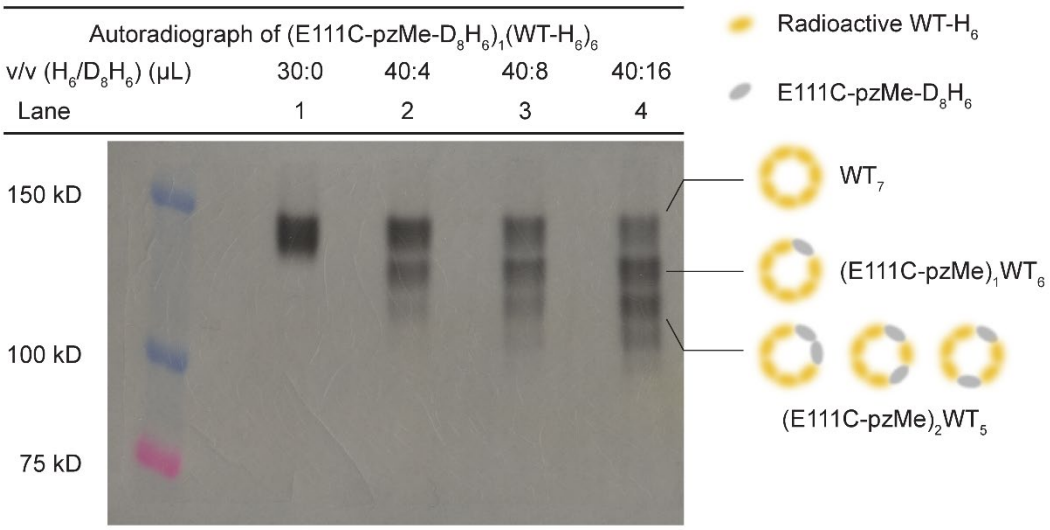


Fig. 3 | Autoradiograph of a 5.5% SDS-PAGE gel for the (E111C-pzMe-D$_8$H$_6$)(WT-H$_6$)$_6$ **purification. The** WT-H$_6$ monomers were labelled with ^{35}S-methionine. The yield of desired heteroheptamer was optimized by mixing different ratios of monomers.

3.3 Photoisomerization in the nanopore

Under applied transmembrane electric potential, an ion flow of K^+ and Cl^- followed through (E111C-photoswitch)$_1$WT$_6$ across the lipid bilayer. To align with the convention of αHL studies and clarify the sign of ionic current and ion flow, we denoted the signal ground and LED side of the membrane as trans side; and the opposite of applied potential as cis side (**Fig. 1c**). Nanopore was always added to the cis side where the cap domain is located. Then we defined the positive current as the movement of K^+ moving from the trans to the cis side of the membrane.

In the dark, (E111C-pzMe)$_1$WT$_6$ exhibited a constant conductance of 1.84 ± 0.06 (*Z*) and 1.80 ± 0.06 (*E*) nS under 50 mV applied potential (N = 20 pores); and likewise for the (E111C-pzH)$_1$WT$_6$ of 1.89 ± 0.04 (*Z*) and 1.85 ± 0.04 (*E*) nS (N = 10 pores). Under irradiation from the cis side of membrane, the (E111C-pzMe)$_1$WT$_6$ photoisomerized between the *E*- and *Z*-states, visualized as the binary current

levels. The residual current (I_{res} = I_E/I_Z) by photoswitching was 97.6 ± 0.6% for $(E111C\text{-}pzMe)_1WT_6$ and 98.1 ± 0.1% for $(E111C\text{-}pzMe)_1WT_6$ (**Fig. 4-5**)

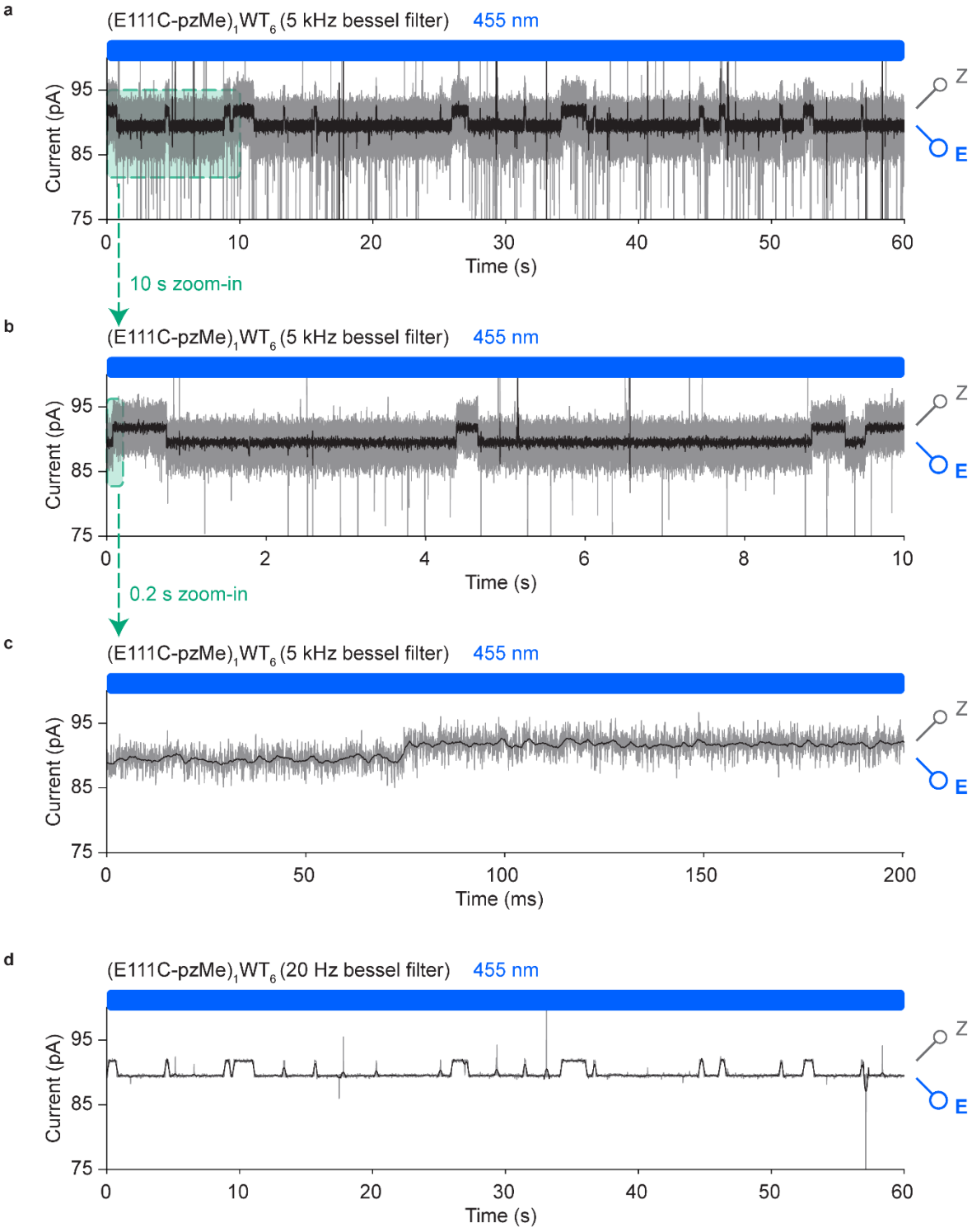


Fig. 4 | Electrical recording of a single $(E111C\text{-}pzMe)_1WT_6$ heteroheptamer nanopore under continuous 455 nm irradiation. The *E*-isomer level (marked in blue) showed a longer dwell time. **a-c,** Recording with 5 kHz Bessel filter at 25 kHz sampling frequency. Each trace is the magnified area in the green box of the previous trace. **d,** Recording in panel **a** filtered by 20 Hz Bessel filter. Filtering did not distort the appearance and dwell time

of events. The moving averages of the ionic currents (black traces) were generated with a Savitzky–Golay filter (window size = 400 ms), and the raw trace is in grey. Recording condition: 10 mM Tris-HCl pH 8.5, 2 M KCl, 0.1 mM EDTA, 50 mV at room temperature.

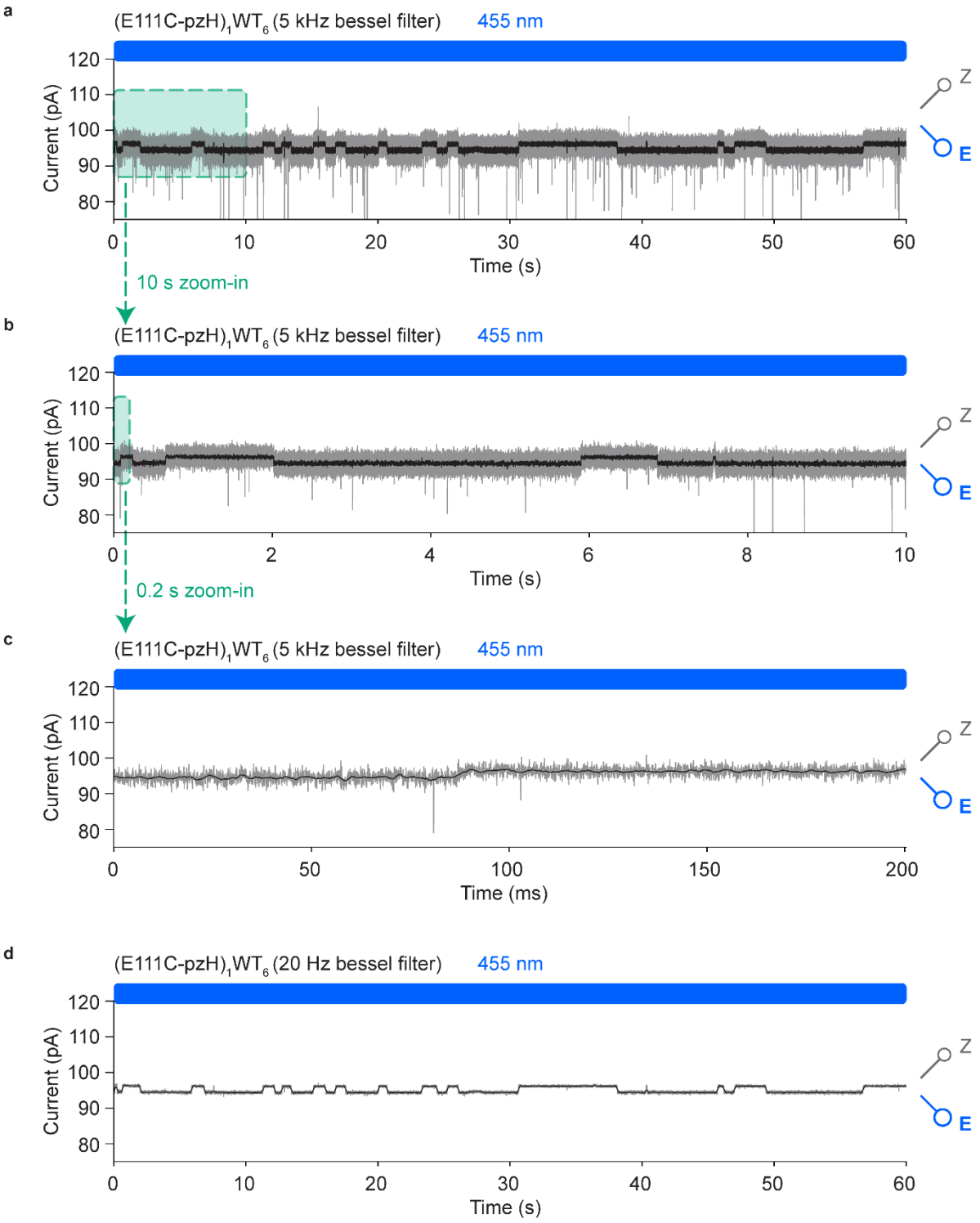


Fig. 5 | Electrical recording of a single (E111C-pzH)$_1$WT$_6$ heteroheptamer nanopore under continuous 455 nm irradiation. a-c, Recording with 5 kHz Bessel filter at 25 kHz sampling frequency. Each trace is the magnified area in the green box of the previous trace. **d,** Recording in panel **a** filtered by 20 Hz Bessel filter. Filtering did not distort the appearance

and dwell time of events. The moving averages of the ionic currents (black traces) were generated with a Savitzky–Golay filter (window size = 400 ms), and the raw trace is in grey. Recording condition: 10 mM Tris-HCl pH 8.5, 2 M KCl, 0.1 mM EDTA, 50 mV at room temperature.

By classifying and aggregating the normally distributed current levels as the *E*- and *Z*-states, we extracted the expected dwell time τ for each state from the dwell time exponential distribution. The dwell time of the *E*- and *Z*-states revealed the photoisomerization kinetic constants (k) for the *E*-to-*Z* and *Z*-to-*E* process, which was inversely proportional to the molar extinction coefficient (ε) (eq. 1). The eq 1. is the theoretical foundation of nanopore-based SMS because the extinction coefficient was plotted against wavelength to estimate the line shape from stochastic photoswitching current trace. Although azo-compound was known to break Vavilov rule because of distinct quantum yields (φ) for π-π* and n-π* transitions, the pzMe has similar φ in the literature (0.46 for $\varphi_{\pi\text{-}\pi^*}$ and 0.56 for $\varphi_{n\text{-}\pi^*}$), leading to an reasonable assumption to neglect the φ difference[32].

$$< \tau_E >^{-1} = k_{E\to Z} \propto \varphi_E \varepsilon_E Q \;\; and \;\; < \tau_Z >^{-1} = k_{Z\to E} \propto \varphi_Z \varepsilon_Z Q \qquad (1)$$

We must clarify that the definition of excitation spectrum based on eq. 1 is different from the convention in fluorophore studies. Instead of choosing fluorescence intensity to quantify excitation, this SMS study measures the product of extinction coefficient and photoswitching quantum yield (εφ), in other words, the kinetic constants of photoisomerization events.

3.4 Irradiance-dependent photoisomerization rates

To validate the irradiance dependence in eq. 1, we irradiated the (E111C-pzMe)$_1$WT$_6$ with 405-nm and 455-nm LED at different irradiance (Q) (**Fig. 6a**). By comparing the current trace of a single (E111C-pzMe)$_1$WT$_6$ under 455 nm (126 and 57 nm mW/cm^2), we observed more frequent photoisomerization events and shorter lifetime at the higher irradiance (**Fig. 6b**), while the current levels remained unchanged switching between 94 and 97 pA. Reproduced with five irradiances of 405 nm (7~76 mW/cm^2) and 455 nm (16~126 mW/cm^2), we observed a linear correlation between the kinetic constants and the intensity of light at 405 and 455 nm (**Fig. 6c**).

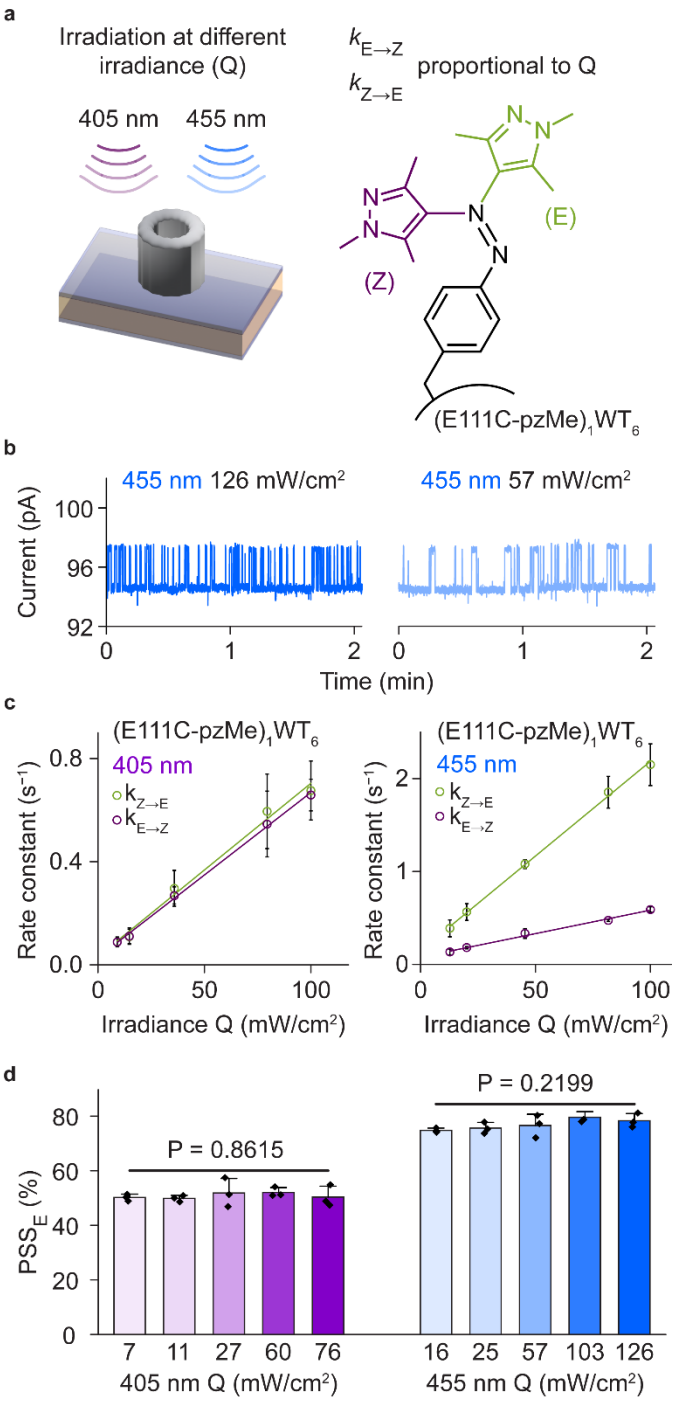


Fig. 6 | Linear correlation between light irradiance and (E111C-pzMe)$_1$WT$_6$ photoisomerization rate. a, Irradiation triggers (E111C-pzMe)$_1$WT$_6$ photoisomerization at irradiance-dependent rates. **b,** Electrical recording under 455 nm at two irradiances. The number of events increased, and dwell time shortened at high irradiance. The trace was filtered by a 20 Hz digital Bessel filter. **c,** Photoisomerization rate constants under 405 and 455 nm irradiation. (N = 3 pores) **d,** ANOVA analysis of *E*-isomer populations at photostationary state (PSS$_E$). F-statistic values (F/F$_{critical}$) are (0.315/3.478) and (1.7285/3.478) for 405 and 455 nm, respectively. The PSS$_E$ at 405 and 455 nm was consistent at tested irradiance. The current traces were recorded at +50 mV using a 5 kHz

in-line Bessel filter at 25 kHz sampling frequency. Recording conditions: 2 M KCl, 10 mM Tris-HCl, 0.1 mM EDTA, pH 8.5, 24 ± 1 °C.

This observation supported eq. 1, which postulated that these unidirectional kinetic constants were directly proportional to the product of the quantum yield φ, molar extinction coefficient ε, and irradiance Q[46]. As the εφ is constant at given wavelength, the ratio between $\varepsilon_Z\varphi_Z$ and $\varepsilon_E\varphi_E$ cancelled out the Q terms, leading to the eq. 2 for the photostationary state. Distinct from the intensity-dependence of kinetic constants, the *E*-isomer population at the photostationary state (PSS_E) is solely a function of wavelength.

$$PSS_E = \frac{k_{Z\to E}}{k_{Z\to E} + k_{E\to Z}} = \frac{\varepsilon_Z\varphi_Z}{\varepsilon_Z\varphi_Z + \varepsilon_E\varphi_E} \quad (2)$$

Accordingly, the analysis of the percentage of *E* isomer at photostationary state (PSS_E) across the five intensities displayed no statistically significant differences at 405 (ANOVA, $F(4/10) = 0.3151$, $p = 0.8615$) and 455 nm (ANOVA, $F(4/10) = 1.7285$, $p = 0.2199$) (**Fig. 6d**).

A reasonable concern for the dwell time determination is the minimum events and time required for a reliable measurement of τ. Increasing number of gathered events in a long recording directly enhances the accuracy and runtime of optimization algorithm for the Markov model[142]. Since we utilized QuB software[142,143] equipped with Davidon-Fletcher-Powell optimization algorithm that requires minimal event sample size for high accuracy, an accurate and rapid convergence (percent RMS: <15% for $k_{E\to Z}$) was achievable with 50 events (N = 3 traces) (**Fig. 7**). Fifty events (~1-minute recording at 455 nm) sufficed for the kinetics estimation to converge.

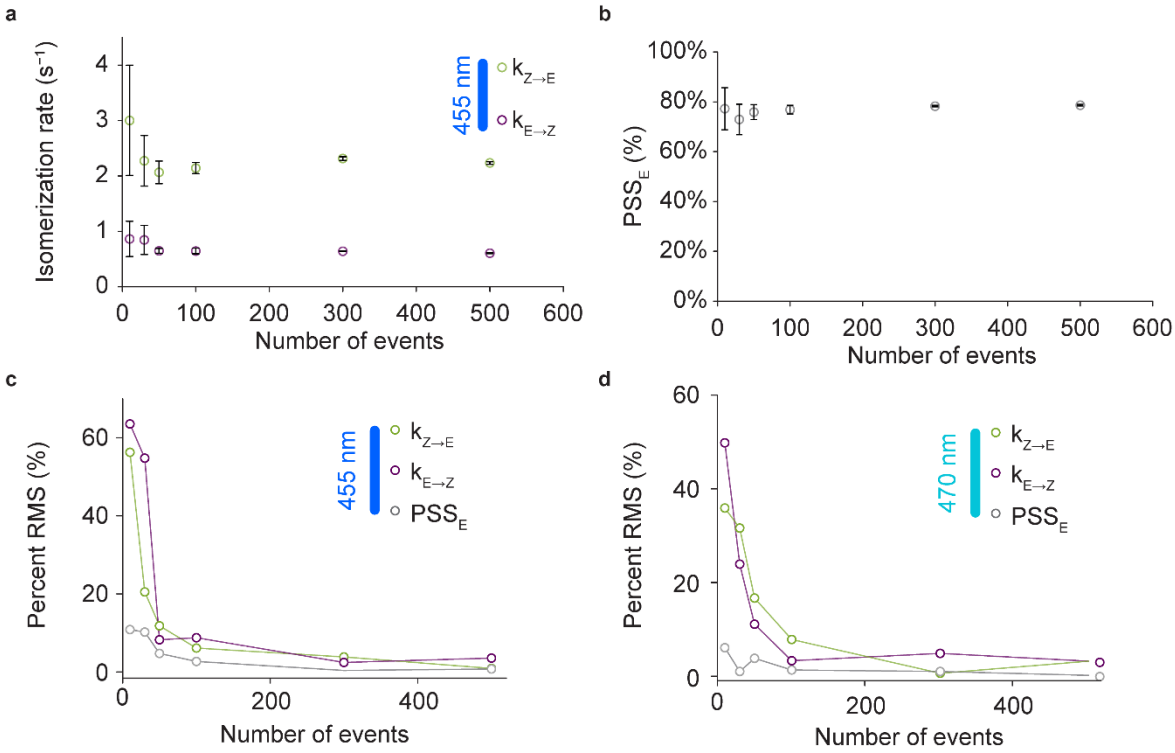


Fig. 7 | Influence of the number of events on the accuracy of QuB software. a, Representative kinetics results from subsets of a 600-events data (N = 3 randomized subsets). $k_{E\to Z}$ converged faster than $k_{Z\to E}$. **b,** Representative PSS_E results from the same dataset. The PSS_E converged accurately with 50 samples. **c-d,** The percent root-mean-square deviation of the estimated isomerization rates and PSS_E of three separate $(E111C\text{-}pzMe)_1WT_6$ under 455 and 470 nm irradiation. The percent RMS is defined as the ratio between the standard deviation of three randomly sampled subsets of a trace and a reference value (600 events). Each data subset was randomly sampled three times from three independent traces.

3.5 Single-molecule excitation spectra

As evidenced by the one-to-one relationship between the wavelength and the kinetic constants, the eq. 1 suggested the possibility of generating a single-molecule excitation spectrum[144] S(λ) of the $(E111C\text{-}pzMe)_1(WT)_6$ and $(E111C\text{-}pzH)_1(WT)_6$ by characterizing the kinetic constants across a range of wavelengths (**Fig. 8a** and eq. 3).

$$S_E(\lambda) = \frac{k_{E\to Z}}{Q} \propto \varphi_E \varepsilon_E \;\; and \; S_Z(\lambda) = \frac{k_{Z\to E}}{Q} \propto \varphi_Z \varepsilon_Z \qquad (3)$$

To calculated the εφ from k at each wavelength, we recorded current traces of $(E111C\text{-}pzMe)_1(WT)_6$ and $(E111C\text{-}pzH)_1(WT)_6$ under continuous irradiation of 365, 405, 455, 470 and 530 nm (**Figs. 9-11**).

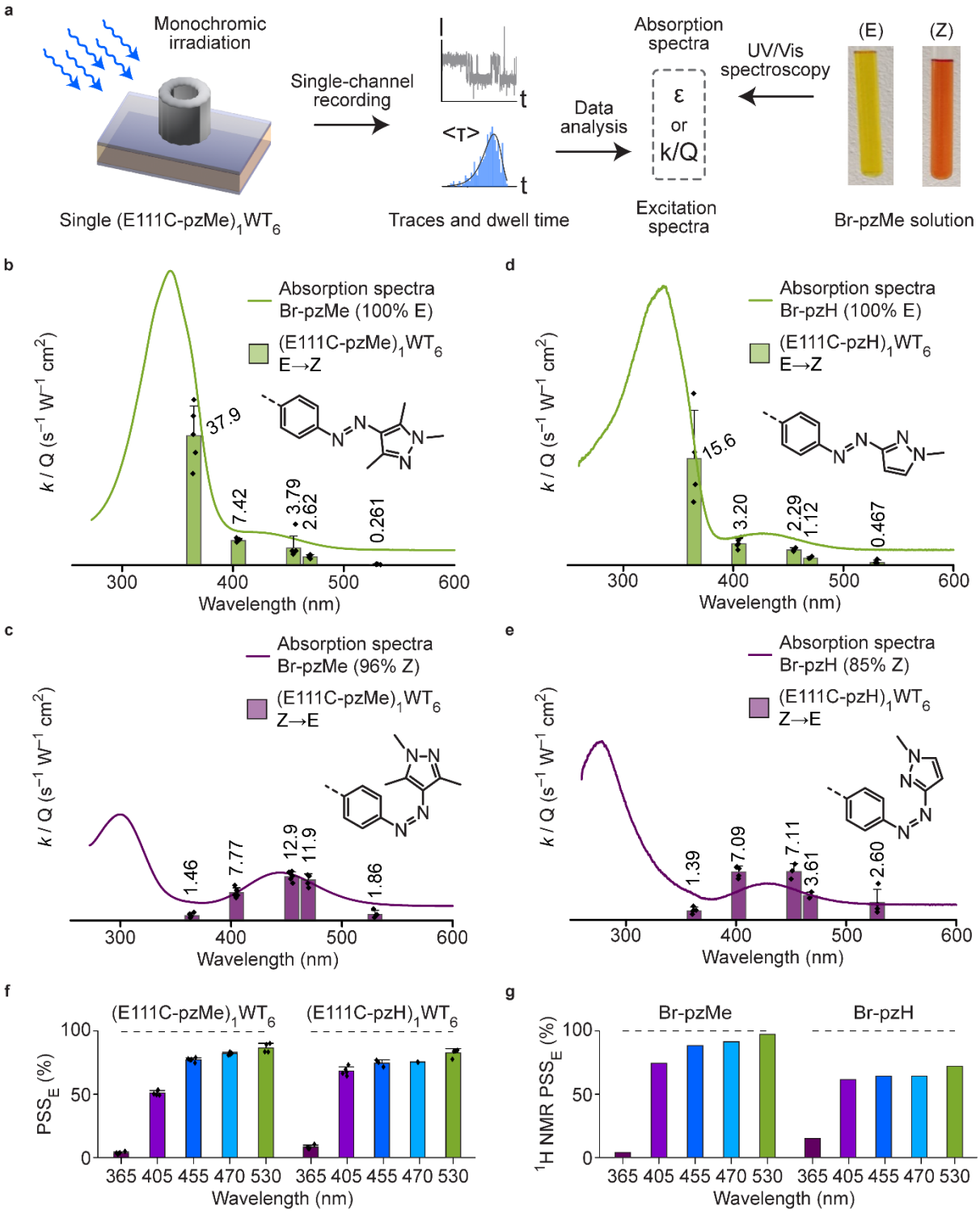


Fig. 8 | Single-molecule excitation spectra. a, Single-molecule and ensemble approaches to pzMe and pzH spectra. Kinetics/light intensity ratio (k/Q) is proportional to the product of quantum yield (φ) and extinction coefficient (ε). **b-e,** k/Q ratios of a single

$(E111C\text{-}pzMe)_1WT_6$ and $(E111C\text{-}pzH)_1WT_6$ (N = 4 pores) matching the line shape of ensemble reference Br-pzMe or Br-pzH spectra. The 15% residual *E*-state Br-pzH in ensemble caused the disagreement in **e**. **f-g,** Wavelength dependence of *E*-isomer population at photostationary state (PSS_E). **h,** PSS_E of Br-pzMe and Br-pzMe measured by ensemble ^1H NMR in d^6-DMSO at room temperature.

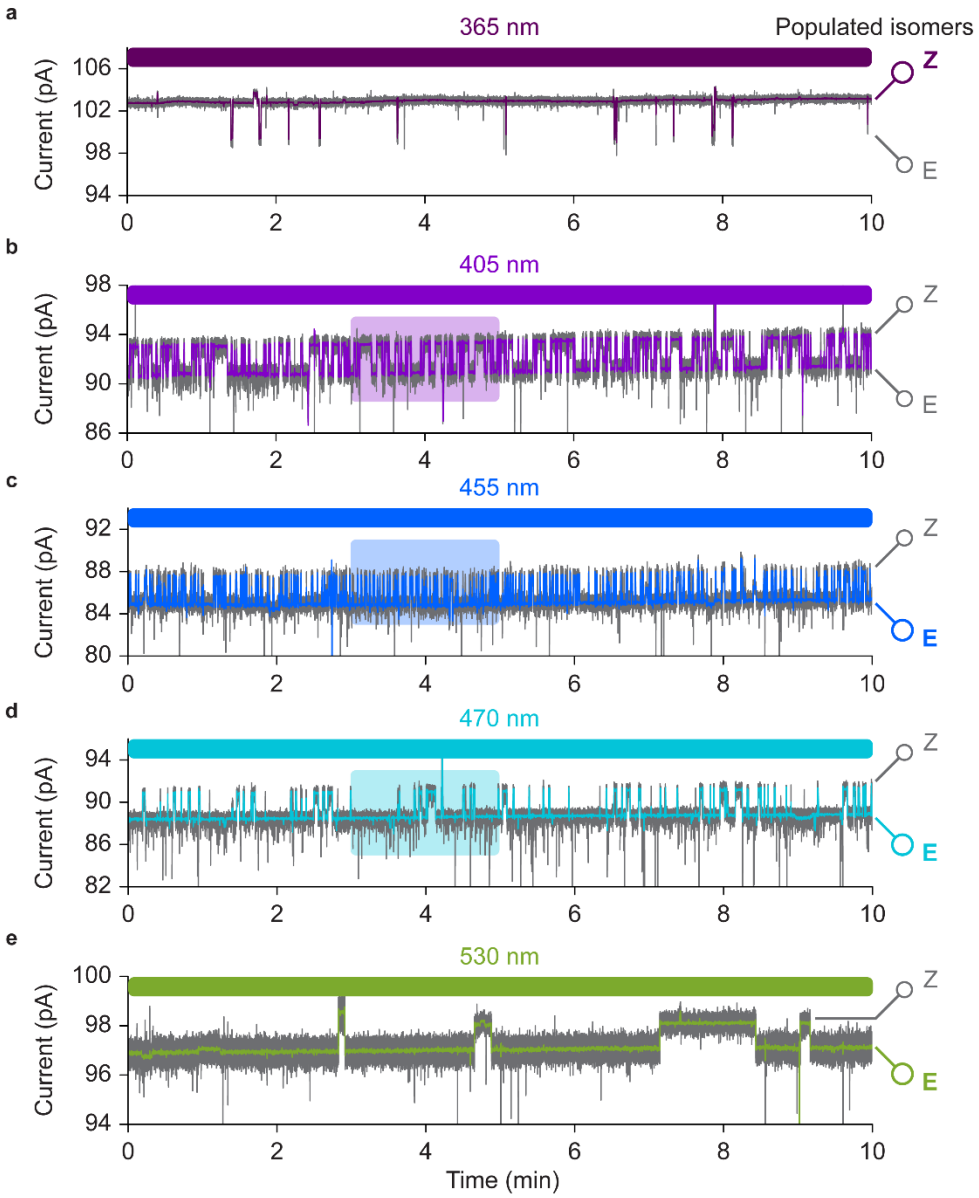


Fig. 9 | Electrical recording of $(E111C\text{-}pzMe)_1WT_6$ under continuous irradiation of 365, 405, 455, 470 and 530 nm. The populated isomer of the longer dwell time is marked at the end of the trace. Each wavelength is associated with a unique pair of dwell times and kinetic constants. Traces in the colored transparent box are magnified in the **Fig. 10**. The moving averages of the ionic currents (colored traces) are generated with a Savitzky–Golay filter (window size = 400 ms). Recording condition: 10 mM Tris-HCl pH 8.5, 2 M KCl, 0.1 mM EDTA, 50 mV at room temperature.

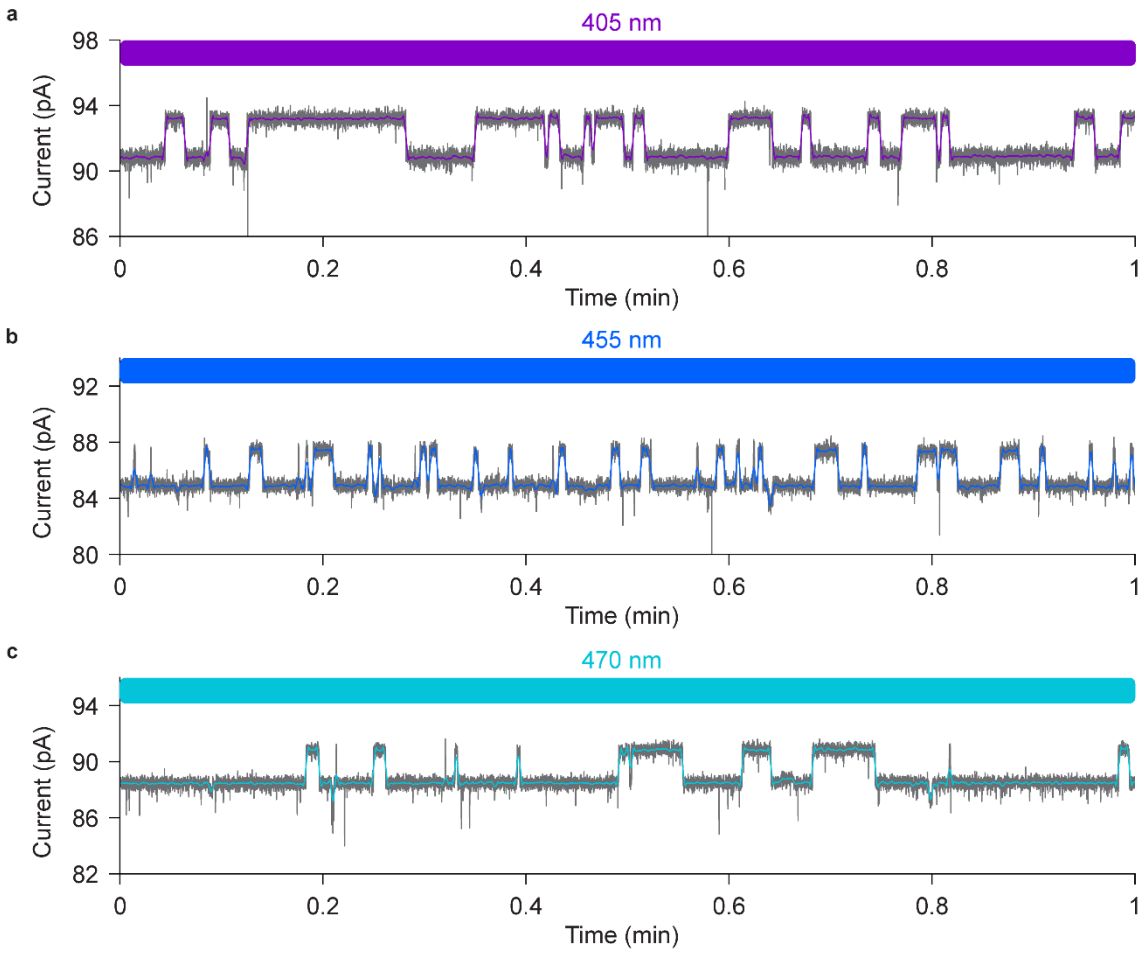


Fig. 10 | Magnified one-minute trace in Fig. 9. Independent of the irradiation wavelength, $(E111C\text{-}pzMe)_1WT_6$ underwent bistate transitions consistently. The moving averages of the ionic currents (colored traces) were generated with a Savitzky–Golay filter (window size = 400 ms). Recording condition: 10 mM Tris-HCl pH 8.5, 2 M KCl, 0.1 mM EDTA, 50 mV at room temperature.

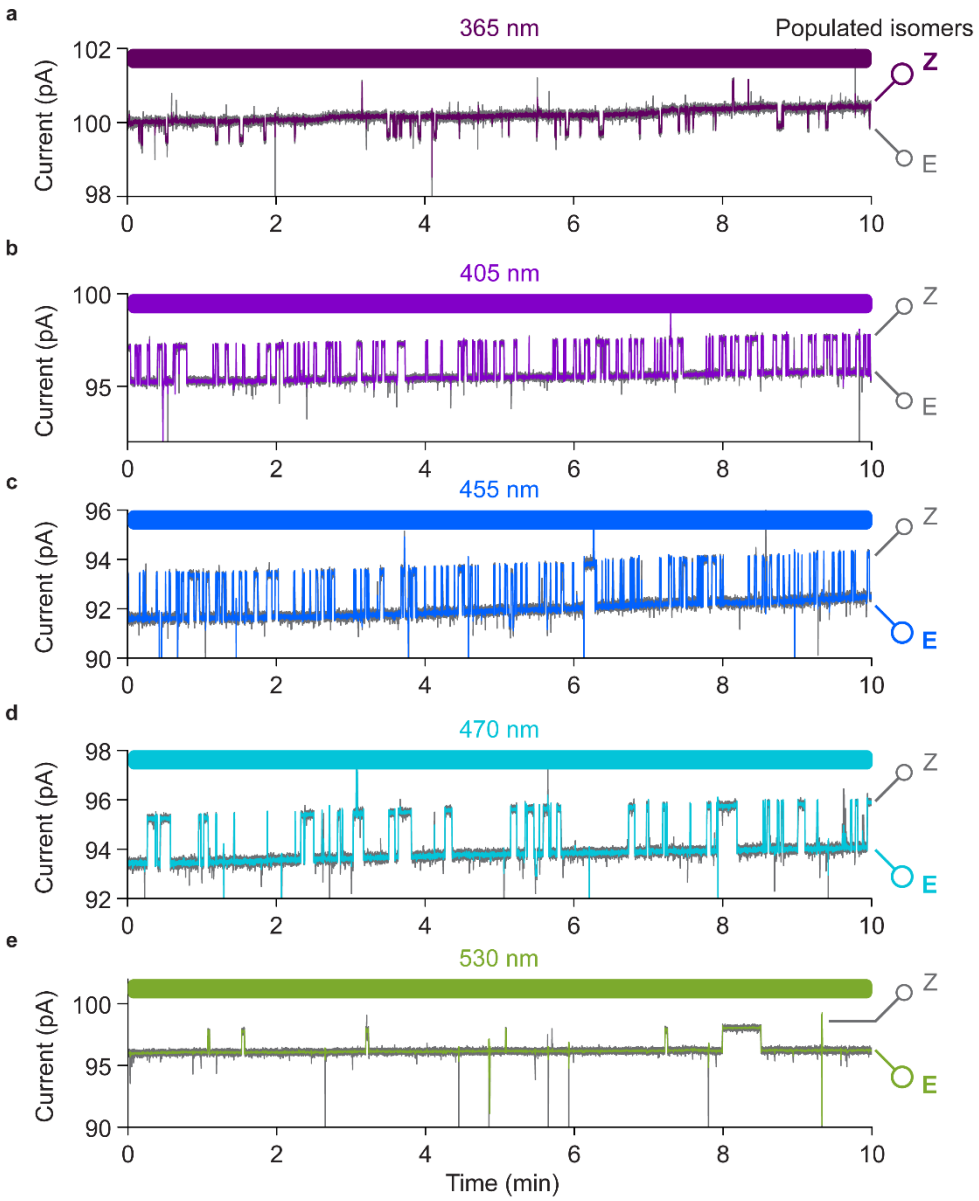


Fig. 11 | Electrical recording of $(E111C\text{-}pzH)_1WT_6$ under continuous irradiation of 365, 405, 455, 470 and 530 nm. The populated isomer of longer dwell time is marked at the end of the trace. Each wavelength is associated with a unique pair of dwell times and kinetic constants. The moving averages of the ionic currents (colored traces) are generated with a Savitzky–Golay filter (window size = 400 ms). Recording condition: 10 mM Tris-HCl pH 8.5, 2 M KCl, 0.1 mM EDTA, 50 mV at room temperature.

These five discrete wavelengths were selected based commercial availability of LED and absorption peaks of arylazopyrazole. The kinetic constants was summarized in **Table 2** and the estimation of light irradiance on the nanopore was described in **Table 3**. As a reference for SMS, the UV/Vis absorption spectra of Br-pzMe and Br-pzH in DMSO was also recorded in the ensemble.

Table 2. Photoisomerization rates and PSS_E determined by SMS at 50 mV applied potential.

a

Single $(E111C\text{-}pzMe)_1WT_6$ kinetics				
Wavelength (nm)	$k_{Z\rightarrow E}$ (s^{-1})	$k_{E\rightarrow Z}$ (s^{-1})	PSS_E (%)	N (pores)
365	0.05 ± 0.02	1.32 ± 0.27	3.6 ± 0.8	5
405	0.56 ± 0.06	0.54 ± 0.03	51.1 ± 1.7	5
455	1.59 ± 0.16	0.47 ± 0.04	77.2 ± 1.4	5
470	1.10 ± 0.14	0.24 ± 0.04	21.1 ± 0.9	5
530	0.054 ± 0.027	0.008 ± 0.002	86.6 ± 3.2	4

b

Single $(E111C\text{-}pzH)_1WT_6$ kinetics				
Wavelength (nm)	$k_{Z\rightarrow E}$ (s^{-1})	$k_{E\rightarrow Z}$ (s^{-1})	PSS_E (%)	N (pores)
365	0.05 ± 0.01	0.54 ± 0.21	8.4 ± 1.4	4
405	0.51 ± 0.05	0.23 ± 0.04	69.1 ± 3.0	5
455	0.88 ± 0.11	0.28 ± 0.03	75.5 ± 2.2	3
470	0.33 ± 0.03	0.10 ± 0.01	76.3 ± 0.2	3
530	0.08 ± 0.05	0.01 ± 0.01	83.7 ± 2.9	4

Table 3. LED irradiance at an Ø300 µm aperture.

Maximum LED irradiance on the Ø300 µm aperture		
Wavelength (nm)	Power (mW)	Irradiance (mW/cm^2)
365	24.6	34.8
405	51.0	72.2
455	87.2	123.4
470	65.4	92.5
530	20.6	29.1

By overlapping the bar chart of the single-molecule spectra S(λ) and the reference Br-pzMe ensemble absorption spectra in 100% *E* state or $PSS_{365\ nm}$, we observed a qualitative similarity between the spectral line shapes for $(E111C\text{-}pzMe)_1(WT)_6$ (**Fig. 8b-c**). However, the Br-pzH spectra could not be aligned with the single-molecule k/Q ratios, regardless of the scaling of ensemble absorbance (**Fig. 8d-e**). This mismatch of line shape was possibly related to a crucial advantage of SMS—to estimate 100% *Z* isomer spectrum. Often 100% *E*-state arylazopyrazole was feasible by heating up to 120ºC in the dark, but the *Z*-state percentage was determined by its photostationary state[59], otherwise, the Z- isomers were purified by chromatography. Here, the Br-pzMe reached the highest $PSS_{365\ nm}$ with 96% *Z*, whereas the Br-pzH reaches $PSS_{365\ nm}$ with merely 85% *Z* based on proton nuclear magnetic resonance spectroscopy (^{1}H-NMR) results. We speculated that the remaining 15% *E*-state pzH (~30% ε of the *Z* state) lowered the overall absorption in the ensemble UV/Vis spectrum and caused this mismatch. The SMS spectra circumvented this limitation of PSS_Z because the photoswitch could only exist in one state at a time (i.e. 100% *Z*). Comparison of PSS_E in the $(E111C\text{-photoswitch})_1WT_6$ and Br-photoswitch in DMSO solution showed robust quantitative switching of pzMe at both single-molecule and ensemble levels.

Based on the eq. 2, we calculated the irradiance-independent PSS_E percentages for $(E111C\text{-photoswitch})_1WT_6$ and compared them with the macroscopic PSS_E measured by ^{1}H-NMR in DMSO-d_6 (**Fig. 8f-g**). Interestingly, both the PSS_E of $(E111C\text{-pzMe})_1(WT)_6$ and $(E111C\text{-pzH})_1(WT)_6$ showed a strong proportionality between the SMS and the ^{1}H-NMR results. Although the pzMe PSS_E retained 4% in ensemble and SMS experiments at 365 nm, the PSS_E decreased from 98% in ensemble to 87% in SMS at 530 nm. In contrast, the pzH PSS_E increased from 4% in ensemble to 8% in SMS at 365 nm, and increased from 73% to 84% at 530 nm. This discrepancy between $(E111C\text{-photoswitch})_1(WT)_6$ and Br-photoswitch might be ascribed to an interaction between bromoacetyl moiety and the photoswitch, which was absent in the pore. Since the pzMe spectral line shape and PSS_E percentage are consistent at single-molecule and ensemble levels, we consequently proceeded to focus on $(E111C\text{-pzMe})_1(WT)_6$.

3.6 pzMe Spectrum in the polarizable environment

The SMS of $(E111C\text{-}pzMe)_1(WT)_6$ was further compared to the ensemble UV/Vis absorption spectra in various solvents to determine the solvent effect in the nanopore confinement. By fitting the four-point SMS k/Q ratios of $(E111C\text{-}pzMe)_1(WT)_6$ at 405, 455, 470 and 530 nm to Lorentzian spectral line shape, we estimated the SMS excitation peak of the *Z*- and *E*- isomers. In the *Z* state, the excitation peak was at 450 nm ; while the *E* state peaks at 407 nm (**Fig. 12a**).

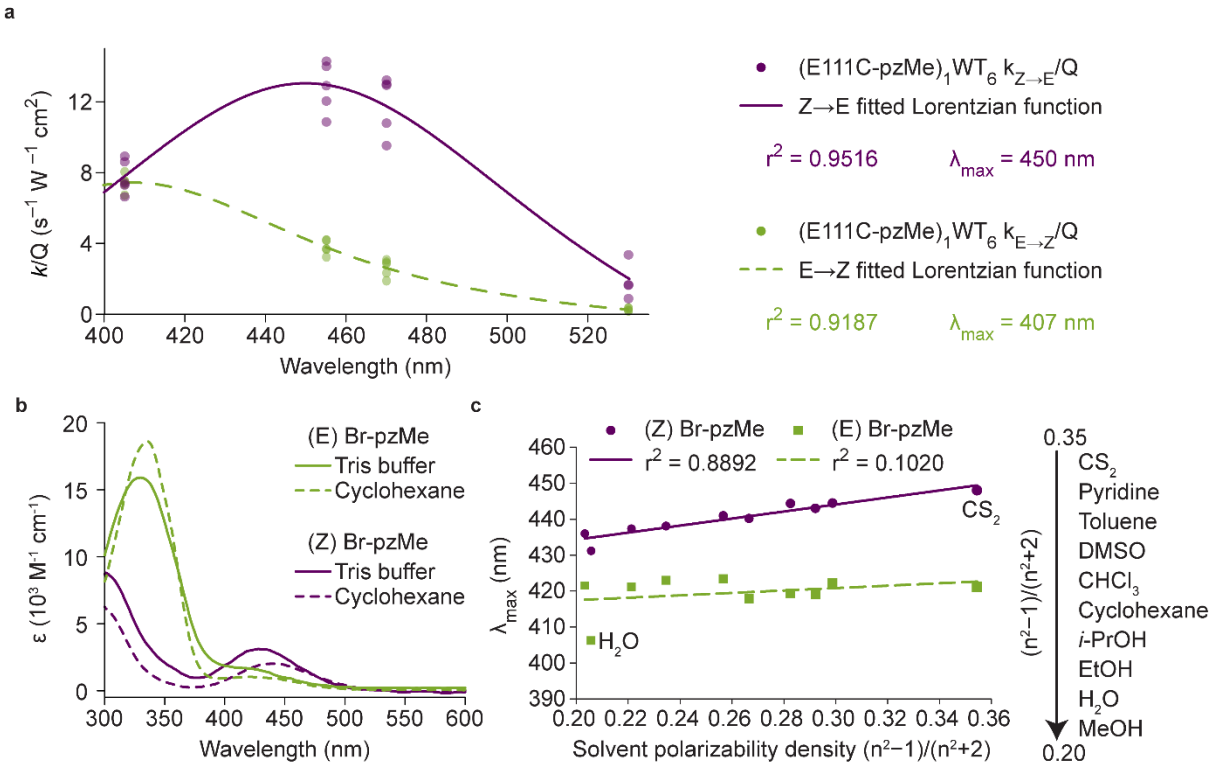


Fig. 12 | Solvatochromism of pzMe in the $(E111C\text{-}pzMe)_1WT_6$ environment and representative solvents. a, Fitted line shape functions of *E*-state $(E111C\text{-}pzMe)_1WT_6$ single-molecule excitation spectra. The four wavelengths of interest are 405, 455, 470 and 530 nm. **b,** Ensemble UV/Vis absorption spectra of Br-pzMe in Tris-HCl recording buffer and Cyclohexane. The maximum absorption (λ_{max}) of *E*- and *Z*- state $(E111C\text{-}pzMe)_1WT_6$ shifted by ~10 nm. **c,** Linear correlation between the maximum absorption and solvent polarizability density. The polarizability density is a function of refractive index (n). (*Z*) Br-pzMe showed strong linear correlation, while the (*E*) isomer showed a non-linear trend. The markers (circles and squares) are sized according to the solvent refractive index. The λ_{max} in *E*-state $(E111C\text{-}pzMe)_1WT_6$ (407 nm) resembled that of Br-pzMe in the Tris-HCl recording buffer (407 nm), while λ_{max} in *Z*-state $(E111C\text{-}pzMe)_1WT_6$ (450 nm) was similar that of Br-pzMe in the pyridine (444 nm). Tris-HCl recording buffer: 2 M KCl, 10 mM Tris-HCl, 0.1 mM EDTA, pH 8.5.

For comparison, we characterized the UV/Vis spectra of Br-pzMe in Tris-HCl recording buffer and cyclohexane. The absorption peak of the *E*-state Br-pzMe, redshifted from 406 nm in Tris-HCl buffer to 423 nm in cyclohexane. The *Z*-state Br-pzMe showed a similar redshift from 431 nm in Tris-HCl buffer to 441 nm in cyclohexane (**Fig. 12b, Figs. 13-15 and Table 4**).

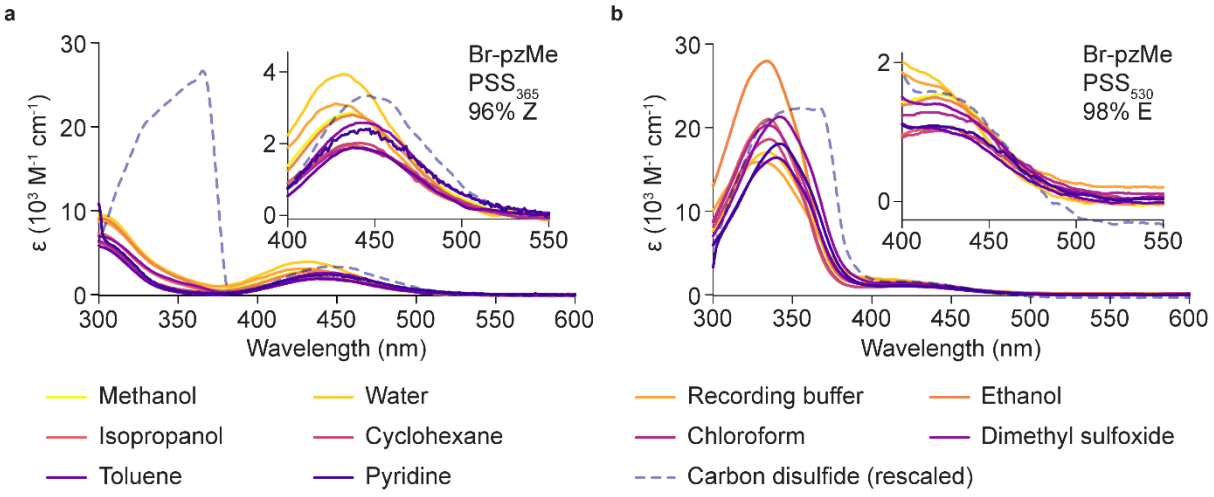


Fig. 13 | Absorption spectra of Br-pzMe in various solvents. The extinction coefficient was calculated from the spectrum of 25, 50 and 75 μM solutions at room temperature. The insets are magnified spectra of the n-π* transition. Carbon disulfide spectrum is rescaled from absorbance due to its unusual vapor pressure and incompatibility with plastic syringes. The color legends of the solvents follow the trend of refractive index.

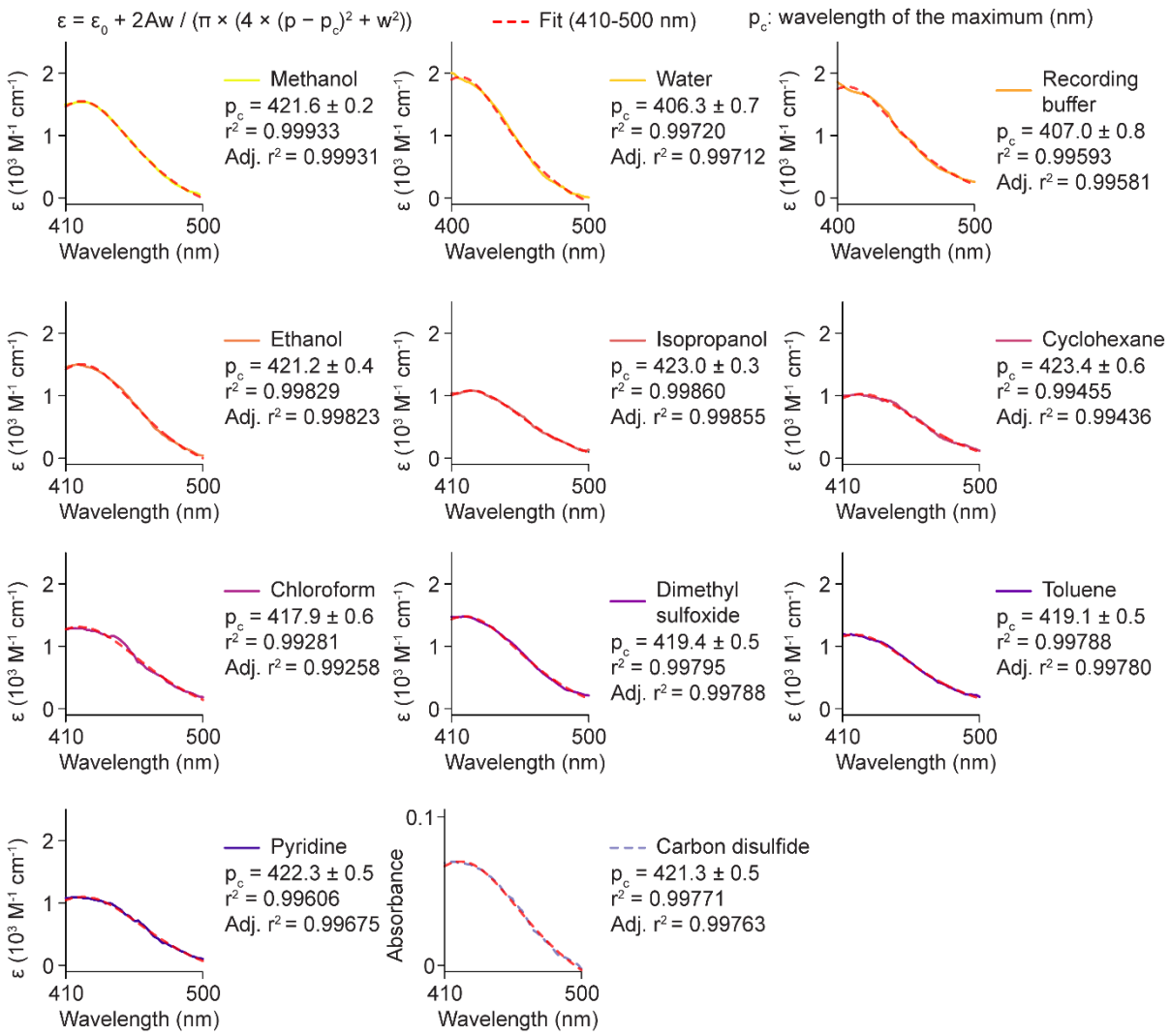


Fig. 14 | Spectral line shape fitting *E*-state Br-pzMe absorptions. The extinction coefficient was calculated from the spectrum of 25, 50 and 75 µM solutions at room temperature. The line shape is fitted by Lorentzian function from 410 to 500 nm. This range was selected to avoid the absorption band of the π-π* transition. As an exception, the spectra in water and recording buffer were fitted down to 400 nm due to the blue-shifted band maxima.

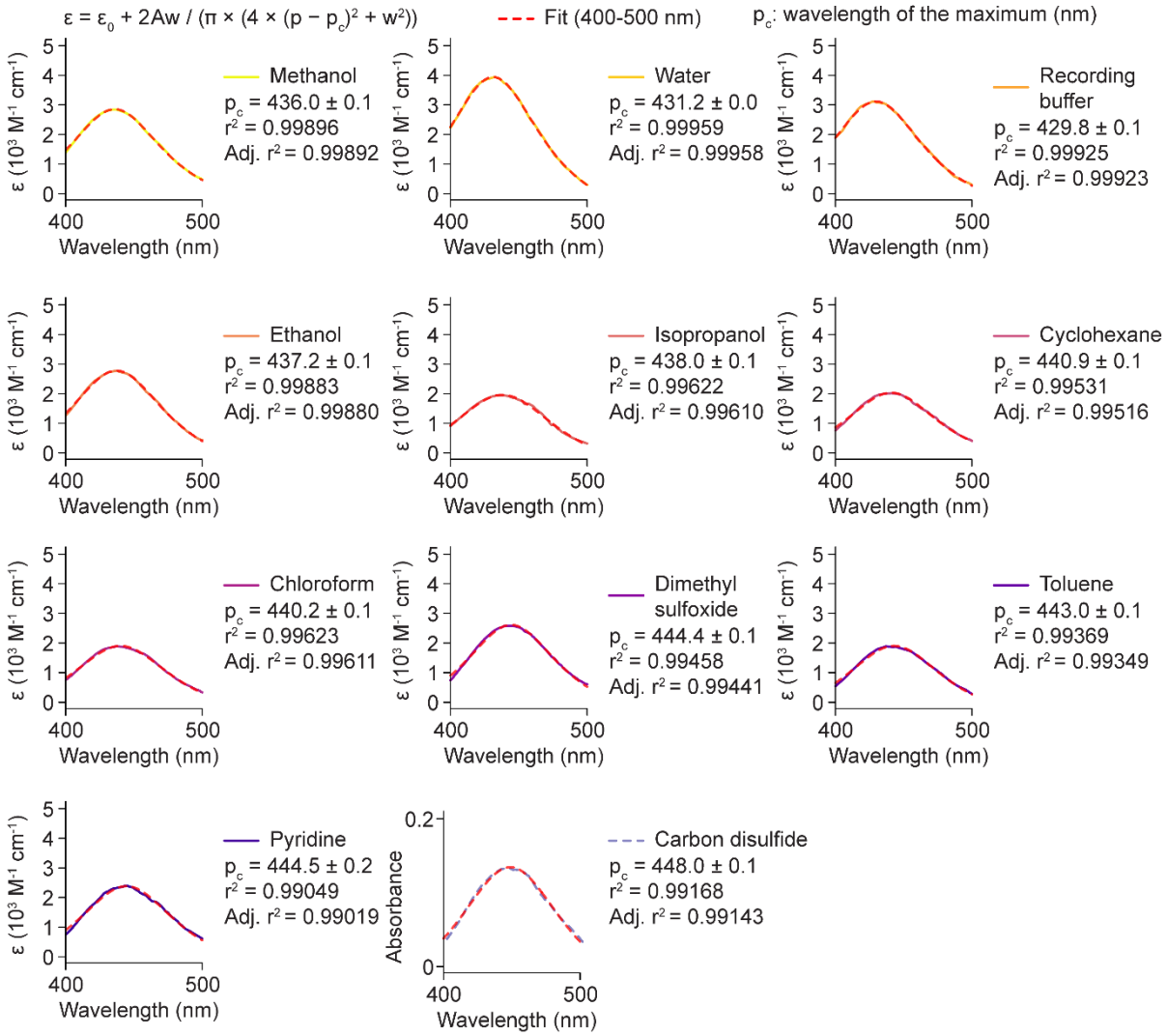


Fig. 15 | Spectral line shape fitting *Z*-state Br-pzMe absorptions. The extinction coefficient was calculated from the spectrum of 25, 50 and 75 μM solutions at room temperature. The line shape is fitted by Lorentzian function from 400 to 500 nm.

Table 4. Solvent characteristics and excitation peak of Br-pzMe.

Solvent	Refractive index (n)	Polarizability density (α)	λ_{max} (Z) Br-pzMe (nm)	λ_{max} (E) Br-pzMe (nm)	Rohrschneider's polarity parameter
Methanol	1.33	0.20	436	422	5.1
Water	1.33	0.21	431	406	10.2
Ethanol	1.36	0.22	437	421	4.3
Isopropanol	1.39	0.23	438	423	4.0
Cyclohexane	1.43	0.26	441	423	−0.2
Chloroform	1.45	0.27	440	418	4.1
Dimethyl sulfoxide	1.48	0.28	444	419	7.2
Toluene	1.50	0.29	443	419	2.4
Pyridine	1.51	0.30	445	422	5.3
Carbon disulfide	1.63	0.35	448	421	1.0

The shifted excitation peak suggested that the arylazopyrazole photoswitch was possibly influenced by the dipole of the solvent[70]. Interestingly, further solvent effect measurement showed that the wavelength of maximum absorption of Br-pzMe was linearly corelated to the polarizability of solvent in the *Z*-state (r^2 = 0.8892) but not in the *E*-state (r^2 = 0.1020) (**Fig. 12c**). The polarizability of solvent (α) was estimated, based on the literature[145], by refractive index (n) and Lorentz–Lorenz equation (eq. 4).

$$\alpha \propto \frac{n^2 - 1}{n^2 + 2} \tag{4}$$

The correlation between absorption peak and α was reported for azobenzene derivatives in both isomers. However, the observation of non-correlated *E*-state Br-pzMe disagreed with the literature of azobenzene[70]. Notably, the 450 nm excitation maxima of SMS *Z*-state $(E111C\text{-}pzMe)_1WT_6$ resembled the UV/Vis spectra in highly polarizable carbon disulfide (CS_2: 448 nm). Whereas the SMS of *E*-state $(E111C\text{-}pzMe)_1WT_6$ peaked at 407 nm, similar to the aqueous environment (H_2O: 406 nm). Hence, the confined constriction of $(E111C\text{-}pzMe)_1(WT)_6$ offered CS_2- and H_2O- like environments for the *Z*- and *E*- state isomer, respectively. In the *Z*- isomer, the pzMe might be directed to the neighboring protein residues or backbones, which offered strong polarizability; whereas the *E*- isomer was probably fully solvated by water molecules passing through the channel.

3.7 Acid-accelerated isomerization

Protonation of azo compound was known to accelerate *Z*-to-*E* thermal relaxation ($k_{thermal}$) in the dark[67,146]. The pK_a of pzMe was estimated to be 1.5~3.5 in the literature *in silico* rather than experimentally[68]. In the dark, the *Z*-state pzMe was protonated as azonium pzMe-H^+ at low pH, and led to acid-accelerated thermal relaxation. Under irradiation, in addition to the neutral pzMe photoisomerization and thermal relaxation, the azonium species also undergoes accelerated photoisomerization (**Fig. 16a** and **Fig. 17**) due to enhanced and red-shifted absorption in the n-π* region[147]. Prior studies on pzMe and arylazoisoxazole photoswitches suggest three potential protonation sites: the nitrogens of the N=N double bond or the nitrogen of the pyrazole ring. According to DFT calculations from previous research[68], the nitrogen adjacent to the benzene ring is the most prone to protonation. This resonance structure enhances the rotational character of the N-N single bond, accelerating Z-E isomerization.

To observe pH dependence of pzMe isomerization at single-molecule level, we applied SMS to $(E111C\text{-}pzMe)_1(WT)_6$ to determine the differentiated *E*-to-*Z* and *Z*-to-*E* apparent photoisomerization rates (k_{app}) at lower pH. Under continuous irradiation, the k_{app} is the overall kinetics of unprotonated photoisomerization, protonation, acid-accelerated photoisomerization and azonium photoisomerization (**Fig. 16a**). We recorded the k_{app} at pH 2.34, 3.25, 5.67, 6.96 and 8.66 at 405 nm (**Fig. 16b and Fig. 18**). At pH 5.67~8.66, the *E*-to-*Z* and *Z*-to-*E* kinetics were equally fast since the $PSS_{405\,nm}$ is 49% (**Fig. 8f**). At acidic pH of 2.34, the difference between apparent photoisomerization rates $k_{app,\ Z\rightarrow E}$ and $k_{app,\ E\rightarrow Z}$ enlarged to 0.33 s^{-1}, suggesting formation of azonium. Based on the trend of k_{app} difference at pH 2.34, 3.25 and 5.67, we estimated that the pK_a of $(E111C\text{-}pzMe)_1WT_6$ is in agreement with the literature[68].

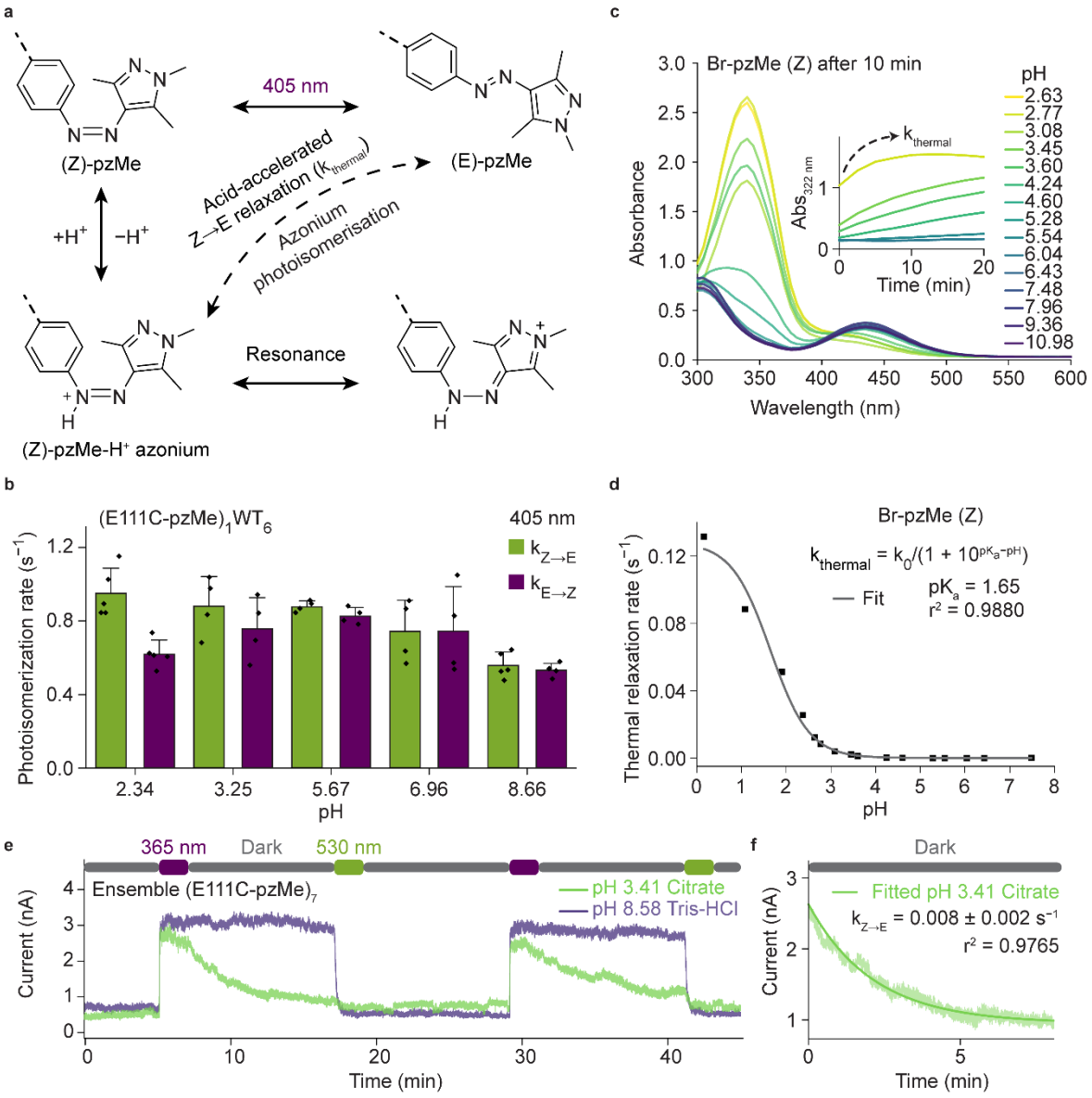


Fig. 16 | Acid catalysis of pzMe thermal relaxation and photoisomerization. a, Scheme of pzMe isomerization under continuous irradiation in acidic buffer. The *Z*-pzMe is protonated to form azonium, which is stabilized by resonance with the pyrazole ring. The azonium undergoes acid-accelerated relaxation and photoismerization. Irradiating $(E111C\text{-}pzMe)_1WT_6$ results in the overall apparent kinetics (k_{app}), including the intrinsic photoisomerization ($k_{Z\rightarrow E}$ and $k_{E\rightarrow Z}$), acid-accelerated thermal relaxation ($k_{thermal}$) and azonium photoisomerization. **b,** Apparent photoisomerization rate of a single $(E111C\text{-}pzMe)_1WT_6$ under 405-nm irradiation. (N = 4 pores). The difference between $k_{app,\ Z\rightarrow E}$ and $k_{app,\ E\rightarrow Z}$ is enlarged at pH 2.34 and 3.25. At high pH, increasing pH reduces both $k_{Z\rightarrow E}$ and $k_{E\rightarrow Z}$. c, Ensemble absorption spectrum of Br-pzMe (96% *Z*) at pH from 2.63 to 10.98. The spectrum was recorded 10 min after adding *Z*-state Br-pzMe to the buffer. pH of the buffer (5 mM sodium citrate, 10 mM sodium phosphate and 5 mM CAPS) was adjusted by NaOH or HCl. Absorbance at 322 nm ($Abs_{332\ nm}$) of Br-pzMe (*Z*) changing over 20 min is shown in the inset. For each pH, the $k_{thermal}$ is calculated by fitting each exponential curves. **d,** pH dependence of acid-accelerated thermal relaxation. **e-f,** Electrical recording of (E111C-

pzMe)$_7$ in acidic and basic buffers. At pH 3.41 in the dark, the ionic current decay rate agreed with the panel **d**.

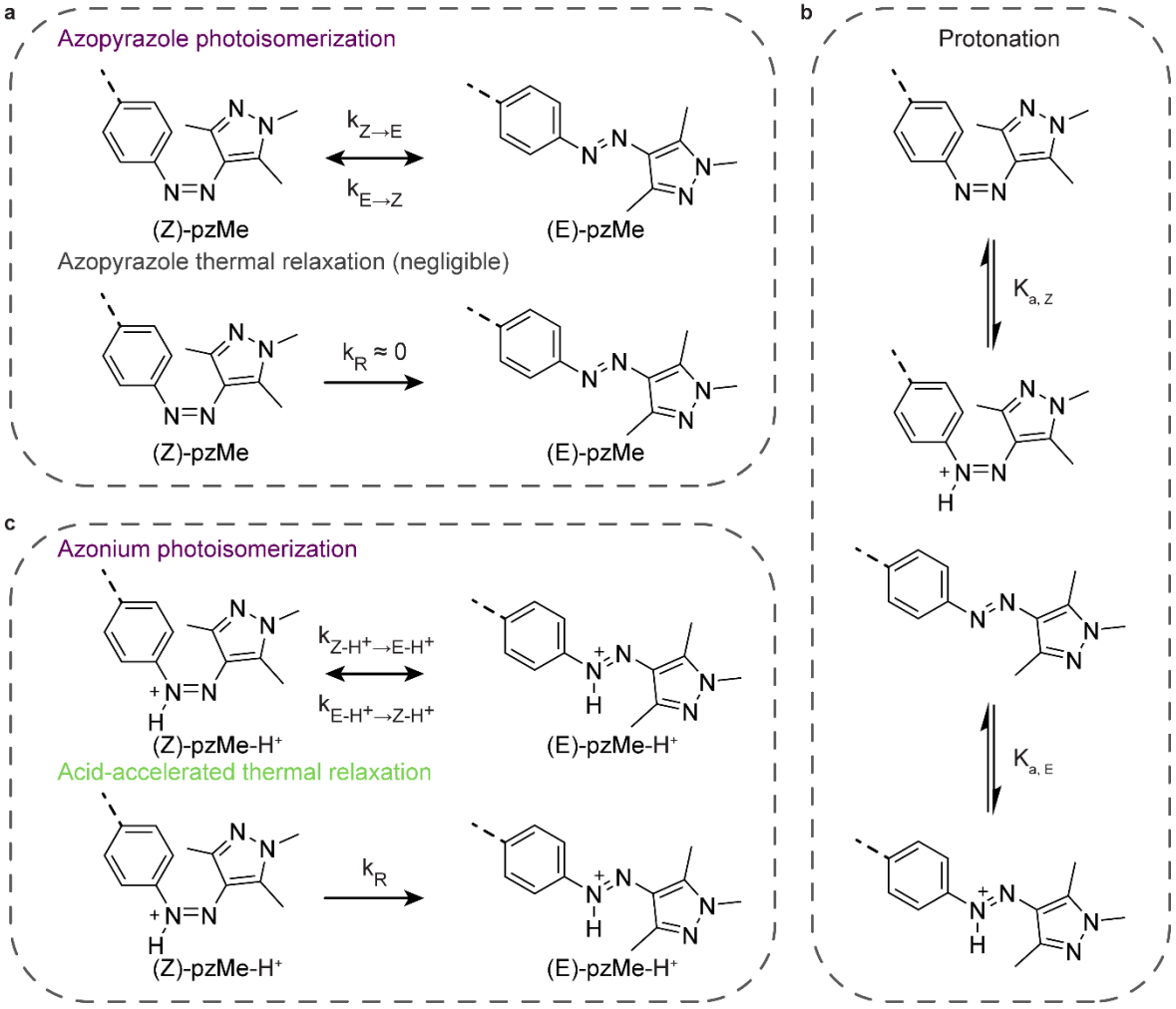


Fig. 17 | Isomerization and protonation of arylazopyrazole. a, Photoisomerization and thermal relaxation of neutral azopyrazole in the neutral or basic condition. The thermal relaxation is negligible for pzMe. **b,** Protonation of pzMe in the acidic condition. **c,** Photoisomerization and acid-accelerated thermal relaxation of azonium. Overall, irradiation at pzMe in acid condition leads to an apparent isomerization rate involving all these processes.

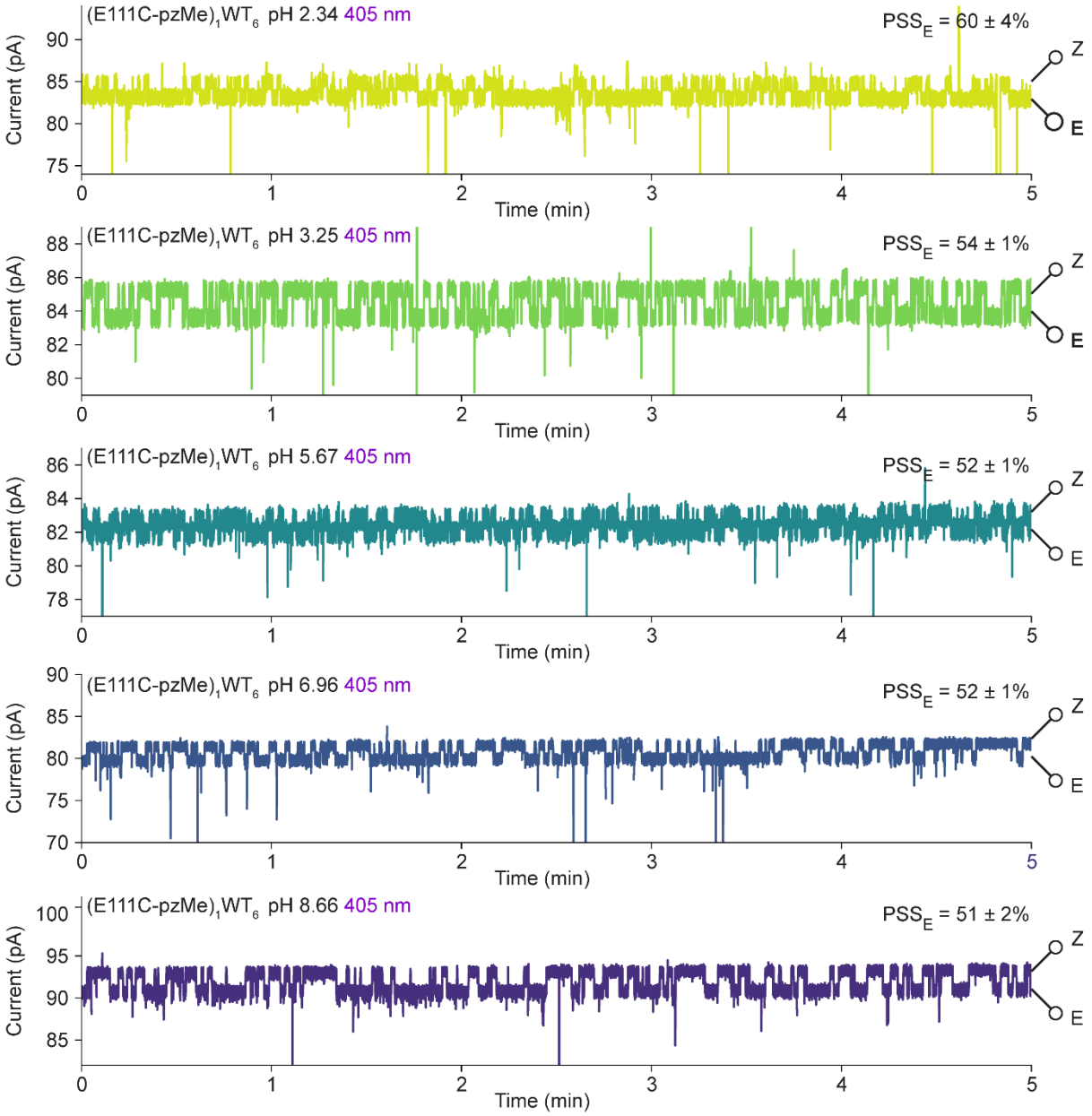


Fig. 18 | Electrical recording of (E111C-pzMe)$_1$WT$_6$ under continuous irradiation of 405 nm in different pH conditions. Recording condition: 10 mM buffering salt, 2 M KCl, 0.1 mM EDTA, 50 mV at room temperature. The buffering salts are 20 mM sodium citrate pH 2.34, sodium citrate pH 3.25, MES pH 5.67, NaPi pH 6.96 or Tris-HCl pH 8.66. The traces were recorded from separate pores.

To determine the accurate pK_a of *Z*-state pzMe, we measured the $k_{thermal}$ of *Z*-state Br-pzMe in the dark once adjusting the pH to a range from 0.16 to 7.48 (**Fig. 16c**). The time-resolved absorption at 322 nm (**Fig. 19**) was fitted to first-order kinetics and yielded the pH-dependent $k_{thermal}$. The kinetics of *E*-state Br-pzMe were not studied due to unaffected absorption at low pH. In this condition, the starting 96% *Z*-state Br-pzMe underwent solely the acid-accelerated relaxation $k_{thermal}$ because

the thermal half-life of pzMe is >10 days[59]. The pK_a of *Z*-state Br-pzMe was characterized to be 1.65 ± 0.06 by fitting[148] the absorption increase at 332 nm over time (eq. 5) (**Fig. 16d and Fig. 20**). The k_0 referred to the thermal relaxation rate of pure *Z*-state azonium.

$$k_{thermal} = k_0/(1 + 10^{pK_a - pH}) \quad (5)$$

This pKa suggests that protonation likely occurs at the N=N nitrogen adjacent to the benzene ring (estimated pKa = 3.77)[68]. Alternatively, the pyrazole nitrogen (estimated pKa = 3.31) may also be protonated, leading to tautomerization into the azonium form. In contrast, the N=N nitrogen next to the pyrazole ring is not easily protonated and requires a significantly lower pH than the observed pKa (estimated pKa = 0.38). Furthermore, the pH-dependence of pzMe might expand the application of $(E111C\text{-}pzMe)_7$ photopore in our previous work and fine-tune the lifetime of high-conductance *Z* state (**Fig. 16e-f**). Accelerated *Z*-to-*E* isomerization occurs in the $(E111C\text{-}pzMe)_7$ at pH 3.41, and shortened the *Z*-state lifetime to 4 min, which was close to 8 min predicted by eq. 5. Hence, the $(E111C\text{-}pzMe)_1(WT)_6$ and $(E111C\text{-}pzMe)_7$ could have pH/light dual-trigger applications in synthetic biology.

In addition, eq. 5 also predicted the $k_{thermal}$ at pH 2.34 to be 0.02 s^{-1} for Br-pzMe, which was a magnitude smaller than the observed 0.33 s^{-1} difference in $(E111C\text{-}pzMe)_7$. It suggested that azonium photoisomerization rather than $k_{thermal}$ might be the predominant reason for the enlarged $k_{Z\rightarrow E}$ and $k_{E\rightarrow Z}$ difference at pH 2.34.

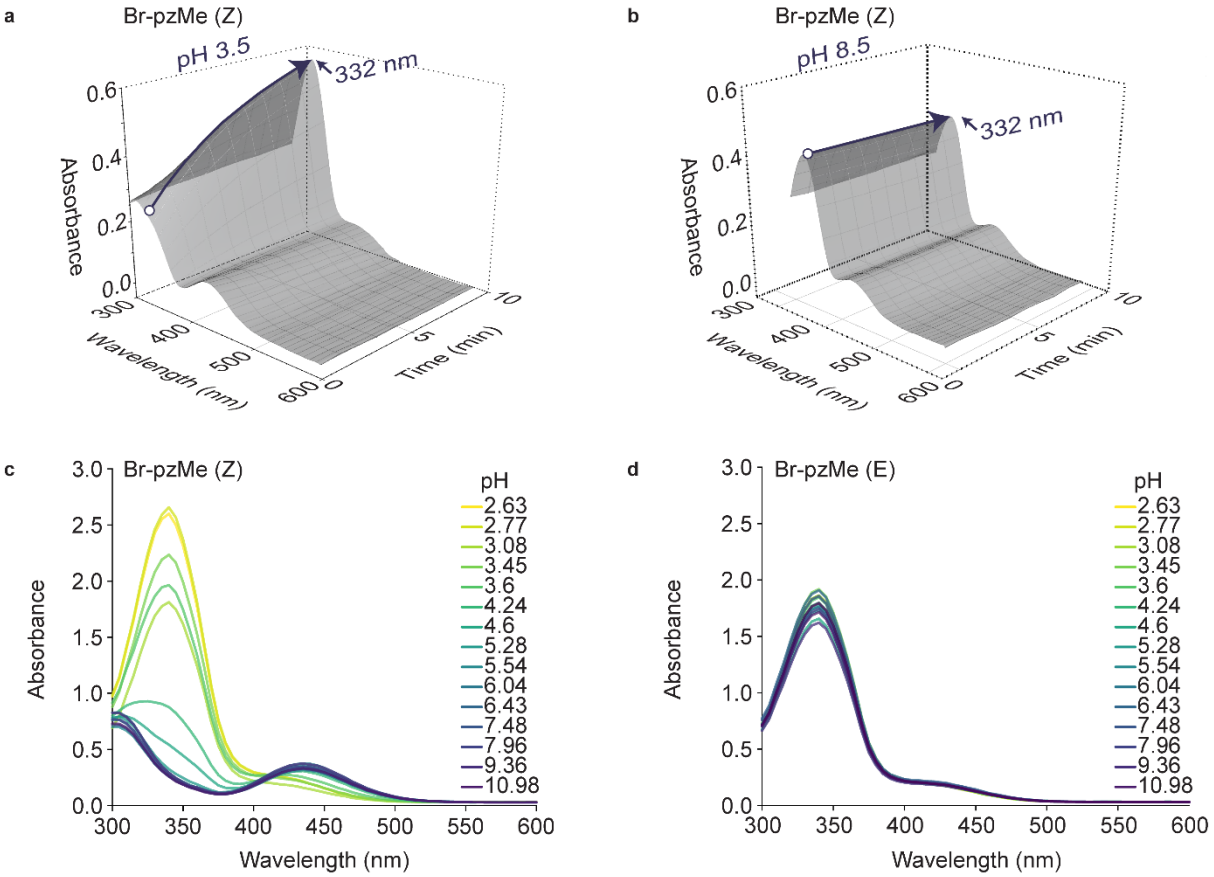


Fig. 19 | Halochromic effect on the acid-catalyzed pzMe thermal relaxation. a-b, Absorbance of *Z*-state Br-pzMe at 322 nm at pH 3.5 and pH 8.5 at room temperature in the dark. Buffer of pH 3.5: 50 mM sodium citrate; pH 8.5: 50 mM Tris-HCl. **c-d**, Absorbance of Br-pzMe at 10 minutes after adding the concentrated Br-pzMe DMSO solution to buffer of different pH. The buffer contained 5 mM sodium citrate, 10 mM sodium phosphate and 5 mM CAPS, and was adjusted by NaOH or HCl. Low pH did not change the absorption maxima of *E*-state Br-pzMe.

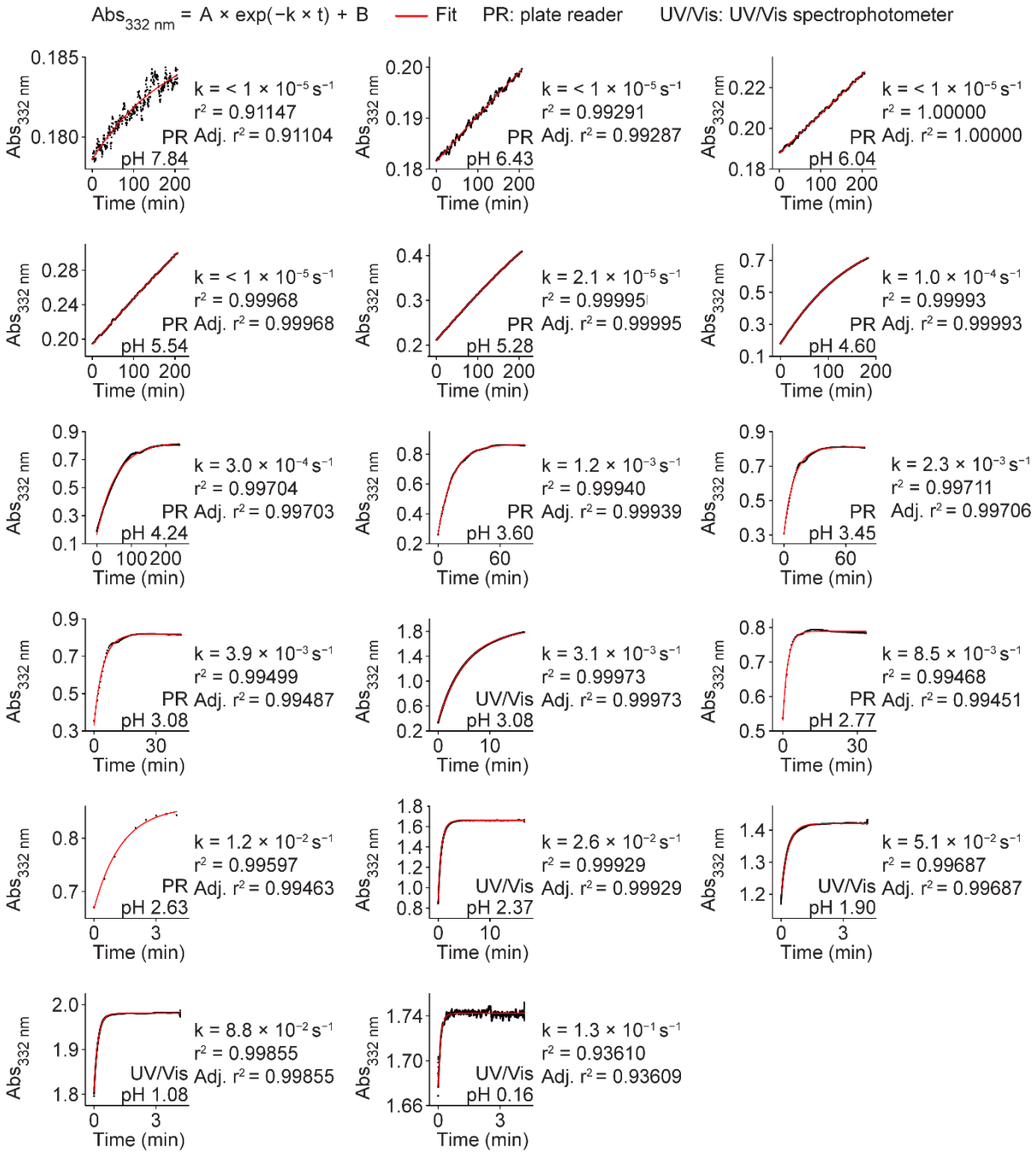


Fig. 20 | Fitted acid-accelerated thermal relaxation rates for Br-pzMe at different pH. The decay rate increased significantly at lower pH. The measurement started right after adding the Br-pzMe DMSO solution to the buffer in the dark. The plate reader and UV/Vis samples were sampled every 15 seconds and 40 microseconds, respectively. The buffer contained 5 mM sodium citrate, 10 mM sodium phosphate and 5 mM CAPS, and was adjusted by NaOH or HCl. Low pH did not change the absorption maxima of *E*-state Br-pzMe.

3.8 A minimum spectrophotometer

With the characterized SMS excitation spectra, we exploited integrating (E111C-pzMe)$_1$WT$_6$ as a photodetector in a minimum spectrophotometer. Unlike conventional photodetectors that convert light to amplified photocurrent or voltage, this single-molecule nanopore photodetector measures light intensity by kinetic constants through photoisomerization events under constant millivolt voltage and picoampere current (**Fig. 1d and Fig. 21**).

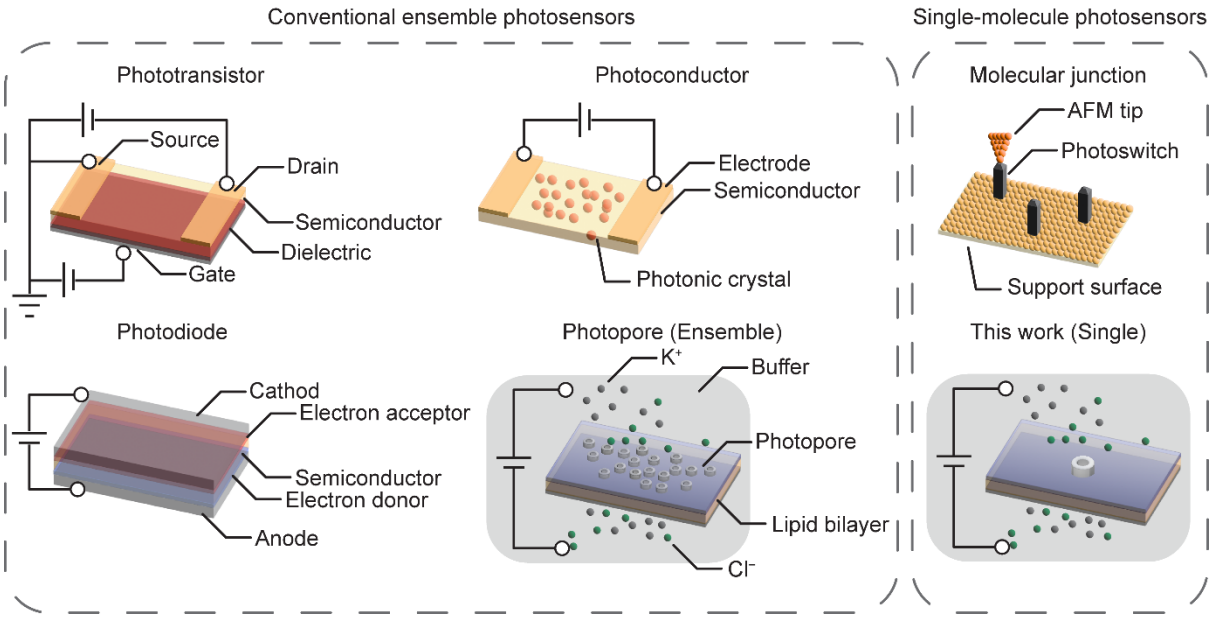


Fig. 21 | General architectures of conventional and single-molecule-based photosensors. Conventional ensemble p-n junction photosensors translate incident photon flux into photoelectric response, resulting in a statistical ensemble electronic current. Single-molecule-based photosensor captures one photon from the flux and detect a photoisomerization event reported by KCl ionic current through the photopore.

In this proof-of-concept setup, an analyte cuvette was positioned along the light path between the collimated LED and the lipid bilayer (**Fig. 22a-b**). The light was absorbed and scattered through the analyte and partially transmitted through, reaching the (E111C-pzMe)$_1$WT$_6$ and inducing stochastic events at an apparent rate ($k_{apparent}$). Consequently, the $k_{apparent}$ of (E111C-pzMe)$_1$(WT)$_6$ contained the transmittance of the analyte ($T_{analyte}$), which followed the eq. 6.

$$k_{apparent} \propto \varphi \varepsilon Q T_{analyte} \qquad (6)$$

Assuming the transmittance of the buffer blank (T_{blank}) was unity, the transmittance spectrum of an analyte was approximated by eq. 7, where the ratio of $k_{apparent}$ with the analyte to kinetic constant of the buffer blank (k_{blank}) should reproduce the transmission features of the analyte (**Fig. 22c**).

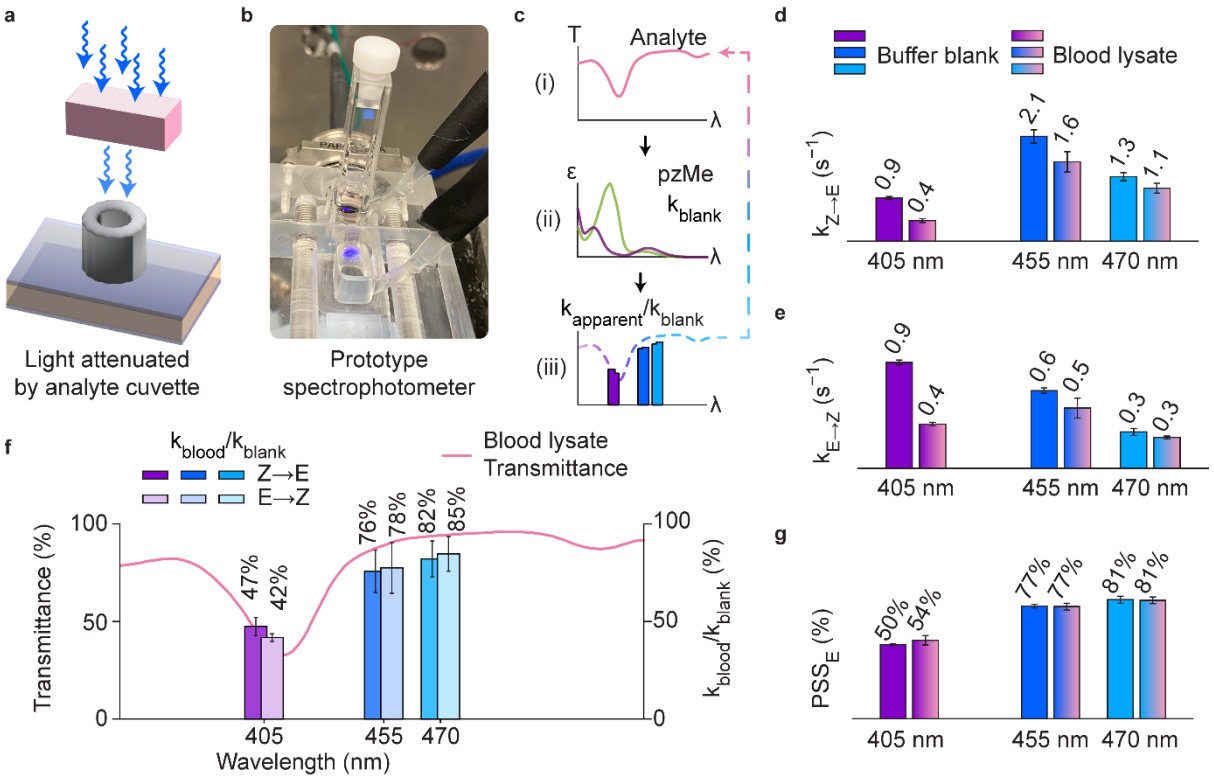


Fig. 22 | A proof-of-concept prototype spectrophotometer based on (E111C-pzMe)$_1$WT$_6$. a, Attenuation of incident light through an analyte cuvette (pink) on the light path. Irradiance: 35, 72, 123, 93 and 29 mw/cm^2 for 365, 405, 455, 470 and 530 nm, respectively. **b,** Insertion of the analyte cuvette (5-mm light path) into the recording chamber. **c,** Transmittance of the analyte measured indirectly by the apparent photoisomerization kinetics. **(i)** Transmittance (T) through the analyte depends on the wavelength (λ). **(ii)** pzMe absorbs transmitted light and isomerizes following the extinction coefficient (ε). **(iii)** The ratio of apparent kinetics ($k_{apparent}$) to reference kinetics (k_{blank}) is equivalent to transmittance in **(i)**. **d-e,** Buffer blank kinetics and apparent kinetics with 0.5% (v/v) filtered rabbit blood lysate. **f,** Overlay of blood lysate transmittance measured with conventional UV/Vis spectrophotometer (pink curve) and the transmittance measured indirectly from the single (E111C-pzMe)$_1$WT$_6$. **g,** Consistent PSS_E of buffer blank and blood lysate.

$$T_{analyte} \approx \frac{T_{analyte}}{T_{blank}} = \frac{k_{apparent}}{k_{blank}} \tag{7}$$

The first model analyte was 0.05% (v/v) rabbit red blood cell lysate in Tris-EDTA (TE) buffer filtered through a 0.22 μm membrane filter. This particle-free lysate

should have non-fluorescent absorption by haem, maximized at 420 nm[149]. The stochastic events of the photopore triggered by the attenuated and transmitted light through the blood analyte were determined under a constant 405, 455, and 470 nm irradiation. At 405 nm, which was close to the major 420 nm absorption peak, the $k_{Z\rightarrow E}$ and $k_{E\rightarrow Z}$ were halved compared to the TE blank (**Fig. 22d-e**). At 455 and 470 nm, where the blood absorbed weakly, kinetic constants remained consistent with the TE blank except for the $k_{Z\rightarrow E}$ at 455nm, which decreased from 2.1 to 1.6 s^{-1}. These decrease in $k_{apparent}$ are ascribed to the transmittance of blood analyte. To evaluate the three-point analyte transmission spectra, we overlaid the ratio between blood apparent kinetics and blank kinetics (k_{blood}/k_{blank}) onto the transmittance spectra of the blood lysate (**Fig. 22f**). As predicted by eq. 7, we found the bar chart of k_{blood}/k_{blank} had a consistent line shape with the UV/Vis transmission spectrum obtained from conventional spectrophotometer. Thus, the three-point characterization of blood analyte transmission spectra was achieved. We also observed the identical PSS_E through the blood and blank, indicating no fluorescence or shifting of wavelength caused by the blood lysate (**Fig. 22g**).

A second example of the photopore spectrophotometer was to determine the optical density of a SiO_2 particle suspension to mimic an optical density (OD) measurement for bacterial culture in a biological experiment[150]. The SiO_2 beads had a diameter of 0.5 μm which was roughly equivalent to the length of an *E. coli*. We continued to use 405 nm rather than the typical 600 nm working wavelength (OD_{600}), because OD_{600} was beyond the range of pzMe absorption. By plotting the observed kinetic constants and the bead concentration ranging from 0 to 0.13 % (m/v), we obtained a linear correlation readily calibrated to perform OD_{405} measurements. (**Fig. 23**).

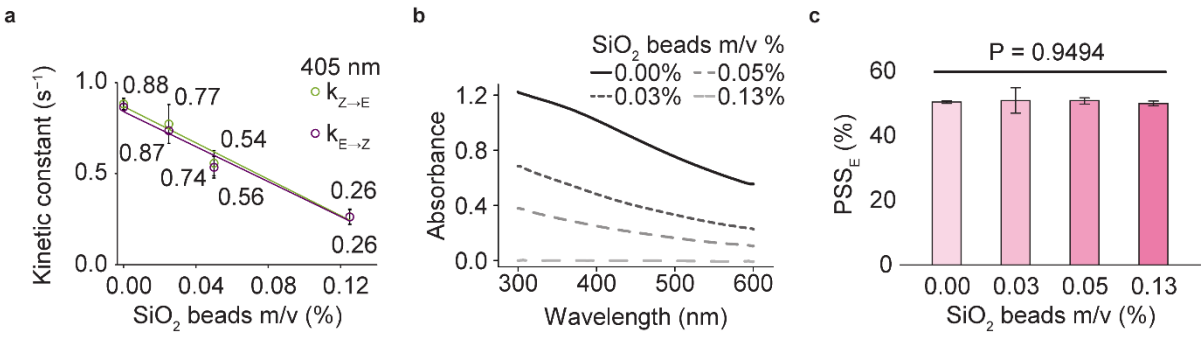


Fig. 23 | Optical density measurement of SiO_2 beads with $(E111C\text{-}pzMe)_1WT_6$ photoswitching kinetics. a, Linear correlation between the SiO_2 beads percent concentration (m/v) and photoswitching kinetics. **b,** Absorbance of SiO_2 beads measured

with conventional UV/Vis spectrophotometer. **c,** Consistent PSS_E independent of SiO_2 beads concentration (ANOVA, F(3/9) = 0.1145, p = 0.9494).

The apparent PSS_E remained consistent throughout the bead concentrations and showed no statistically significant differences (ANOVA, F(3/9) = 0.1145, p = 0.9494) as no fluorescence emission from SiO_2 particle was expected.

Overall, the goal of the minimum spectrophotometer was to prove the possibility of designing optical equipment with a single-molecule photodetector. This result demonstrated a prime example of integrating a protein-based photoresponsive nanopore into a functional optical system.

3.9 Conclusions

In this work, a five-point single-molecule excitation spectrum of arylazopyrazole photoswitch was measured in an $(E111C\text{-}pzMe)_1(WT)_6$ or $(E111C\text{-}pzH)_1(WT)_6$ nanopores. Through a single-channel recording setup with fiber-coupled LED, the SMS, which measures the product of extinction coefficient and photoisomerization quantum yield, was characterized indirectly by detecting photoisomerization events of pzMe and pzH. These events were recorded as binary ionic current flowing through the nanopore, with an arylazopyrazole tethered at the nanopore constriction. Previously, these non-fluorescent photoswitches was not in the scope of conventional SMS that focused on rylene dyes in solid polymer matrices. In contrast, the nanopore-based SMS was tailored for photoswitch tethered to a nanopore in aqueous solution at room temperature. This approach expanded excitation wavelength range of SMS to UV/Vis range (365 to 530 nm), and LEDs at low mW/cm^2 irradiance were adequate for events detection. Besides, a notable advantage of SMS was the characterization of 100% *Z* isomer of arylazopyrazole without separation of *E/Z* isomers. In other words, the our single-molecule approach resembled to photokinetic spectroscopy, where the E/Z isomer photoisomerization kinetics were inferred from an exponential decay curve.

Regarding the absorption spectrum of Br-pzMe in various solutions and pzMe in nanopore confinement, we observed that the excitation maxima of *E*- and *Z*-isomers of Br-pzMe were red-shifted by approximately 15 nm in more polarizable solvents, such as carbon disulfide, than water. For example, the absorption peak of the Br-

pzMe *Z*-isomer shifted from 431 nm in water to 448 nm in carbon disulfide. Overall, the absorption maxima of the *Z*-isomer exhibited a moderate correlation with solvent polarizability.

Using the absorption maxima of Br-pzMe as a reference, we estimated which solvent provides a solvation environment similar to that of nanopore confinement. The *Z*-isomer in the $(E111C\text{-}pzMe)_1WT_6$ pore appeared to reside in a more polarizable environment than the *E*-isomer, likely due to interactions with nearby M113 or K147 residues.

The polarizability of protein residues within the nanopore suggests that the photoswitch experiences a unique polarizable environment distinct from that of bulk solvents like water, such as in $(E111C\text{-}pzMe)_1WT_6$, the active site of a drug target, or a polymer matrix. Additionally, we also detected the acid-accelerated thermal relaxation and azonium photoisomerization, which elucidated the pH dependence of pzMe and broadened the application scope of pzMe photopores.

Furthermore, the use of a single $(E111C\text{-}pzMe)_1WT_6$ as a photodetector in a minimum spectrophotometer for the absorption and transmission spectra held promise for integrating single-molecule electronics into optical systems. Here, we circumvented the need for a complicated amplification system and detect the intensity completely depending on the frequency of events. This could catalyze development of future single-molecule-based devices.

Beyond the pzMe and pzH, potential alternative analytes by SMS could include any molecules causing conformational change under irradiation. Photoswitches including spiropyran, diarylethene, fulgide, hydrazone and thioindigo might be interesting options. For instance, the K/L isomerization[151] of rhodamine dyes for super-resolution microscopy might be studied in the pore. However, the nanopore-based SMS is limited by the events sampling rate (50 kHz), residual current of photoswitching events, amount of data to determine the kinetics (> 50 events) and wavelengths of LEDs.

Overall, nanopore-based SMS represents a powerful tool for studying the photochemical properties of individual molecules in aqueous environments at room temperature, expanding the horizons of single-molecule spectroscopy beyond

traditional fluorophores embedded in polymers. This methodology not only enhances our fundamental understanding of single-molecule photochemistry but also holds significant potential for applications in novel photodetector development, biophysics, and nanotechnology.

3.10 Methods

3.10.1 General information

All chemicals were purchased from Merck and used as received unless otherwise stated. Synthesis of Br-pzMe, Br-pzH were performed and delivered by Aidan Kerckhoffs.. These bromoacetyl photoswitches were stored at −20˚C in the dark as stock solutions (3 mM in dimethyl sulfoxide (DMSO)). The fibre-coupled LEDs were purchased from Thorlabs (M365FP1, M405FP1, M455F3, M470F4 and M530F3). By default, the LEDs were operated through an LED driver (1000 mA, LEDD1B) modulated through pClamp software (Molecular Devices). An optical fibre (Ø1000 µm, 0.39 NA) supplied by Mightex was used to connect the LED to the recording chamber. Molecular modelling was carried out by using open-source PyMol on GitHub (Schrodinger).

3.10.2 Expression and purification of αHL cysteine monomers

Genes encoding the C-terminal D_8H_6-tagged E111C and C-terminal H_6-tagged wild type αHL were obtained from the previous work . BL21 (DE3) pLysS E. coli cells (Agilent) were transformed with the mutated plasmid containing the E111C-D_8H_6 or WT-H_6 gene and inoculated onto Luria Broth (LB) medium agar plate containing antibiotics (carbenicillin, 50 µg mL^{-1}; chloramphenicol, 34 µg mL^{-1}) at 37 ˚C. A single colony from the plate was picked and used to inoculate 10 mL LB medium as a pre-culture. The main LB culture (400 mL) supplemented with the same concentration of carbenicillin and chloramphenicol was inoculated with 4 mL overnight pre-culture. With continuous shaking at 37 ˚C at 250 rpm for around 3 h until the optical density (OD600) reached 0.6, this culture was further cooled at 18 ˚C for 10 min before induction of protein expression. Protein expression was induced with isopropyl-β-D-1-thiolgalactopyranoside (2 mL, 0.1 M). After further incubation at 18 ˚C at 250 rpm overnight, the cells were harvested by centrifugation (10 min, 5000 rpm, Beckman J25), and resuspended in lysis buffer (10 mL, 50 mM

Tris-HCl, pH 8.0, 150 mM NaCl, 10 mM imidazole, 0.1% Triton X-100, 5% glycerol, 2 mM tris(2-carboxyethyl)phosphine (TCEP) with an EDTA-free protease-inhibitor tablet; ThermoFisher). Lysis of the cells was performed by adding lysozyme solution (250 µL, 40 mg/mL), universal nuclease (2 µL, 250 U/µL; ThermoFisher) and magnesium chloride solution (25 µL, 2 M) to the suspension and incubating the suspension on ice for 1 h. Complete lysis was assured by sonication on ice at 40% amplitude for 3 min in a 30 s-ON-30 s-OFF pulse train (VCX 500, Sonics). Cell debris was removed by centrifugation at 29000 × g for 45 min at 4 ˚C, and the supernatant was loaded to a Ni-NTA spin column pre-loaded with Ni-NTA resin (1 mL; ThermoFisher) by gravity. The column was washed with washing buffer (2 × 15 mL, 50 mM Tris-HCl, pH 8.0, 500 mM NaCl, 20 mM imidazole, 0.1% Triton X-100, 5% glycerol, 2 mM TCEP) and eluted with elution buffer (12 × 1 mL, 50 mM Tris-HCl, pH 8.0, 500 mM NaCl, 250 mM imidazole, 0.1% Triton X-100, 5% glycerol, 2 mM TCEP) by centrifuging at 700 × g. The fractions containing αHL monomers were combined and purified through a HiLoad 26/600 Superdex 200pg (Cytiva) size-exclusion column (buffer: 10 mM Tris-HCl, pH 8.0, 150 mM NaCl, 5% glycerol, 2 mM TCEP). The purified αHL monomers were concentrated, aliquoted and flash frozen for storage (~ 1 mg/mL). The quality of αHL monomer was verified by SDS-PAGE.

3.10.3 Conjugation of photoswitches

Br-pzMe, Br-pzH stock solutions (3 mM in DMSO) were added to freshly-buffer exchanged E111C monomers (0.5 mg/mL in 10 mM Tris-HCl, pH 8.0, 0.1 mM EDTA) stepwise over 18 h, typically at time points of 0, 4, 8 and 11 h, to a final concentration of 750 µM. After 18 h, the temperature was cooled to 4 ˚C to prevent overreaction. The progress and completion of the reaction was verified by LC-MS. Excessive photoswitch reagent was removed by passing the mixture through a Zeba desalting spin column (ThermoFisher), and the eluent was aliquoted and flash frozen for storage.

3.10.4 Oligomerization and purification of photopore heteroheptamers

C-terminal D_8H_6-tagged E111C-photoswitch and [^{35}S]-*L*-methionine labelled C-terminal H_6-tagged WT were mixed (1:8 v/v) with rabbit erythrocyte membrane (2% v/v%). The oligomerization mixture (~50 µL in 10 mM Tris-HCl, pH 8.5) was

incubated at 37˚C for 1 h and solubilized in SDS-PAGE loading buffer. The heteroheptamers were separated by SDS-PAGE visualized by autoradiography following established protocol[38]. The protein was extracted from the dehydrated gel by excising the band, grinding the dry gel with a pestle, and rehydrate in the buffer (100 uL 10 mM Tris-HCl, pH 8.5 for each band). The crushed gel was filtered through microcentrifuge tubes with PVDF membranes by centrifuging at 14000 × *g* for 30 min. Samples were aliquoted and stored at −80˚C.

3.10.5 Ensemble electrical recording

Ensemble planar lipid bilayer recording experiment of homoheptamer was adapted from the single-channel electrical recording. Photopore monomer (5 µL, 0.2 mg/mL) was added to the cis compartment instead of pre-heptamerized pores. Immediately after adding the monomer, the LED was switched on at 530 nm, and alternating potential of ±20 mV was applied for 15 min to ensure the yield and quality in pore assembly reproducible. Excess monomers were removed by perfusing the cis compartment. For the experiment involving changing the buffer pH, concentrated sodium citrate buffer (122 µL, 0.5 M, pH 3.5) was added to the cis compartment to overcome the pH of the default recording buffer (1 mL, 10 mM Tris-HCl pH 8.5, 2 M KCl, 0.1 mM EDTA). The typical changed pH was 3.41 at 22˚C.

3.10.6 UV/Vis absorption spectrum and ^{1}H-NMR of Br-photoswitches

The UV/Vis absorption spectra were recorded with a Chirascan V100 spectrophotometer (AppliedPhotophysics) at room temperature (22˚C). The Br-pzMe or Br-pzH were dissolved in isopropanol (10 mM sample with 5% (v/v) DMSO). This 5% DMSO in isopropanol solvent was miscible to all tested solvents while retaining the solubility. Note that DMSO was not miscible with cyclohexane or toluene and caused turbidity. The Br-photoswitch solution was irradiated at 365, 405, 455, 470 and 530 nm for 1 h with fiber-coupled LED at room temperature. The solution was kept on ice in the dark to prevent isopropanol evaporation, thermal relaxation and photoisomerization caused by the ambient light. The spectra were recorded with three concentrations (25, 50 and 75 µM) by diluting the 10 mM stock solution in the target solvent and performing the measurement in a 1-cm-pathlength quartz cuvette. The extinction coefficients were calculated from the gradient for the thee concentrations for each wavelength.

^{1}H-NMR spectra were recorded on a Bruker AVIII 400. The sample concentration was ~ 4.6 mM in d^6-DMSO. Chemical shifts were reported as δ values in ppm. The PSS_E was calculated from the integral of aryl hydrogens as reported previously.

3.10.7 Acid-accelerate thermal relaxation kinetics

The pH-dependent absorbance at 332 nm were determined with plate reader (pH 7.84-2.77) and UV/Vis spectrophotometer (pH 3.08-0.16) due to huge difference in the half-life of the decay. For the plate reader, the pre-irradiated (365 nm, 1 h) Br-photoswitch solution (10 mM in DMSO) was added to the UV-transparent 96-well plate (Greiner) containing buffers (100 µL, 5 mM sodium citrate, 10 mM sodium phosphate and 5 mM CAPS) to a final concentration of 75 µM. The absorbance at 332 nm was measured every 15 seconds for 1.5 h. In the spectrophotometer approach, the stock solution (10 mM in DMSO) was diluted to 75 µM in the 1-cm-pathlength quartz cuvette, and measured with the Chirascan V100. The absorbance at 332 nm was monitored every 40 µs for 20 min. The absorbance curve was fitted to first-order kinetics to extract the thermal relaxation kinetic constants.

3.11 Equations

The pzMe photoisomerization reaction is a reversible bistable conversion between the *E*- and *Z*-states. To describe this first-order-kinetics reaction, we write it conventionally as follows:

$$E \xleftrightarrow{h\nu} Z$$

The reaction rate constants are denoted as $k_{E\rightarrow Z}$ and $k_{Z\rightarrow E}$, which, along with the concentration of *E* and *Z* isomers, describe how fast the concentration of one isomer decreases and the other increases under irradiation. However, from the angle of single-molecule chemistry, a pzMe can only be observed in either *E*- or *Z*-state rather than a superposition of two, and the concentration is no longer valid as there is only one molecule. To analyze this system, we first focus on the *E*→*Z* transition. As shown in **Fig. 1c** in the main text, the photoisomerization of a single (*E*)-pzMe in $(E111C\text{-}pzMe)_1WT_6$ switches to *Z*-state in a short period of time (dwell time) during the irradiation, and the dwell time appears to follow an exponential distribution.

Intuitively, the probability of observing the *E* state, before isomerization takes place, is accumulative over time as follows:

$$dp_E = -p_E * k_{E\to Z} dt \tag{1}$$

Where the p_E is the probability of staying in *E*-state; the $k_{E\to Z}$ is the rate constant, which is interpreted as the probability of *E*→*Z* transition occurring in a unit time dt. Then we integrate equation (1) from time 0 to t, where $p_{E,0}$ is 1 because the transition starts from the *E*-state:

$$\int_{p_{E,0}}^{p_{E,t}} \frac{dp_E}{p_E} = -k_{E\to Z} \int_0^t dt \tag{2}$$

$$p_{E,t} = p_{E,0} e^{-k_{E\to Z} t} = e^{-k_{E\to Z} t} \tag{3}$$

Equation (1.3) describes the probability of staying in *E*-state following an exponential decay over time. Thus, the equation (1.1) can be rewritten as follows to describe the probability of *E*→*Z* transition:

$$-dp_{E,t} = -de^{-k_{E\to Z} t} = k_{E\to Z} e^{-k_{E\to Z} t} dt \tag{4}$$

Since the integral of this transition probability should be unity, it means the *E*→*Z* transition must happen if we wait for infinitely long:

$$\int_0^\infty -dp_{E,t} = \int_0^\infty k_{E\to Z} e^{-k_{E\to Z} t} dt = 1 \tag{5}$$

Moreover, we can calculate the expected value of the time required to observe the transition from the transition distribution, which leads to:

$$\langle \tau_E \rangle = \int_0^\infty t * k_{E\to Z} e^{-k_{E\to Z} t} dt = \frac{1}{k_{E\to Z}} \tag{6}$$

Equation (1.6) shows the expected value of *E*-state dwell time $\langle \tau_E \rangle$ is reciprocal of kinetic constant of *E*→*Z* transition $k_{E\to Z}$. The *Z*-state dwell time $\langle \tau_Z \rangle$ is reciprocal of kinetic constant of *Z*→*E* transition $k_{Z\to E}$, *vice versa*.

$$\langle \tau_Z \rangle = \frac{1}{k_{Z\to E}} \tag{7}$$

3.12 Appendix

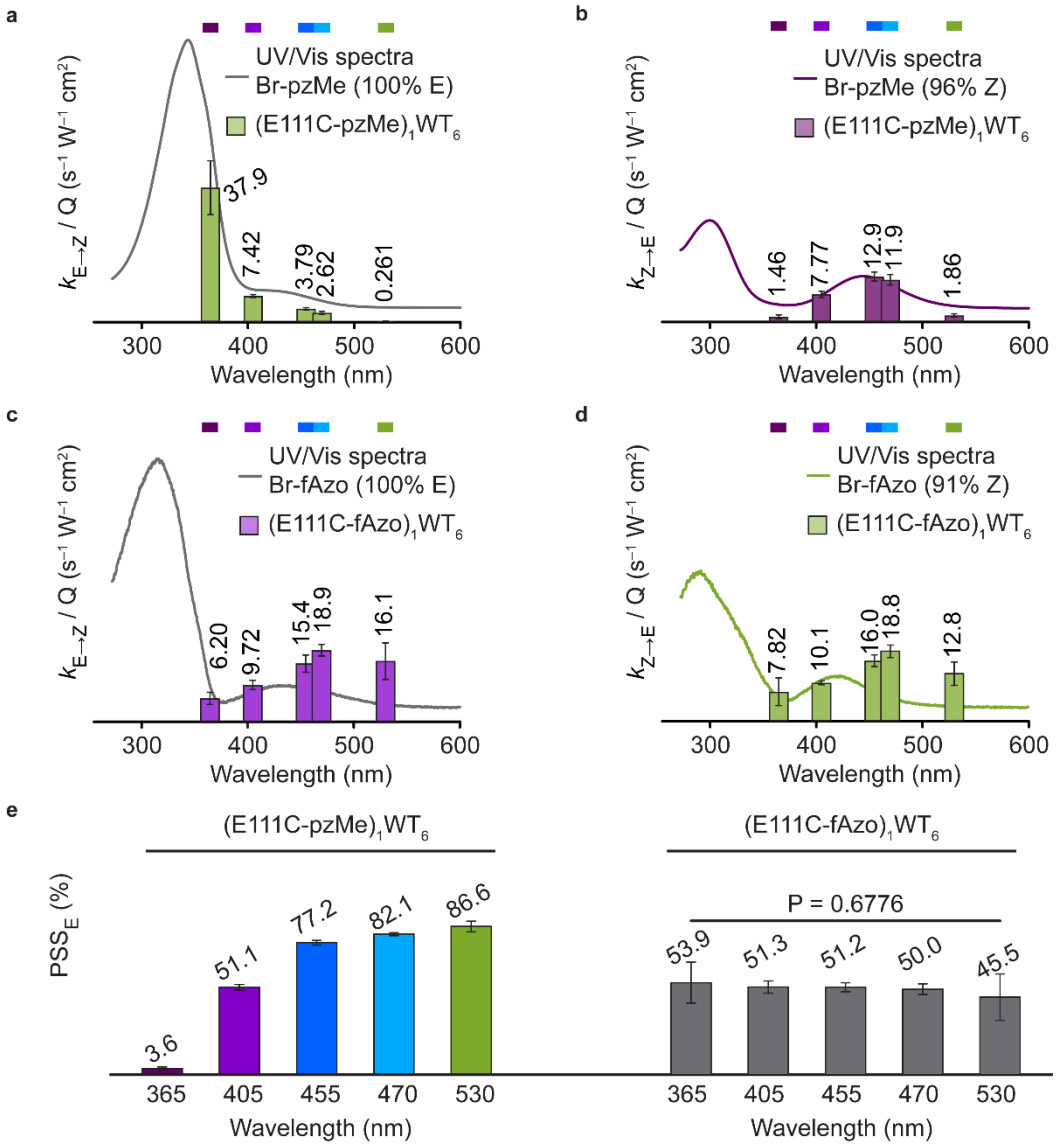


Fig. 24 | Reconstructed (E111C-pzMe)$_1$WT$_6$ and (E111C-fAzo)$_1$WT$_6$ UV/Vis absorption spectra from single-channel stochastic events. a-d, Bar charts of k/Q ratios representing the reconstructed (E111C-pzMe)$_1$WT$_6$ and (E111C-fAzo)$_1$WT$_6$ spectra overlayed onto the reference Br-pzMe or Br-fAzo spectra. In contrast to (E111C-pzMe)$_1$WT$_6$, the (E111C-fAzo)$_1$WT$_6$ showed significant mismatch of spectral line shape to the Br-fAzo. **e,** Wavelength dependence of percent *E*-isomer population at photostationary state (PSS_E). PSS_E of (E111C-pzMe)$_1$WT$_6$ increased at high wavelengths, while (E111C-fAzo)$_1$WT$_6$ remained constant (ANOVA, $F(4/22) = 0.5838$, $p = 0.6776$).

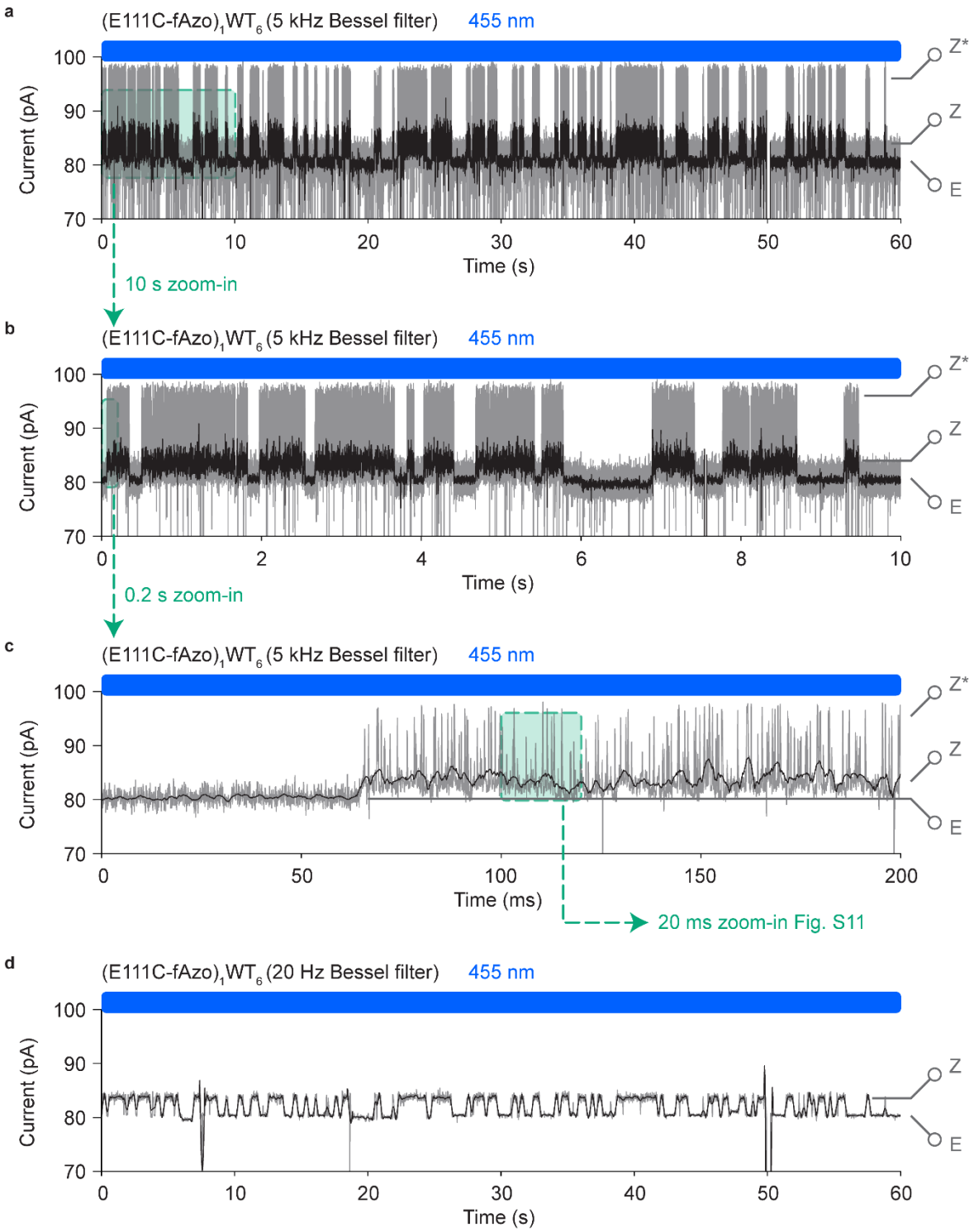


Fig. 25 | Electrical recording of a single (E111C-fAzo)$_1$WT$_6$ heteroheptamer nanopore under continuous 455 nm irradiation. a-c, Recording with 5 kHz Bessel filter at 25 kHz sampling frequency. Each trace is the magnified area in the green box of the previous trace. The rapid interconverting events between *Z* and *Z** levels are magnified in **Fig. 26**. **d,** Recording in panel **a** filtered by 20 Hz Bessel filter. The *Z** level is filtered off and integrated into the *Z* state. The moving averages of the ionic currents (black traces) were generated with a Savitzky–Golay filter (window size = 400 ms), and the raw trace is in grey. Recording condition: 10 mM Tris-HCl pH 8.5, 2 M KCl, 0.1 mM EDTA, 50 mV at room temperature.

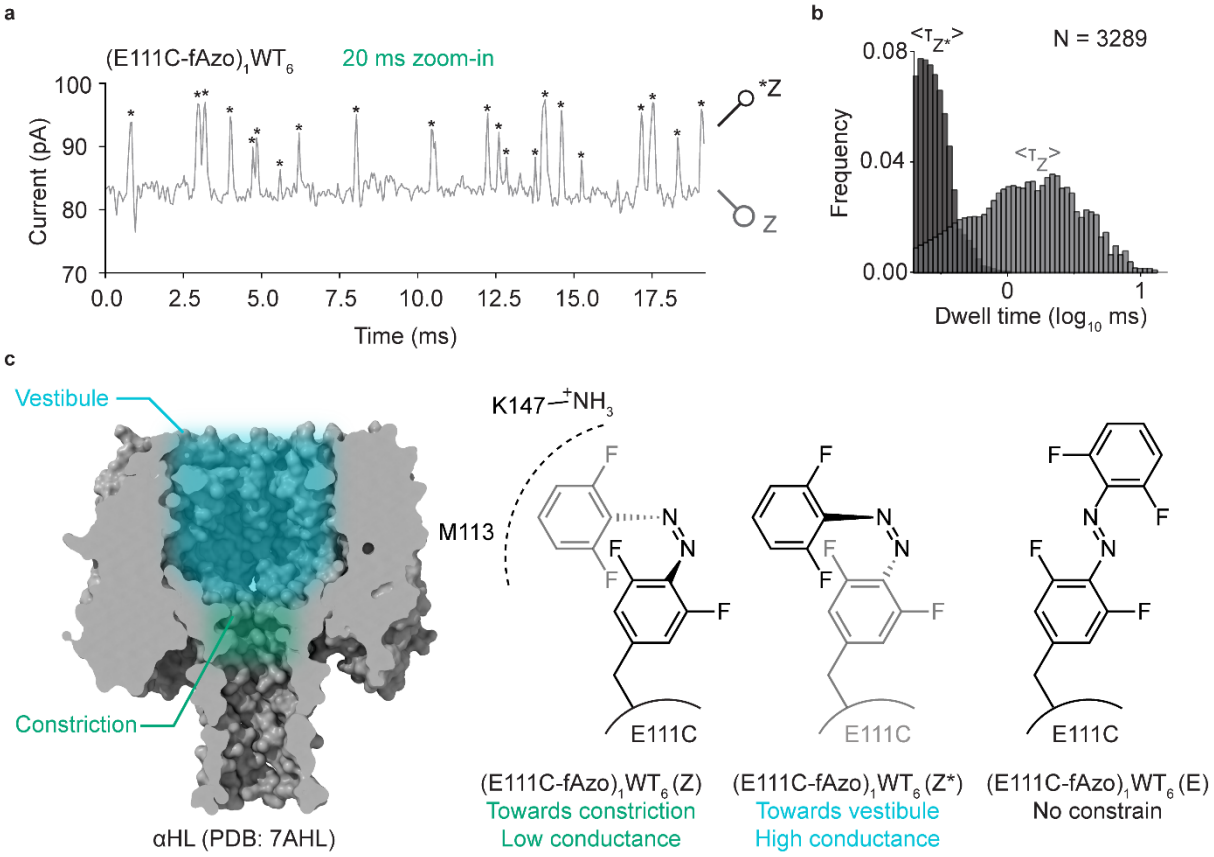


Fig. 26 | Rapid interconversion between *Z* and *Z levels of the (E111C-fAzo)$_1$WT$_6$ *Z* isomer. a,** The magnified 20-millisecond trace under continuous 455 nm irradiation in a *Z*-state (E111C-fAzo)$_1$WT$_6$. These transient events (<1 ms) variated in the current levels, and they were grouped as *Z** level for simplification of analysis. **b,** Dwell time distribution of the *Z* and *Z** levels. **c,** Schematic explanation for the *Z*-*Z** transitions. The E111C modification is at the interface between the vestibule (blue) and constriction (green), where fAzo might interact with the adjacent M113 and K147 residues in the more stabilized *Z* isomer (long dwell time, towards constriction and low conductance) than the *Z** isomer (short dwell time, towards vestibule and high conductance).

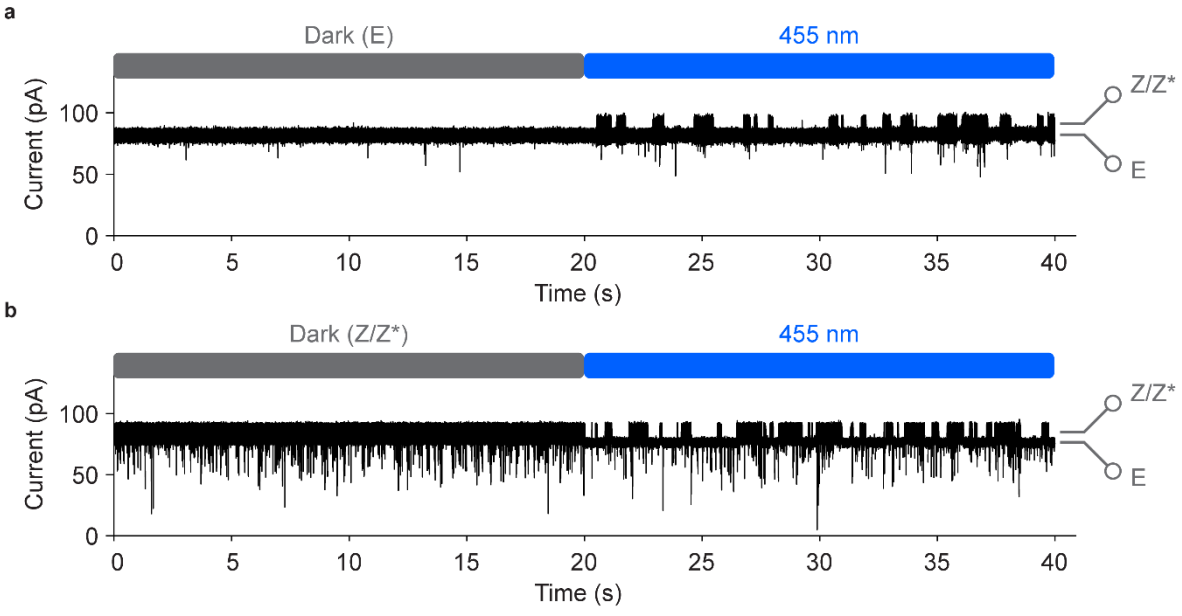


Fig. 27 | Photoswitching of a single (E111C-fAzo)$_1$WT$_6$ heteroheptamer nanopore from the *E*- or *Z*/*Z-state.** Transient interconversion events between *Z*- and Z*-states occurred in the dark. Recording condition: 10 mM Tris-HCl pH 8.5, 2 M KCl, 0.1 mM EDTA, 50 mV at room temperature.

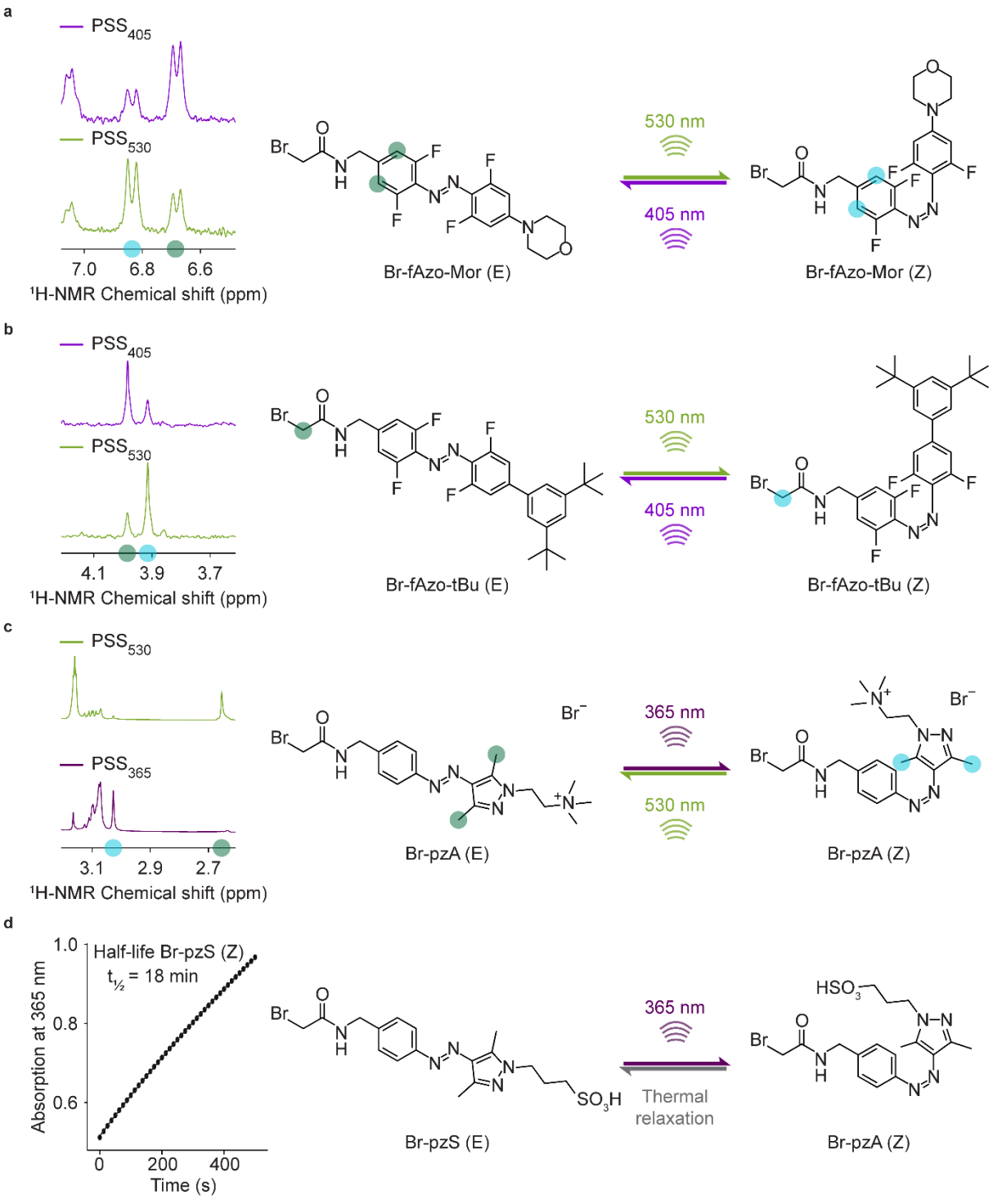


Fig. 28 | ^{1}H-NMR of 3 mM Br-fAzo-Mor, Br-fAzo-tBu, Br-pzA and Br-pzS in *d*$_6$-DMSO at room temperature. The left panel shows the representative chemical shifts used to distinguish and quantify the isomer populations at the photostationary state. The short half-life of Br-pzS (*Z*) prevented the ^{1}H-NMR characterization. The thermal relaxation half-life

was determined by monitoring the absorption at 365 nm in the dark. The right schemes depict the photoisomerization reactions with typical wavelengths used to maximize or minimize the PSS_E. The short half-life in Br-pzS implies an intramolecular acid-mediated relaxation.

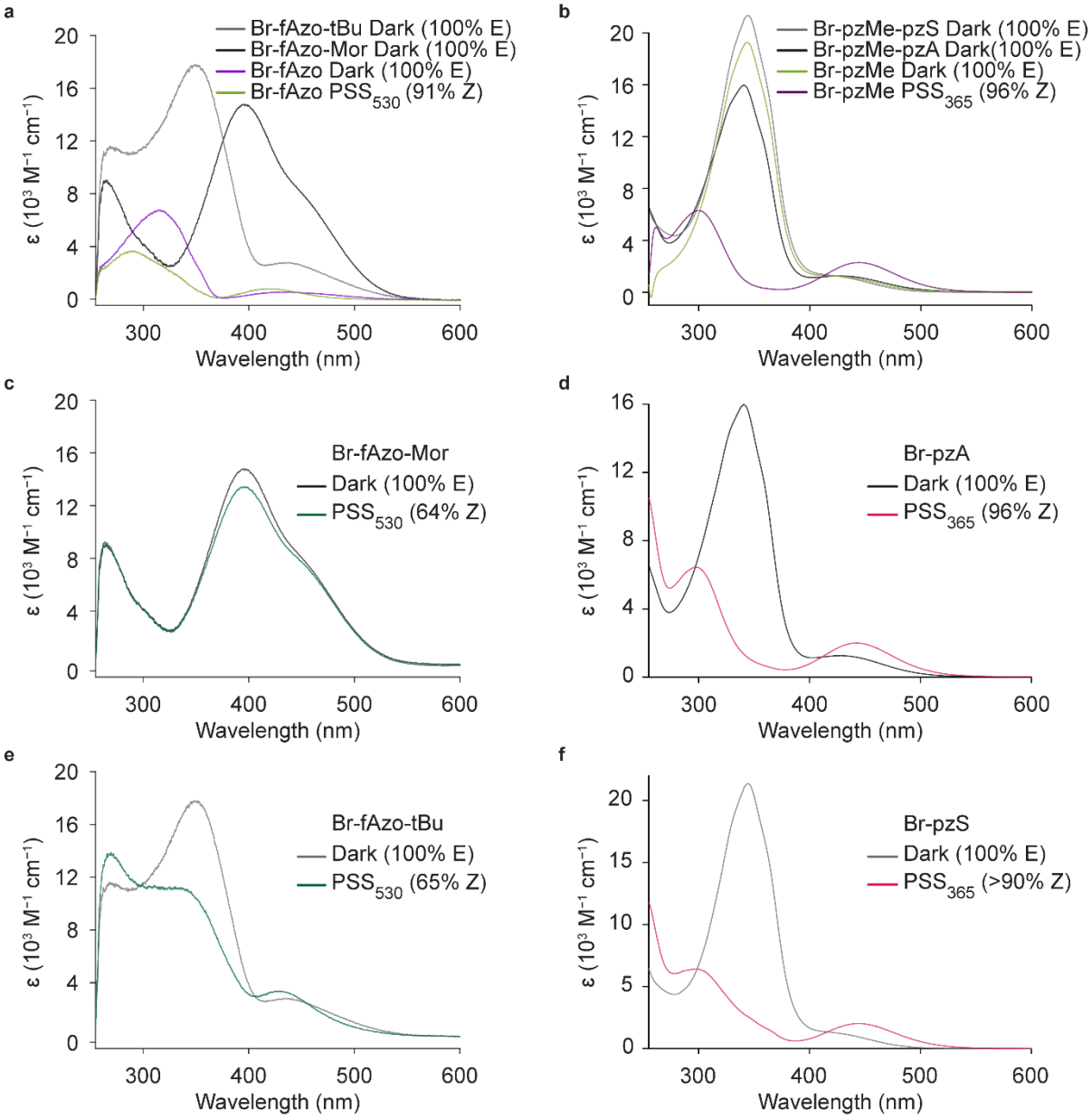


Fig. 29 | UV/Vis spectra of 3 mM Br-fAzo-Mor, Br-fAzo-tBu, Br-pzA and Br-pzS in DMSO. *E* isomers of the listed compounds were prepared by heating the sample in the dark. The photostationary state of the sample was prepared by continuous irradiation at the wavelength that theoretically generates the highest population of *Z* isomer (530 nm for fAzo derivatives and 365 nm for pzMe derivatives). The Br-fAzo (*E*) derivatives deviated from the Br-fAzo absorption spectra significantly in panel **a**, while Br-pzMe (*E*) derivatives were resilient to substitution at the 1*H*-nitrogen.

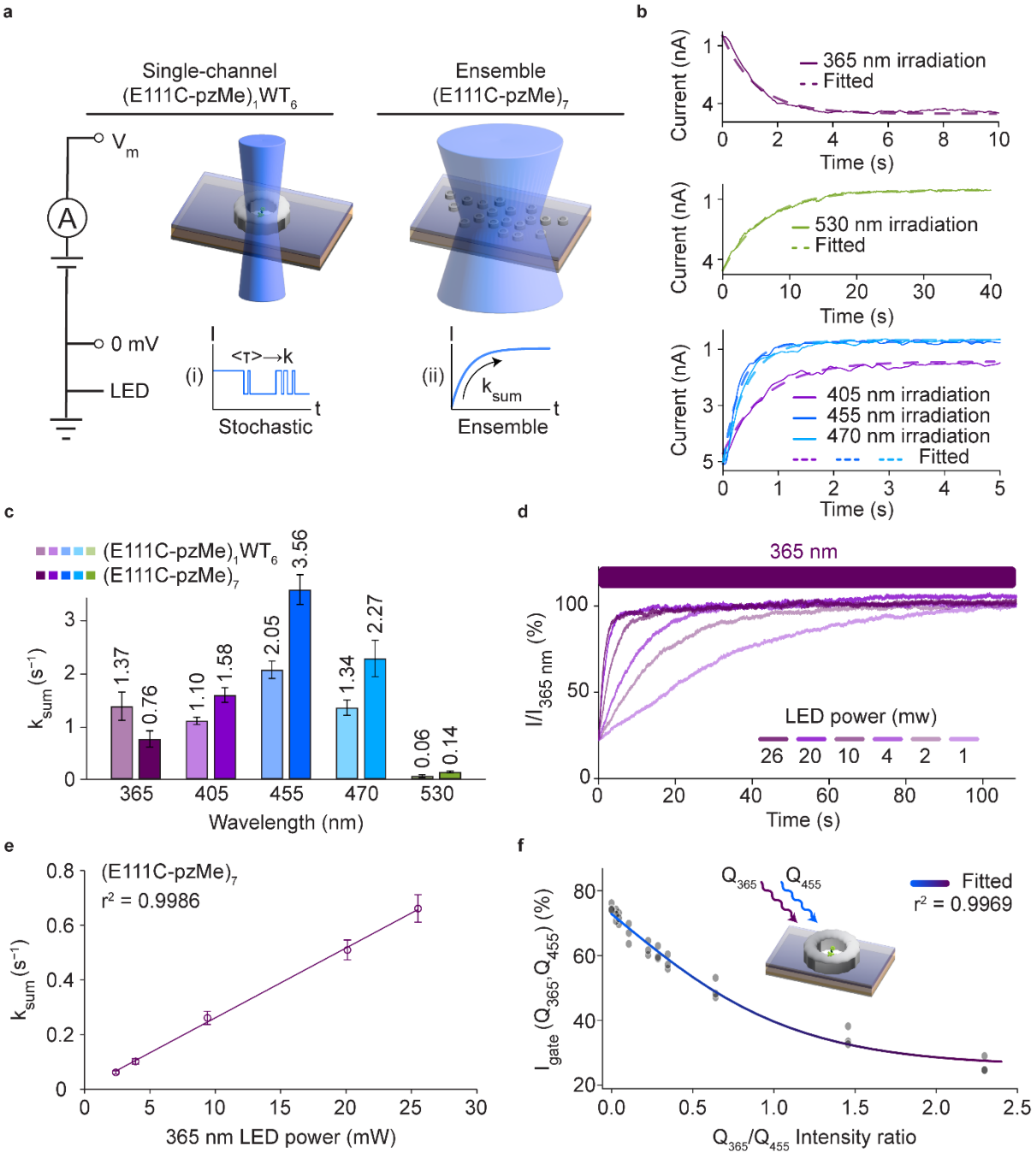


Fig. 30 | Ensemble photoisomerization kinetics characterization with (E111C-pzMe)$_7$. **a,** Difference between the single-channel (E111C-pzMe)$_1$WT$_6$ stochastic sensing and ensemble (E111C-pzMe)$_7$ sensing. The former computes the dwell time and kinetics from the stochastic events, while the latter fit the curve of current transition to extract summed kinetics ($k_{sum} = k_{E\rightarrow Z} + k_{Z\rightarrow E}$). **b,** Fitted current of *E*→*Z* (365 nm) and *Z*→*E* (530, 405, 455 and 470 nm) transitions. **c,** Summed kinetic constants of (E111C-pzMe)$_1$WT$_6$ and (E111C-pzMe)$_7$. The sum of (E111C-pzMe)$_1$WT$_6$ kinetics (light color) is calculated from **Table. 2**, and the (E111C-pzMe)$_7$ kinetics is from the fitted model. **d-e,** Transition kinetics linearly correlated to the light intensity. **f,** Dual-wavelength control of PSS_E. Mixed 365 and 455 nm intensity (Q365 and Q455) follows a hyperbolic relationship to the current level relative to that in the PSS_{365}.

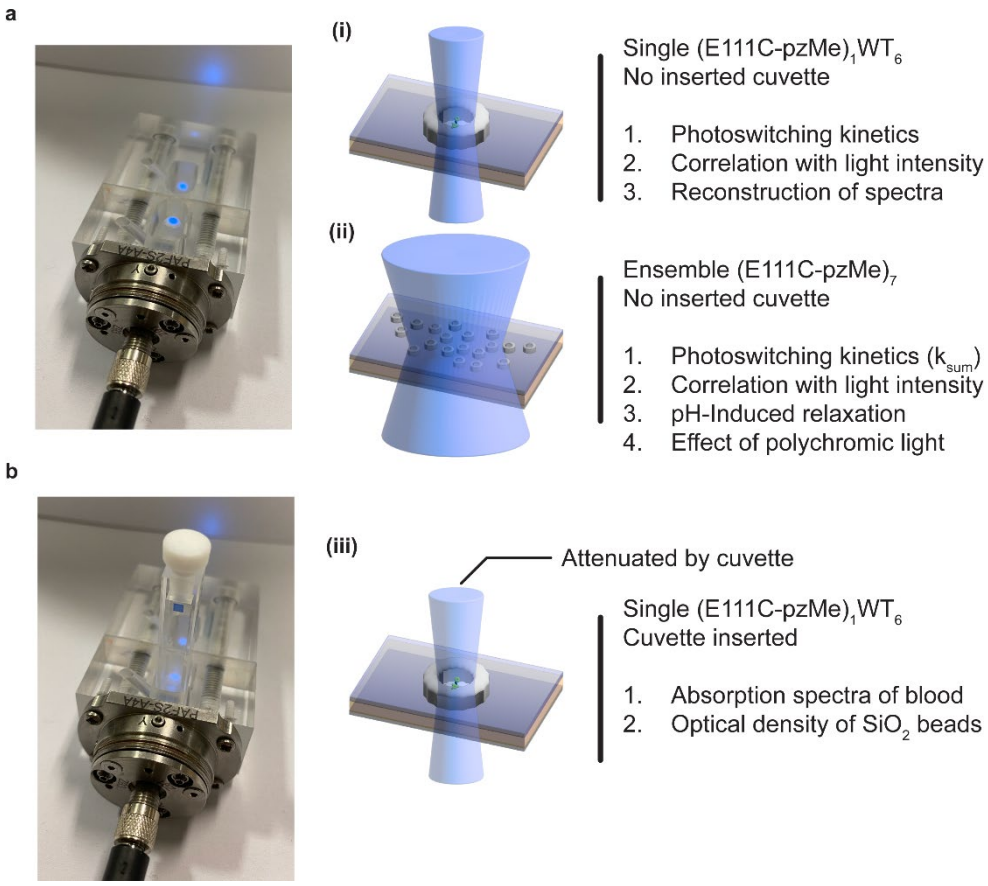


Fig. 31 | Three experimental setups for the versatile electrical recording chamber with and without sample cuvette. a, Recording without sample cuvette. **(i)** With a single $(E111C\text{-}pzMe)_1WT_6$. **(ii)** With multiple $(E111C\text{-}pzMe)_7$. **b,** Recording with a sample cuvette attenuating the light intensity projected to the photopore. **(iii)** With a single $(E111C\text{-}pzMe)_1WT_6$: the transmittance of the sample could be derived from the stochastic events.

Chapter 4

Conclusions and outlook

From the story of a big soup (chapter 1) to a photopore (chapter 2) and further to the nanopore-based single-molecule spectroscopy (chapter 3), this thesis presented how photoresponsive nanopore was designed, produced and characterized. Equipped with this nanoscale photoswitchable protein, precise spatiotemporal control of transmembrane communication could facilitate studies in synthetic biology[47,108], neuroscience[100,107] and bioelectronics[17].

We covalently modified pore-forming toxin αHL with azo photoswitches, including methylarylazopyrozole (pzMe), arylazopyrazole (pzH) and ortho-fluoroazobenzene (fAzo)[59,63]. The photopores switched between ON and OFF states by irradiating them with UV and green light, respectively. The orthogonal wavelengths of irradiation enabled reversible and quantitative switching. This tool was not developed to compete with the mature field of optogenetics[13], but as an alternative bottom-up approach to build models of synthetic biological systems *in vitro*.

In chapter 1, we started with an easy-to-read story explaining the central role of compartmentalization and transmembrane communication in synthetic biology. The photopore is particularly interesting to these applications where the spatiotemporal trigger of biological function is crucial. The researchers need to know when the reaction of interest starts and ends. Considering a synthetic biological applicationm using ion gradient as an energy source or trigger, the photopore is an ideal light-controlled tool for the following reasons.

1. Photopore is easy and cheap to produce and purify in milligram quantities for *in vitro* applications.

2. Photopore relies on azo photoswitches that determine its customizable photochemical property. In particular, the absorption spectrum, photostationary states, thermal relaxation, sensitivity to pH, sensitivity to reducing reagent and channel-ion selectivity can all be tuned by manipulating the photoswitch structure[62].

3. Compared to the complicated multi-state mechanism[152] of the retinal chromophore of optogenetics, the photoswitching in the photopore only has ON/OFF (*Z/E*) states. So, the behavior of photopore is straightforward to be fine-tuned and analyzed.

4. Unlike most optogenetics tools that require constant irradiation that potentially causes photo- or thermal- damage to synthetic tissue, it takes 10 days[32] for an ON-state photopore to thermal relax to the OFF state in theory, and indirectly improves the photosensitivity[21].

5. To the author's knowledge, photopore, with a defined and characterizable number of photoswitches, is the first photoreversible biological nanopore that reduces ionic current by 95% when switching from the ON state to the OFF state. This claim is limited to such pores with defined and characterizable number of photoswitch because some literature reported quantitative ON-OFF switching in solid-state nanopore[84] or metal-organic-framework[85], where the whole lumen of the nanopore is covered and crowded by countless photoswitches.

After filtering the azo photoswitches of low PSS or short lifetime out, we summarized eleven promising photoswitches in chapter 1. Interestingly, the reader might immediately realize that fAzo and pzH showed poor current gating efficiency in chapter 2, which implied that the theoretical photochemical properties of the photoswitch, such as PSS, were not the only decisive factors for the experimental photopore performance. Chapter 3 also supported the observation of the poor performance of pzH and fAzo from the angle of single-molecule kinetics. The pzH and fAzo were found to have barely quantitative switching at the single-molecule level in the confinement of the nanopore. Factors contributing to this observation included photoswitch size, shape, charge, rigidity and conformational preference. In other words, the ionic current was a function of the population of *E/Z* isomers and the individual contribution to the ionic current. The connectivity network shown in chapter 2 confirmed that each *E/Z* isomer in the seven photoswitches in a homoheptamer contributed unevenly. The first photoswitching from the all-*Z* state could reduce the current from 64 pA to 33 pA, while the final photoswitching to the all-*E* state might only reduce the current from 3.2 pA to 1.6 pA. Finally, in chapter 1, we also discussed the contribution of αHL mutation sites. The location of the photoswitch conjugation site in the β barrel of αHL influenced the current gating performance as well. αHL was chosen as the model pore for its well-characterized crystal structure and robustness for modifications.

In chapter 2, homoheptameric photopore $(E111C\text{-}pzMe)_7$ fulfilled most of the requirements proposed for an ideal photopore except for the remaining issues of voltage-dependent directionality, marginal current leakage and red-light absorption. By ON-OFF switching, the photopore exhibited a reversible current change of as much as 95% of the ON-state current. Notably, the photopore in the OFF-state showed unexpected diode-like behavior. In this diode mode, a voltage-dependent rectification ratio of >5 was achieved with direct or alternating voltage up to 200 mV. Since all tested and proposed azo photoswitches in chapter 1 were neutral, the origin of the diode-like behavior was controversial. A promising explanation was ascribed to electroosmosis, as the $(E111C\text{-}pzMe)_7$ was an anion-selective pore. The permeability of $(E111C\text{-}pzMe)_7$ to chloride was seven times as much as potassium, according to reversal potential measurement.

Unlike conventional electronic phototransistors with intensity-dependent photoelectric responses, the photopores regulated current output solely based on the wavelength(s) of monochromatic or dual-wavelength irradiation. However, the rate or kinetics of photoresponse still depends on the light intensity. This dependence was qualitatively analyzed in chapter 2 by fitting an exponential curve to the first few minutes of current transition in $(E111C\text{-}pzMe)_7$ during irradiation. Meanwhile, the quantitative analysis was characterized in chapter 3 with $(E111C\text{-}pzMe)_1WT_6$ photopore, which allowed fitting of an Markovian model to the binary photoswitching events of a single azo photoswitch. These two results lead to similar conclusions that photopore responds to commercially available fiber-coupled LED in few seconds under 365 or 455 nm irradiation, and in few minutes under 530 nm irradiation. The characterization of wavelength and intensity dependence lead to the use of dual- or multi- wavelength irradiation at different intensity ratios.

The dual-wavelength irradiation shown in chapter 2 allowed graded adjustment of ensemble photopore conductance. We demonstrated this principle through remote signal transmission of transmembrane ionic current. Photonic signals encoded with Morse code or pixel art were converted into transmembrane ionic flow, and detected by the Ag/AgCl electrodes. The recorded current trace were digitized as bits of information to recover the encoded message. Although the bit rate of information transmission was merely 20 seconds per bit, it could be maximized to <2 seconds

per bit with the LED used in this research. The underlying limiting factor of the maximum signal transmission rate or current response to irradiation was the molar extinction coefficient of photoswitch in the nanopore, as detailed in the chapter 3. By using these properties, photonic signals encoding text or graphic messages were converted into ionic signals, highlighting the potential applications of photopores as components of smart devices in synthetic biology. The photopores described in chapter 2 differed from previously described photoregulated nanopores in two aspects. First, the azo photoswitches reversibly controlled the geometry and charge distribution of the nanopore constriction, which synergistically determined the transmembrane ionic flow. In contrast, previous studies mostly relied on controlling the nanopore by allosteric conformational changes[55,87] or by inhibition of nanopore formation[53,153]. Second, the OFF-state (E111C-pzMe)$_7$ exhibited diode-like current-voltage response curve. In the diode mode, there was no delay in the rectification of (E111C-pzMe)$_7$ after the reversal of the polarity of the applied potential, in contrast to the previous (non-photoswitchable) arginine-rich αHL diode[44] that collapsed due to significant conformational change.

In the future, we potentially expand the concept of light-to-ionic current signalling and construct artificial retina. In human eyes, Visual phototransduction contains four types of photoreceptor cells, namely the blue cones (420 nm), rods (498 nm), green cones (534 nm) and red cones (564 nm)[100]. Each photoreceptor absorbs light according to its absorption spectrum and triggers a change in membrane potential. The mechanistic and applicational similarity between photopore and photoreceptor cells lays the foundation for creating an artificial system for vision reconstruction. Previous work in our group attempted to use droplet-hydrogel-bilayer bio-pixels to detect monochromic 530 nm light[108].

Another promising direction of photopore is to move from the ions to molecules. The transmembrane communication covers a broader range of molecules such as energy molecules, enzyme cofactors, ligands, peptides, nucleotides, etc. The photopores might be incorporated into 3D-printed synthetic tissue[51], as mentioned in chapter 1, to control the translocation of the molecules impermeable to the lipid bilayer. Again, the spatiotemporal control is the key, and the (E111C-pzMe)$_7$ reported in chapter 2 is naturally a good starting point. Successful application of

photopore in synthetic tissue could mediate the development of drug delivery[82], shape change[109], propelling motions[110] and eventually chemotaxis[47]. We further envisage the development of additional photopores by the conjugation protocol reported here to gain control over additional properties, such as enhanced ion selectivity, reversed ion selectivity, or *E/Z*-dependent ion selectivity.

In chapter 3, a heteroheptamer photopore $(E111C\text{-}pzMe)_1WT_6$ was used as a 'nanocuvette' to characterize the single-arylazopyrazole photoswitching kinetics in the confinement of the photopore. Unlike the complicated seven-photoswitch reaction network of homoheptamer $(E111C\text{-}pzMe)_7$ in chapter 2, the heteroheptamer pore simplified the ionic current change to binary *E/Z* states. The change in size, shape, charge and conformation at the photoswitchable constriction could be monitored by ionic current. Because the lifetime of these binary-current events was determined by the molar extinction coefficient of the photoswitch, and the absorption spectrum of a chromophore consisted of the extinction coefficient at a range of wavelengths, the first single-molecule spectrum of nonfluorescent photoswitch in room-temperature aqueous solution was determined.

Compared to the first single-molecule excitation spectrum of pentacene, which was measured in a cryogenic solid matrix in 1989[120], optical studies of single molecules have been hindered by the sensitivity of photodetector and the molecules of interest was limited to highly fluorescent dyes immobilized on polymer matrices. Our indirect measurement of the excitation spectrum of a arylazopyrazole photoswitch circumvented the difficulty of measuring the absorption of a single photon or deciphering complicated interference patterns by nanopore recording. Instead of detecting light transmission or emission, the photoisomerization events of an arylazopyrazole tethered in a nanopore were measured through the photoresponsive nanopore conductance. Nanopore-based 'nanocuvette' enabled spectral characterization of '100%' *Z*-arylazopyrazole, which was not feasible for direct measurement in conventional methodology.

Solvatochromism[154] and nanoconfinement[69] alter the absorption maxima of azo compound. Thus, we compared the single-molecule excitation maxima of $(E111C\text{-}pzMe)_1WT_6$ to the absorption peak of pzMe in ten solvents ranging from low to high polarizability. While *E* isomer excitation peak was almost invariable, the *Z* isomer

indeed showed solvent dependence. The surroundings of the conjugated pzMe at E111C position provided a water-like environment for the *E* isomer, while the *Z* isomer behaves as if in carbon disulfide. To enhance the quantitative switching, the photoswitch in confinement like (E111C-pzMe)1WT6, the active site of drug target, and matrix of polymer should be treated as a unique polarizable environment rather than assuming similar behavior in bulk solvent. Additionally, we also detected the acid-accelerated thermal relaxation and azonium photoisomerization, which elucidated the pH dependence of pzMe and broadened the application scope of pzMe photopores.

Based on the single-molecule excitation spectrum of $(E111C\text{-}pzMe)_1WT_6$, we incorporated the nanopore as a photodetector into a minimum functional spectrophotometer repurposed from the nanopore-recording device. The goal of this proof-of-concept application was to demonstrate the promise of integrating single-molecule electronics into optical systems. Here, we circumvented the need for a complicated amplification system and detected the intensity completely depending on the frequency of events. This could catalyze the development of future single-molecule-based devices.

In the future, we potentially characterize more photoswitches in the 'nanocuvette' photopore, including spiropyran, diarylethene, fulgide, hydrazone and thioindigo, as long as they can be conjugated onto the E111C nanopore. It is also interesting to study the influence of conjugation positions ranging from E111 to T129. As mentioned in chapter 2, the E111C was the only position causing the 95% current change. For comparison, $(T115C\text{-}pzMe)_7$ reduced current by 61% and $(T129C\text{-}pzMe)_7$ reduced it by 47%. It was questionable how much contribution was due to the change of the PSS influenced by the nanopore environment, and how much was caused by the unitary current-change contribution by each photoswitch. Beyond the pzMe and pzH, potential alternative analytes by SMS could include any molecules causing conformational change under irradiation. For instance, the K/L isomerization[151] of rhodamine dyes for super-resolution microscopy might be studied in the pore. However, the nanopore-based SMS was limited by the events sampling rate (50 kHz), residual current of photoswitching events, amount of data to determine the kinetics (> 50 events) and wavelengths of LEDs.

Here, we propose three interesting follow-up experiments or case studies that might expand the scope of both chapter 2 and chapter 3 in the future.

4.1 Case study 1 : Photopore in the droplet network

As the title of chapter 2 promised, the photopore should be applied in synthetic biological systems such as 3D-printed droplet networks. However, the characterization and demonstration of photopore $(E111C\text{-}pzMe)_7$ were only on the planar lipid bilayer that generally had higher membrane stability under a voltage above 100 mV. A trial of photopore synthetic tissue was designed to contain a linear chain of six droplets (**Fig. 1a-b**). When the six droplets contained no nanopore, the lipid bilayer was considered as a capacitor. Insertion of photopores from both sides of the bilayers formed a light-controlled potentiometer-like conducting path in the network. If a junction of two droplets containing photopores were only in one of the two droplets, the photopore would be inserted unidirectionally, behaving as a diode in the OFF state. Finally, a train of droplets with wildtype αHL behaved like a resistor. Due to the limitation of the droplet printer, we simplified the experiment by printing an 8 × 8 × 8 droplet network contains photopore droplets only (**Fig. 1c-d**). By connecting two Ag/AgCl electrodes to the two sides of the network, we obtained the electrical recording of reversible photoresponse (**Fig. 1e**).

However, this trial experiment raised a few challenges. First, the light scattered in the droplet network. Although a solution with a matched refraction index (solution/lipid/oil) was developed by the author, droplets became too viscous to be printed; and the droplets were invisible after printing. Second, the Ag/AgCl electrodes generate photocurrent under 365-530 nm irradiation. Although the author also invented a carbon-doped agarose to block the light, the carbon seemed to absorb organic molecules such as dye and quench the dye. Finally, in some trial experiments of photopore diode junctions, the network behaved as an electrical oscillator that overwhelmed the diode behavior. Thus, this case study was not further pursued in this thesis. In the future, the author hopes someone can tackle these challenges and demonstrate the useful application of photopore in synthetic tissue.

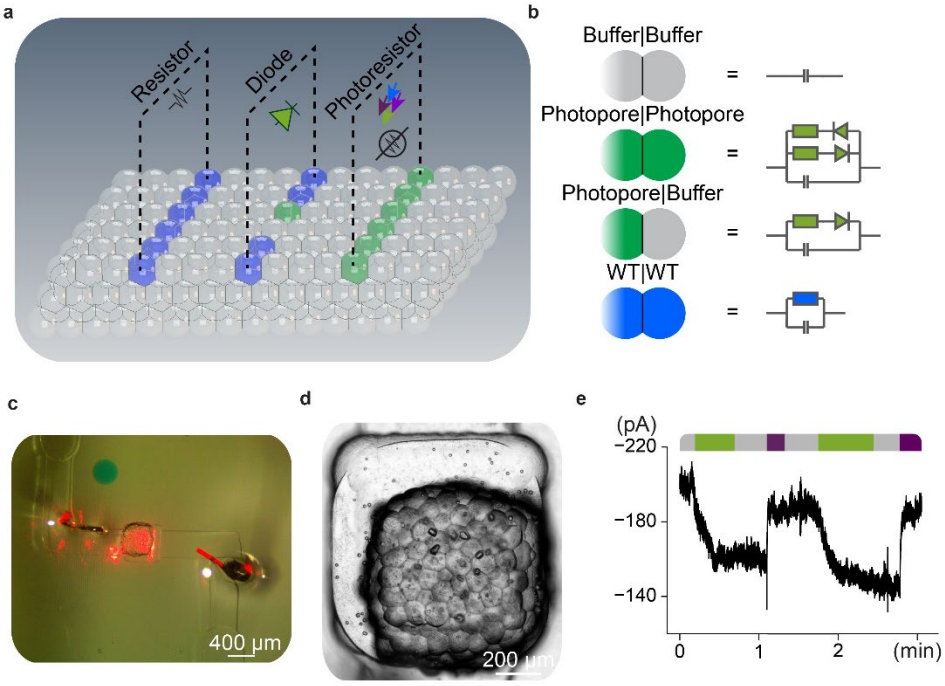


Fig. 1 | Photopore in a droplet network. a, Schematics of a modular droplet network. In theory, the nanopore compositions on the lipid bilayers change the transmembrane electrical properties. The colors of droplets are for illustrative purposes. **b,** Equivalent circuit of the droplet interfaces. **c,** Droplet network under 640 nm irradiation. The 8 × 8 × 8 droplet network contains photopore droplets and is characterized by electrical recording. **d,** A bright field image of the droplet network. **e,** ON-OFF photoswitching of photopores in the droplet network. This network shown in **d** was made from photopore droplets only.

4.2 Case study 2 : Illumination setup for the photopore droplet network

Following up on case study 1, the light path of illumination through the oil chamber and droplet was an interesting subject to model and simulate. Initially, vertical irradiation from the bottom of the droplet was applied, but no photoresponse of photopore droplets was observed. As the light path simulated in **Fig. 2a**, only a neglectable amount of the light passed through the droplet interface bilayer (DIB). For most photocontrolled droplet systems where water-soluble protein was located in the vast aqueous solution in the droplet[11,17], it was not an issue to have low light intensity on the membrane. However, in this case, the assembled photopores that controlled the ionic current were only present on the membrane. The author's solution to this problem was to use a plano-convex lens to focus a 30~40° angled light on the bilayer (**Fig. 2b-c**). The angle was determined by observing the diameter change of the round light spot from a vertical irradiation source to the elliptic spot from the angled irradiation (**Fig. 2d**). With the angle irradiation, the next problem was how to confirm that the light spot was aimed at the lipid bilayer. Since the droplet was transparent, the observable light spot on the droplet was often not indicative of whether the bilayer was irradiated. Instead, the light spot was a projection at the bottom of the PMMA chamber after all diffractions and scattering. The author developed a 'Spear-Fishing' method to tackle this problem. First, two Cyanine 5 labelled droplets were placed ~0.5 mm away from the bilayer of interest (**Fig. 2e**). Then 640 nm irradiation allowed us to observe the fluorescence of these Cyanine 5 droplets through stereoscope with a home-made 660 nm filter. Adjusting the irradiation field between the upper and lower limits to see the fluorescence, we managed to align the light spot right at the center of the bilayer (**Fig. 2f-g**). This was the critical step in observing the photoresponse in case study 1. Future work on this part will be development of a whole photonic illumination system that can be pre-calibrated for this purpose. New PMMA chamber could be designed to have permanent fluorescent references, such as gridlines or dots, for more efficient 'Spear-Fishing'.

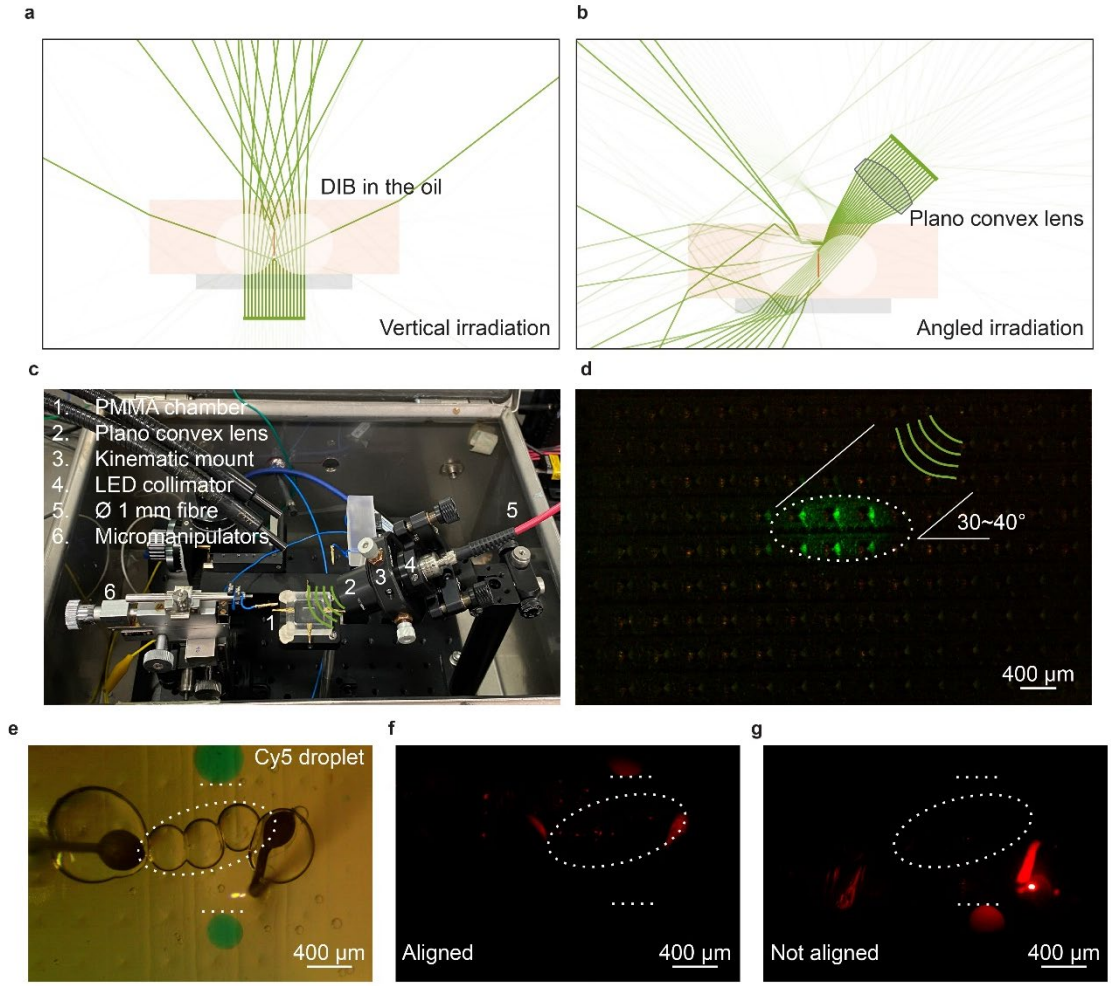


Fig. 2 | Angled illumination setup for the droplets. a, Droplet-interface bilayer (DIB) under vertical irradiation. Due to the refractive index (RI) difference between the oil (orange), and droplet (white), the beam had only a marginal cross-section with the DIB where pores inserted. **b,** DIB under angled irradiation. With a plano-convex lens focusing on an angled beam, the light was focused and maximized on the bilayer. **c,** Experimental setup in a Faraday cage. **d,** Angled illumination on the PMMA chamber in **c**. The angle was estimated from the elliptic light spot. **e-g.** Alignment of beam spot to the droplets. Due to refraction, the light spot requires alignment to maximize the cross-section between the beam and membrane. With a 640 nm LED excitation and 660 nm emission filter on the stereomicroscope, the beam position can be estimated with the two sulfo-Cyanine 5 reference droplets. The white dashed circle shows where the droplets are.

4.3 Case study 3 : A ‘nanodrop’ based on single-molecule photosensor

In chapter 3, the heteroheptamer pore $(E111C\text{-}pzMe)_1WT_6$ was introduced as a ‘nanocuvette’ to study single-molecule photoswitching, and led to the concept of single-molecule excitation spectroscopy. However, a primitive idea that the author proposed was to use the photopore as a new type of photosensor to determine the light wavelength and intensity simultaneously, provided that the incident light was

monochromic. Compared to the dominating market share of the p-n junction type of photosensors, the primary strengths of stochastic light sensor includes its unique p-n junction free mechanism, ease of fabrication, biocompatibility and versatility. The p-n junction free stochastic photosensing analyzes the wavelength and light intensity of a monochromic light ranging from 365 to 530 nm by a single-step statistical analysis without the necessity of prisms or spectral filters. Operating a photopore was significantly simpler and biocompatible in an aqueous solution of physiological pH and at room temperature. In contrast, other single-molecule stochastic methods such as molecular junction[58,155] requires AFM and SEM facilities working at ultra-low temperature and vacuum. The $(E111C\text{-}pzMe)_1(WT)_6$ synthesis requires no electron-beam lithography or chemical vapor deposition like conventional p-n junction semiconductors[156]. Moreover, leveraging the halochromic photoisomerization and thermal relaxation enabled the pH-sensing with the same setup, proving the versatility of this stochastic sensing platform. However, it has multiple drawbacks as well. The response time and sensitivity of this sensor is significantly lower than semiconductor photosensors. We might mitigate these by improving extinction coefficient of the photoswitch design[29,62], or use photosensitizer[117].

Protein engineering of the αHL pore with demonstrated tetrafluoroazobenzene and arylazopyrazole derivatives greatly increased the possibility for stochastic photosensing in UV/Vis range, however, near-IR region remains challenging. In chapter 1 and **Fig. 3**, we proposed three alternative azobenzene-based photoswitches[65,66,73] which broadens absorption range to 250-760 nm (**Fig. 3**), despite the organic photodetector could achieve up to 1400 nm[157]. Increased resolution and accuracy of wavelength detection might be realized by multiplexing four different classes of photoswitch with different overlapping absorption range. By inserting them on one membrane, the overall electrical trace could be deconvoluted altogether and yield the estimation of wavelength and kinetics by all pores because the individual events could be classified by its signature residual current. A step further on the four-in-one photosensor design will be assembling them on a conducting planar supports, which is similar to pixels in the CMOS design. Ultimately, arrays of photosensing units could be considered as a flexible artificial retina. Conversely, by housing this unit in a design inspired by nanodrop

spectrophotometer, photopore sensor could be an versatile hybrid of spectrophotometer and a pH sensor for microvolume samples.

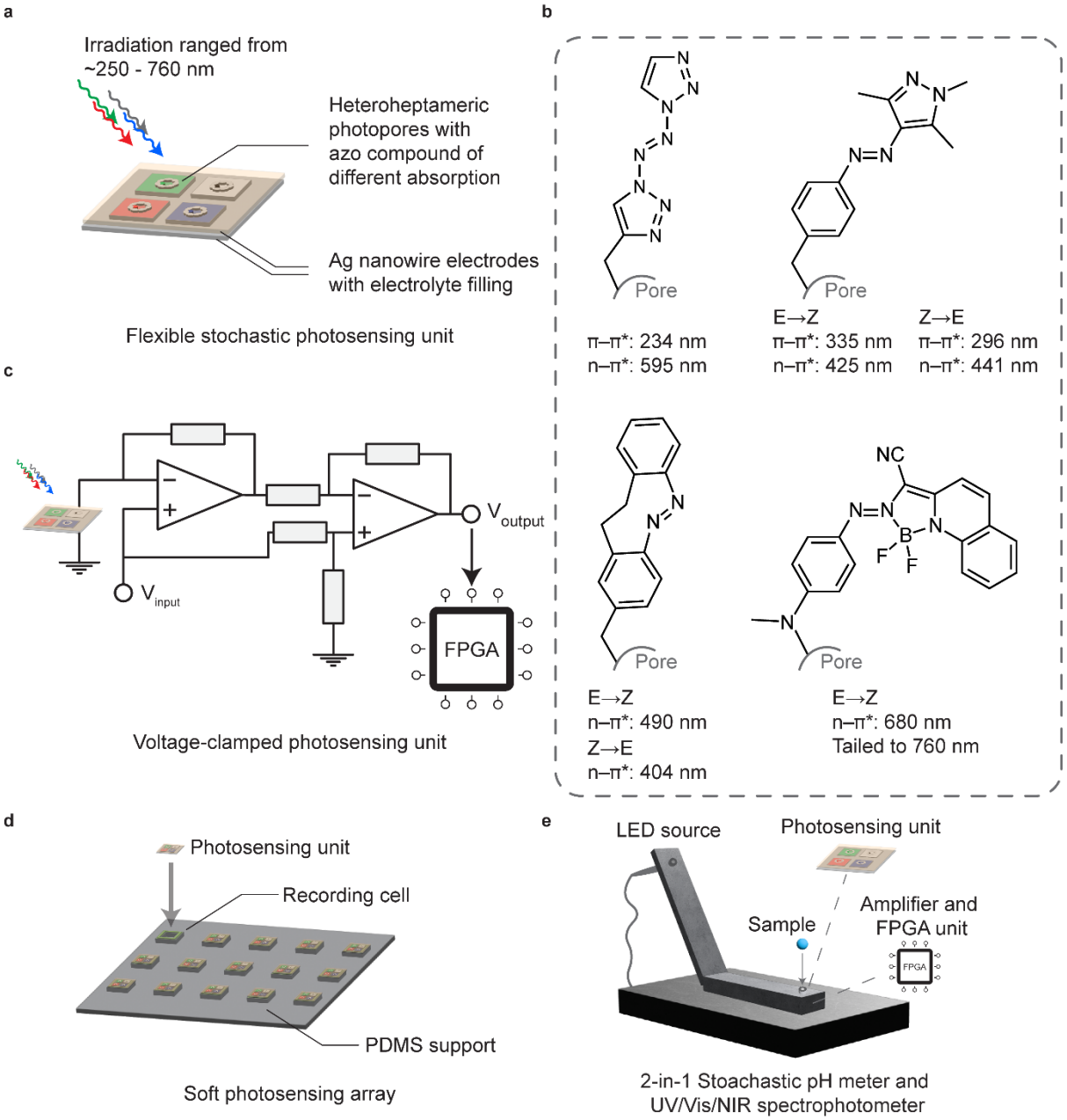


Fig. 3 | Outlook for the photopore stochastic sensor. a, Expansion of detection range by incorporation of multiple photopores. **b,** Proposed azo compound combination that absorbs in the 250-760 nm range. **c,** Photosensing unit functions through voltage clamping. Coupling the amplification electrical circuit with a field programmable gate array (FPGA) might allow rapid analysis of the analyte in place. **d,** An array of photosensing units. With soft PDMS support, this array might serve as a soft CMOS-like material or artificial retina. **e,** A portable imaginary stochastic sensing device that analyses microliter sample absorbance and pH.

References

1. Ward, L. C. Human body composition: yesterday, today, and tomorrow. *European Journal of Clinical Nutrition* **72**, 1201–1207 (2018).
2. Heinz Big Soup Soup - Beef vegetable; chicken vegetable soup; backed potato chunky vegetable MANUFACTURER: H.J. Heinz Co. Ltd. CATEGORY: 070 - Soup. *International Product Alert* vol. 18 at (2001).
3. Hirschi, S., Ward, T. R., Meier, W. P., Müller, D. J. & Fotiadis, D. Synthetic biology: bottom-up assembly of molecular systems. *Chem. Rev.* **122**, 16294–16328 (2022).
4. Gaitzsch, J., Hirschi, S., Freimann, S., Fotiadis, D. & Meier, W. Directed insertion of light-activated proteorhodopsin into asymmetric polymersomes from an ABC block copolymer. *Nano Lett.* **19**, 2503–2508 (2019).
5. Ritzmann, N. *et al.* Fusion domains guide the oriented insertion of light-driven proton pumps into liposomes. *Biophys. J.* **113**, 1181–1186 (2017).
6. Racker, E. & Stoeckenius, W. Reconstitution of purple membrane vesicles catalyzing light driven proton uptake and adenosine triphosphate formation. *J. Biol. Chem.* **249**, 662–663 (1974).
7. Tanner, P. *et al.* Can polymeric vesicles that confine enzymatic reactions act as simplified organelles? *FEBS Letters* **585**, 1699–1706 (2011).
8. Chen, Q., Schönherr, H. & Vancso, G. J. Block-copolymer vesicles as nanoreactors for enzymatic reactions. *Small* **5**, 1436–1445 (2009).
9. Staufer, O., Schröter, M., Platzman, I. & Spatz, J. P. Bottom-up assembly of functional intracellular synthetic organelles by droplet-based microfluidics. *Small* **16**, (2020).
10. Qiu, L. *et al.* Cell membrane-anchored biosensors for real-time monitoring of the cellular microenvironment. *J. Am. Chem. Soc.* **136**, 13090–13093 (2014).
11. Booth, M. J., Schild, V. R., Graham, A. D., Olof, S. N. & Bayley, H. Light-activated communication in synthetic tissues. *Sci. Adv.* **2**, 1–12 (2016).
12. Catterall, W. A. Ion channel voltage sensors: structure, function, and pathophysiology. *Neuron* **67**, 915–928 (2010).
13. Emiliani, V. *et al.* Optogenetics for light control of biological systems. *Nat. Rev. Methods Primers* **2**, 55 (2022).
14. Bollschweiler, D. Study of the archaeal motility system of Halobacterium salinarum by cryo-electron tomography. 1–118 (2015).
15. Gruber, C. *et al.* Halobacterium noricense sp. nov., an archaeal isolate from a bore core of an alpine Permian salt deposit, classification of Halobacterium sp. NRC-1 as

a strain of H. salinarum and emended description of H. salinarum. *Extremophiles* **8**, 431–439 (2004).

16. Berhanu, S., Ueda, T. & Kuruma, Y. Artificial photosynthetic cell producing energy for protein synthesis. *Nat. Commun.* **10**, (2019).
17. Hoskin, C. E. G., Schild, V. R., Vinals, J. & Bayley, H. Parallel transmission in a synthetic nerve. *Nat. Chem.* **14**, 650–657 (2022).
18. Zabelskii, D. *et al.* Structure-based insights into evolution of rhodopsins. *Communications Biology* **4**, (2021).
19. Bada Juarez, J. F. *et al.* Structures of the archaerhodopsin-3 transporter reveal that disordering of internal water networks underpins receptor sensitization. *Nat. Commun.* **12**, 1–10 (2021).
20. Chung, D. Y. *et al.* Determinants of optogenetic cortical spreading depolarizations. *Cerebral Cortex* **29**, 1150–1161 (2019).
21. Gong, X. *et al.* An ultra-sensitive step-function opsin for minimally invasive optogenetic stimulation in mice and macaques. *Neuron* **107**, 38-51.e8 (2020).
22. Wizinger-Aust, R. Peter Griess und seine zeit. *Angew. Chem.* **70**, 199–204 (1958).
23. Alsantali, R. I. *et al.* Miscellaneous azo dyes: a comprehensive review on recent advancements in biological and industrial applications. *Dyes and Pigments* **199**, 110050 (2022).
24. Wainwright, M. & Kristiansen, J. E. On the 75th anniversary of prontosil. *Dyes and Pigments* **88**, 231–234 (2011).
25. HARTLEY, G. S. The cis-form of azobenzene. *Nature* **140**, 281 (1937).
26. Campbell, N., Henderson, A. W. & Taylor, D. Geometrical isomerism of azo-compounds. *Journal of the Chemical Society* 1281–1285 (1953).
27. Bandara, H. M. D. & Burdette, S. C. Photoisomerization in different classes of azobenzene. *Chem. Soc. Rev.* **41**, 1809–1825 (2012).
28. Yu, J. K., Bannwarth, C., Liang, R., Hohenstein, E. G. & Martínez, T. J. Nonadiabatic dynamics simulation of the wavelength-dependent photochemistry of azobenzene excited to the nπ* and ππ* excited states. *J. Am. Chem. Soc.* **142**, 20680–20690 (2020).
29. Jerca, F. A., Jerca, V. V. & Hoogenboom, R. Advances and opportunities in the exciting world of azobenzenes. *Nat. Rev. Chem.* **6**, 51–69 (2021).
30. Fuchter, M. J. On the promise of photopharmacology using photoswitches: a medicinal chemist's perspective. *J. Med. Chem.* **63**, 11436–11447 (2020).
31. Reis, S. A. *et al.* Light-controlled modulation of gene expression by chemical optoepigenetic probes. *Nat. Chem. Biol.* **12**, 317–323 (2016).
32. Weston, C. E., Richardson, R. D., Haycock, P. R., White, A. J. P. & Fuchter, M. J.

Arylazopyrazoles: azoheteroarene photoswitches offering quantitative isomerization and long thermal half-lives. *J. Am. Chem. Soc.* **136**, 11878–11881 (2014).

33. Bléger, D., Schwarz, J., Brouwer, A. M. & Hecht, S. *O*-fluoroazobenzenes as readily synthesized photoswitches offering nearly quantitative two-way isomerization with visible light. *J. Am. Chem. Soc.* **134**, 20597–20600 (2012).
34. Wiseman, G. M. The hemolysins of Staphylococcus aureus. *Bacteriol. Rev.* **39**, 317–344 (1975).
35. Song, L. *et al.* Structure of staphylococcal alpha-hemolysin, a heptameric transmembrane pore. *Science.* **274**, 1859–1865 (1996).
36. HLADKY, S. B. & HAYDON, D. A. Discreteness of conductance change in bimolecular lipid membranes in the presence of certain antibiotics. *Nature* **225**, 451–453 (1970).
37. Bayley, H. & Cremer, P. S. Stochastic sensors inspired by biology. *Nature* **413**, 226–230 (2001).
38. Braha, O. *et al.* Designed protein pores as components for biosensors. *Chem. Biol.* **4**, 497–505 (1997).
39. Steffensen, M. B., Rotem, D. & Bayley, H. Single-molecule analysis of chirality in a multicomponent reaction network. *Nat. Chem.* **6**, 603–607 (2014).
40. Ramsay, W. J. & Bayley, H. Single-molecule determination of the isomers of d-glucose and d-fructose that bind to boronic acids. *Angew. Chem. Int. Ed.* **57**, 2841–2845 (2018).
41. Akeson, M., Branton, D., Kasianowicz, J. J., Brandin, E. & Deamer, D. W. Microsecond time-scale discrimination among polycytidylic acid, polyadenylic acid, and polyuridylic acid as homopolymers or as segments within single RNA molecules. *Biophys. J.* **77**, 3227–3233 (1999).
42. Ying, Y. L. *et al.* Nanopore-based technologies beyond DNA sequencing. *Nat. Nanotechnol.* **17**, 1136–1146 (2022).
43. Harrington, L., Alexander, L. T., Knapp, S. & Bayley, H. Single-molecule protein phosphorylation and dephosphorylation by nanopore enzymology. *ACS Nano* **13**, 633–641 (2019).
44. Maglia, G. *et al.* Droplet networks with incorporated protein diodes show collective properties. *Nat. Nanotechnol.* **4**, 437–440 (2009).
45. Stoddart, D. *et al.* Functional truncated membrane pores. *Proc. Natl. Acad. Sci. U.S.A.* **111**, 2425–2430 (2014).
46. Loudwig, S. & Bayley, H. Photoisomerization of an individual azobenzene molecule in water: an on−off switch triggered by light at a fixed wavelength. *J. Am. Chem. Soc.* **128**, 12404–12405 (2006).

47. Roberts, M. A. J., Cranenburgh, R. M., Stevens, M. P. & Oyston, P. C. F. Synthetic biology: biology by design. *Microbiology (United Kingdom)* **159**, 1219–1220 (2013).
48. Miller, D. M. & Gulbis, J. M. Engineering protocells: prospects for self-assembly and nanoscale production-lines. *Life* **5**, 1019–1053 (2015).
49. Brieke, C., Rohrbach, F., Gottschalk, A., Mayer, G. & Heckel, A. Light-controlled tools. *Angew. Chem. Int. Ed.* **51**, 8446–8476 (2012).
50. Lee, K. Y. *et al.* Photosynthetic artificial organelles sustain and control ATP-dependent reactions in a protocellular system. *Nat. Biotechnol.* **36**, 530–535 (2018).
51. Alcinesio, A. *et al.* Modular synthetic tissues from 3D-printed building blocks. *Adv. Funct. Mater.* **32**, (2022).
52. Booth, M. J., Restrepo Schild, V., Box, S. J. & Bayley, H. Light-patterning of synthetic tissues with single droplet resolution. *Sci. Rep.* **7**, 1–10 (2017).
53. Koçer, A., Walko, M., Meijberg, W. & Feringa, B. L. A light-actuated nanovalve derived from a channel protein. *Science.* **309**, 755–758 (2005).
54. Banghart, M., Borges, K., Isacoff, E., Trauner, D. & Kramer, R. H. Light-activated ion channels for remote control of neuronal firing. *Nat. Neurosci.* **7**, 1381–1386 (2004).
55. Volgraf, M. *et al.* Allosteric control of an ionotropic glutamate receptor with an optical switch. *Nat. Chem. Biol.* **2**, 47–52 (2006).
56. Walker, B. & Bayley, H. Key residues for membrane binding, oligomerization, and pore forming activity of staphylococcal α-hemolysin identified by cysteine scanning mutagenesis and targeted chemical modification. *J. Biol. Chem.* **270**, 23065–23071 (1995).
57. Schelté, P., Boeckler, C., Frisch, B. & Schuber, F. Differential reactivity of maleimide and bromoacetyl functions with thiols: application to the preparation of liposomal diepitope constructs. *Bioconjugate Chem.* **11**, 118–123 (2000).
58. Diez Cabanes, V., Van Dyck, C., Osella, S., Cornil, D. & Cornil, J. Challenges for incorporating optical switchability in organic-based electronic devices. *ACS Appl. Mater. Interfaces* **13**, 27737–27748 (2021).
59. Calbo, J. *et al.* Tuning azoheteroarene photoswitch performance through heteroaryl design. *J. Am. Chem. Soc.* **139**, 1261–1274 (2017).
60. Dang, T. *et al.* Thiazolylazopyrazoles as nonsymmetric bis-heteroaryl azo switches: high-yield visible-light photoisomerization and increased *Z*-isomer stability by O-carbonylation. *Angew. Chem. Int. Ed.* **62**, (2023).
61. Dang, T., Zhang, Z.-Y. & Li, T. Visible-light-activated heteroaryl azoswitches: toward a more colorful future. *J. Am. Chem. Soc.* **146**, 19609–19620 (2024).
62. Crespi, S., Simeth, N. A. & König, B. Heteroaryl azo dyes as molecular photoswitches. *Nat. Rev. Chem.* **3**, 133–146 (2019).

63. Knie, C. *et al. Ortho*-fluoroazobenzenes: visible light switches with very long-lived *Z* isomers. *Chem. - Eur. J.* **20**, 16492–16501 (2014).
64. Dong, M., Babalhavaeji, A., Samanta, S., Beharry, A. A. & Woolley, G. A. Red-shifting azobenzene photoswitches for in vivo use. *Acc. Chem. Res.* **48**, 2662–2670 (2015).
65. Siewertsen, R. *et al.* Highly efficient reversible *Z-E* photoisomerization of a bridged azobenzene with visible light through resolved $S_1(n\pi^*)$ absorption bands. *J. Am. Chem. Soc.* **131**, 15594–15595 (2009).
66. Yang, Y., Hughes, R. P. & Aprahamian, I. Near-infrared light activated azo-BF_2 switches. 4–7 (2014).
67. Medved', M. *et al.* Mechanistic basis for red light switching of azonium ions. *J. Am. Chem. Soc.* **145**, 19894–19902 (2023).
68. Gibson, R. S. L., Calbo, J. & Fuchter, M. J. Chemical *Z* − *E* isomer switching of arylazopyrazoles using acid. *ChemPhotoChem* **3**, 372–377 (2019).
69. Grommet, A. B., Lee, L. M. & Klajn, R. Molecular photoswitching in confined spaces. *Acc. Chem. Res.* (2020) doi:10.1021/acs.accounts.0c00434.
70. Rusu, E., Dorohoi, D. O. & Airinei, A. Solvatochromic effects in the absorption spectra of some azobenzene compounds. *Journal of Molecular Structure* **887**, 216–219 (2008).
71. Fink, M., Stäuble, J., Weisgerber, M. & Carreira, E. M. Aryl azocyclopropeniums: minimalist, visible-light photoswitches. *J. Am. Chem. Soc.* **146**, 9519–9525 (2024).
72. Samanta, S., McCormick, T. M., Schmidt, S. K., Seferos, D. S. & Woolley, G. A. Robust visible light photoswitching with *ortho*-thiol substituted azobenzenes. *Chem. Commun.* **49**, 10314 (2013).
73. Li, Y.-C. *et al.* 1,1′-Azobis-1,2,3-triazole: a high-nitrogen compound with stable N_8 structure and photochromism. *J. Am. Chem. Soc.* **132**, 12172–12173 (2010).
74. Wang, Y., Zhao, Y., Bollas, A., Wang, Y. & Au, K. F. Nanopore sequencing technology, bioinformatics and applications. *Nat. Biotechnol.* **39**, 1348–1365 (2021).
75. Bhakdi, S., Fuessle, R. & Tranum-Jensen, J. Staphylococcal α-toxin: oligomerization of hydrophilic monomers to form amphiphilic hexamers induced through contact with deoxycholate detergent micelles. *Proc. Natl. Acad. Sci. U.S.A.* **78**, 5475–5479 (1982).
76. Ayub, M. & Bayley, H. Engineered transmembrane pores. *Curr. Opin. Chem. Biol.* **34**, 117–126 (2016).
77. Montoya, M. & Gouaux, E. β Barrel membrane protein folding and structure viewed through the lens of α-hemolysin. *Biochim. Biophys. Acta - Biomembr.* **1609**, 19–27 (2003).

78. Hammerstein, A. F., Shin, S.-H. & Bayley, H. Single-molecule kinetics of two-step divalent cation chelation. *Angew. Chem. Int. Ed.* **49**, 5085–5090 (2010).
79. Chang, C., Niblack, B., Walker, B. & Bayley, H. A photogenerated pore-forming protein. *Chem. Biol.* **2**, 391–400 (1995).
80. Borisenko, V., Burns, D. C., Zhang, Z. & Woolley, G. A. Optical switching of ion−dipole interactions in a gramicidin channel analogue. *J. Am. Chem. Soc.* **122**, 6364–6370 (2000).
81. Mutter, N. L., Volarić, J., Szymanski, W., Feringa, B. L. & Maglia, G. Reversible photocontrolled nanopore assembly. *J. Am. Chem. Soc.* **141**, 14356–14363 (2019).
82. Offenbartl-Stiegert, D., Rottensteiner, A., Dorey, A. & Howorka, S. A light-triggered synthetic nanopore for controlling molecular transport across biological membranes. *Angew. Chem. Int. Ed.* **61**, (2022).
83. Hagan, J. T., Gonzalez, A., Shi, Y., Han, G. G. D. & Dwyer, J. R. Photoswitchable binary nanopore conductance and selective electronic detection of single biomolecules under wavelength and voltage polarity control. *ACS Nano* **16**, 5537–5544 (2022).
84. Li, P. *et al.* Light-controlled ion transport through biomimetic DNA-based channels. *Angew. Chem. Int. Ed.* **55**, 15637–15641 (2016).
85. Liu, Y. *et al.* Photo-controllable ion-gated metal-organic framework MIL-53 sub-nanochannels for efficient osmotic energy generation. *ACS Nano* **16**, 16343–16352 (2022).
86. Miedema, H. *et al.* A biological porin engineered into a molecular, nanofluidic diode. *Nano Lett.* **7**, 2886–2891 (2007).
87. Bozovic, O., Jankovic, B. & Hamm, P. Using azobenzene photocontrol to set proteins in motion. *Nat. Rev. Chem.* **6**, 112–124 (2022).
88. Kramer, R. H., Chambers, J. J. & Trauner, D. Photochemical tools for remote control of ion channels in excitable cells. *Nat. Chem. Biol.* **1**, 360–365 (2005).
89. Vriens, J., Nilius, B. & Voets, T. Peripheral thermosensation in mammals. *Nat. Rev. Neurosci.* **15**, 573–589 (2014).
90. Huang, H., Delikanli, S., Zeng, H., Ferkey, D. M. & Pralle, A. Remote control of ion channels and neurons through magnetic-field heating of nanoparticles. *Nat. Nanotechnol.* **5**, 602–606 (2010).
91. Ankenbruck, N., Courtney, T., Naro, Y. & Deiters, A. Optochemical control of biological processes in cells and animals. *Angew. Chem. Int. Ed.* **57**, 2768–2798 (2018).
92. SzymaŃski, W., Yilmaz, D., Koçer, A. & Feringa, B. L. Bright ion channels and lipid bilayers. *Acc. Chem. Res.* **46**, 2910–2923 (2013).

93. Govorunova, E. G., Sineshchekov, O. A., Li, H. & Spudich, J. L. Microbial rhodopsins: diversity, mechanisms, and optogenetic applications. *Annu. Rev. Biochem.* **86**, 845–872 (2017).
94. Zhang, F. *et al.* The microbial opsin family of optogenetic tools. *Cell* **147**, 1446–1457 (2011).
95. Maltan, L., Najjar, H., Tiffner, A. & Derler, I. Deciphering molecular mechanisms and intervening in physiological and pathophysiological processes of Ca^{2+} signaling mechanisms using optogenetic tools. *Cells* vol. 10 (2021).
96. Nguyen, N. T. *et al.* CRAC channel-based optogenetics. *Cell Calcium* **75**, 79–88 (2018).
97. Jiang, S., Wu, X., Rommelfanger, N. J., Ou, Z. & Hong, G. Shedding light on neurons: optical approaches for neuromodulation. *Natl. Sci. Rev.* **9**, (2022).
98. Xu, X., Mee, T. & Jia, X. New era of optogenetics: from the central to peripheral nervous system. *Crit. Rev. Biochem. Mol. Biol.* **55**, 1–16 (2020).
99. Nyns, E. C. A. *et al.* An automated hybrid bioelectronic system for autogenous restoration of sinus rhythm in atrial fibrillation. *Sci. Transl. Med.* **11**, 1–12 (2019).
100. Tochitsky, I. *et al.* How Azobenzene photoswitches restore visual responses to the blind retina. *Neuron* **92**, 100–113 (2016).
101. Lam, P. Y. *et al.* TRPswitch - a step-function chemo-optogenetic ligand for the vertebrate TRPA1 channel. *J. Am. Chem. Soc.* **142**, 17457–17468 (2020).
102. Fehrentz, T. *et al.* Optical control of L-type Ca^{2+} channels using a diltiazem photoswitch. *Nat. Chem. Biol.* **14**, 764–767 (2018).
103. Kerckhoffs, A., Bo, Z., Penty, S. E., Duarte, F. & Langton, M. J. Red-shifted tetra-*ortho*-halo-azobenzenes for photo-regulated transmembrane anion transport. *Org. Biomol. Chem.* **19**, 9058–9067 (2021).
104. Johnson, T. G., Sadeghi-Kelishadi, A. & Langton, M. J. A Photo-responsive transmembrane anion transporter relay. *J. Am. Chem. Soc.* **144**, 10455–10461 (2022).
105. Pravda, L. *et al.* ChannelsDB: database of biomacromolecular tunnels and pores. *Nucleic Acids Res.* **46**, D399–D405 (2018).
106. Braha, O. *et al.* Designed protein pores as components for biosensors. *Chem. Biol.* **4**, 497–505 (1997).
107. Frank, J. A. *et al.* Photoswitchable fatty acids enable optical control of TRPV1. *Nat. Commun.* **6**, (2015).
108. Schild, V. R. *et al.* Light-patterned current generation in a droplet bilayer array. *Sci. Rep.* **7**, 1–9 (2017).
109. Villar, G., Graham, A. D. & Bayley, H. A Tissue-like printed material. *Science.* **340**,

48–52 (2013).

110. Li, J. *et al.* Metal-organic frameworks as micromotors with tunable engines and brakes. *J. Am. Chem. Soc.* **139**, 611–614 (2017).
111. Pulcu, G. S., Mikhailova, E., Choi, L. S. & Bayley, H. Continuous observation of the stochastic motion of an individual small-molecule walker. *Nat. Nanotechnol.* **10**, 76–83 (2015).
112. Lewis, C. A. Ion-concentration dependence of the reversal potential and the single channel conductance of ion channels at the frog neuromuscular junction. *J. Physiol.* **286**, 417–445 (1979).
113. Gu, L.-Q., Cheley, S. & Bayley, H. Electroosmotic enhancement of the binding of a neutral molecule to a transmembrane pore. *Proc. Natl. Acad. Sci. U.S.A.* **100**, 15498–15503 (2003).
114. Klymchenko, A. S. Solvatochromic and fluorogenic dyes as environment-sensitive probes: design and biological applications. *Acc. Chem. Res.* **50**, 366–375 (2017).
115. Wang, L., Frei, M. S., Salim, A. & Johnsson, K. Small-molecule fluorescent probes for live-cell super-resolution microscopy. *J. Am. Chem. Soc.* **141**, 2770–2781 (2019).
116. Sen, A., Putra, M. H., Biswas, A. K., Behera, A. K. & Groβ, A. Insight on the choice of sensitizers/dyes for dye sensitized solar cells: a review. *Dyes and Pigments* **213**, (2023).
117. Gemen, J. *et al.* Disequilibrating azobenzenes by visible-light sensitization under confinement. *Science.* **381**, 1357–1363 (2023).
118. Moerner, W. E. A dozen years of single-molecule spectroscopy in physics, chemistry, and biophysics. *J. Phys. Chem. B* **106**, 910–927 (2002).
119. Kukura, P., Celebrano, M., Renn, A. & Sandoghdar, V. Single-molecule sensitivity in optical absorption at room temperature. *J. Phys. Chem. Lett.* **1**, 3323–3327 (2010).
120. Moerner, W. E. & Kador, L. Optical detection and spectroscopy of single molecules in a solid. *Physical Review Letters* **62**, 2535–2538 (1989).
121. Celebrano, M., Kukura, P., Renn, A. & Sandoghdar, V. Single-molecule imaging by optical absorption. *Nat. Photonics* **5**, 95–98 (2011).
122. Thyrhaug, E. *et al.* Single-molecule excitation–emission spectroscopy. *Proc. Natl. Acad. Sci. U.S.A.* **116**, 4064–4069 (2019).
123. A, G., M, Y., Ruijgrok, P. V. & M, O. Room-temperature detection of a single molecule's absorption by photothermal contrast. *Science.* **330**, 353–356 (2010).
124. Min, W. *et al.* Imaging chromophores with undetectable fluorescence by stimulated emission microscopy. *Nature* **461**, 1105–1109 (2009).
125. Piatkowski, L., Gellings, E. & Van Hulst, N. F. Broadband single-molecule excitation spectroscopy. *Nat. Commun.* **7**, 1–9 (2016).

126. Liebel, M., Toninelli, C. & Van Hulst, N. F. Room-temperature ultrafast nonlinear spectroscopy of a single molecule. *Nat. Photonics* **12**, 45–49 (2018).
127. Betzig, E. & Chichester, R. J. Single molecules observed by near-field scanning optical microscopy. *Science.* **262**, 1422–1425 (1993).
128. Svishchev, G. M. A dark-field method for measuring absorption cross sections of single molecules. *Optics and Spectroscopy (English translation of Optika i Spektroskopiya)* **97**, 340–345 (2004).
129. Feist, F. A., Tommaseo, G. & Basché, T. Observation of very narrow linewidths in the fluorescence excitation spectra of single conjugated polymer chains at 1.2 K. *Physical Review Letters* **98**, 1–4 (2007).
130. Gaiduk, A., Yorulmaz, M., Ruijgrok, P. V & Orrit, M. Room-temperature detection of a single molecule's absorption by photothermal contrast. *Science.* **330**, 353–356 (2010).
131. Chong, S., Min, W. & Xie, X. S. Ground-state depletion microscopy: Detection sensitivity of single-molecule optical absorption at room temperature. *J. Phys. Chem. Lett.* **1**, 3316–3322 (2010).
132. Stopel, M. H. W., Blum, C. & Subramaniam, V. Excitation spectra and stokes shift measurements of single organic dyes at room temperature. *J. Phys. Chem. Lett.* **5**, 3259–3264 (2014).
133. Samanta, S. *et al.* Photoswitching azo compounds in vivo with red light. *J. Am. Chem. Soc.* **135**, 9777–9784 (2013).
134. Yang, X. *et al.* Optical control of CRAC channels using photoswitchable azopyrazoles. *J. Am. Chem. Soc.* **142**, 9460–9470 (2020).
135. Matsuo, K. *et al.* Spatiotemporal regulation of CENP-E-guided chromosomes using a fast-relaxing arylazopyrazole photoswitch. *Chem. Commun.* 6611–6614 (2024) doi:10.1039/d4cc01922a.
136. Gerkman, M. A. *et al.* Arylazopyrazoles for long-term thermal energy storage and optically triggered heat release below 0 °C. *J. Am. Chem. Soc.* **142**, 8688–8695 (2020).
137. Tian, J. *et al.* A conjugated polymer containing arylazopyrazole units in the side chains for field-effect transistors optically tunable by near infra-red light. *Angew. Chem. Int. Ed.* **59**, 13844–13851 (2020).
138. Arndt, N. B., Adolphs, T., Arlinghaus, H. F., Heidrich, B. & Ravoo, B. J. Arylazopyrazole-modified thiolactone acrylate copolymer brushes for tuneable and photoresponsive wettability of glass surfaces. *Langmuir* **39**, 5342–5351 (2023).
139. Li, H. *et al.* Arylazopyrazole-modulated stable dual-mode phototransistors. *Sci. Adv.* **10**, (2024).

140. Walden, S. L., Carroll, J. A., Unterreiner, A. & Barner-kowollik, C. Photochemical action plots reveal the fundamental mismatch between absorptivity and photochemical reactivity. *Adv Sci (Weinh)* **11**, 1–8 (2024).
141. Satzger, H. *et al.* Fluorescence spectra of trans- and cis-azobenzene - emission from the Franck-Condon state. *Chemical Physics Letters* **372**, 216–223 (2003).
142. Feng Qin, Anthony Auerbach, F. S. Maximum likelihood estimation of aggregated Markov processes. *Proc. R. Soc. B* 375–383 (1997) doi:10.1214/aoap/1069786500.
143. Qin, F. & Li, L. Model-based fitting of single-channel dwell-time distributions. *Biophys. J.* **87**, 1657–1671 (2004).
144. Plakhotnik, T., Donley, E. A. & Wild, U. P. Single-molecule spectroscopy. 181–212 (1997).
145. Renge, I. Refractive index dependence of solvatochromism. *Journal of Photochemistry and Photobiology A: Chemistry* **353**, 433–444 (2018).
146. Dunn, N. J., Humphries IV, W. H., Offenbacher, A. R., King, T. L. & Gray, J. A. cis → trans isomerization rates for azobenzene dyes in aqueous solution. *J. Phys. Chem. A* **113**, 13144–13151 (2009).
147. Kortekaas, L. *et al.* Acid-catalysed liquid-to-solid transitioning of arylazoisoxazole photoswitches. *Chem. Sci.* **12**, 11338–11346 (2021).
148. Bo, Z., Lim, Z. H., Duarte, F., Bayley, H. & Qing, Y. on a *Angew. Chem.* **135**, (2023).
149. Friebel, M. *et al.* of in the 400 – 2500 . *J. Biomed. Opt.* **4**, 36–46 (1999).
150. Mira, P., Yeh, P. & Hall, B. G. Estimating microbial population data from optical density. *PLoS One* **17**, 1–8 (2022).
151. Zheng, Q. *et al.* Rational of and for *ACS Cent. Sci.* **5**, 1602–1613 (2019).
152. Nagel, G. *et al.* Cation- *Proc. Natl. Acad. Sci. U.S.A.* **100**, 13940–13945 (2003).
153. Udasin, R. *et al.* Photopharmacological modulation of native CRAC channels using azoboronate photoswitches. *Proc. Natl. Acad. Sci. U.S.A.* **119**, 1–12 (2022).
154. Hofmann, K. *et al.* Solvatochromism and acidochromism of azobenzene-functionalized poly(vinyl amines). *New Journal of Chemistry* **36**, 1655–1664 (2012).
155. Cao, Y., Dong, S., Liu, S., Liu, Z. & Guo, X. Toward functional molecular devices based on graphene-molecule junctions. *Angew. Chem. Int. Ed.* **52**, 3906–3910 (2013).
156. Hwang, J. *et al.* A single-molecule optical transistor. *Nature* **460**, 76–80 (2009).
157. Lin, Y. C., Yang, W. C., Chiang, Y. C. & Chen, W. C. *Small Sci.* **2**, (2022).